

WETI c/o Hochschule Flensburg

Postal Address:

Kanzleistraße 91-93
24943 Flensburg, Germany

Visitors:

Nordstraße 2

24937 Flensburg, Germany

Tel: +49 (0)461-48161-407

Fax: +49 (0)461 48161-131

E-mail: Laurence.alhrshy@hs-flensburg.de

Development of a Lightweight Hydraulic- Pneumatic Flywheel System for Wind Turbine Rotors

Laurence Alhrshy
Clemens Jauch
Niclas Bünning
Alois Peter Schaffarczyk

A research project in cooperation with HYDAC Technology GmbH.



Financially supported by



Gesellschaft für Energie und
Klimaschutz Schleswig-Holstein GmbH

Content

List of symbols and abbreviations	6
List of figures	10
List of tables	15
Abstract	16
Zusammenfassung.....	17
Acknowledgement	20
Contributions.....	21
1 Introduction.....	22
2 Design of a Hydraulic Pump System for the Hydraulic-Pneumatic Flywheel Accumulator in a Wind Turbine Rotor	24
2.1 System specification	24
2.2 System configuration	25
2.2.1 Pump.....	25
2.2.2 Fluid	25
2.3 Pump design	26
2.3.1 Hydraulic design	26
2.3.2 Efficiency.....	29
2.3.3 Mechanical design	29
2.3.4 Speed control.....	31
2.3.5 NPSH	33
2.3.6 Motor design	33
2.4 Moment of inertia	35
3 Modelling of Motor Driven Pump System.....	37
3.1 Modelling of Induction Motor.....	37
3.2 Modelling of Hydraulic Pump.....	40
3.2.1 Power, Torque, Speed and Pressure of Pump	40
3.2.2 Numerical Aspects	41
4 Pump Systems for the Flywheel Configurations	43
5 Controls of the Flywheel for Steadying the Power Infeed	48
5.1 General Layout of the Bypass Controller for Power Steadying.....	48

5.2	Transfer Functions.....	50
5.2.1	Block Diagram of System from P_dem to P_gen.....	50
5.2.2	Linearizations in the Block Diagram	50
5.2.3	Block Diagram Reduction	56
5.3	Transfer Function of Bypass Controller for P-Steadying	58
5.4	Transfer Function of Hydraulic FW.....	58
5.5	Transfer Function of 2 Masses Drive Train from Inspection	60
5.5.1	Drive Train Parameters.....	61
5.5.2	Mechanical Impedances	62
5.5.3	Torques Acting on Inertias.....	62
5.6	Transfer Function of Generator-Converter-Unit.....	64
5.7	Control Circuit for P-Steadying.....	65
5.7.1	Block Diagram of the Control Circuit	65
5.7.2	Transfer Functions in the Linearised Operating Points	66
5.8	P-Steadying Controller (Proportional) Design	67
5.8.1	Step Response Approach	68
5.8.2	Result from Proportional Controller Design	68
5.9	Control Strategy for P-Steadying.....	71
5.10	Flywheel Settings for Balancing Rotor	74
5.10.1	R_var Limits	74
5.10.2	R_fw Limits for P-Steadying Operation	75
5.10.3	Optimal perunit_lower_lim for Maximum Energy Yield	75
5.11	Adaptation of Simulation Time Step.....	78
6	Piston Accumulators Made of Composite Materials.....	80
6.1	Initial Carbon Fibre-Reinforced Plastics Design	80
6.1.1	Specification of Initial Carbon Fibre-Reinforced Plastics Accumulator	80
6.1.2	Durability Test of the Rigid Carbon Fibre-Reinforced Plastics Accumulator	81
6.1.3	Flywheel Configurations with Initial Carbon Fibre-Reinforced Plastics Accumulators	82
6.2	Flexible Carbon Fiber-Reinforced Plastic Designs	91
6.2.1	Need for Flexible Piston Accumulators	91
6.2.2	Bending of Conventional Piston Accumulators	91
6.2.3	Preliminary Design of Flexible Piston Accumulators	92

6.2.4	Preliminary Estimation of the Fatigue of Flexible Piston Accumulators	94
6.2.5	Specification of Flexible Carbon Fibre-Reinforced Plastics Design.....	102
6.2.6	Carbon fiber-reinforced plastic Flywheel Types	104
6.2.7	Load Analysis	108
7	Implementation of Flywheel System in OpenFAST	113
7.1	Installing and Testing of OpenFAST.....	113
7.2	Architecture of OpenFAST.....	114
7.3	Blade Structural-Dynamic Model	114
7.4	Module Structure of ElastoDyn.....	117
7.5	Data Types	117
7.6	ElastoDyn Source Code	119
7.7	Code Adjustment.....	120
7.7.1	Implementation of Variable Blade Element Mass.....	121
7.7.2	Criteria for Changing Blade Element Masses	122
7.7.3	Extension of ElastoDyn Input File	126
8	Economical Evaluation of the Hydro Pneumatic Flywheel in a Wind Turbine Rotor for the Application of Steady Power Feed-in	127
8.1	Purpose of this Chapter.....	127
8.2	Reference Wind Turbine, NREL 5-MW	127
8.3	Choice of Location	128
8.4	System Description.....	128
8.5	Working Principle	129
8.6	Advantages and Disadvantages of the Proposed FW System	131
8.7	Model in SIMULINK	131
8.8	Simulated Variables.....	132
8.9	Scenario Operating Points.....	134
8.9.1	Steadying and Non-Steadying Operation	134
8.9.2	Full Load Mode Average $v_{\text{wind}} = 20 \text{ m/s}$ and Turbulence	134
8.9.3	Reduced Power Setpoint $P_{\text{dem}} < 100 \%$	134
8.9.4	Variation of Turbulence Intensity TI	135
8.10	Simulation	138
8.10.1	Expectations	138

8.10.2	Simulation Results	139
8.11	Evaluation	148
8.12	Economical Evaluation	148
8.12.1	Energy Infeed	148
8.12.2	Outlook of Profits	149
9	Aerodynamic Investigations Aiming at Increasing Space inside the Blades.....	153
9.1	Aerodynamic Profiles with Increased Thickness to Cord Ratio	153
9.2	Impact on Blade Structure	155
9.3	Summary and Conclusion	156
	References	157

List of symbols and abbreviations

Variables and parameters of the wind turbine simulation model, with which the operation of the flywheel is simulated, are not listed here, because these are introduced in the documentation of the simulation model [1].

Abbreviation, variable, constant	Description	Unit
CAE	Computer-Aided-Engineering	
CFK	Kohlefaserverstärkten Kunststoff (German)	
CFRP	Carbon Fiber-Reinforced Plastic	
cVs	complex stator voltage	V or pu
cZrotor	Rotor impedance	Ohms or pu
DLC	Design load case	
DOF	Degree-of-Freedom	
E _{kin_fw}	Kinetic energy stored in the flywheel	Ws
EPDM	ethylene-propylene-diene-rubber	
f	grid frequency	[Hz]
FW	Flywheel	
<i>g</i>	gravity acceleration in	m/s ²
GEBT	Geometrically Exact Beam Theory	
<i>H</i>	delivery head	m
<i>H_{s geo}</i>	altitude difference between fluid level inside suction tank and the middle of pump suction nozzle	m
<i>H_{v,s}</i>	Pump head losses in pipes on the section side	m
<i>H₁</i>	delivery head at rated speed	m
<i>H₂</i>	delivery head at reduced speed	m

I_{ges}	Moment of inertia of the whole system	kg·m ²
I_M	Moment of inertia of motor	kg·m ²
I_P	Moment of inertia of pump	kg·m ²
I_S	Moment of inertia of Flywheel	kg·m ²
J	Inertia	kgm ²
J_fw_bl	Inertia of flywheel in one blade	kgm ²
J_iss	Inertia on low speed side of WT drive train	pu
m	Fluid mass	kg
n	Rotation speed	rpm
NREL	National Renewable Energy Laboratory	
NWTC	National Wind Technology Center	
NPSH	Net Positive Suction Head	
n_1	Rotational speed at outlet	rpm
n_2	Reduced rotational speed	rpm
p_b	Air pressure	N/m ²
p_D	Evaporation pressure	N/m ²
p_e	Overpressure in suction tank	N/m ²
perunit_lower_lim	Lowest charging level to which the flywheel may be discharged in P-steadying operation	
P_fw	Power produced by the flywheel	kW
P _{pump_W}	Pump power	W
pu	Per unit	
P_1	Shaft power by outlet speed	W
P_2	shaft power by reduced speed	W
Q	Volume flow	m ³ /h

Q_1	volume flow by outlet speed	m^3/h
Q_2	volume flow by reduced speed	m^3/h
rpm	Revolutions per minute	
R_{rotor}	Rotor resistance	Ohms or pu
R_{stator}	Stator resistance	Ohms or pu
$R_{\text{stator_220V}}$	Stator resistance referred to 220 V	Ohms
$R_{\text{stator_690V}}$	Stator resistance referred to 690 V	Ohms
s	Laplace operator	
s'	Altitude difference between the middle of pump suction nozzle and the middle of impeller inlet	m
slip	Slip of induction machine	-
t	Time	s
T	Torque	Nm or pu
T_{elec}	Electric torque	pu
$T_{\text{geno_PT1}}$	Time constant of PT1 equivalent of generator-converter unit	s
T_{shaft}	Mechanical torque at shaft	pu
V	Volume	m^3
v_e	Flow speed in suction tank	m/s
VS	Visual Studio	
WEA	Wind Energie Anlagen (German)	
WT	Wind Turbine	
X_{mag}	magnetising reactance	Ohms or pu
X_{rotor}	Rotor reactance	Ohms or pu
X_{stator}	Stator reactance	Ohms or pu
Z_{base}	Base impedance	Ohms

$Z_{d_dt}(s)$	Mechanical impedance of damping in drive train	pu
$Z_{J_hss}(s)$	Mechanical impedance of inertia on high speed shaft of drive train	pu
$Z_{J_lss}(s)$	Mechanical impedance of inertia on low speed shaft of drive train	pu
$Z_{s_dt}(s)$	Mechanical impedance of stiffness in drive train	pu
δ	fluid density	kg/m ³
$\eta_{P\ max}$	Efficiency at maximum power	
η_{new}	pump efficiency by reduced speed	
σ_y	circumference stress	MPa
σ_x	longitudinal stress	MPa
ε_y	circumference strain	-
ε_x	longitudinal strain	-

List of figures

Figure 1 Simplified sketch of the FW system; Left: FW in discharged state; Right: FW in charged state.	22
Figure 2: Schematic representation of pumps and motors in the hub and the blade roots of a WT.	24
Figure 3: Hydraulic performance range MP-50B [6]	27
Figure 4: Operation characteristic of e-MP50B [6]	28
Figure 5: Identification code [6]	29
Figure 6 . Characteristic of discharge nozzle [3]	30
Figure 7: Operation characteristics of 1450 rpm [6]	32
Figure 8: Machine power dependent on pump power; (x-axis) power consumption of the pump by design conditions; (y-axis) power of the drive machine relative to the power consumption of the pump by design conditions in percent [6].	34
Figure 9: Start-up methods of asynchronous motor [6]	35
Figure 10: Static equivalent circuit diagram of induction motor.	37
Figure 11: Torque and power vs. speed characteristic of induction motors.	39
Figure 12: Reactive power demand vs. rotor speed of induction motors.	39
Figure 13: Masses per blade of the motor-pump combinations for the different FW configurations and for the different desired charging durations.....	43
Figure 14: Masses per blade of the motor-pump combinations, conventional piston accumulators and fluid for the different FW configurations and for the different desired charging durations.	44
Figure 15: Masses per blade of the motor-pump combinations, conventional piston accumulators and fluid for the different FW configurations and for the different desired charging durations as percentage of the original blade mass.	45
Figure 16: Inertia per blade of the motor-pump combinations, conventional piston accumulators and fluid for the different FW configurations and for the different desired charging durations.	46
Figure 17: Inertia per blade of the motor-pump combinations, conventional piston accumulators and fluid for the different FW configurations and for the different desired charging durations as percentage of the original blade inertia.	46
Figure 18: Electric active power consumed by the motors of all three blades for the different FW configurations and for the different desired charging durations.	47
Figure 19 Overview block diagram of WT with controllable FW in its rotor. Variable names are introduced in the documentation of the simulation model [1].	49
Figure 20 Full block diagram of WT with P-Steadying Bypass controller. Variable names are introduced in the documentation of the simulation model [1].	50
Figure 21 flowrate as a function of the integrated fluid acceleration. Variable names and parameter names (red) are introduced in the documentation of the simulation model [1].	51
Figure 22 R_var as a function of the integrated flowrate. Variable names and parameter names (red) are introduced in the documentation of the simulation model [1].	51
Figure 23 R_var and the slope of R_var as a function of the integrated flowrate, i.e. Vol_fluid_tank2. .	52

Figure 24 R_var vs. Vol_fluid_tank2 and its linearization in different operating points.	52
Figure 25 Top: J_fw_SI_bl as a function of R_var^2 for finding appropriate linearizations. Bottom: only the points of linearization are shown.	54
Figure 26 P_table_pu as a function of speed_gen for finding appropriate linearisations.....	55
Figure 27 Block diagram with simplifying assumptions. Bottom: resulting block diagram for deriving transfer functions. Variable names are introduced in the documentation of the simulation model [1].	57
Figure 28 Block diagram for deriving the transfer functions. Variable names and parameter names (red) are introduced in the documentation of the simulation model [1]......	58
Figure 29 Block diagram of linearized J_fw_SI_bl from flowrate model. Block diagram simplification by reorganisation in three steps: from top to bottom. Variable names are introduced in the documentation of the simulation model [1]......	59
Figure 30 Block diagram of linearized FW model. Variable names and parameter names (red) are introduced in the documentation of the simulation model [1].	60
Figure 31 Diagram of two masses spring and damper representation of drive train. Variable names and parameter names are introduced in the documentation of the simulation model [1].	61
Figure 32 Free-body diagrams of drive train inertias for two masses model.	63
Figure 33 Bode plot of derived transfer function <i>G2mDTs = speed_gensTs</i>	64
Figure 34 Block diagram of linearized generator-converter model. Variable names are introduced in the documentation of the simulation model [1].	65
Figure 35 Block diagram of closed P-steady control loop. Top: combination of all linearized transfer functions. Bottom: Rearranged block diagram with closed control loop that contains linear components only.	66
Figure 36 Bode diagrams of open P-steady control loop.	67
Figure 37 Block diagram of P-controller.	68
Figure 38 Bode plots for all operating points and all K_P_bypass_Psteady gains as shown in Table 8....	70
Figure 39 Pole-Zero plots of closed loop transfer functions of all operating points and all K_P_bypass_Psteady gains as shown in Table 8. Top: full size, bottom: only fraction near imaginary axis.	71
Figure 40 Simplified flow chart of power steadying control strategy.	72
Figure 41 Flow chart of P-steadying control strategy.	73
Figure 42 Inertia of FW in one blade, kinetic energy in the whole FW and power from the whole FW. .	76
Figure 43 250s scenario for finding the optimal perunit_lower_lim value. The simulation shown here is conducted with perunit_lower_lim = 0.5.....	77
Figure 44 Energy yield versus perunit_lower_lim (top). R_var limits of blade 1, 2 and 3 versus perunit_lower_lim (bottom).	78
Figure 45 Adaptation of the simulation step size to avoid numerical oscillations.	79
Figure 46: Prototype of rigid CFRP accumulator without liner.	81
Figure 47: Prototype of rigid CFRP accumulator failed in durability test.....	82
Figure 48 Masse of piston accumulator type I	83

Figure 49 Masse of piston accumulator type IV.....	83
Figure 50 Masse of piston accumulator type VI.....	84
Figure 51 Masse of piston accumulator type VII.....	84
Figure 52 Masse of piston accumulator type VIII.....	85
Figure 53 Masse of lighter piston accumulator type I.....	86
Figure 54 Masse of lighter piston accumulator type IV	87
Figure 55 Masse of lighter piston accumulator type VI	87
Figure 56 Masse of lighter piston accumulator type VII	88
Figure 57 Masse of lighter piston accumulator type VIII	88
Figure 58 Comparison of changing in ultimate loads between steel accumulator and lighter CFRP accumulator	89
Figure 59 Comparison of changing in fatigue loads between steel accumulator and lighter CFRP accumulator	90
Figure 60 For illustration strongly exaggerated visualization of a bent rotor blade section.	91
Figure 61 Illustration of a bent piston accumulator in side view (not to scale).	92
Figure 62 Cylinder made of an isotropic material. Left: in resting position with circular cross section. Right: bent in longitudinal direction, which turns the cross section into an ellipse.	92
Figure 63 Qualitative illustration of the different winding directions that can be applied in the manufacturing process of a CFRP cylinder. (The angles are only examples for illustrating the concept.)	93
Figure 64 Flexible piston. Left: with naming of components. Right: in bent state.	94
Figure 65: Blade model as viewed in the NuMAD GUI.....	96
Figure 66: PreComp main input file	97
Figure 67: PreComp output file	98
Figure 68: (a) flap deflection, slope and curvature of the first eigenmode of the considered WT blade; (b) Location of tip accumulator of type I (c) Location of tip accumulators of type IV (d) Location of tip accumulators of type VI	100
Figure 69: (a) flap deflection, slope and curvature of the second eigenmode of the considered WT blade; (b) Location of tip accumulator of type I (c) Location of tip accumulators of type IV (d) Location of tip accumulators of type VI	101
Figure 70: A prototype of a CFRP piston accumulator with a steel liner on the inner surface of the CFRP tube.	103
Figure 71: Cross sections of the Sandia 61.5 m blade at the 38 blade nodes and the piston accumulators with fluid pipe of (a) FW type I; (b) FW type IV; (c) FW type VI	106
Figure 72 Masse comparison of blade tip and blade root accumulators from steel and from CFRP with steel liner for (a) type I; (b) type IV; (c) type VI.....	108
Figure 73 Comparison of changes in ultimate loads between steel accumulator and CFRP with metal liner accumulator, both with respect to the ultimate loads of the original WT without FW system	110

Figure 74 Comparison of changes in fatigue loads between steel accumulator and CFRP with metal liner accumulator, both with respect to the ultimate loads of the original WT without FW system.	111
Figure 75 Architecture of FAST 8 [27].....	115
Figure 76: Coupled interaction between BeamDyn, ElastoDyn and FAST [26]	116
Figure 77: Inputs, Outputs, States and Parameters for ElastoDyn (left) and for BeamDyn (right) [27] .	116
Figure 78: Subroutines required for the FAST modular framework [29]	117
Figure 79: Derived data types required for the FAST modular framework [29]	118
Figure 80: Schematic body text diagram of ElastoDyn source code	119
Figure 81: An example for blade input file of NRELOffshrBsline5 MW_Blade.dat	120
Figure 82: Blade element mass addition via the local signal criterion.....	123
Figure 83: Extreme blade element mass addition via the external signal criterion.....	125
Figure 84: Example for an extended ElastoDyn input file	126
Figure 85: Properties NREL 5-MW [17]	128
Figure 86: Hydraulic–pneumatic FW system in a WT rotor. Discharged state (left) and charged state (right) [30]	129
Figure 87: Block diagram of the WT model.....	131
Figure 88: Power curve of NREL-5 MW	133
Figure 89: NREL 5-MW pitch angle control [17].....	133
Figure 90: Hydraulic fluid system of one rotor blade [33]	134
Figure 91: Turbulence intensity TI [-] versus wind speed [m/s] [38]	136
Figure 92: Block diagram of wind model [1]	136
Figure 93: Comparison of different values of timeconstant (average $v_{wind} = 20$ m/s).....	137
Figure 94: Comparison of different values of magnitude (average $v_{wind} = 20$ m/s).....	138
Figure 95: Full load operation ($v_{wind} = 20$ m/s): different signals.....	139
Figure 96: Full load operation ($v_{wind} = 20$ m/s): variable distance R_{var}	141
Figure 97: Reduced power setpoint ($v_{wind} = 10$ m/s): different signals	141
Figure 98: Reduced power setpoint ($v_{wind} = 10$ m/s): variable distance R_{var}	143
Figure 99: Reduced power setpoint ($v_{wind} = 20$ m/s): different signals	143
Figure 100: Reduced power setpoint ($v_{wind} = 20$ m/s): variable distance R_{var}	144
Figure 101: Varying turbulence intensities from different values of <i>timeconstant</i> ($v_{wind} = 20$ m/s, <i>magnitude</i> = 250)	145
Figure 102: Varying turbulence intensities from different values of <i>timeconstant</i> ($v_{wind} = 20$ m/s, <i>magnitude</i> = 250)	145
Figure 103: Varying turbulence intensities from different values of <i>timeconstant</i> ($v_{wind} = 20$ m/s, <i>magnitude</i> = 250)	146
Figure 104: Varying turbulence intensities from different values of <i>timeconstant</i> ($v_{wind} = 20$ m/s, <i>magnitude</i> = 250)	147

Figure 105: Varying turbulence intensities from different values of <i>timeconstant</i> ($v_{wind} = 20$ m/s, <i>magnitude</i> = 250)	147
Figure 106: Varying turbulence intensities from different values of <i>timeconstant</i> ($v_{wind} = 20$ m/s, <i>magnitude</i> = 250)	148
Figure 107: Relative thickness distribution (t/c) as function of relative blade-length. r is the distance from the rotational center, R_tip is the radius from the rotational centre to the tip.	153
Figure 108: Power and thrust versus t/c for pitch angle of 0 deg.	154
Figure 109: Geometrical shape of three most outer profiles from.	156

List of tables

Table 1 Volume flow for different accumulator types for charging times 20, 40 and 60 seconds [11]....	25
Table 2: Fluid properties for Clykosol N [5]	26
Table 3: data sheet of charging pump [3]	29
Table 4: Single phase equivalent circuit parameters in pu and base impedance in Ω of induction machine models	38
Table 5 Different operating points for linearization.	52
Table 6 Operating points for linearization.	53
Table 7 Operating points for linearization.	55
Table 8 K_P _bypass_ P_{steady} gains for the different operating points.	68
Table 9 Settling times in seconds for the different operating points.	69
Table 10 % overshoot for the different operating points.	69
Table 11 Laminate lay-up and the material properties of the CFRP with steel liner prototype	103
Table 12 Flexible piston accumulator prototype dimensions	104
Table 13 Properties of the CFRP piston accumulators of the three FW types.....	105
Table 14 Properties of the CFRP and the conventional piston accumulators of the three FW types.....	106
Table 15: Turbulence classes.....	136
Table 16: Switching operations of power demand P_{dem} [10].....	142
Table 17: Energy infeed [kWh] of the 250 s simulations of non-steadying (charged/discharged) and steadying operation (v = average wind speed, t_c = <i>timeconstant</i> , m = <i>magnitude</i>).....	149
Table 18: Annual revenue [€/a] in non-steadying (charged/discharged) and steadying operation (v = average wind speed, t_c = <i>timeconstant</i> , m = <i>magnitude</i>) for the initial remuneration of 0.149 €/kWh	150
Table 19: Annual revenue [€/a] in non-steadying (charged/discharged) and steadying operation (v = average wind speed, t_c = <i>timeconstant</i> , m = <i>magnitude</i>) for the optional remuneration of 0.184 €/kWh	150
Table 20: Annual revenue [€/a] in non-steadying (charged/discharged) and steadying operation (v = average wind speed, t_c = <i>timeconstant</i> , m = <i>magnitude</i>) for the basic remuneration of 0.039 €/kWh	151
Table 21: Power and thrust as calculated with w_{t_perf} for the original and for the modified blades...	154
Table 22: Basic geometrical properties of used profiles.	155

Abstract

This report describes the results of a research project conducted by the Wind Energy Technology Institute of Flensburg University of Applied Sciences in cooperation with HYDAC Technology GmbH. This project was financially supported by the Gesellschaft für Energie und Klimaschutz Schleswig-Holstein GmbH (EKSH). The project aimed to develop a lightweight hydraulic-pneumatic flywheel system in wind turbine rotors. The flywheel system enables a wind turbine to vary the inertia of its rotor blades to control the power output and, most importantly, to influence the vibratory behaviour of wind turbine components. The method used for developing the lightweight hydraulic-pneumatic flywheel system is based on the one hand on the design of flexible lightweight hydraulic-pneumatic piston accumulator, and on the other hand, on the design of a bypass controller to control the flywheel system for steadying power infeed. For designing the bypass controller pump-motor combinations are implemented for different flywheel configurations. Due to the proposed design of the flywheel system, the impact on the mechanical loads of a wind turbine is analysed. The simulation results show that the new design of the piston accumulators causes a lower impact on the mechanical loads of the wind turbine than a previously published design of piston accumulators made of steel and aluminium. It is further shown that the considered wind turbine can take on the flywheel system without the need for reinforcements in the rotor blades. Simultaneously, investigations for modifying the geometrical blade shapes are performed, with the intention to increase the installation spaces of the flywheel system inside the rotor blade of a wind turbine. Finally, an economical evaluation shows the yielded additional energy and the financial savings of a wind turbine with flywheel system in some selected operation points.

Zusammenfassung

Ziel des Forschungsprojektes “Entwicklung eines hydropneumatischen Schwungradspeichersystems für Windenergieanlagenrotoren” ist die Weiterentwicklung eines Systems, durch welches Windenergieanlage (WEA) einen Beitrag zur Systemträgheit leisten und unerwünschte Schwingungen in den Rotorblättern und im Turm einer WEA vermieden werden.

Mit der Dekarbonisierung der Energiesysteme werden immer mehr Kern- und Kohlekraftwerke durch erneuerbare Energie, wie Photovoltaik- und WEA, ersetzt. Allerdings verliert das Stromnetz durch diesen positiven Trend einen wesentlichen Teil seiner Trägheit, welche aber sehr notwendig ist, um die Stabilität im Netz zu gewährleisten. Da WEA im Vergleich zu konventionellen Kraftwerken über Frequenzumrichter mit dem Stromnetz verbunden sind, tragen sie nicht zur Systemträgheit bei. Seit einigen Jahren wird am Institut für Windenergietechnik (WETI) der Hochschule Flensburg ein hydraulisch-pneumatischer Schwungradspeicher im Rotor einer WEA entwickelt, der das Ziel verfolgt einen Beitrag zur Systemträgheit leisten zu können, und gleichzeitig das Schwingungsverhalten der WEA positiv zu beeinflussen. Die Entwicklung des Systems ist so weit fortgeschritten, dass in diesem Forschungsprojekt, gemeinsam mit der Firma HYDAC Technology GmbH, eine Weiterentwicklung auf Komponentenebene durchgeführt werden konnte. Dieses Projekt wurde von der Gesellschaft für Energie und Klimaschutz Schleswig-Holstein GmbH (EKSH) finanziell gefördert.

Die bisher vorgesehenen Speicher für das Schwungradsystem sind überwiegend aus Stahl und Aluminium gefertigt. Da es beim Einsatz in Rotorblätter von WEA sehr wichtig ist die stationären Massen der Speicherkomponenten so gering wie möglich zu halten, um den Einfluss auf die Lasten der WEA zu minimieren, hat sich der Optimierungsfokus in diesem Projekt auf den Stahlmantel des Speicherzylinders gerichtet, welcher einen enormen Beitrag zum gesamten Gewicht des Speichers leistet. HYDAC stellt bereits heute Leichtbauspeicher für die Luftfahrt- und die Fahrzeugindustrie her. Allerdings müssen die Leichtbauspeicher für die Anwendung in WEAs für größere Verschiebevolumen entwickelt werden. Um das zu erreichen, hat HYDAC einen ersten Prototyp eines Leichtbaukolbenspeichers mit relativ großem Volumen gebaut, dessen Zylinder ausschließlich aus kohlefaserverstärkten Kunststoff (CFK) besteht. Allerdings müssen Kolbenspeicher nicht nur leicht, sondern auch flexible sein, um in Rotorblätter von WEA eingebaut werden zu können. Das liegt daran, dass die Rotorblätter einer WEA im Betrieb durch die aerodynamischen Kräfte stark verbogen werden. Das heißt, wenn ein Kolbenspeicher nah der Blattspitze in das Blatt eingebaut werden soll, muss sich dieser Kolbenspeicher im Betrieb ebenfalls verbiegen lassen. Verbiegung von Kolbenspeicher ist jedoch nach derzeitigem Stand der Technik nicht erlaubt, weil dabei der Kolben klemmt und/oder undicht wird.

Um das Problem zu lösen, entwickelt HYDAC in Zusammenarbeit mit dem WETI einen Kolbenspeicher, der sowohl leicht als auch flexible ist. Diese besonderen Eigenschaften des Kolbenspeichers werden erreicht durch die Umwicklung eines dünnwandigen Metallrohrs (dem sogenannten Liner) mit Kohlenfasern in verschiedenen Wickelrichtungen. Durch diese Konstruktion ist sichergestellt, dass der Zylinder des Kolbenspeichers auf der einen Seite leicht ist, und auf der anderen Seite die gewünschten mechanischen Eigenschaften zeigt, wenn er verbogen wird. Damit der Kolben in einem verbogenen Zylinder nicht klemmt, muss er ebenfalls flexibel ausgeführt werden. Das wird erreicht, indem der Kolben aus drei flexibel miteinander verbundenen Scheiben besteht, die mit einem Dichtring am Umfang den

Spalt zum Liner abdichten. Dieser neuartige Kolben kann sich an die Biegungen des Kolbenspeichers anpassen. Vollständige Prototypentests des flexiblen Speichers im Prüffeld von HYDAC waren für den Sommer 2020 geplant. Allerdings können, aufgrund der Coronavirus-Pandemie, die Versuche voraussichtlich erst Ende des Jahres abgeschlossen werden.

Angelehnt an die Geometrie des flexiblen Kolbenspeicher Prototyps, wurden die Geometrien der verschiedenen Schwungradspeicherkonfigurationen hergeleitet. Drei Schwungradspeicherkonfigurationen sind ausgewählt, die die meistrelevanten Installationsorte nah der Blattwurzel, der Blattmitte, und der Blattspitze darstellen. Diese drei Speicherkonfigurationen sind im Programm COMPOSITOR modelliert, um zu prüfen, dass die maximalen Ausdehnungen der Speicher unter dem Betriebsdruck nicht überschritten werden. Dabei werden sowohl der Laminatplan, als auch die Materialeigenschaften des Kolbenspeicher Prototyps berücksichtigt. COMPOSITOR ist ein computergestütztes Designwerkzeug, das von dem Institut für Kunststoffverarbeitung an der Uni RWTH Aachen entwickelt wurde, und bei HYDAC angewendet wird. Die aus den Modellen berechneten stationären Massen der flexiblen Speicher zeigen eine eindeutige Gewichtsreduktion im Vergleich zu den konventionalen Speichern aus Stahl und Aluminium.

Um die Auswirkung der Gewichtsreduktion der flexiblen Speicher auf die mechanischen Lasten der WEA zu quantifizieren, wurden Lastsimulationen der WEA mit konventionalem Schwungradspeicher, mit flexiblem Schwungradspeicher, und ohne Schwungradspeicher durchgeführt. Diese Simulationsergebnisse werden zum direkten Vergleich einander gegenübergestellt. Der Lastenvergleich zeigt, dass durch den Einsatz der flexiblen Speicher sowohl die Extremlasten als auch die Ermüdungslasten an allen WEA Komponenten sinken. Das führt dazu, dass beim Einsatz von flexiblen Schwungradspeichern keine Notwendigkeit zu Strukturverstärkungen besteht, weder an Rotorblättern noch am Turm.

Die durchgeführten Lastsimulationen können das Schwungradsystem entweder im geladen oder im entladenen Zustand berücksichtigen. Das dynamische Verändern des Ladezustandes des Schwungradspeichers ist während der Lastsimulation nach derzeitigem Stand nicht möglich. Diese Beschränkung liegt daran, dass keines der derzeit am Markt verfügbaren Lastsimulationsprogramme in der Lage ist das Massenträgheitsmoment und die Steifigkeiten der Rotorblätter während der Simulation zu verändern. Eine solch umfangreiche Erweiterung der Funktionalität eines Simulationsprogramms würde erfordern, den Quelltext des Programmes umfangreich zu ändern. Aus diesem Grund wird im Rahmen dieses Projekt untersucht, wie der Quelltext von dem Lastsimulationsprogramm OpenFAST geändert werden muss, um das dynamischen Verhalten des Schwungradsystems implementieren zu können. OpenFAST ist ein open-source WEA Lastsimulationswerkzeug, welches von dem National Renewable Energy Laboratory in den USA entwickelt wurde. Bis zum Abschluss dieses Projektes konnten der Quelltext des Programms soweit angepasst werden, dass variablen Massen an beliebigen Blattknoten während einer laufenden Simulation gesteuert werden. Basierend auf dieser Anpassung wird in zukünftigen Arbeiten das Schwungradsystem mit einer geeigneten Reglungsfunktion verlinkt, um dessen Verhalten in OpenFAST dynamisch simulieren zu können.

Bevor ein Regler für das Schwungradsystem entwickelt wird, müssen zuerst die physikalischen Komponenten des gesteuerten Systems, hier vor allem die Aktoren, bestimmen werden. Deshalb wurden

im Rahmen einer Projektarbeit von zwei Bachelor Studenten des Studiengangs „Energiewissenschaften“ verschiedene am Markt verfügbare Motoren-Pumpen Kombinationen zusammengestellt und analysiert. Diese Kombinationen sind an die verschiedenen Konfigurationen des Schwungradsystems angepasst.

Um den Einfluss der verschiedenen Motor-Pumpe Kombinationen auf das Verhalten der Referenz WEA zu analysieren, werden diese Kombinationen in Matlab/Simulink modelliert. Die Simulationsergebnisse zeigen, dass, obwohl die Massen der Motor-Pumpeneinheiten einen großen Einfluss auf die Gesamtmasse des Rotors haben, sich ein kaum spürbarer Einfluss auf die Trägheit des Rotors ergibt. Das konnte durch den Installationsort der Motor-Pumpeneinheiten in den Blattwurzeln erreicht werden.

Der für das Schwungradsystem entwickelte Controller muss in der Regel die Motor-Pumpeneinheit nur beim Ladevorgang steuern. Beim Entladevorgang werden die Pumpen nicht gebraucht, da in diesem Betriebsmodus das komprimierte Gas im Blattspitzenspeicher das Fluid in den Speicher in der Blattwurzel verschiebt. Um das Entladen zu steuern, werden hydraulische Ventile in der Leitung zwischen dem Speicher in der Blattwurzel und der Blattspitze angesteuert. Diese Ventile können sowohl die Verbindung unterbrechen, als auch die Pumpe bypassen. Aus diesem Grund heißt dieser Controller Bypass Controller. Mit dem Bypass Controller können vielfältige Regelungsfunktionalitäten umgesetzt werden. Der in diesem Projekt entwickelte Bypass Controller hat das Ziel die Leistung, die die WEA ins Netz einspeist, zu verstetigen. Bei der Leistungsverstetigung handelt es sich um Energiespeicherung, wenn die Windgeschwindigkeit über die Nennwindgeschwindigkeit steigt, und um Energiefreisetzung, wenn die Windgeschwindigkeit temporär unter ihren Nennwert sinkt. Bei der Auslegung des Bypass Controller wurden die Reglerverstärkungen in Abhängigkeit der Übertragungsfunktion der Regelstrecke bestimmt. Da das gesamte System hochgradig nichtlinear ist mussten Bereiche identifiziert werden in denen das System linearisiert werden konnte. Über den dynamischen Regler hinaus beinhaltet der Bypass Regler auch eine Regelungsstrategie für die Leistungsverstetigung die auch die Auswuchtung des Rotors beinhaltet.

Die wirtschaftliche Auswirkung der Leistungsverstetigung auf das Verhalten der WEA wurde im Rahmen einer Abschlussarbeit eines Studenten des Studiengangs „Energiewissenschaften“ analysiert. Dabei werden verschiedenen Simulationsszenarien vorgestellt, und der Mehrertrag der WEA durch den Einsatz von dem Schwungradsystem wirtschaftlich bewertet.

Im Laufe des Projektes wurde an der Fachhochschule Kiel eine Methode entwickelt, um den Installationsbauraum für das Schwungradsystem in einem Rotorblatt zu vergrößern. Die Methode basiert darauf, dass dickere Blattprofile, die normalerweise nur näher an der Blattwurzel eingesetzt werden, auf weiter außen liegende Blattsegmente extrapoliert werden. Dadurch erhalten die Blattsegmente in denen ein Kolbenspeicher installiert werden könnte einen größeren Bauraum. Der Einfluss solcher Blattgeometrieänderungen auf den Energieertrag und den Schub einer WEA wurde mit Hilfe der Blatt-Element-Momentum-Theorie untersucht.

Acknowledgement

The Authors would like to thank the Gesellschaft für Energie und Klimaschutz Schleswig-Holstein GmbH (EKSH) for the financial support of the project number 8/12-20. Special thanks also goes to the project partner HYDAC Technology GmbH. Their contribution in the form of Know-How, work performance, design and construction of prototypes, as well as prototype tests went far beyond the initially agreed commitment. Furthermore, HYDAC Technology GmbH also financed the project extension by one month.

The Authors would also like to thank Marcel Maack and Nico Thomsen who contributed and supported this project with their student research project. Last, but certainly not least, all staff members of the Wind Energy Technology Institute spent many hours in open and frank discussions, and by doing so contributed to the success of this project. The authors are also very grateful for that.

Contributions

Not all authors contributed equally to all sections of this report. Instead, each author is responsible for the content of the sections listed in the following.

Laurence Alhrshy contributed with the sections 1 and 7. He also translated the text in section 2 to English, which originates from a student project report that was written in German by Marcel Maack and Nico Thomsen.

Laurence Alhrshy and Clemens Jauch created section 6 together.

Clemens Jauch contributed with the sections 3, 4 and 5.

Niclas Bünning composed most of the text of section 8, which originates from his Bachelor thesis. Laurence Alhrshy fitted the text in the final report format. Clemens Jauch did the simulations and supplemented the text contained in section 8.

Alois Peter Schaffarczyk contributed with section 9.

1 Introduction

For many years, the Wind Energy Technology Institute (WETI) of Flensburg University of Applied Science has been developing a hydraulic-pneumatic flywheel (FW) system in the rotor of a wind turbine (WT). The general idea of the FW system is based on the variation of the inertia of the rotor blades in a WT. This is done by moving a fluid mass between two piston accumulators in the rotor blade (see Figure 1).

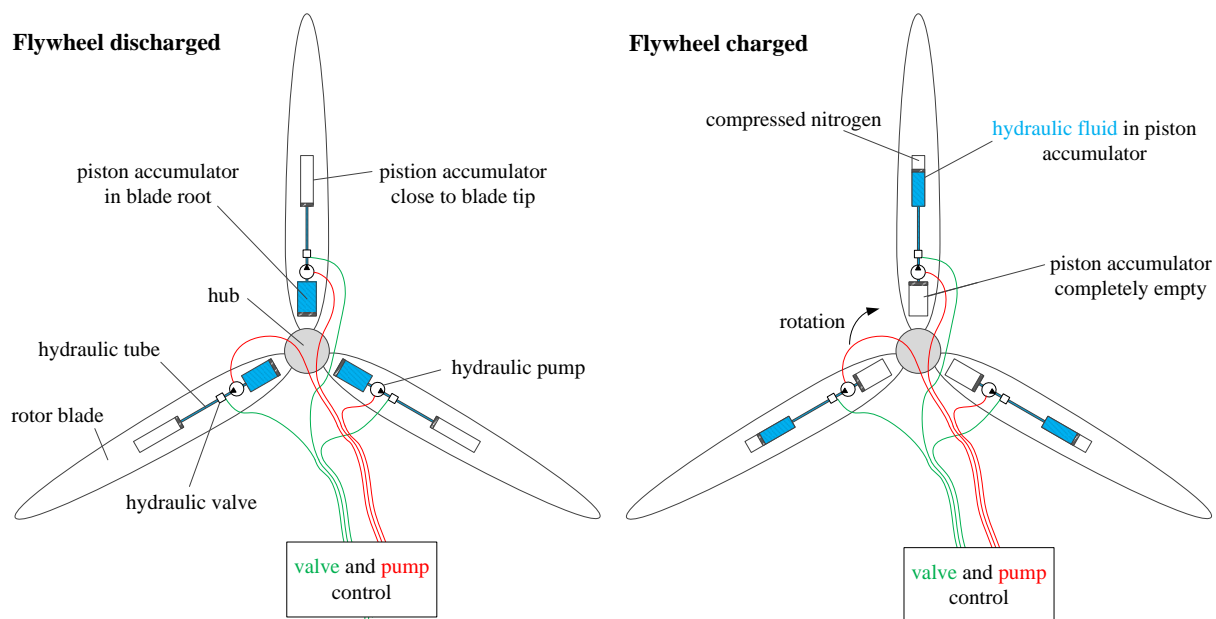


Figure 1 Simplified sketch of the FW system; Left: FW in discharged state; Right: FW in charged state

Kinetic energy is stored or released by varying the inertia of the rotor blades, which allows a certain variation of the electrical power of the WT, independent of the prevailing wind conditions. Additionally, and most importantly, the vibratory behaviour of the WT can be influenced. The physical description of such an energy storage system is introduced in previous work of the authors, and this covers the kinetics [22] and the hydraulics [30].

As most of the conventional hydraulic piston accumulators are made of steel, the initial design of the piston accumulator for the FW system was made of steel, too. This increases the additional stationary masses of the FW system enormously, and thus the total mass of the rotor blade. Moreover, conventional steel accumulators are not designed to bend with the rotor blade bending. Hence, in the initial design of the FW system, the dimensions of the accumulators, and the location where the accumulators are located in the rotor blades, are chosen such that the accumulators are never bent, even when the rotor blades are bent most [11]. Because of these two disadvantages, conventional steel accumulators are less suitable for installation in the rotor blades of a WT. Consequently, the intention of the research conducted in this project is to design a new piston accumulator for the FW system, that is lighter than steel accumulators on the one hand, and which, on the other hand, allows the piston accumulator to be bent whenever the rotor blade is bent. The challenge of bending a piston accumulator is to prevent the piston from getting stuck and to prevent gas leakages across the piston rings. Carbon fibre-reinforced plastic (CFRP) is a material which is lighter and at the same time more

bending-flexible than steel. Also, rotor blades of WT are made of composite material. This offers better options for attaching the CFRP accumulators to the structure of a rotor blade, compared to steel accumulators. One of the biggest unsolved problems related to conventional steel accumulators is that their attachment to the rotor blade structure should allow the rotor blade to bend around the accumulator without inflicting a bending moment on the accumulator. Since this problem could so far not be solved in an economically feasible manner, steel accumulators were abandoned. Consequently, the focus shifted to the design of flexible CFRP accumulators that are allowed to be bent and that can be attached to the rotor blade structure along their entire length.

This report summarises the results of the research project “Development of a Lightweight Hydraulic-Pneumatic Flywheel System for Wind Turbine Rotors” conducted by WETI in cooperation with HYDAC Technology GmbH. The structure of this report roughly follows the work packages as defined in the project plan.

In chapter 2 the specifications of five hydraulic pump systems are discussed as a part of the project thesis of two bachelor students from the course “Energiewissenschaften” at Flensburg University of Applied Science [2]. In order to drive the hydraulic pumps that are introduced in chapter 2 induction motor models are designed and presented in chapter 3. The different motor-pump combinations resulting from chapter 2 and chapter 3 are implemented in chapter 4. The implementation depends on the FW configurations in rotor blade of the 5 megawatt (MW) WT of the National Renewable Energy Laboratory (NREL) and on the desired charging time (20 s, 40 s or 60 s). In chapter 5 a bypass controller is developed that controls the FW system for steadying power infeed. The controller does the power steadying by storing energy in the FW whenever the power in the wind exceeds the demand power, and by releasing energy from the FW whenever the power in the wind drops below the demand power. A flexible piston accumulator for application in the FW system in a WT is developed in chapter 6. Due to the proposed new design of the piston accumulator the FW system should cause less impact on the mechanical loads of the WT. Furthermore, the considered WT should take on the FW system without the need for reinforcements in the rotor blades. In chapter 7 the implementation of the dynamic behaviour of the FW system in a load simulation tool is discussed. For this purpose the blade structural properties have to be changed dynamically during a load simulation. Chapter 3, 4, 5, 6 and 7 were in the scope of work of WETI. As a part of a bachelor thesis of a bachelor student from the course “Energiewissenschaften” of Flensburg University of Applied Science an economical evaluation of the FW system in a WT rotor blades is summarised in chapter 8. The evaluation should show a trend for the economic potential of the FW system in some selected operation points of a WT. Finally, chapter 9 summarizes investigations for modified geometrical blade shapes of the NREL’s 5 MW reference blade with increased thicknesses close to the blade tip. This increases the spaced for installing piston accumulators inside the rotor blade. The consequences of such drastic changes in the aerodynamic design are the investigated impact on the energy yield and on the thrust of the WT. This work is done at University of Applied Sciences Kiel.

2 Design of a Hydraulic Pump System for the Hydraulic-Pneumatic Flywheel Accumulator in a Wind Turbine Rotor

The hydraulic pumps to charge the FW shall be located partly in the blade root and partly in the hub, see Figure 2. As indicated in Figure 2, the centre of gravity of each of these motor-pump units is at the rotor radius of the blade flanges.

As a part of the project thesis [2] of two bachelor students from the course “Energiewissenschaften” the specification of five hydraulic pump systems will be discussed in this chapter.

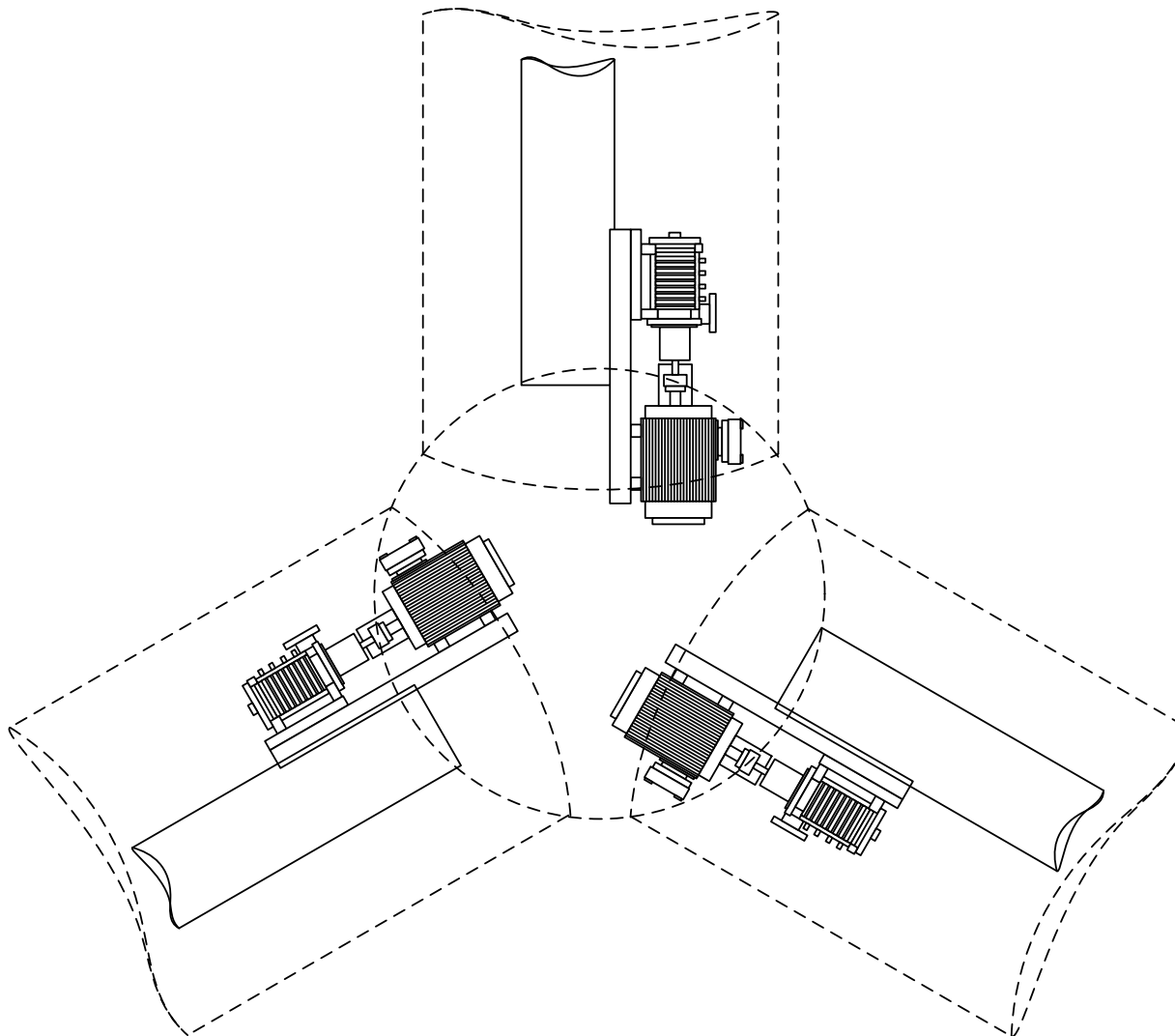


Figure 2: Schematic representation of pumps and motors in the hub and the blade roots of a WT.

2.1 System specification

The proposed pump system should be mounted inside a WT rotor, see Figure 2, and it has to pump fluid from the blade-root-accumulator to the blade-tip-accumulators. Pumping fluid in the opposite direction within 20 seconds takes place through compression of nitrogen in the blade-tip-accumulator. The five pump systems vary according to fluid mass, number of accumulators, and position of these accumulators in blade tip.

Ideally the pump system should pump the total fluid mass in 20 seconds in both directions. However, the charging time is extended to 40 and 60 seconds to ensure a wider selection of pump systems.

2.2 System configuration

All necessary steps to select and dimensioning the adequate pump, motor and fluid for charging time from 20 to 60 Seconds are illustrated in the following sections. Subsequently five systems are chosen according to the selection criteria below.

2.2.1 Pump

The maximum volume flow and pressure are needed to determine the dimension of the pump. Equation 1 defines volume flow according to charging time, fluid mass and fluid density.

$$Q = \frac{m}{\delta \cdot t} \quad \text{Equation 1}$$

Where Q is the volume flow in [m³/h], δ is the fluid density in [kg/m³], m is the mass in [kg] and t is the time in [s]

Table 1 Volume flow for different accumulator types for charging times 20, 40 and 60 seconds [11]

Type	Pressure at rated speed [bar]	fluid mass [kg]	Volume flow [l/min] [60s]	Volume flow [l/min] [40s]	Volume flow [l/min] [20s]
I	16.34	1302.77	1302.77	1954.160597	3908.321
IV	36.74	518.56	518.56	777.8433737	1555.687
VI	21.87	925.52	925.52	1388.274425	2776.549
VII	38.15	736.71	736.71	1105.066387	2210.133
VIII	38.21	651.48	651.48	977.214686	1954.429

The desired pump for the aspired system can be determined according to calculated volume flow and pressure in Table 1.

2.2.2 Fluid

When selecting a suitable fluid for the system there are many properties that have to be considered.

The fluid density should be as high as possible, in order to reduce the volume of the accumulator.

$$V = \frac{m}{\delta} \quad \text{Equation 2}$$

Where V is the Volume in [m³], m is the mass in [kg] and δ is the density in [kg/m³]

Additionally, frost and corrosion protection must be assured.

In order to reduce the required power and pressure losses, the kinetic viscosity of fluid at operation temperature should not be greater than 20 mm²/s (Newtonian fluid).

It is found that water-glycol-mixture is one which has the suitable fluid properties for the FW system.

In this work the water-glycol-mixture "Clykosol N" is used, the corresponding fluid properties are shown in Table 2.

Table 2: Fluid properties for Clykosol N [5]

Antifreeze [C°]	Concentration [%]	Temperature [C°]	Density [kg/m ³]	Dynamic viscosity [MPa*s]	Kinematic viscosity [mm ² /s]
-30	44	-30	1090	44.47	40.8
		-20	1086	21.89	20.16
		20	1066	3.46	3.25

When kinematic viscosity is greater than 20 mm²/s, the Reynolds number reduces and the pressure losses increase. Hence, to keep Clykosol N within the range of Newtonian fluids, correction factors have to be multiplied by delivery head, volume flow and efficiency. For this reason shaft power has to be reassessed.

Table 2 shows that at operating temperatures < -20 °C the kinetic viscosity becomes greater than 20 mm²/s. Hence, to avoid extra losses and extra power consumption the operating temperature has to be kept above -20 °C.

2.3 Pump design

2.3.1 Hydraulic design

The estimated data from Table 1, i.e. the volume flow Q, delivery head H and grid frequency f enable further parameters of pump from the characteristic diagrams to be extracted.

EXAMPLE FOR VERSION IV40

Volume flow: Q: 46.67 m³/h

Delivery head: H: 376.4 m (corresponding to charging pressure of 37.64 bar)

Grid frequency: f: 50 Hz

According to delivery head value has been decided to select an e-MP pump series with rotational speed of 2950 RPM.

e-MP SERIES

HYDRAULIC PERFORMANCE RANGE AT 50 Hz, 2 POLES

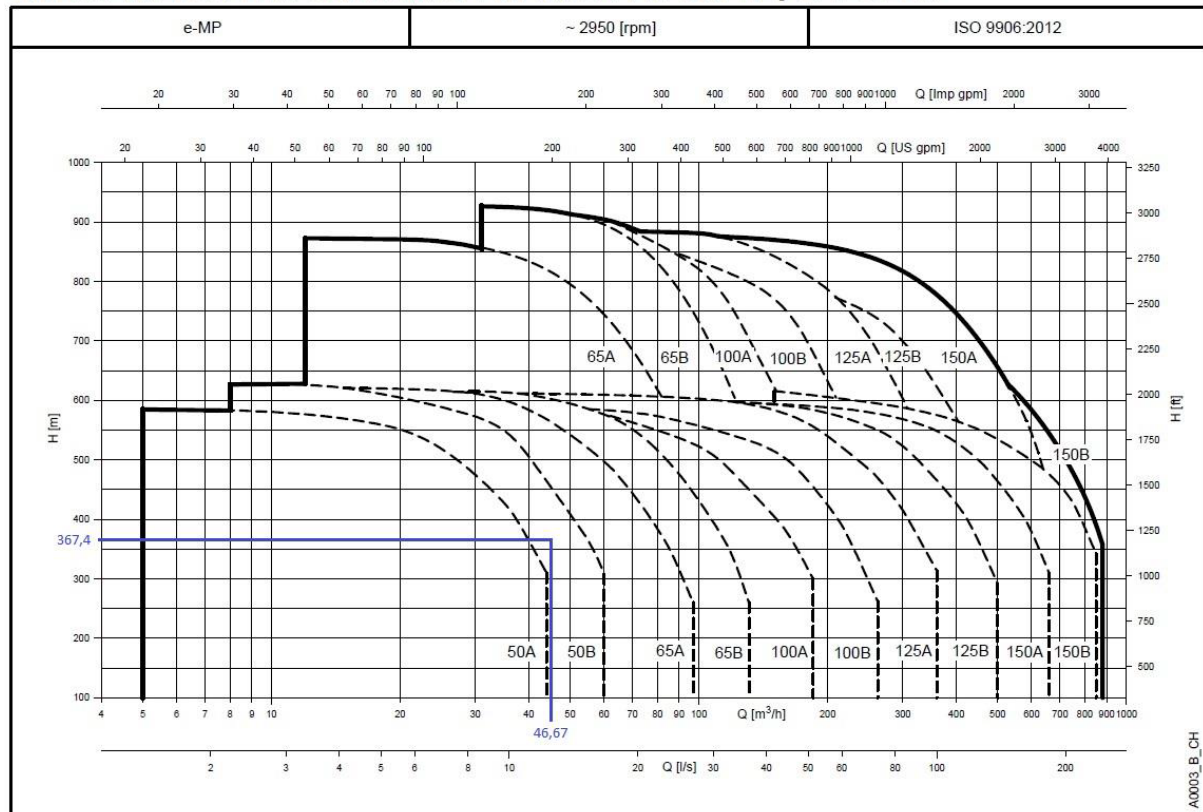


Figure 3: Hydraulic performance range MP-50B [6]

Figure 3 shows that the intersection between volume flow and delivery head is in the range of 50B. With this information further characteristic curves can be selected (see Figure 4).

By drawing of volume flow and delivery head on Figure 4 the intersection point refers to the characteristic curve of 11A with efficiency of circa 74.6%. Subsequently, the Net Positive Suction Head (NPSH) value for e-MPA series and shaft power for the line 11A can be read from Figure 4. Where the value of NPSH and shaft power are about 2.8 and 62 kW, respectively.

Figure 5 represents the information that can be extracted from the identification code of the pumps.

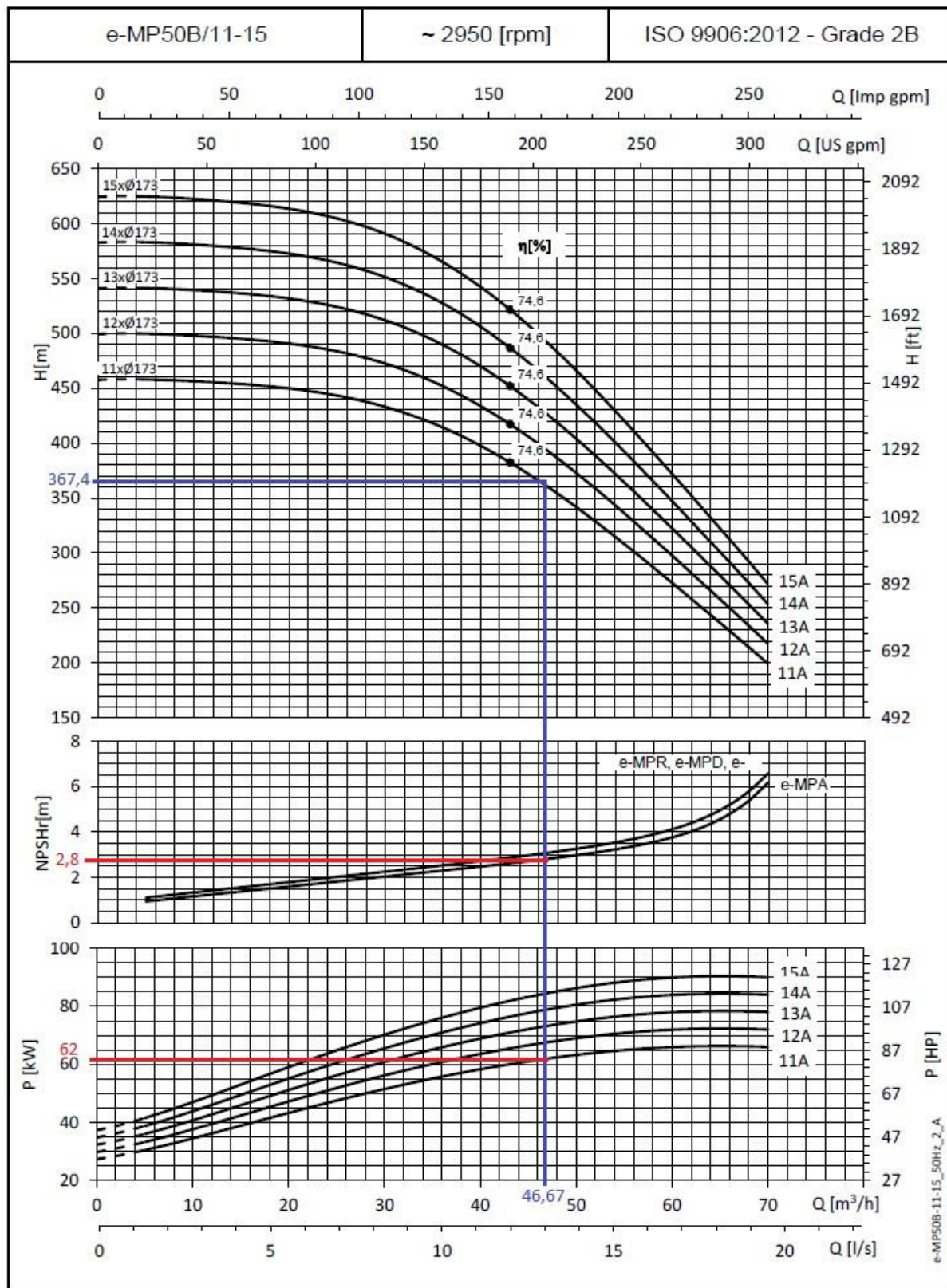


Figure 4: Operation characteristic of e-MP50B [6]

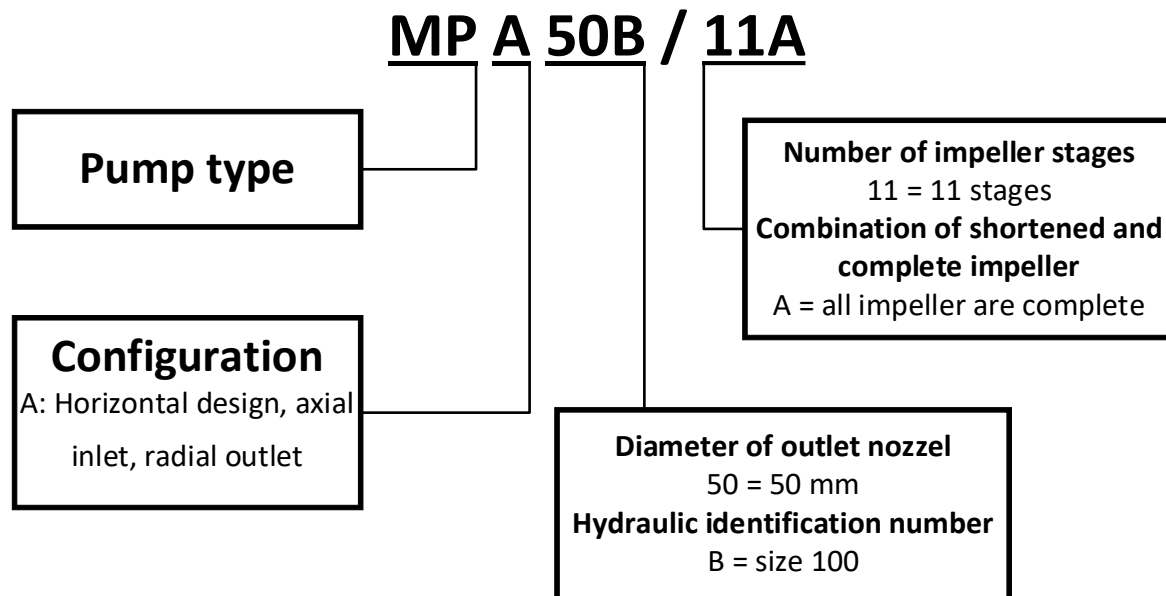


Figure 5: Identification code [6]

2.3.2 Efficiency

A computational estimation can often not be used to determine the pump efficiency. Hence, the pump efficiency of operating points are obtained from the pump manufacturer. Only in this way it is possible to perform an exact calculation of the system.

2.3.3 Mechanical design

The mechanical loads play an important role in this project, because pumps and motors are normally designed to be operated horizontally, but in this work the pump system should be mounted inside a rotational system, which makes the mechanical loads greater.

The pressure nozzle at the outlet of the pump has to be checked if the material is suitable for the intended pressure and temperature range. For this reason those parameters are considered more precisely in the following table:

Table 3: data sheet of charging pump [3]

13	Suction nozzle		DNs 100/PN10/16/EN1092-2 (D-MPA)
14	Discharge nozzle		DNd 50/PN63/EN1092-2 (D-MPAF)
15	Max. cabinet pressure	kPa	6300
16	Max. operation pressure	kPa	4868.5

Table 3 is a section from the data sheet MPA50B/11A/BE750/W25VDCC4 line 13-16.

The maximum cabinet pressure, the maximum delivery pressure and the maximum operation pressure are equal to 63 bar, 46.23 bar and 48.69 bar respectively for the selected pump. Thus, the cabinet pressure is sufficient.

Lines 13 and 14 in Table 3 show suction nozzle and discharge nozzle respectively with the corresponding diameter, pressure and EN number.

Figure 6 demonstrates the characteristic PN 63 for the discharge nozzle. This characteristic shows the effect of operating temperature on pressure resistance of the flange. Figure 6 clearly shows that the

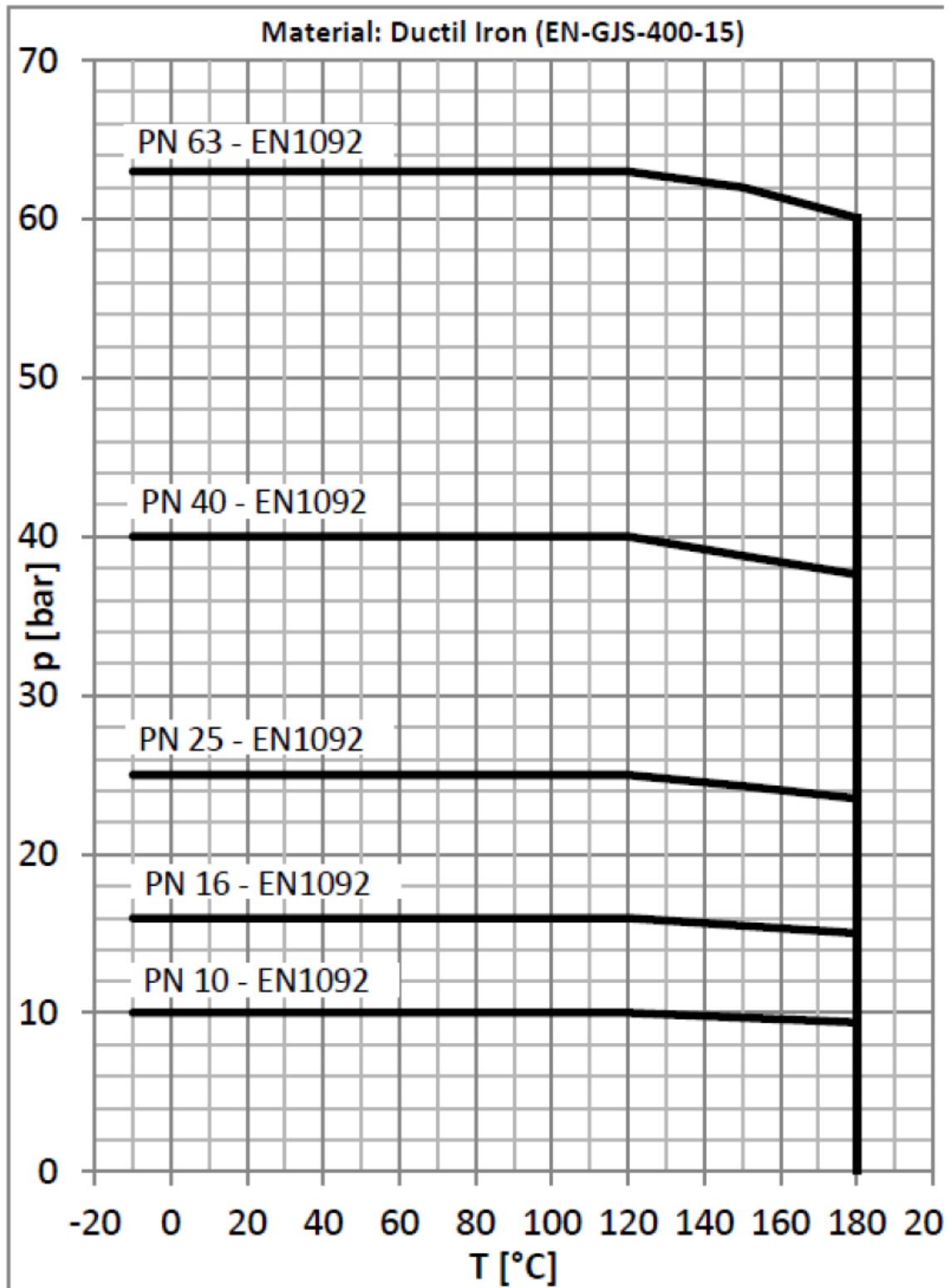


Figure 6 . Characteristic of discharge nozzle [3]

pressure resistance begins to drop at 120 °C till the maximum temperature of 180 °C is achieved. Since the maximum operating temperature in the FW system is below 60 °C, the pressure resistance can be estimated.

Most parts of the pump consist of grey cast iron, spheroidal graphite iron and stainless steel. The pump seals are made from ethylene-propylene-diene-rubber (EPDM). Those materials are stable in the operating temperature range from -60 to 160 °C. Furthermore, EPDM shows a high resistance to chemicals. Only grease and mineral oil, which are not discussed in this section, affect the plastic parts.

2.3.4 Speed control

Changing operating data such as delivery head or volume flow can be possible by controlling the rotational speed of the pump shaft.

$$Q_2 = Q_1 \cdot \frac{n_2}{n_1} \quad \text{Equation 3}$$

Where Q_2 is the volume flow by reduced speed in [m^3/s], Q_1 is the volume flow by outlet speed in [m^3/s], n_2 is the reduced rotational speed in [rpm] and n_1 is the rotational speed at outlet in [rpm].

$$H_2 = H_1 \cdot \left(\frac{n_2}{n_1}\right)^2 \quad \text{Equation 4}$$

Where H_2 is the delivery head at reduced speed in [m] and H_1 is the delivery head in [m] at rated speed.

$$P_2 = P_1 \cdot \left(\frac{n_2}{n_1}\right)^3 \quad \text{Equation 5}$$

For the same efficiency

Where P_2 is the shaft power by reduced speed in [W] and P_1 is the shaft power by outlet speed in [W]

$$P_2 = \frac{Q_2 \cdot H_2 \cdot \delta \cdot g}{\eta_{new}} \quad \text{Equation 6}$$

Where δ is the fluid density in [kg/m^3], g is the gravity acceleration in [m/s^2] and η_{new} is the pump efficiency by reduced speed

EXAMPLE FOR VERSION IV40

Q_1 :	46.67	[m^3/h]
H_1	376.4	[m]
P_1	68.4	[kW]
$Q_2 = 46.67 \cdot \frac{1450}{2975} = 22.75$		[m^3/h]
$H_2 = 376.4 \cdot \left(\frac{1450}{2975}\right)^2 = 87.27$		[m]

The new pump efficiency can be read now from Figure 7.

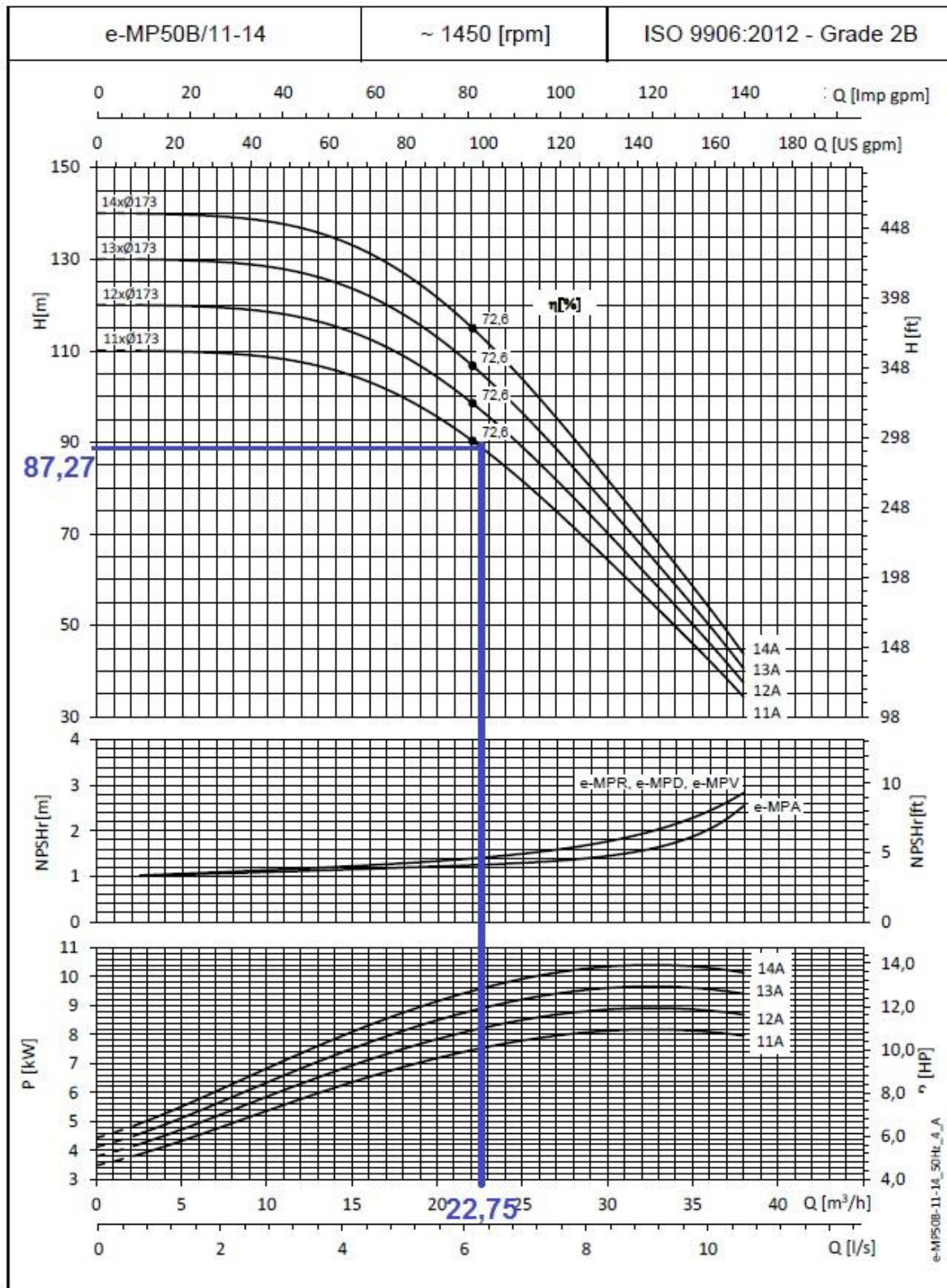


Figure 7: Operation characteristics of 1450 rpm [6]

$$\eta_{new} = 72.6\% \quad [-]$$

$$P_2 = \frac{\left(\frac{22.75}{3600}\right) \cdot 87.27 \cdot 9.81 \cdot 1070}{0726} = 7.973 \quad [\text{kW}]$$

2.3.5 NPSH

The NPSH is an important factor to identify the section behaviour of a centrifugal pump. Hence, two NPSH-values should be compared to evaluate the cavitation phenomena of such pumps, on one hand the required NPSH-value and the available NPSH-value on the other hand.

Because of the complexity of calculation of NPSH-value, a brief introduction of the required equations to get this is represented below:

$$NPSH_{avai} = \frac{p_e + p_b + p_D}{\rho \cdot g} + \frac{v_e^2}{2g} - H_{v,s} - H_{s\ geo} \mp s' \quad \text{Equation 7}$$

Where p_e is the overpressure in suction tank in $[\text{N/m}^2]$, p_b is the air pressure in $[\text{N/m}^2]$, p_D is the evaporation pressure in $[\text{N/m}^2]$, ρ is the density in $[\text{kg/m}^3]$, g is the gravitational acceleration in $[\text{m/s}^2]$, v_e is the flow speed in suction tank in $[\text{m/s}]$, $H_{v,s}$ is the pump head losses in pipes on the section side in $[\text{m}]$, $H_{s\ geo}$ is the altitude difference between fluid level inside suction tank and the middle of pump suction nozzle in $[\text{m}]$. and s' is the altitude difference between the middle of pump suction nozzle and the middle of impeller inlet in $[\text{m}]$.

Only 3% of delivery head reduction is allowed for the selected pump.

The NPSH-Value for version IV40 is equal to 2.8 m at nominal delivery head of 369.1 m, i.e. the NPSH-value is clearly below the allowed 3%.

2.3.6 Motor design

The designed motor should supply the pump with the needed power at every operating point. The shaft power can be determined either from computation or from using the characteristic diagrams (see Figure 7).

Due to the dependency of the pump characteristic on the water density, the power should be recalculated, in case of significant deviation of the selected fluid density from water density.

CALCULATION OF MOTOR POWER

$$P_W = \frac{\delta \cdot g \cdot H \cdot Q}{\eta_P} \quad \text{Equation 8}$$

$$P_M = \frac{P_W}{\eta_M} \quad \text{Equation 9}$$

Where η_P pump is the efficiency, δ is the fluid density in $[\text{kg/m}^3]$, g is the gravitation $[\text{m/s}^2]$, H is the delivery head $[\text{m}]$, Q is the volume flow in $[\text{m}^3/\text{s}]$, P_W is the shaft power in $[\text{W}]$, P_M is the Motor power in $[\text{W}]$ and η_M is the Motor efficiency.

EXAMPLE FOR VERSION IV40

Fluid: Glykosol N

Operating temperature: 20°C

$$P_W = \frac{1070 \cdot 9.81 \cdot 376 \cdot 46367}{0.7311} = 68.4 \quad [\text{kW}]$$

$$P_M = \frac{68.4}{0.949} = 72.07 \quad [\text{kW}]$$

Electric motor power versus required mechanical pump power are expressed as a percentage in Figure 8. This will be the guideline values for motor and pump in this work due to the limitation of safety factors from the producer. Hence, precise analysis cannot be expected. However, a power reserve of 10% is ensured for almost all versions. All selected motors are from the protection class IP55. They are thus well protected against dust in a critical quantity and also against hose water from any angle of attack.

A limitation of the number of possible start-ups of the electric motors in a certain period should be considered, because of excessive warming up during starting of such motors. As a standard value of 10 (Z) starts per hour is determined for electric motors with power of 30 kW and above. Moreover, due to the direct coupling between pump and motor, the start-up behaviour of the pump must be considered. Hence, the start-up period is adjusted in order to minimize the heating of the motor.

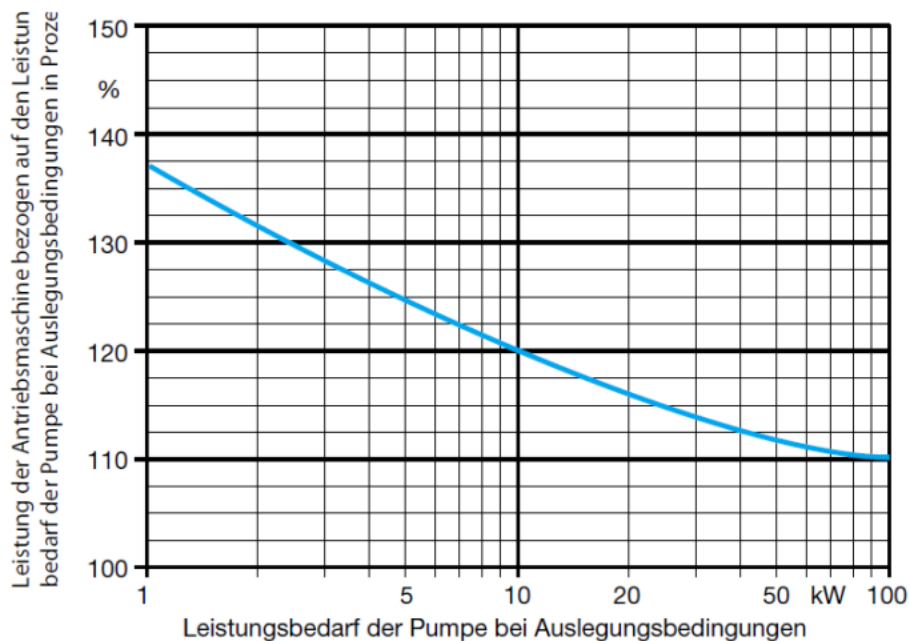


Figure 8: Machine power dependent on pump power; (x-axis) power consumption of the pump by design conditions; (y-axis) power of the drive machine relative to the power consumption of the pump by design conditions in percent [6].

Anlaufverfahren	Bauart	Stromaufnahme (Netzbelastung)	Hochlaufzeit	Motor-Anlauf-erwärmung	Mechan. Belastung	Hydraul. Belastung	Kostenrelation	Empfohlene Motorbauarten	Anmerkungen
Direktanlauf	Schütz (mechanisch)	$4-8 \cdot I_N$	ca. 0,5–5 s	hoch	sehr hoch	sehr hoch	1	alle	Seitens der EVU's meist begrenzt auf ≤ 4 kW
Stern-Dreieck-Anlauf	Schützkombination (mechanisch)	$\frac{1}{3}$ der Werte von Direktanlauf	ca. 3–10 s	hoch	sehr hoch	sehr hoch	1,5–3	alle; bei Spaltrohr- und U-Motoren tritt beim Umschalten ein größerer Drehzahlabfall auf	bei Motoren > 4 kW üblicherweise von den EVU's gefordert.
Teilspannungsanlauf	Anlass-transformator mit zumeist 70%iger Anzapfung	0,49 mal der Werte von Direktanlauf	ca. 3–10 s	hoch	hoch	hoch	5–15	alle	Beim Umschalten keine stromlose Phase. (Anwendung zugunsten Sanftanlauf rückläufig)
Sanftanlauf	Softstarter (Leistungselektronik)	frei einstellbar; üblich: $3 \cdot I_N$	ca. 10–20 s	hoch	gering	gering	5–15	alle	An- u. Abfahren stufenlos über Rampen auf jeweiligen Lastfall einstellbar: Keine hydraul. Stöße
Frequenzanlauf	Frequenzumrichter (Leistungselektronik)	$1 \cdot I_N$	0–60 s	gering	gering	gering	ca. 30	alle	Für reines An- u. Abfahren zu teuer. Besser geeignet für Stell- u. Regelbetrieb

Figure 9: Start-up methods of asynchronous motor [6]

Figure 9 shows different start-up methods for the asynchronous motors. The table in Figure 9 gives information about the type of the motor, current consumption, start-up period, mechanical load, hydraulic load, cost relation, recommended motor type, and general comments. Unfortunately, the German terms in Figure 9 were unavoidable, due to dependence on the German manufactories in this section.

A soft-start-up is usually used for asynchronous motors. Despite the high start-up warming, the mechanical and the hydraulic load is low. The required run-up time of such start-up motors is between 10 to 20 seconds. Hence, it is necessary to consider whether a star-delta or a partial voltage start-up could be a better alternative, when the aim is to achieve the 20 seconds charging.

All motors selected in this work, with the start-up method as described in Figure 9, can be mounted in the FW system.

2.4 Moment of inertia

Values of the moment of inertia of the motors and pumps used for precise calculation can be obtained from manufactures.

Wylie et al.'s equations can be used for approximate calculation of moment of inertia.

$$I_M = 118 \cdot \left(\frac{P}{n}\right)^{1.48} \quad \text{Equation 10}$$

$$I_P = 1.5 \cdot 10^7 \cdot \left(\frac{P}{n^3}\right)^{0.9556} \quad \text{Equation 11}$$

$$I_S = m \cdot r^3 \quad \text{Equation 12}$$

$$I_{ges} = I_S + I_P + I_M \quad \text{Equation 13}$$

Where P is the shaft power at $\eta_{P \max}$ in [W], n is the rotation speed in [rpm], I_M is the moment of inertia of motor in [kg·m²], I_P is the moment of inertia of pump in [kg·m²], I_S is the moment of inertia of FW in [kg·m²] and I_{ges} is the moment of inertia of the whole system in [kg·m²]

3 Modelling of Motor Driven Pump System

3.1 Modelling of Induction Motor

The hydraulic pumps to charge the FW are driven by induction motors. They are directly connected to the grid voltage, i.e. there is no frequency converter. Instead the motors are turned on and off by connecting and disconnecting the grid voltage to the terminals of the motors (bang-bang control).

As discussed above, there are different FW configurations conceivable. Depending on the chosen configuration the motor varies in rating and number of pole pairs. While the parameters of the hydraulic pumps are found in a market survey, the parameters of the motors do not need to be based on motors that are actually available on the market. Instead they only need to be realistic, to make sure that the simulations of response times and absorbed electric power are realistic too. Therefore, the motor parameters are found by interpolating between two known induction machines. The applied motor model is derived from the steady state equivalent circuit diagram of an induction machine [12], see Figure 10.

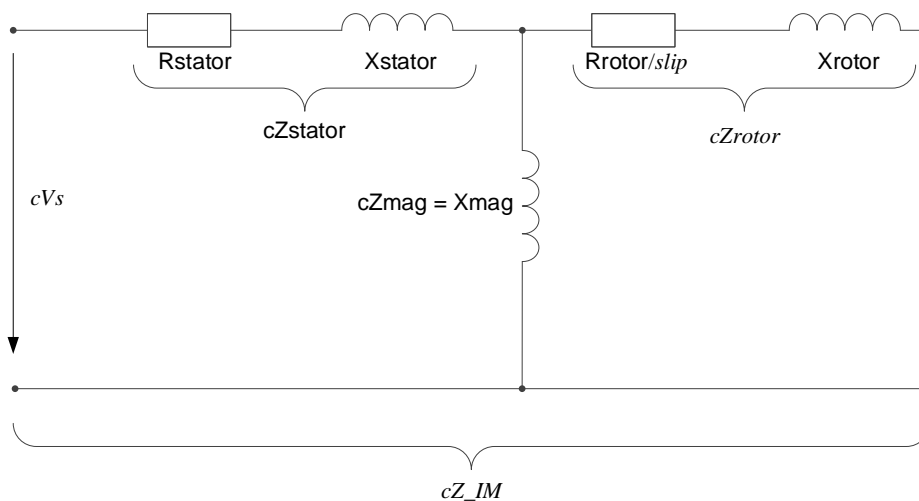


Figure 10: Static equivalent circuit diagram of induction motor.

Hence, Figure 10 shows that the parameters (constants) to be found are the stator resistance, R_{stator} , the stator reactance, X_{stator} , the magnetising reactance, X_{mag} , the rotor resistance, R_{rotor} , and the rotor reactance, X_{rotor} . The variables in this model are shown in italic letters in Figure 10, i.e. the complex stator voltage, cVs , and the slip, which leads to a variable rotor impedance, cZ_{rotor} .

To generate motor parameters for any conceivable FW configuration, known parameters of a 2 MW induction machine and of a 22 kW induction machine [13] are applied to interpolate between their parameters. For this purpose all values in Ohms must be converted to per unit (pu). However, since the 22 kW machine runs on a rated voltage of 220 V, while the 2 MW machine runs on a rated voltage of 690 V, the parameters in Ohms must first be referred to the same voltage. Here 690 V is chosen as base, as this is also the terminal voltage of the generator in the WT. Equation 14 illustrates this for the example of the stator resistance of the 22 kW machine.

$$R_{\text{stator}_{690V}} = R_{\text{stator}_{220V}} \cdot \frac{690^2}{220^2} \quad \text{Equation 14}$$

Once all resistance values and reactance values are referred to the same voltage, they can be divided by the base impedance of the applicable machine. The base impedance is calculated for each machine as shown in Equation 15.

$$Z_{\text{base}} = \frac{V_{\text{rated}}^2}{P_{\text{rated}}} \quad \text{Equation 15}$$

However, Figure 10 shows that the equivalent circuit of the induction machine is a single phase equivalent. In reality induction machines of considerable rating are three phase machines. The resistance and reactance values in Ohms are usually given per phase. Therefore, the single phase equivalent parameters in pu can be calculated as shown in Equation 16 for the example of the stator resistance.

$$R_{\text{stator}_{pu}} = \frac{R_{\text{stator}_{\Omega}}}{Z_{\text{base}} \cdot 3} \quad \text{Equation 16}$$

Table 4 lists the parameters of the 2 MW induction machine and of the 22 kW induction machine.

Table 4: Single phase equivalent circuit parameters in pu and base impedance in Ω of induction machine models

	2 MW induction machine	22 kW induction machine
Zbase [Ω]	0.23805	22
Rstator [pu]	0.0069	0.0212
Xstator [pu]	0.0908	0.0682
Xmag [pu]	5.1051	1.9697
Rrotor [pu]	0.008	0.0303
Xrotor [pu]	0.0972	0.0606

Figure 11 shows the electric torque and the electric power (each in pu) of the 2 MW, the 22 kW and a fictive 500 kW induction machine. The 500 kW machine parameters are yielded by interpolating between the parameters of the 2 MW and the 22 kW machines.

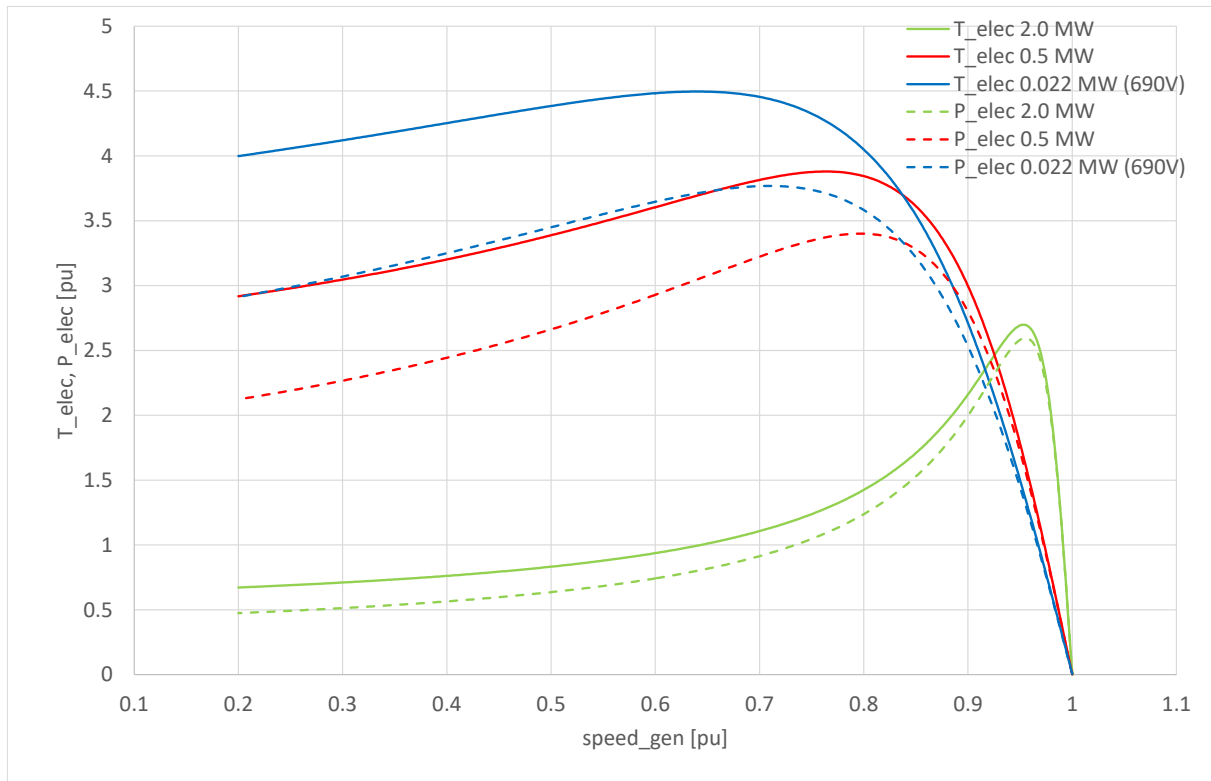


Figure 11: Torque and power vs. speed characteristic of induction motors.

Figure 12 shows the reactive power demand of the three induction machines introduced above.

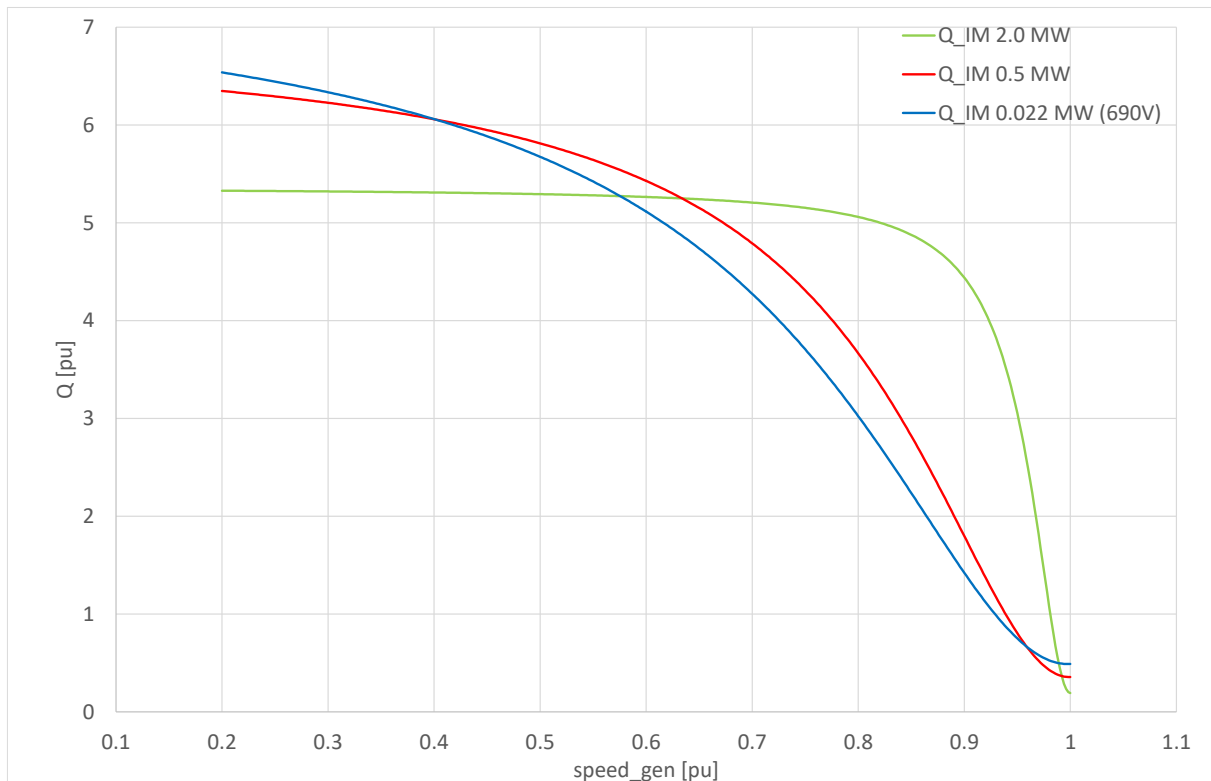


Figure 12: Reactive power demand vs. rotor speed of induction motors.

The full equation system of the induction machine model is given in the documentation of the 1st Eigenmodes Simulation Model of a Wind Turbine [1].

In order to turn the steady state induction machine model shown in Figure 10 into a dynamic model of the first order, the equation of mechanical acceleration has to be applied, see Equation 17.

$$\frac{d\omega}{dt} = \frac{T_{elec} - T_{shaft}}{J} \quad \text{Equation 17}$$

Where T_{elec} is the electric driving torque (see Figure 11), T_{shaft} is the mechanical counter torque of the machine to be driven with the motor, and J is the inertia of rotating masses. While the electric parameters are yielded from interpolation, as discussed above; the inertia of different induction machines can be found on the web site of energie.ch [14].

3.2 Modelling of Hydraulic Pump

The block diagram of the hydraulic pump model visualises the implementation in the WT model. In the report at hand only derivations and explanations are given. The complete equation system is contained in the block diagram [1].

3.2.1 Power, Torque, Speed and Pressure of Pump

A pump absorbs its rated power at its shaft, when it runs at rated speed and with rated torque. Varying the speed leads to a variation of the shaft power as shown in Equation 5.

Hence, for any arbitrary speed, n_2 , the applicable power P_{pump_W} , can be calculated.

Since the model of the induction motor is in pu, the calculation of the torque produced by the pump is simplified drastically. It has to be noted here, that the base for the pu system of the induction motor model is not the one of the WT model, instead it is the rated values of the induction motor. Applying P_1 and n_1 from Equation 5 as the base values (P_{base} and n_{base} respectively) allows calculating the pump power in pu, P_{pump_pu} , see Equation 18.

$$P_{pump_pu} = 1 \cdot \left(\frac{n_2}{n_{rated}} \right)^3 \quad \text{Equation 18}$$

However, the shaft speed n_2 is already calculated in pu in the induction machine model. The base value for this variable is also n_{rated} . Hence, the shaft speed can be expressed as follows:

$$n_{2_pu} = \frac{n_{2_RPM}}{n_{rated}} \quad \text{Equation 19}$$

Substituting n_2 in Equation 18 with Equation 19 leads to Equation 20.

$$P_{pump_pu} = 1 \cdot \left(\frac{\frac{n_{2_RPM}}{n_{rated}}}{\frac{n_{rated}}{n_{rated}}} \right)^3 = (n_{2_pu})^3 \quad \text{Equation 20}$$

However, the power at the shaft of a pump is also proportional to the volumetric flow rate, Q in m³/s, times pressure. The pressure of a pump is usually given by the height, H , in meters, to which the pump

with its efficiency, η , can push the fluid with density, ρ , against the gravitational acceleration, g , see Equation 6.

This pressure can be turned into the SI unit Pa with Equation 21,

$$p = H \cdot \rho \cdot g \quad \text{Equation 21}$$

which turns Equation 6 into Equation 22.

$$p = \frac{P_z \cdot \eta}{Q} \quad \text{Equation 22}$$

Hence, power in Watts at the shaft is given by Equation 23

$$P_{\text{pump}_W} = \frac{Q \cdot p}{\eta} \quad \text{Equation 23}$$

Torque is power divided by angular speed; hence, Equation 23 can be rearranged and extended to derive torque in Nm.

$$T_{\text{pump}_Nm} = \frac{Q \cdot p \cdot 30}{\eta \cdot n_{2_RPM} \cdot \pi} \quad \text{Equation 24}$$

Dividing T_{pump_Nm} in Equation 24 with the torque base, T_{base} , in Equation 25,

$$T_{\text{base}} = \frac{P_{\text{base}} \cdot 30}{n_{\text{base}} \cdot \pi} \quad \text{Equation 25}$$

and at the same time applying n_{2_RPM} from Equation 19, leads to the torque of the pump in pu, T_{pump_pu} , which is a function of the shaft speed in pu:

$$T_{\text{pump}_pu} = \frac{Q \cdot p \cdot 30}{\eta \cdot n_{2_RPM} \cdot \pi} \cdot \frac{n_{\text{base}} \cdot \pi}{P_{\text{base}} \cdot 30} = \frac{Q \cdot p \cdot 30}{\eta \cdot n_{2_pu} \cdot n_{\text{rated}} \cdot \pi} \cdot \frac{n_{\text{rated}} \cdot \pi}{P_{\text{base}} \cdot 30} = \frac{Q \cdot p}{\eta \cdot n_{2_pu} \cdot P_{\text{base}}} \quad \text{Equation 26}$$

A pressure release valve can be modelled by limiting the pressure of the pump to a certain value. If this pressure limit is made variable then bypass operation can be emulated. It has to be noted though, that the flow rate, which is an input variable to the pump model, comes from the FW model (this variable is called “flowrate” in the 1st Eigenmodes simulation model of the WT [1]). Hence, in bypass operation this variable “flowrate” is not the same as Q in the equations above.

3.2.2 Numerical Aspects

To make the simulation results of bypass operation more realistic the torque as derived in Equation 26 should be limited to a minimum value. This way no load friction can be represented. In order to avoid that there is a torque while there is no rotational speed, this torque limitation has to be made dependent on the rotational speed.

However, in Equation 26 the rotational speed enters into the denominator. Hence, zero speed means division by zero, which has to be avoided. In the simulation model the rotational speed is limited to a value called `lower_limit` before it enters into Equation 26. To avoid that this limitation leads to numerical instability, the value of `lower_limit` is made a function of the maximum pressure of the pump (the variable that allows bypass operation) and the simulation step size.

Another potential division by zero is contained in Equation 22. Here the flowrate has to be prevented from becoming zero before entering into the denominator. The flowrate is also limited with the variable `lower_limit`. The pressure calculated with Equation 22 enters into the numerator of Equation 26, i.e. the equation for the torque at the shaft of the pump. Consequently, the limitations with `lower_limit` affect both the torque and the pressure of the pump. Zero rotational speed and zero flowrate cannot be simulated without further adjustments. Therefore, the torque of the pump is limited to an upper limit, whenever the speed is limited. If the speed is limited, i.e. if the speed used in Equation 26 is `lower_limit`, the maximum value of the torque is set to zero. When there is no speed the torque has to be zero, otherwise the drive train gradually accelerates to negative speeds. This facility is basically an anti-windup for the drive train model, see Equation 17.

Equation 4 reveals that the pressure is a function of the square of the rotational speed. This means that the pressure is close to zero whenever the motor has just started to accelerate the pump. However, when the speed is no longer zero (numerator in Equation 22) and the flowrate is limited to a small value that is greater than zero (to avoid division by zero), then the pressure becomes unrealistically large. To prevent this numerical error the upper limitation of pressure has to be made a function of the square of the rotational speed, as given by Equation 4.

4 Pump Systems for the Flywheel Configurations

The different motor-pump combinations vary in rating and size, depending on the FW configuration in the rotor blade of the NREL 5 MW reference WT and on the desired charging time (20 s, 40 s or 60 s). In the following the pump system parameters as yielded by Thomsen and Maack [2] are put into perspective with the parameters of the NREL 5 MW reference WT.

Figure 13 shows that the masses of the motor-pump combinations vary drastically with the charging time. However, since fast charging is desired, the high masses are inevitable.

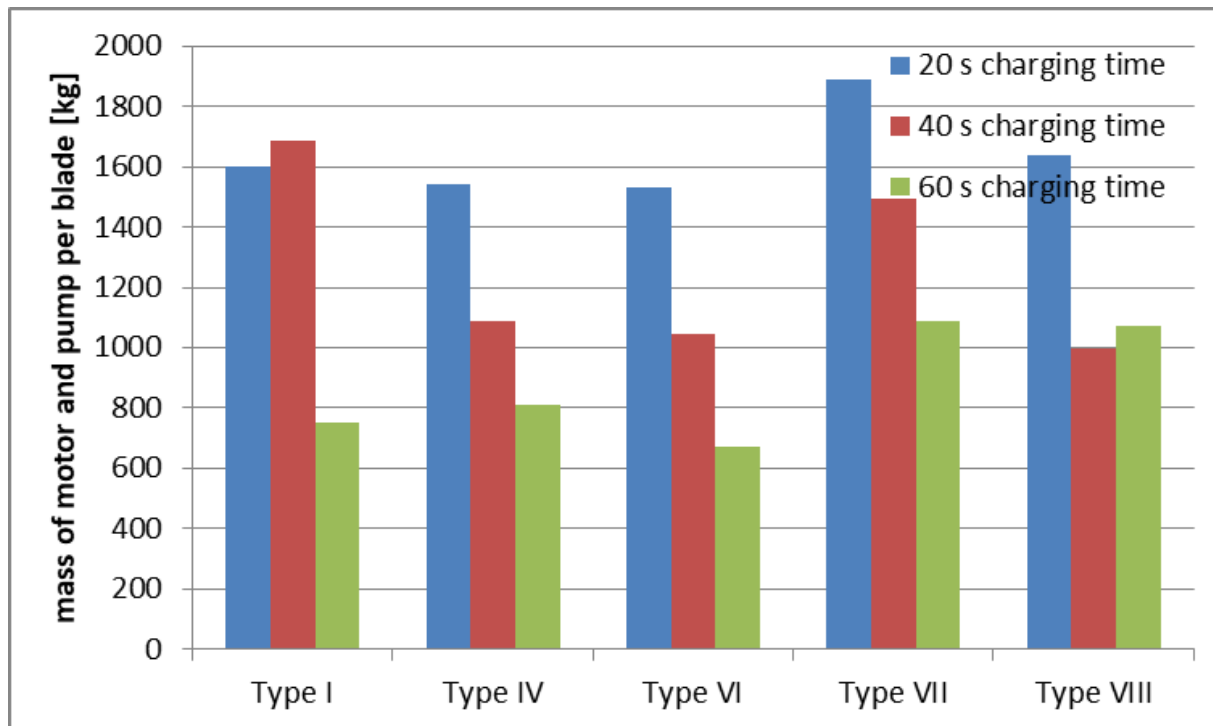


Figure 13: Masses per blade of the motor-pump combinations for the different FW configurations and for the different desired charging durations.

Comparing Figure 13 and Figure 14 reveals that the motor-pump combinations have a strong impact on the overall masses of the FW systems. It has to be kept in mind that the FW components considered here are still the conventional piston accumulators made of steel and aluminum [15].

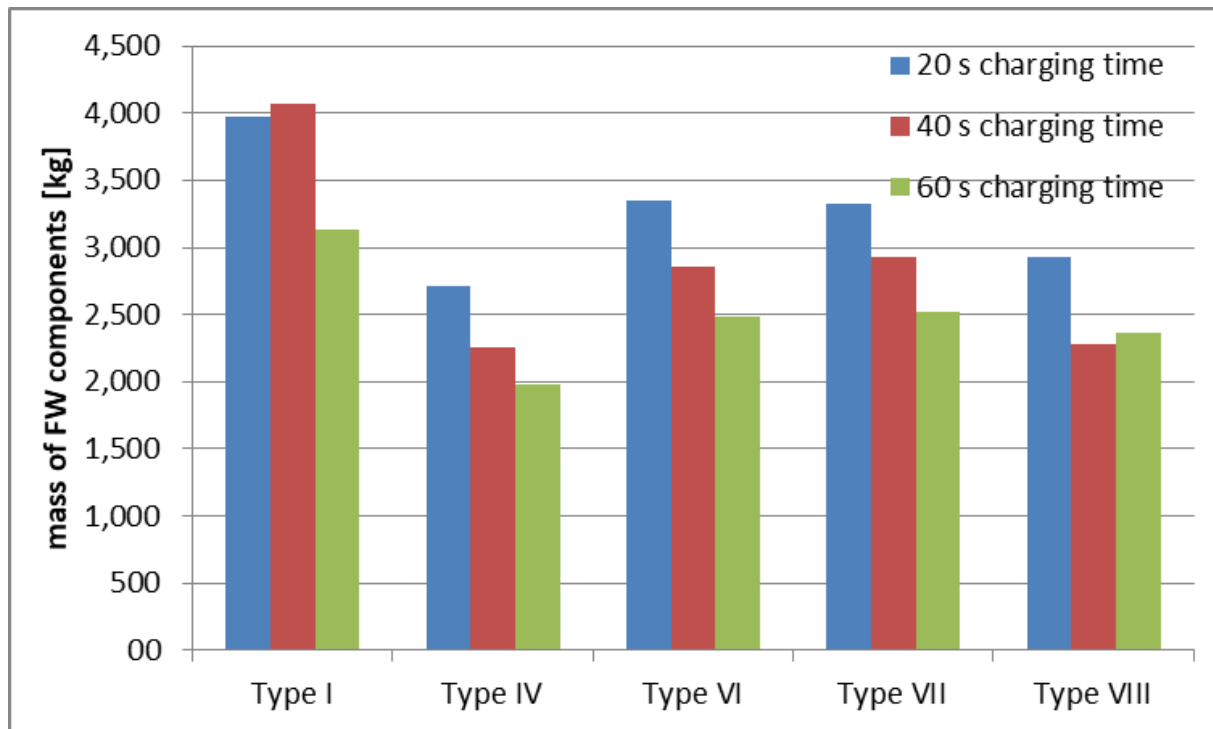


Figure 14: Masses per blade of the motor-pump combinations, conventional piston accumulators and fluid for the different FW configurations and for the different desired charging durations.

These masses are put into perspective with the masses of the original NREL 5 MW blade as designed by Rasor [10]. Figure 15 shows the comparison in terms of masses and Figure 16 the comparison in terms of blade inertia.

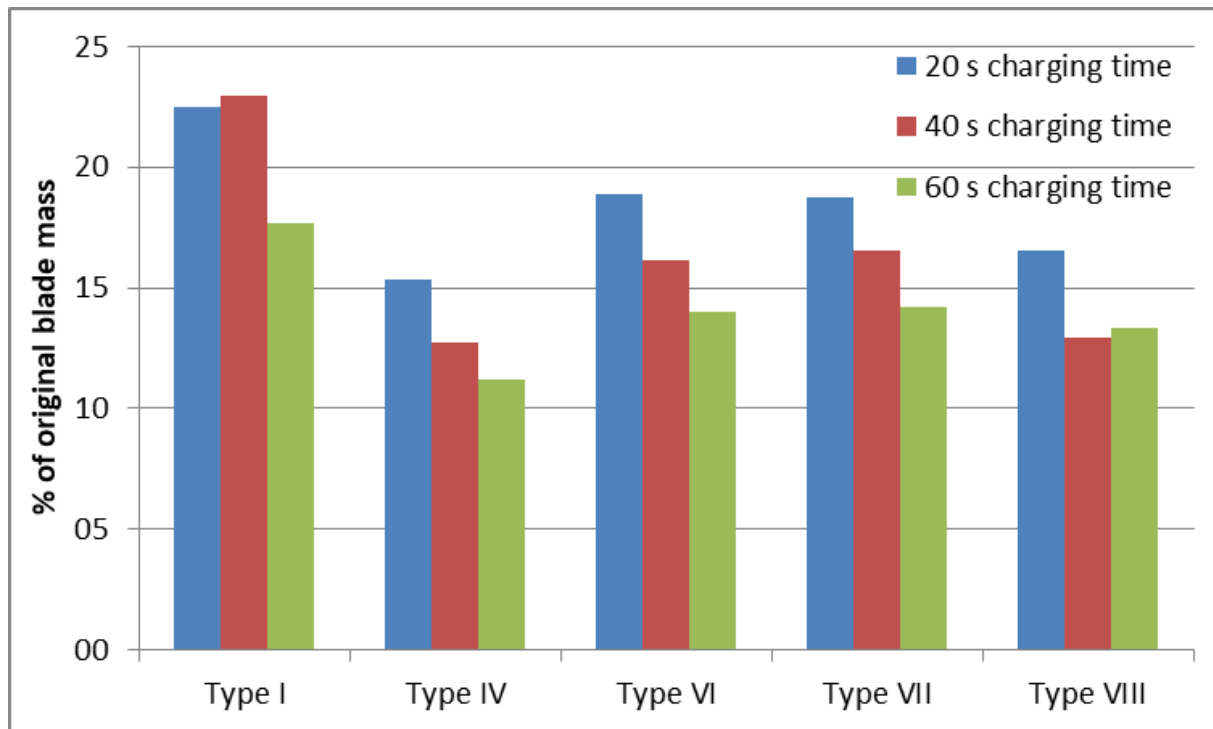


Figure 15: Masses per blade of the motor-pump combinations, conventional piston accumulators and fluid for the different FW configurations and for the different desired charging durations as percentage of the original blade mass.

Although the masses vary strongly with the desired charging time, this difference constitutes itself in the mass of the motor-pump combination only. Since the motor-pump combination is located in the blade root, Figure 16 shows that it has hardly any impact on the blade inertia.

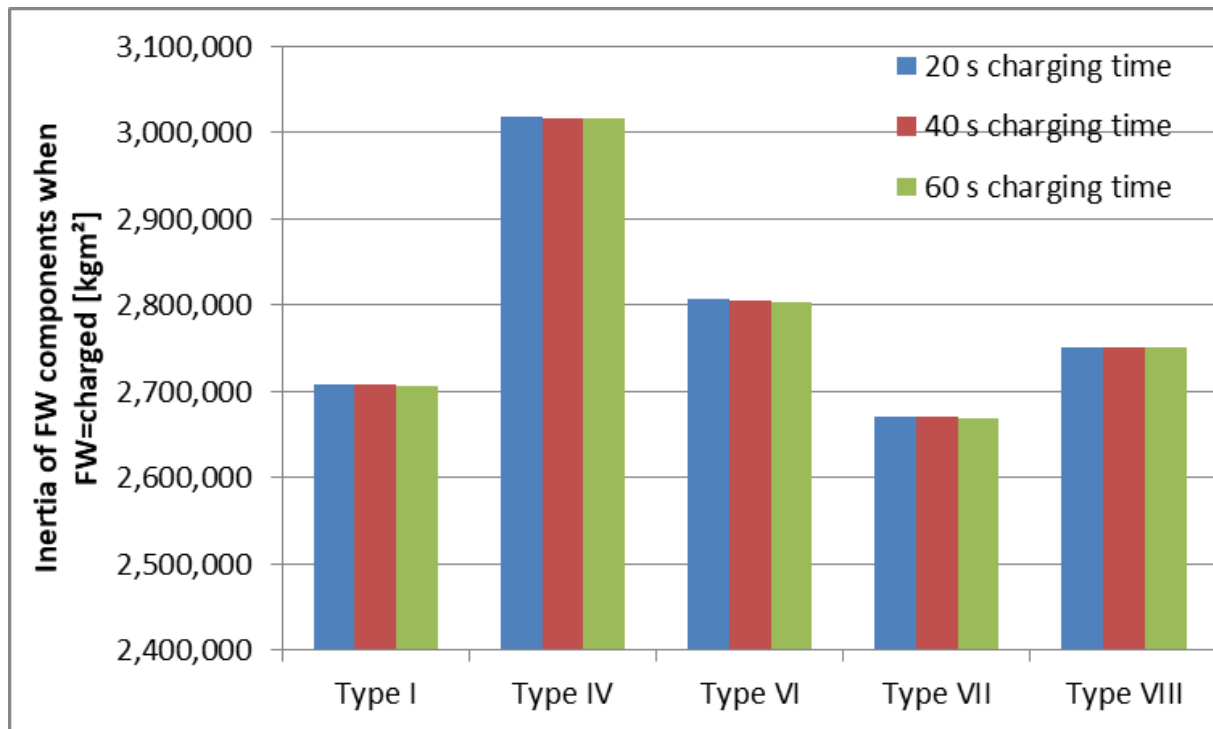


Figure 16: Inertia per blade of the motor-pump combinations, conventional piston accumulators and fluid for the different FW configurations and for the different desired charging durations.

The difference in inertia is put into perspective with the original blade inertia in Figure 17.

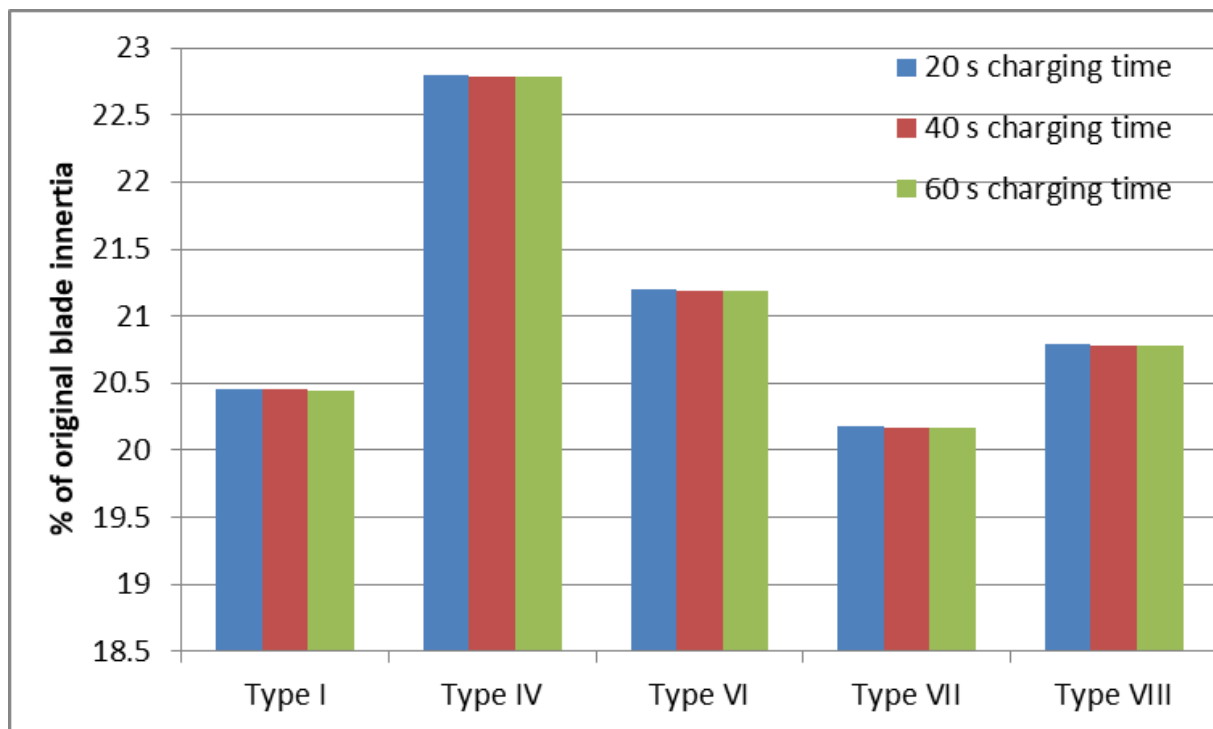


Figure 17: Inertia per blade of the motor-pump combinations, conventional piston accumulators and fluid for the different FW configurations and for the different desired charging durations as percentage of the original blade inertia.

When controlling the FW in a WT, the impact on the power is of utmost importance. Therefore, Figure 18 shows the electric power, which the pumps in all three blades consume when they charge the FW in the NREL 5 MW reference WT rotor.

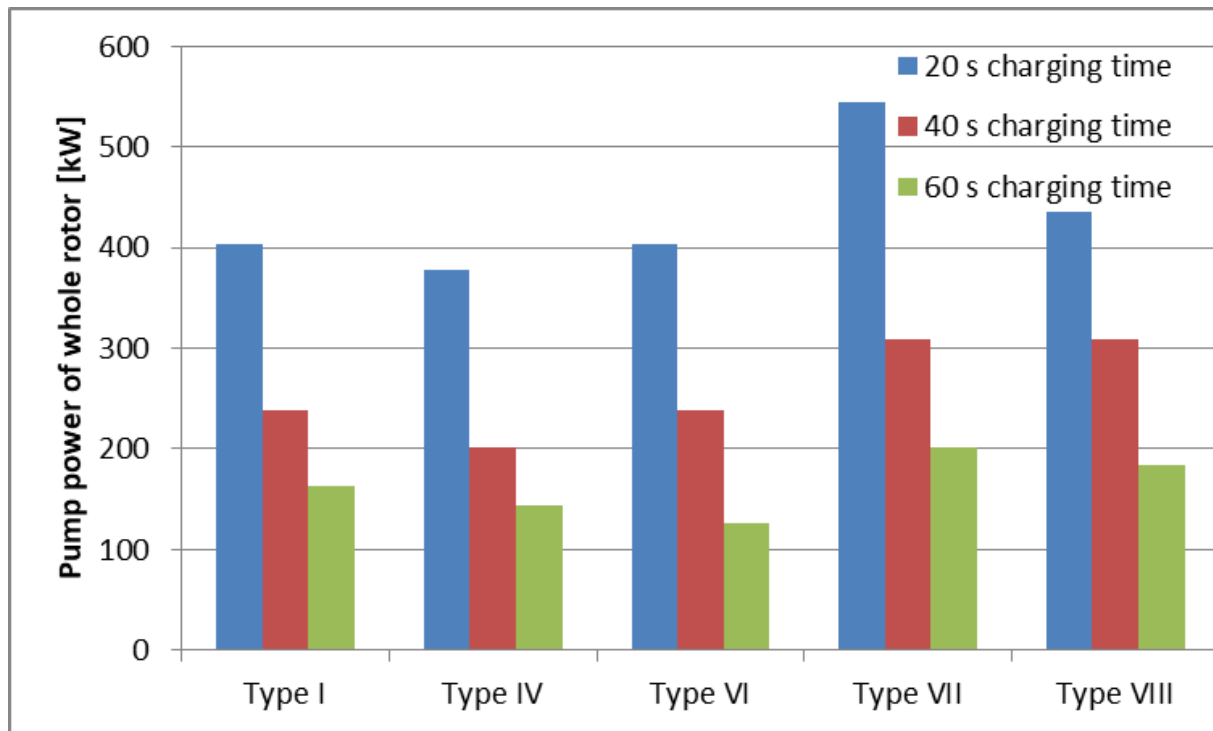


Figure 18: Electric active power consumed by the motors of all three blades for the different FW configurations and for the different desired charging durations.

From Figure 18 it becomes obvious the charging time of 20 seconds is most advantageous. It has the largest impact on the power. Since the power consumed by the pumps is produced by the generator of the WT, 20 seconds charging time allows the largest manipulation of the electric torque in the generator of the WT.

5 Controls of the Flywheel for Steadying the Power Infeed

The FW in the rotor of a WT is visualised in Figure 1. The FW can be controlled with different variables. If the state of charge of the FW is to be changed, the pressure that acts on the pistons of the piston accumulators in the FW system, as well as the valves that impact on the flow rate of the fluid, have to be controlled [30]. The pressure on the pistons is determined by the balance between the pre-charge pressure in the compressed gas, the pressure resulting from centrifugal acceleration, the pressure that results from gravitational acceleration, pressure losses from motion in the fluid and the pressure produced by the pumps. Provided that these pressures could lead to a flowrate in any direction, the valves in the hydraulic tubes determine whether the pistons move or not. Hence, to control the FW the rotor speed, the pumps and the valves could be controlled. The pre-charge pressure cannot be varied during operation. The impact of gravity and the pressure losses from fluid motion have to be accepted as they are. However, in the FW control that is proposed here, the pressure from the pumps is used as the main control variable. In order to make the system rapidly responding, the pumps are kept turned on and their pressure is downregulated by a bypass valve that allows the pumps to pressure less circulate the fluid. Since the purpose of the pumps is only to charge the FW, the charging pressure can be fine-tuned by this bypass valves. The discharging shall be driven by the gas pressure in order to yield an accelerating torque in the rotor, hence, the flowrate in discharging operation is fine-tuned by pulse-width-modulating the flow in the hydraulic tubes. In discharging, the fluid does not flow through the pump but is bypassing the pumps. Hence, since bypass operation of the pumps is in the core of the proposed method, the controller that controls the FW is called bypass controller.

5.1 General Layout of the Bypass Controller for Power Steadying

Figure 19 shows in an overview block diagram how the hydraulic pumps, the FW and the controls of the FW interact with each other and eventually impact on the torque of the FW. The variable names in Figure 19 are, as far as possible, identical with the variable names used in the block diagram of the first eigenmodes model of a WT [1]. Therefore, these variable names are neither introduced here, nor are they contained in the List of symbols and abbreviations.

The purple text in Figure 19 is explanations. Light blue names indicate variables that allow controlling the FW. Marked in red is the variable $v_fluid_max_bl1$, which is the output signal of the Pump Bypass Controller for blade 1. Hence, the task is to design a controller that generates the maximum fluid speeds $v_fluid_max_bl1$, $v_fluid_max_bl2$ and $v_fluid_max_bl3$ for the three blades. While the Pump Bypass controller could serve different purposes, the controller to be designed here shall only do power steadying. Therefore, in the following the variables $v_fluid_max_bl$, as shown in Figure 19, are in the following called $v_fluid_max_steady_bl$.

For the purpose of controller design transfer functions of the plant to be controlled have to be found, and with these transfer functions suitable controller gains have to be calculated.

The intention of power steadying is to store energy in the FW whenever the power in the wind exceeds the demanded power, and to release energy from the FW whenever the power in the wind drops below the demanded power.



Project Report
Revision 1

5.2 Transfer Functions

5.2.1 Block Diagram of System from P_{dem} to P_{gen}

In power steadying operation the FW has to level out variations in the generator power, P_{gen} , to follow the power setpoint, P_{dem} . The initial (full) block diagram is shown in Figure 20.

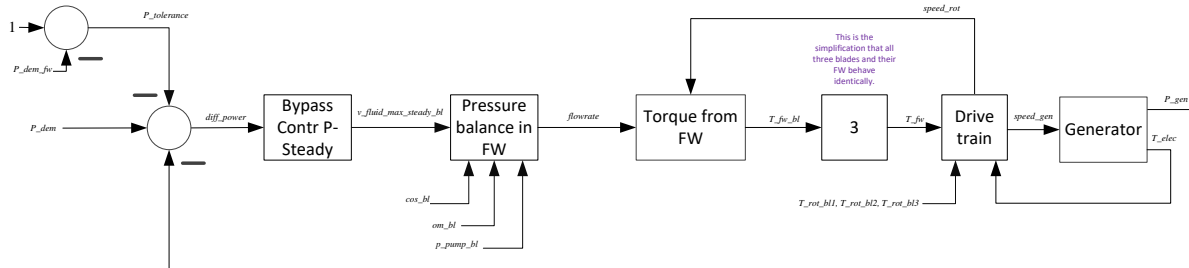


Figure 20 Full block diagram of WT with P-Steadying Bypass controller. Variable names are introduced in the documentation of the simulation model [1].

To derive the transfer function of the blocks in Figure 20, the following relationships need to be considered.

- In the FW $v_fluid_max_steady_bl$ can be translated linearly into flowrate. Although flowrate is the result of an integration of the acceleration of the fluid [1], $v_fluid_max_steady_bl$ is the limitation of the flow speed, i.e. the flowrate. See section flowrate from $v_fluid_max_bl$.
- The centre of gravity of the FW weights, R_var , (not shown in Figure 20) is the result of the integration of the flowrate $R_var = f(\int flowrate)$ and some linear equations [1].
- The torque contribution of the FW in one blade, T_fw_bl , is a function of the square of R_var and $speed_rot$: $T_fw_bl = f(R_var^2, speed_rot)$ [1]
- The aggregated FW torque: $T_fw = T_fw_bl \cdot 3$. This is the simplification that all three blades and their FW behave identically.
- The generator speed, $speed_gen$, is the balance between the drive torques, T_rot_bl1 , T_rot_bl2 , T_rot_bl3 and the decelerating torque, T_elec . The FW torque, T_fw is a disturbance.
- The generator model translates $speed_gen$ to P_{gen} via the P vs. speed characteristic [1].

5.2.2 Linearizations in the Block Diagram

In the block diagram in Figure 20, several blocks require linearization in order to be able to create transfer functions.

5.2.2.1 flowrate from $v_fluid_max_bl$

The balance between gas pressure and fluid pressure determines whether the piston can move. Provided that there is sufficient pressure in the desired direction, i.e. either from the gas or from the pumps plus the other fluid pressure components, the fluid can flow in the desired direction as soon as the valves are open.

In Figure 21 the pressure balance is $p_fw_fluid_tank2$. As shown in Figure 19 the control variable is $v_fluid_max_bl$, which is turned into $upper_lim$ and $lower_lim$ when fluid is allowed to flow in either direction. I.e. the fluid is no longer free to flow, but it is forced to flow with the desired fluid speed $v_fluid_max_bl$. The variables $upper_lim$ and $lower_lim$ act on the integration of the fluid acceleration,

see Figure 21. The eventually resulting flowrate is fluid speed, v_{fluid} , times the cross section of the tube, A_{tube} .

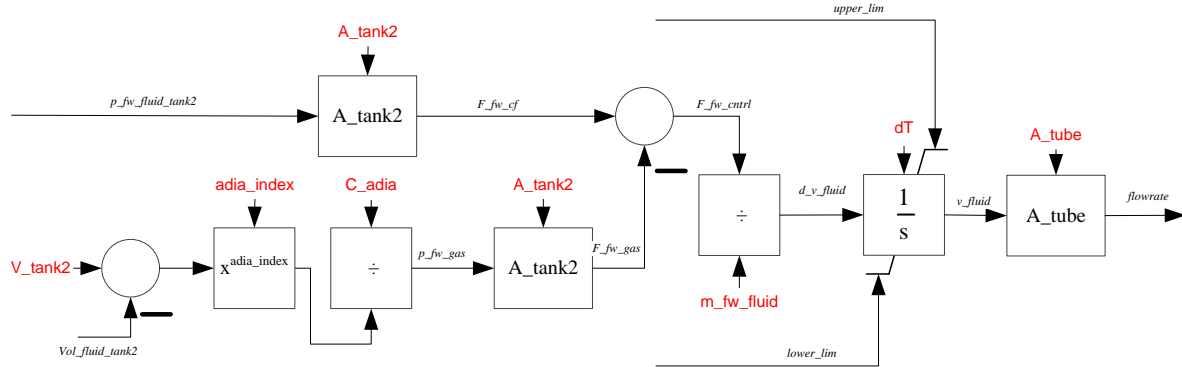


Figure 21 flowrate as a function of the integrated fluid acceleration. Variable names and parameter names (red) are introduced in the documentation of the simulation model [1].

Hence, it can be concluded that flowrate is the desired fluid speed, $v_{\text{fluid_max_bl}}$, times the cross section of the tube, A_{tube} .

5.2.2.2 R_{var} from Vol_fluid_tank2

R_{var} is a function of the fluid volume in the piston accumulator, Vol_fluid_tank2 , which is the integral of flowrate. However, R_{var} is not linearly dependent on Vol_fluid_tank2 , see Figure 22.

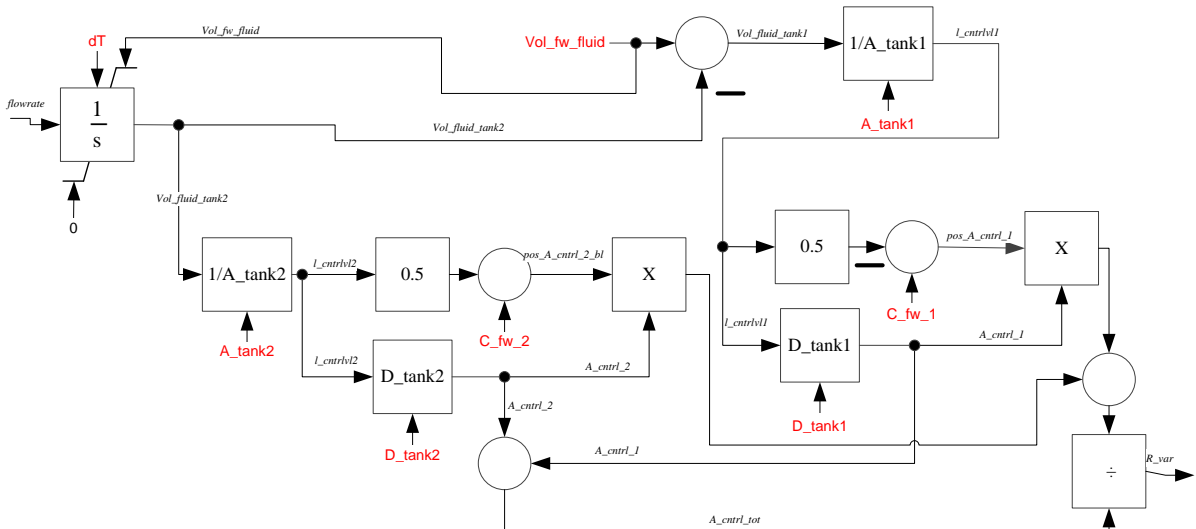


Figure 22 R_{var} as a function of the integrated flowrate. Variable names and parameter names (red) are introduced in the documentation of the simulation model [1].

Figure 23 shows R_{var} and for illustration also the slope of R_{var} , each vs. Vol_fluid_tank2 , as they result in case of a FW configuration Type VI [11] in the NREL 5 MW reference WT [17]. Since the slope is not a constant number, R_{var} is nonlinearly dependent on Vol_fluid_tank2 .

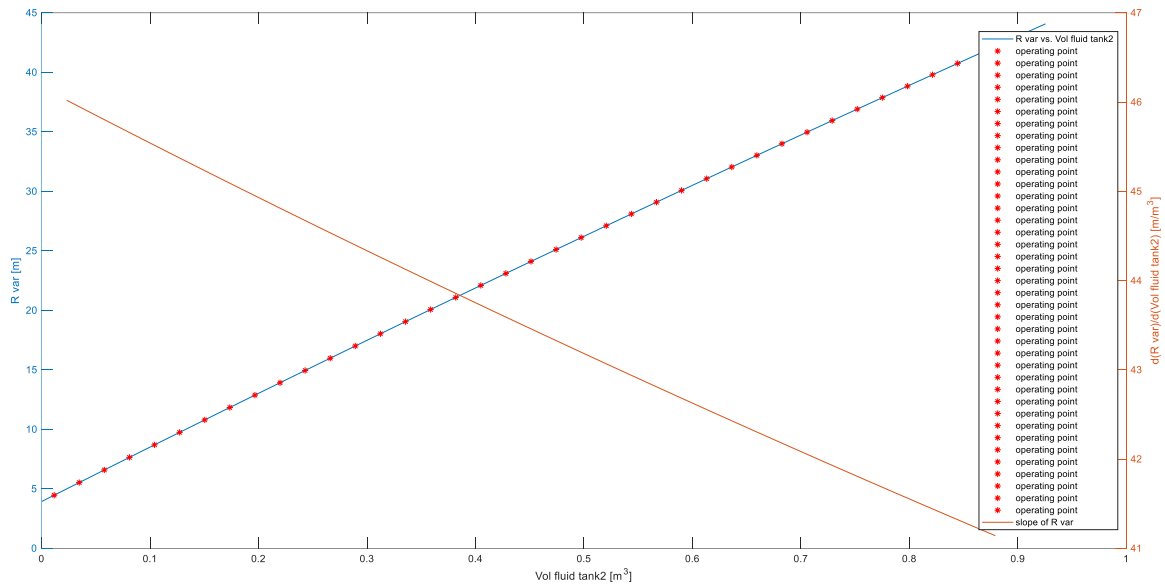


Figure 23 R_{var} and the slope of R_{var} as a function of the integrated flowrate, i.e. Vol_fluid_tank2 .

Hence, in order to be able to generate a transfer function R_{var} vs. Vol_fluid_tank2 has to be linearised. This is shown in Figure 24

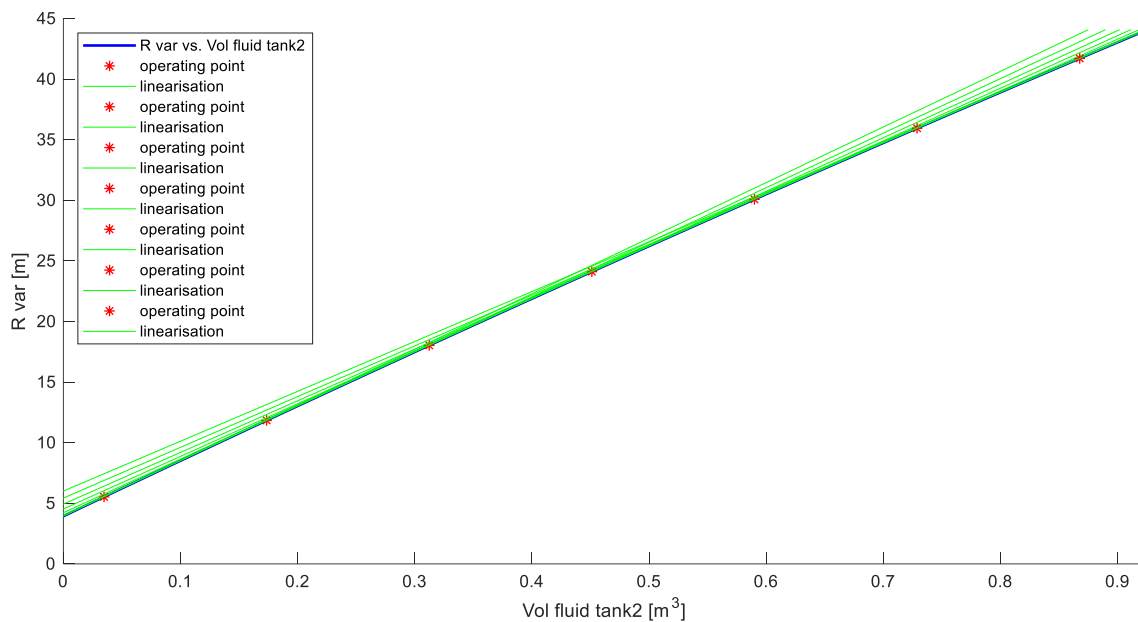


Figure 24 R_{var} vs. Vol_fluid_tank2 and its linearization in different operating points.

The R_{var} vs. Vol_fluid_tank2 values, the slope values plotted in Figure 24, as well as the FW inertias, $J_{fw_SI_bl}$, that result from the different R_{var} , are shown in Table 5.

Table 5 Different operating points for linearization.

n = operating point	$Vol_fluid_tank2(n)$ [m ³]	$slope_R(n)$ [m/m ³]	$R_var(n)$ [m]	$J_{fw_SI_bl}(n)$ [kgm ²]
1	3.47E-02	4.59E+01	5.53E+00	2.83E+04
2	1.74E-01	4.50E+01	1.18E+01	1.30E+05

3	3.12E-01	4.42E+01	1.80E+01	3.01E+05
4	4.51E-01	4.34E+01	2.41E+01	5.38E+05
5	5.90E-01	4.26E+01	3.01E+01	8.37E+05
6	7.29E-01	4.19E+01	3.59E+01	1.20E+06
7	8.68E-01	4.11E+01	4.17E+01	1.61E+06
8	8.91E-01	4.10E+01	4.27E+01	1.68E+06

Applying the equation for linear interpolation ($y_i = \frac{y_2 - y_1}{x_2 - x_1} \cdot (x_i - x_1) + y_1$) allows yielding the translation from Vol_fluid_tank2 to R_var. Using the names as stated in Table 5 leads to Equation 27.

$$R_var = slope_R(n) \cdot (Vol_fluid_tank2 - Vol_fluid_tank2(n)) + R_var(n) \quad \text{Equation 27}$$

5.2.2.3 FW torque as function of (R_var)² and speed_rot

Since the FW torque is a function of the square of R_var and the rotor speed, speed_rot, the plant gain of the FW has to be determined for different states of charge of the FW (R_var). As shown in the following, speed_rot contributes linearly to T_fw_bl.

The torque from the angular momentum results from changes, dJ_fw_SI, in the inertia of the FW, J_fw_SI_bl:

$$J_fw_SI_bl = R_var^2 \cdot m_fw_fluid$$

$$dJ_fw_SI = \frac{J_fw_SI_bl}{dt} \quad \text{Equation 28}$$

With this change in inertia the torque can be derived from the angular speed of the rotor:

$$speed_rot_rad = \frac{speed_rot \cdot speed_base_Lss \cdot 30}{\pi} \quad \text{Equation 29}$$

$$T_fw_bl = \frac{-dJ_fw_SI \cdot speed_rot_rad}{T_base}$$

Hence, the relation between R_var and J_fw_SI_bl has to be linearised. In case of a FW configuration of the Type VI [11] in the NREL 5 MW reference WT [17], R_var can range from R_fw_min = 3.9324131 m to R_fw_max = 44.0765 m. With m_fw_fluid = 925.46 kg the linearization can be done. Figure 25 shows the linearization of the FW inertia for different R_var values. The slope values plotted in Figure 25 are also shown in Table 6.

Table 6 Operating points for linearization.

n = operating point	R_var(n) [m]	slope_J(n) [kgm ² /m]	J_fw_SI_bl(n) [kgm ² /m]
1	5.53E+00	1.61E+04	2.83E+04
2	1.18E+01	2.76E+04	1.30E+05
3	1.80E+01	3.90E+04	3.01E+05
4	2.41E+01	5.02E+04	5.38E+05
5	3.01E+01	6.11E+04	8.37E+05
6	3.59E+01	7.19E+04	1.20E+06
7	4.17E+01	7.81E+04	1.61E+06

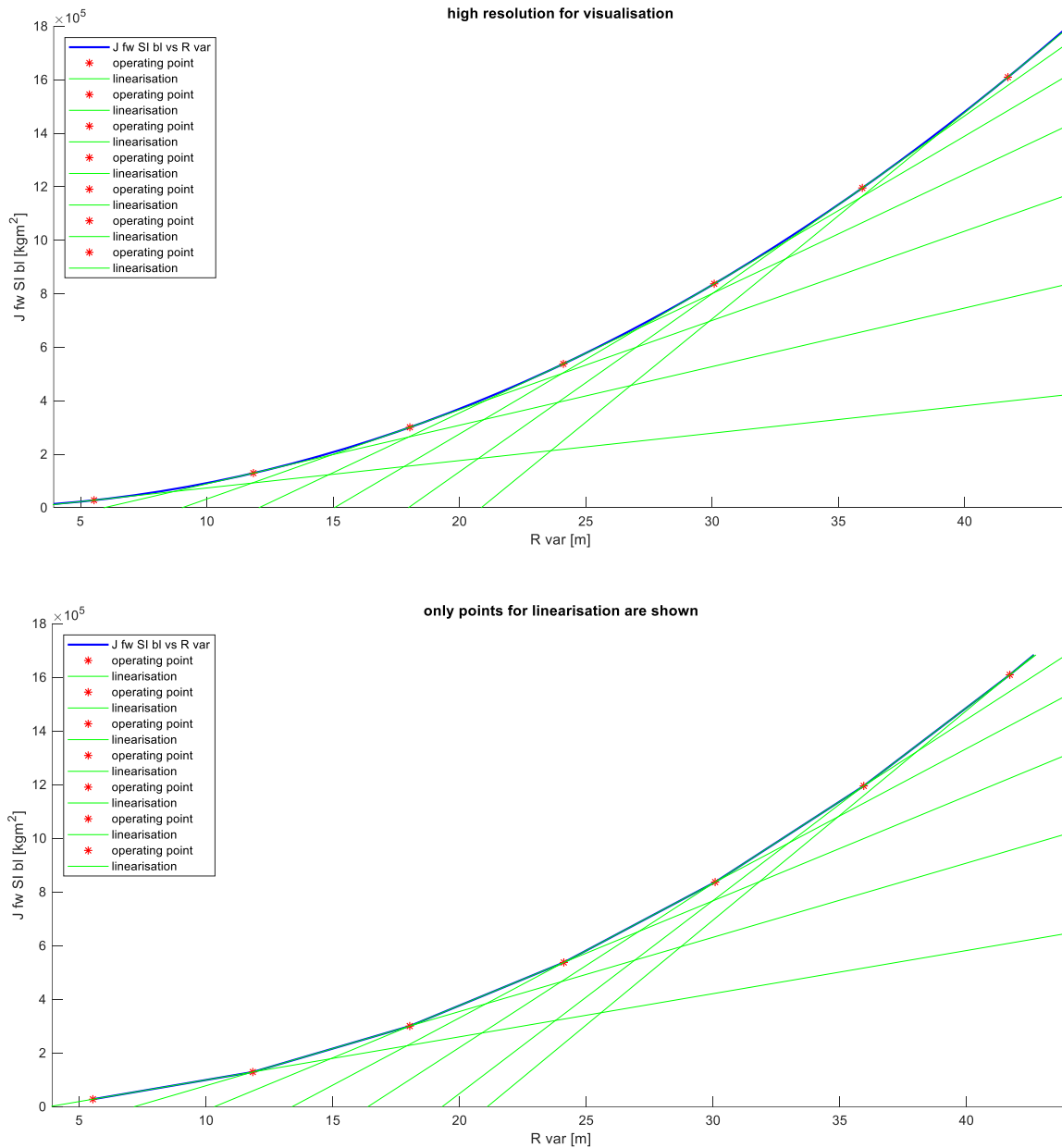


Figure 25 Top: $J_{fw_SI_bl}$ as a function of R_{var}^2 for finding appropriate linearizations. Bottom: only the points of linearization are shown.

Applying the equation for linear interpolation allows yielding the translation from R_{var} to $J_{fw_SI_bl}$. Using the names as stated in Table 6 leads to the following equation:

$$J_{fw_SI_bl} = \text{slope}_J(n) \cdot (R_{var} - R_{var}(n)) + J_{fw_SI_bl}(n) \quad \text{Equation 30}$$

5.2.2.4 P vs. speed characteristic

The P vs. speed characteristic contains different operating points around which linearization can be performed. The content of the P vs. speed characteristic is documented in the documentation of the simulation model [1]. The equation for linear interpolation ($y_i = \frac{y_2 - y_1}{x_2 - x_1} \cdot (x_i - x_1) + y_1$) allows yielding

the translation from speed to power for any generator speed in the P vs. speed characteristic. A premise for this calculation is the slope of the characteristic in the different operating points. Figure 26 shows the P vs. speed characteristic, the different operating points and the linearization in these operating points.

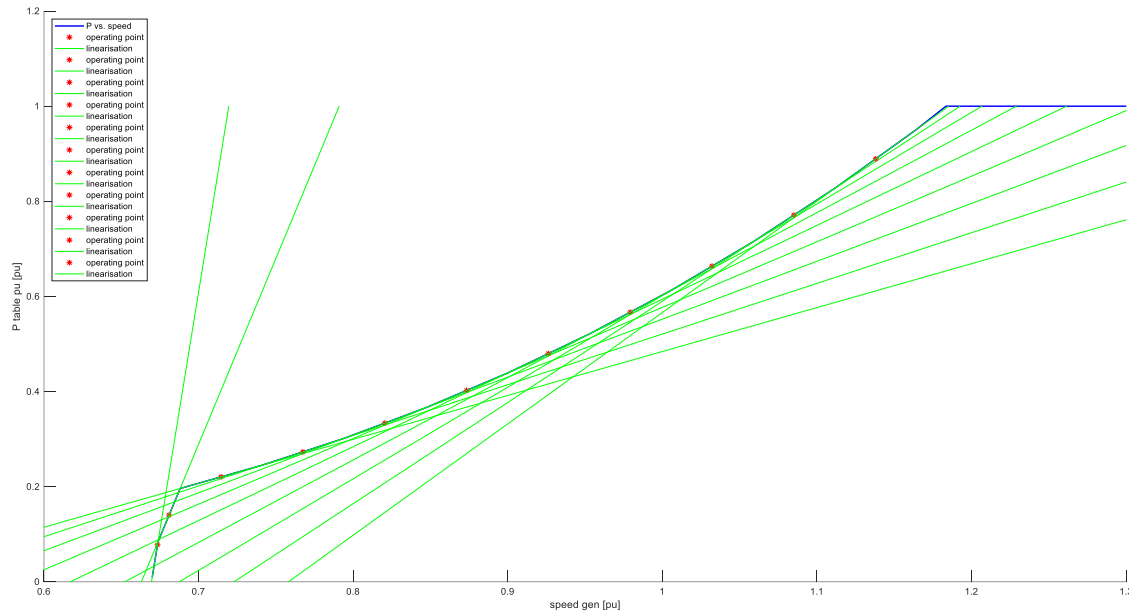


Figure 26 P_table_pu as a function of speed_gen for finding appropriate linearisations.

The slope values plotted in Figure 26 together with the power values and the speed values are also shown in Table 7.

Table 7 Operating points for linearization.

n = operating point	speed_gen(n) [pu]	slope_P(n) [pu/pu]	P_gen(n) [pu]
1	6.73E-01	2.00E+01	7.80E-02
2	6.81E-01	7.81E+00	1.40E-01
3	7.15E-01	9.23E-01	2.21E-01
4	7.67E-01	1.07E+00	2.73E-01
5	8.20E-01	1.22E+00	3.34E-01
6	8.73E-01	1.38E+00	4.02E-01
7	9.26E-01	1.55E+00	4.80E-01
8	9.79E-01	1.73E+00	5.67E-01
9	1.03E+00	1.93E+00	6.64E-01
10	1.09E+00	2.13E+00	7.71E-01
11	1.14E+00	2.34E+00	8.89E-01

The translation from any arbitrary speed to power is done with the following equation:

$$P_{gen} = slope_P(n) \cdot (speed_gen - speed_gen(n)) + P_{gen}(n) \quad \text{Equation 31}$$

5.2.3 Block Diagram Reduction

The block diagram shown in Figure 20 has to be reduced to a familiar form in order to derive a transfer function. Figure 27 shows the simplified block diagram, where the following simplifications are implemented:

- The torque contributions of the FW in the three blades are considered identical: $T_{fw} = 3 \cdot T_{fw_bl}$
- The motions of the three blade tip masses are considered identical.
- The blade tip masses are assumed to rotate synchronously around the centre of rotation with the same speed as the hub, i.e. there is no flexibility in the blades considered.
- It is assumed that all blades are in horizontal position all the time, i.e. gravity has no impact on the pressure in the FW fluid.
- The pump pressures are constantly at the value when the pumps run in steady state and the flowrate is maximum, i.e. transients in pump operation are neglected.
- The tolerance in the power setpoint is neglected.
- The drive train speed is not influenced by the aerodynamic rotor torque. The drive train speed is merely determined by the operating point around which the system is linearized.
- The generator torque, T_{elec} , is also assumed to be constant. In part load P_{gen} responds to any speed variations, i.e. increasing speed_{gen} leads to increasing P_{gen} and vice versa. Hence, the feedback from the generator torque to drive train speed is neglected as only small signal variations are considered.

The resulting block diagram in the bottom of Figure 27 is a simple closed control loop.

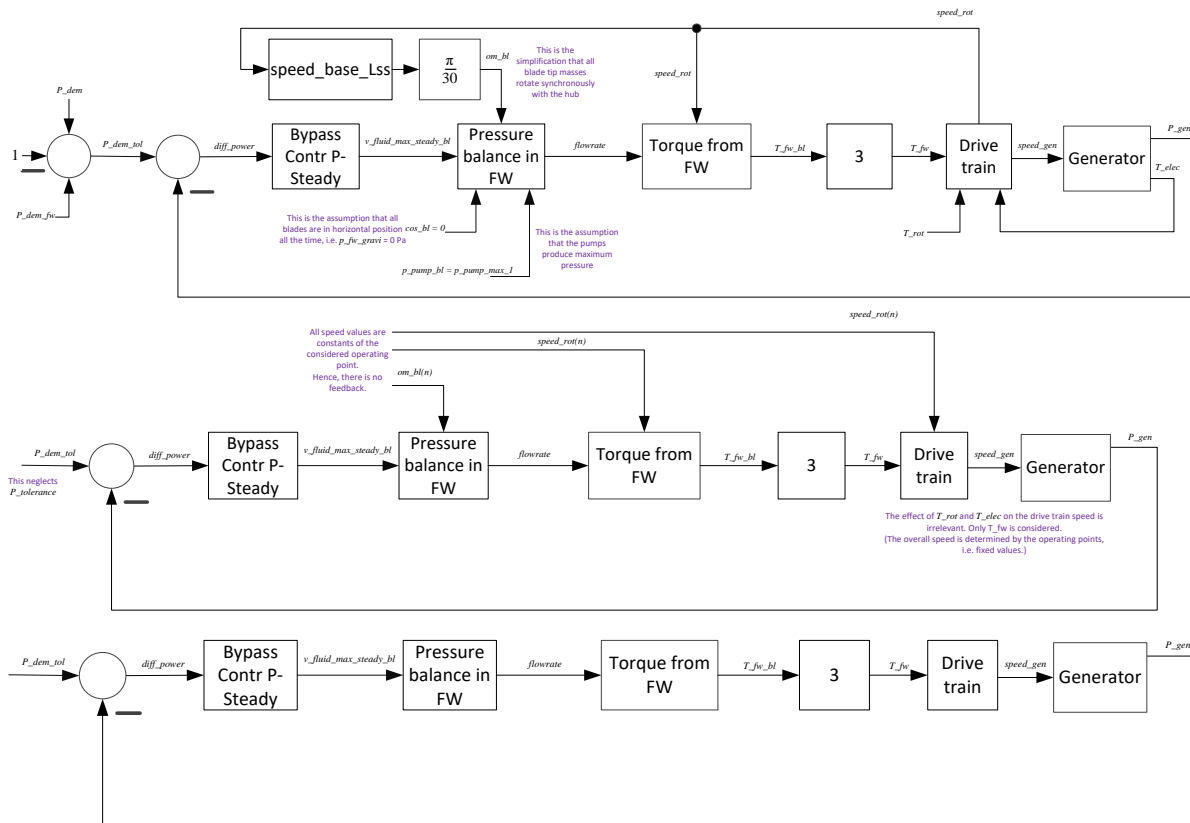


Figure 27 Block diagram with simplifying assumptions. Bottom: resulting block diagram for deriving transfer functions. Variable names are introduced in the documentation of the simulation model [1].

The content of the blocks in Figure 27 is listed in the following, with links to the applicable sections in this report:

- Bypass Contr P-Steady: P controller to control $v_fluid_max_steady_bl$, see section 5.3 Transfer Function of Bypass Controller for P-Steady
- Pressure balance in FW: Since the Bypass Controller controls the upper and lower limit of the integration of the fluid acceleration; it is assumed that when the pressures acting on the fluid are constant, the Bypass Controller alone determines v_fluid . Hence, $flowrate = v_fluid_max_steady_bl \cdot A_tube$. For an explanation on this see also section flowrate from $v_fluid_max_bl$.
- Torque from FW: Linearization of R_var as a function of Vol_fluid_tank2 , which is the integral of flowrate and linearization of FW torque as function of R_var^2 , see section 5.4 Transfer Function of Hydraulic FW.
- Drive train: See section 5.5 Transfer Function of 2 Masses Drive Train from Inspection
- Generator: Linearization of P vs. speed characteristic and PT1 filter that represents the dynamics of the generator-converter unit, see section 5.6 Transfer Function of Generator-Converter-Unit.

This leads to the block diagram in Figure 28 that is the basis for deriving the transfer functions in the following sections.

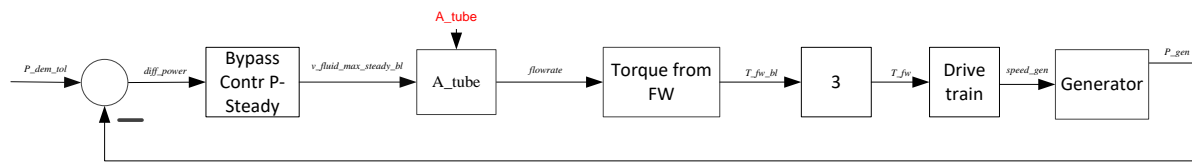


Figure 28 Block diagram for deriving the transfer functions. Variable names and parameter names (red) are introduced in the documentation of the simulation model [1].

The transfer function of the complete control circuit is further discussed in section 5.7 Control Circuit.

5.3 Transfer Function of Bypass Controller for P-Steadying

Due to the integral nature of the plant the pump bypass controller is merely a proportional (P) controller. Hence its transfer function is:

$$G_{P_steady}(s) = K_{P_bypass_Psteady} \quad \text{Equation 32}$$

Where $K_{P_bypass_Psteady}$ is the proportional gain that has to be defined for the different operating points.

5.4 Transfer Function of Hydraulic FW

Integrating flowrate yields Vol_fluid_tank2 , see Figure 22. The linearizations in the sections above lead to Equation 27 and Equation 30. Substituting R_var in Equation 30 with Equation 27 reveals that $R_var(n)$ cancels out, provided that the operating points (n) in the linearizations of R_var and $J_fw_SI_bl$ are identical. However, this has been taken care of.

Figure 29 shows the block diagram of the equation that yields the FW torque, $J_fw_SI_bl$, from flowrate. Applying the rules for reorganising block diagrams allows moving the summation points to the right [18]. Hence, the block diagram of the hydraulic FW transfer function simplifies like shown in the bottom of Figure 29.

The torque of the FW is derived from the derivative of the FW inertia (see Equation 29):

Offsets have no effect on the derivative of a signal. Therefore, when moving the summation point in Figure 29 beyond the differentiation block, the summation, i.e. the offset is eliminated, see Figure 30.

Also the speed (speed_rot_rad in Equation 29) is only a constant in the linearized model. This simplifies the block diagram even further, see bottom in Figure 30.

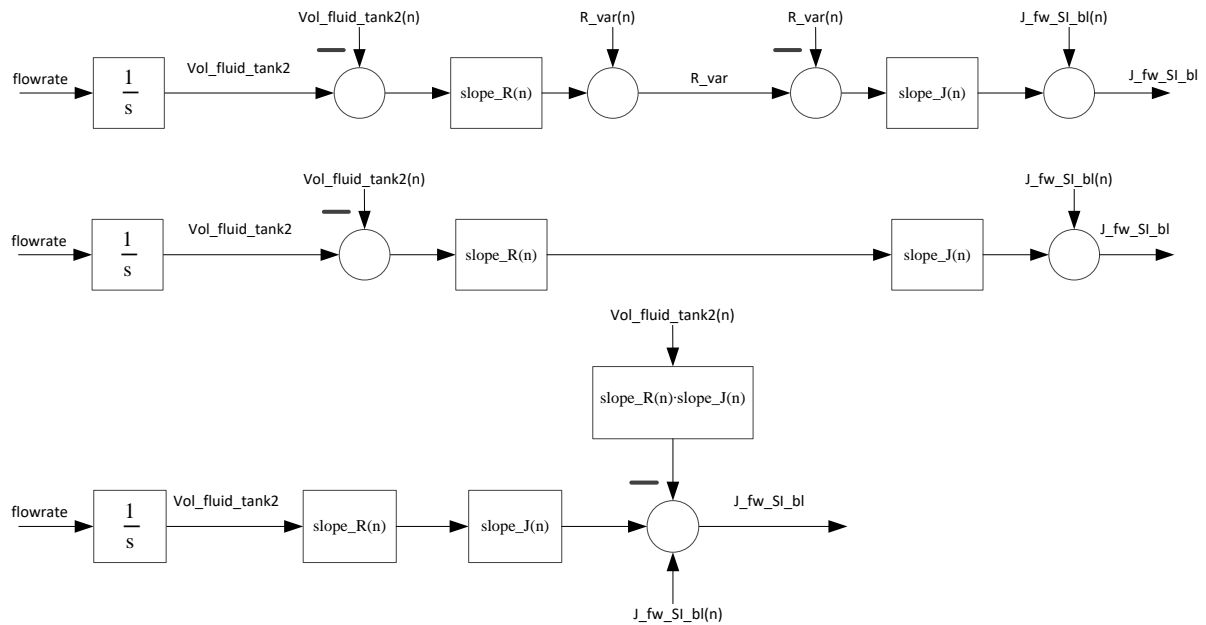


Figure 29 Block diagram of linearized $J_{fw_SI_bl}$ from flowrate model. Block diagram simplification by reorganisation in three steps: from top to bottom. Variable names are introduced in the documentation of the simulation model [1].

The bottom of Figure 30 shows the block diagram of the FW from its input signal, flowrate, to the resulting torque, T_{fw_bl} . This FW torque is the variable that is input to the drive train model.

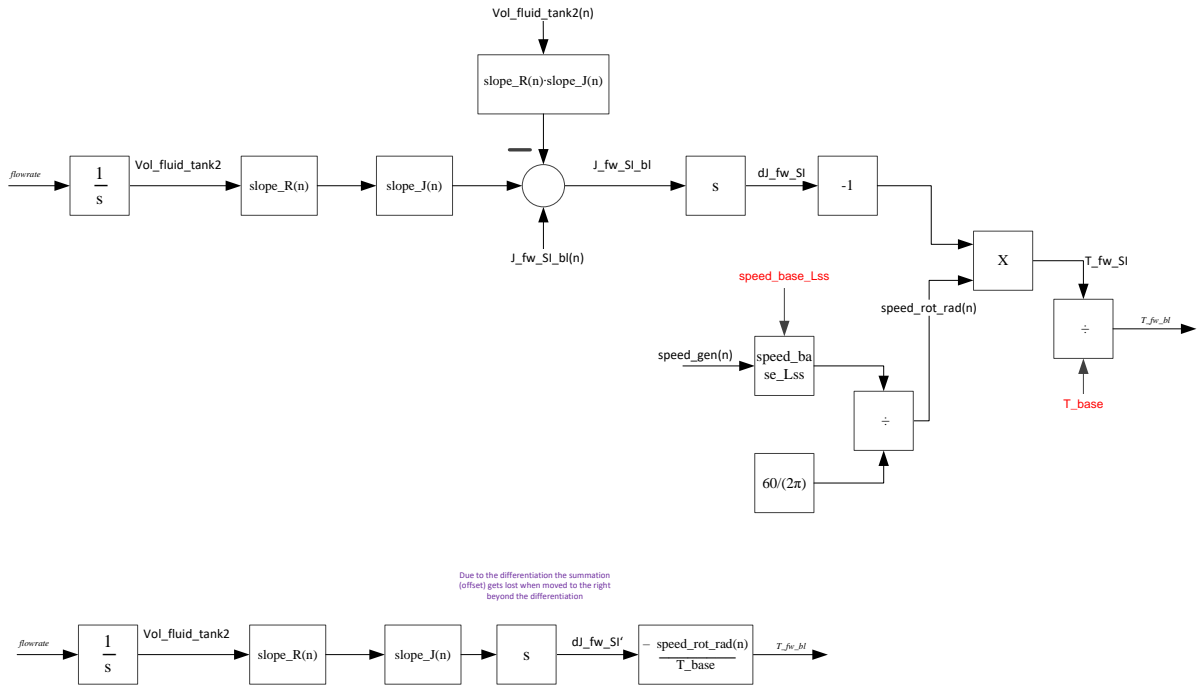


Figure 30 Block diagram of linearized FW model. Variable names and parameter names (red) are introduced in the documentation of the simulation model [1].

Considering Figure 28 and Figure 30 allows listing all transfer functions that represent the hydraulic FW:

$$G_{A_tube}(s) = A_tube \quad \text{Equation 33}$$

Where A_tube is the cross sectional inner area of the hydraulic tube [1].

$$G_{integrator}(s) = \frac{1}{s} \quad \text{Equation 34}$$

$$G_{slopes_FW}(s) = slope_R(n) \cdot slope_J(n) \quad \text{Equation 35}$$

With values for $slope_R(n)$ and $slope_J(n)$ as resulted from linearization.

$$G_{diff_FW}(s) = s \quad \text{Equation 36}$$

And finally

$$G_{sp_T_base}(s) = \frac{-speed_rot_rad(n)}{T_base} \quad \text{Equation 37}$$

Where T_base is the torque base needed for translating to pu [1].

5.5 Transfer Function of 2 Masses Drive Train from Inspection

For the purpose of designing the Pump Bypass Controller a simplified two masses drive train model is derived from the more complex five masses model that is contained in the 1st Eigenmodes model of a WT [1] with which the simulations are conducted.

Nise introduces the concept for deriving the transfer function of a rotating system from inspection [19]. With this methodology the transfer function of the generator speed (*speed_hss*) from FW torque $G_{DT}(s) = \frac{\text{speed_hss}}{T_{fw}}$ is looked for.

The drive train is aggregated to a two masses, spring and damper system, hence, the motions of the individual blades are assumed to be synchronized and the blades are assumed to be stiffly connected to the hub. This means that the blade tip masses, the blade root masses and the hub oscillate in synchronism like one single mass, see Figure 31.

$$J_{lss} = ((J_{hub_SI} + 3 \cdot J_{bladeroot}) + m_{bladetip} \cdot 3 \cdot (R_{cntr_gravi_bladetip})^2) / J_{base_lss}$$

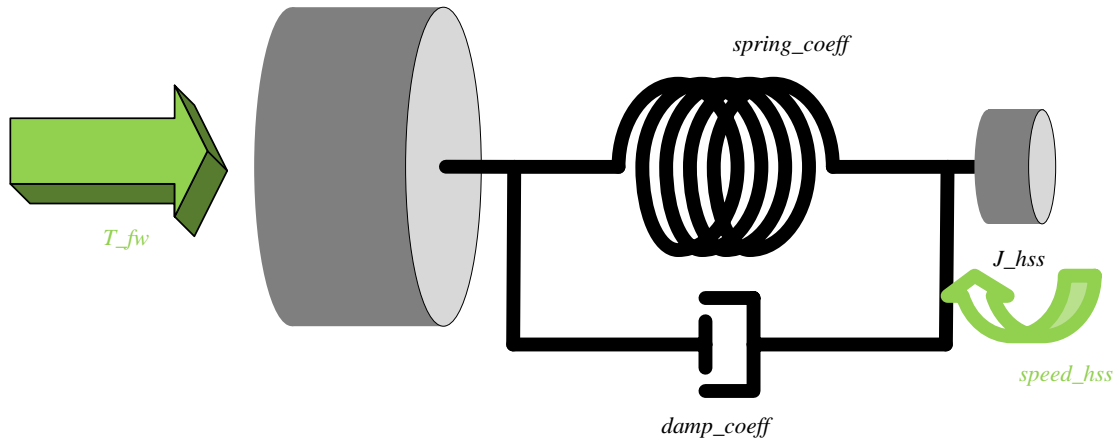


Figure 31 Diagram of two masses spring and damper representation of drive train. Variable names and parameter names are introduced in the documentation of the simulation model [1].

5.5.1 Drive Train Parameters

For the aggregated blade tip inertia the mass of blade 2 is taken (the deliberate imbalance in the rotor is introduced by an extra mass in blade 1 [1]). Hence, the inertia of the blade tip mass of one blade, J_{blade} , in pu with the unit s is:

$$J_{blades} = \frac{m_{bladetip} \cdot 3 \cdot (R_{cntr_gravi_bladetip})^2}{J_{base_lss}} = 6.5982 \text{ s} \quad \text{Equation 38}$$

The inertia of the hub, J_{hub} , also in pu, i.e. with the unit s:

$$J_{hub} = \frac{(J_{hub_SI} + 3 \cdot J_{bladeroot})}{J_{base_lss}} = 3.3593 \text{ s} \quad \text{Equation 39}$$

This leads to the aggregated inertia on the low speed shaft, J_{lss} :

$$J_{lss} = J_{blades} + J_{hub} = 9.9575 \text{ s} \quad \text{Equation 40}$$

The stiffness and damping, $\text{spring_coeff} = 115.0094407 \text{ 1/s}$ and $\text{damp_coeff} = 1.448721469 \text{ pu}$, respectively, together with the inertia of the high speed shaft $J_{hss} = 1.171447472 \text{ s}$ can be extracted from the documentation of the simulation model [1].

5.5.2 Mechanical Impedances

The concept for deriving the transfer function of a rotating system from inspection is based on mechanical impedance. Since the transfer function from torque (T) to speed is looked for, the following impedances are defined for the system shown in Figure 31.

Impedance of stiffness:

$$Z_{s_dt}(s) = \frac{T(s)}{speed(s)} = \frac{spring_coeff}{s} \quad \text{Equation 41}$$

Impedance of damping:

$$Z_{d_dt}(s) = \frac{T(s)}{speed(s)} = damp_coeff \quad \text{Equation 42}$$

Impedance of inertias in general:

$$Z_{inertia}(s) = \frac{T(s)}{speed(s)} = J \cdot s \quad \text{Equation 43}$$

Impedance of inertia on low speed shaft:

$$Z_{J_lss}(s) = J_{lss} \cdot s \quad \text{Equation 44}$$

Impedance of inertia on high speed shaft:

$$Z_{J_hss}(s) = J_{hss} \cdot s \quad \text{Equation 45}$$

5.5.3 Torques Acting on Inertias

To derive the transfer function in frequency domain of a rotational system merely from inspection the free-body diagrams of the inertias have to be drawn, see Figure 32. NB: although in the simulation model the rotational speed of the high speed shaft is called speed_gen, because it is the speed of the generator, in the following speed_gen is called speed_hss to make obvious that it is the speed of the inertia J_hss.

The external torque that is considered is merely the FW torque, T_fw. The rotor torque and the electric torque are neglected as they are assumed to be constant and in balance. The system is assumed to be in steady state in one operating point. Only T_fw disturbs the system.

Figure 32 shows the two inertias for the situations when they are kept standing still. This allows identifying the torques that act on each inertia and on its adjacent inertia. For simplicity the Laplace operator s is omitted.

The right column in Figure 32 shows the torques that are summed up in the following equations.

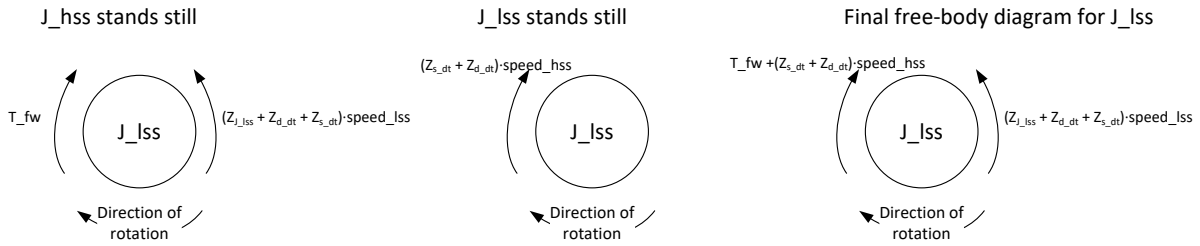
Torques acting on J_lss:

$$(Z_{J_lss} + Z_{d_dt} + Z_{s_dt}) \cdot speed_lss - (Z_{s_dt} + Z_{d_dt}) \cdot speed_hss = T_fw \quad \text{Equation 46}$$

Torques acting on J_hss:

$$-(Z_{s_dt} + Z_{d_dt}) \cdot speed_lss + (Z_{J_hss} + Z_{d_dt} + Z_{s_dt}) \cdot speed_hss = 0 \quad \text{Equation 47}$$

Torques on J_{lss}



Torques on J_{hss}

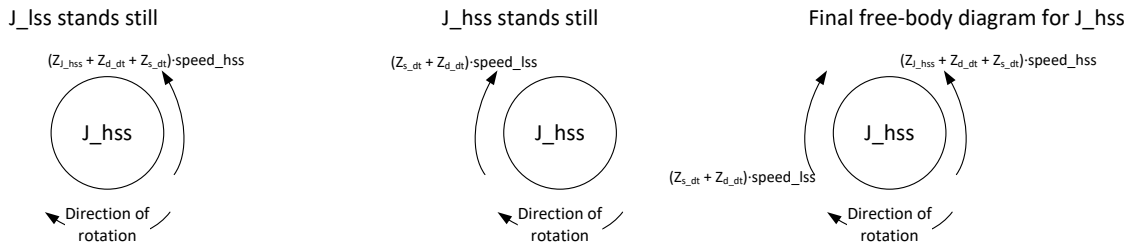


Figure 32 Free-body diagrams of drive train inertias for two masses model.

The above is an equation system that comprises two equations in order to express two variables (speed_{lss} and speed_{hss}). Writing this equation system in matrix form yields

$$Ax = c = \begin{pmatrix} a_{11} & a_{12} \\ a_{21} & a_{22} \end{pmatrix} \begin{pmatrix} x_1 \\ x_2 \end{pmatrix} = \begin{pmatrix} c_1 \\ c_2 \end{pmatrix} \quad \text{Equation 48}$$

In order to solve a linear, squared (the dimension of the coefficients matrix 2 by 2) equation system in matrix form, the Cramer's rule can be applied. Since the transfer function from T_{fw} to speed_{hss} is looked for, the unknown in the above equation system is x_2 , i.e. speed_{hss}. Hence, according to Cramer's rule [19], x_2 can be calculated from the determinant of the coefficients matrix Δ and the determinant of the auxiliary matrix Δ_2 .

First the equation system is written in matrix form:

$$Ax = c = \begin{pmatrix} (Z_{J_{lss}} + Z_{d,dt} + Z_{s,dt}) & -(Z_{s,dt} + Z_{d,dt}) \\ -(Z_{s,dt} + Z_{d,dt}) & (Z_{J_{hss}} + Z_{d,dt} + Z_{s,dt}) \end{pmatrix} \begin{pmatrix} \text{speed}_{lss} \\ \text{speed}_{hss} \end{pmatrix} = \begin{pmatrix} T_{fw} \\ 0 \end{pmatrix} \quad \text{Equation 49}$$

The determinant of the coefficients matrix **A** is:

$$\Delta = a_{11} \cdot a_{22} - a_{12} \cdot a_{21} \quad \text{Equation 50}$$

Since the variable speed_{hss} is looked for, which is in the second row of vector x , the second column of matrix **A** has to be replaced with the result vector c in order to get the auxiliary matrix A_2 and the auxiliary determinant Δ_2 .

$$A_2 = \begin{pmatrix} a_{11} & c_1 \\ a_{21} & c_2 \end{pmatrix} \rightarrow \Delta_2 = a_{11} \cdot c_2 - c_1 \cdot a_{21} \quad \text{Equation 51}$$

According to Cramer's rule the desired variable can be calculated:

$$speed_{hss} = \frac{\Delta_2}{\Delta}$$

Equation 52

Since the desired transfer function is from T_{fw} to $speed_{hss} = speed_{gen}$:

$$G_{DT}(s) = \frac{speed_{gen}(s)}{T(s)} = \frac{\Delta_2}{\Delta \cdot T_{fw}(s)}$$

Equation 53

Equation 54 shows the resulting transfer function that is yielded by inserting the above expression for $speed_{hss}$, substituting back the equations for the impedances and cancelling out identical zeros and poles.

$$G_{2mDT}(s) = \frac{-0.1449 s^2 + 11.5 s}{1.166 s^4 + 1.612 s^3 + 128 s^2}$$

Equation 54

The bode plot of $G_{2mDT}(s)$ is shown in Figure 33.

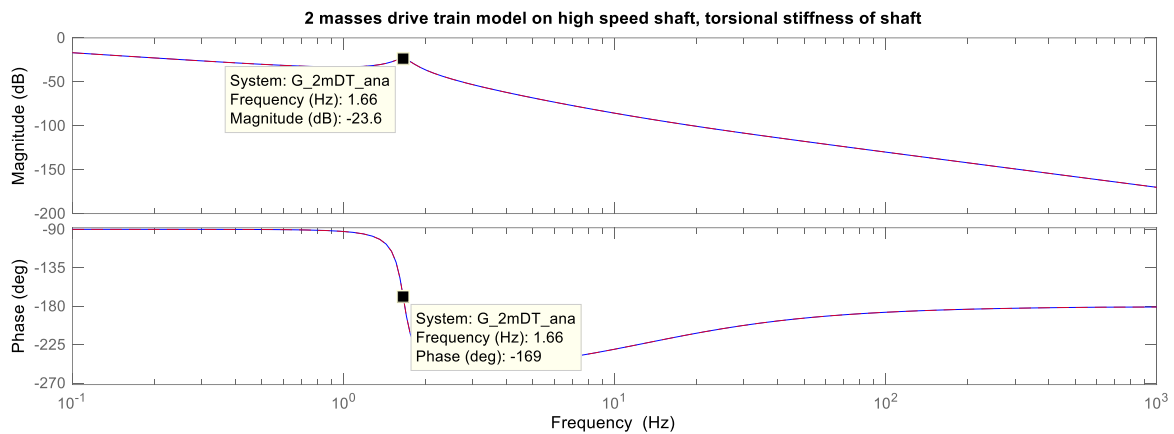


Figure 33 Bode plot of derived transfer function $G_{2mDT}(s) = \frac{speed_{gen}(s)}{T(s)}$.

If the drive train rotates with a pre-defined speed (see section Linearizations in the Block Diagram) T_{rot} and T_{elec} are in balance. If T_{fw} varies around the value of T_{rot} , then $speed_{gen}$ can only differ from the initial speed if this torque variation happens slow enough. This reasoning is supported by Figure 33, where the largest gain is at low frequencies. Only if the T_{fw} variations excite a resonance between the inertias and the torsional spring in the drive train, $speed_{gen}$ can respond to fast (with a frequency of 1.66 Hz) T_{fw} variations.

5.6 Transfer Function of Generator-Converter-Unit

The generator-converter unit, including its controls, is the content of the block “Generator” in Figure 27, which is modelled as a PT1 filter and the P_{gen} vs. $speed_{gen}$ characteristic.

Input to this subsystem is $speed_{gen}$ from the drive train model, which is applied in the P vs. $speed$ characteristic to derive the P reference. After passing the power controller (output variable: $P_{setpoint}$) a PT1 filter represents the response time of the generator and the converter.

The generator-converter unit behaves similarly to a PT1 filter. The step response of the generator-converter unit reveals that, with the current parameter settings, it can be modelled with a PT1 and a time constant of $T_{geno_PT1} = 0.556$ s.

Consequently, the transfer function of the PT1 equivalent of the generator-converter unit is:

$$G_{geno_PT1}(s) = \frac{1}{1+s \cdot 0.556} \quad \text{Equation 55}$$

The linearization of the P vs. speed characteristic lead to Equation 31. Hence, the block diagram of the generator-converter unit with its controls looks like shown in Figure 34. Reorganisation allows moving the summation beyond the PT1 filter, because the offsets have no impact on the dynamic response of the system, see bottom of Figure 34. The power signal that does not comprise the offsets is called P_{gen}' . This is the variable that will be fed back in the closed power control loop.

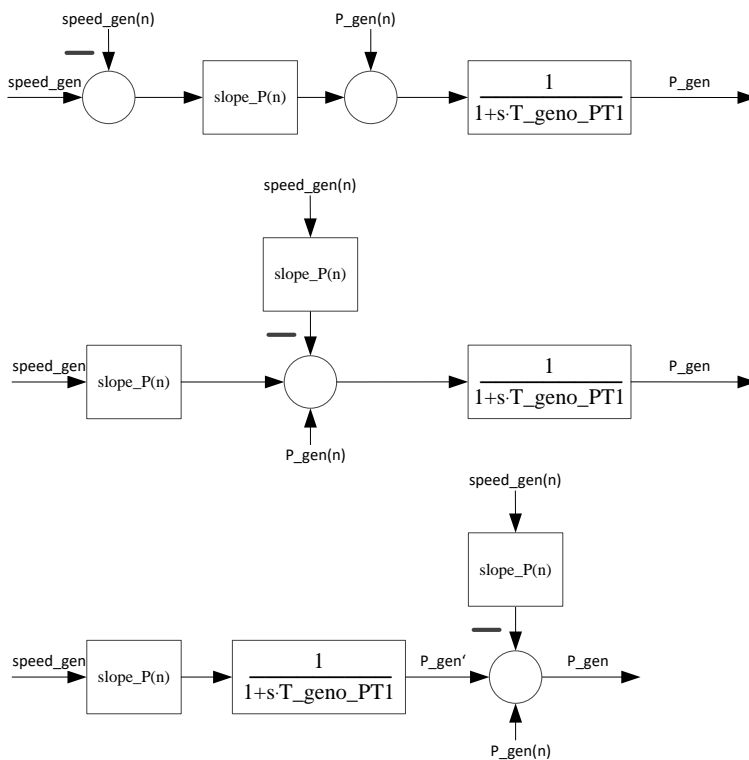


Figure 34 Block diagram of linearized generator-converter model. Variable names are introduced in the documentation of the simulation model [1].

5.7 Control Circuit for P-Steadying

5.7.1 Block Diagram of the Control Circuit

In section “Block Diagram Reduction” the block diagram is reduced and reorganised to get a familiar form. This allows deriving the transfer function of the whole control circuit, which then leads to the bode plots.

The block diagram in Figure 28 in section “Block Diagram Reduction” is shown again in Figure 35, this time, however, the blocks that are derived in the previous subsections are also incorporated. Figure 35 also shows the rearranged block diagram, where the closed control loop only comprises linear components, i.e. the summation points are moved out of the loop.

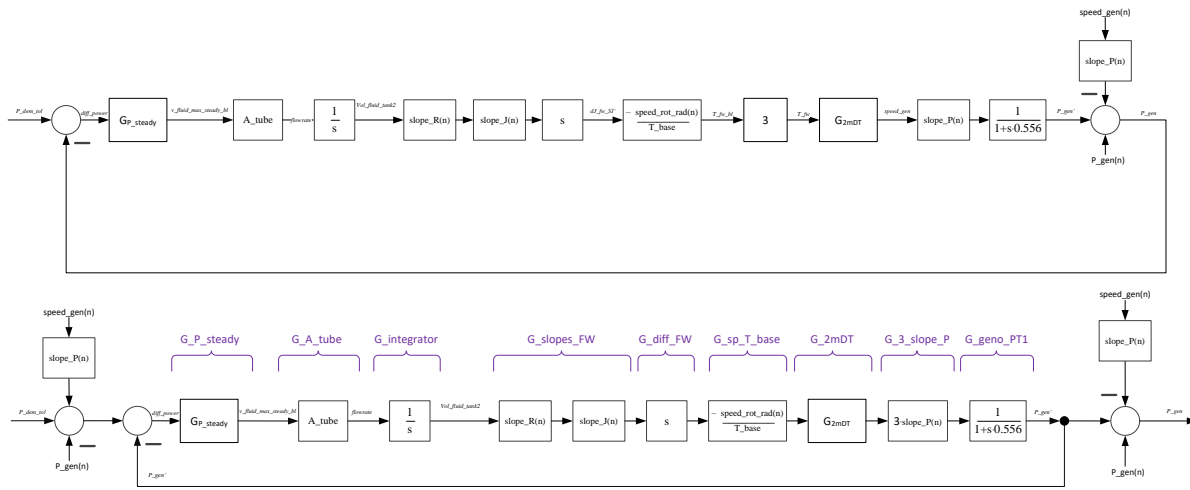


Figure 35 Block diagram of closed P-steady control loop. Top: combination of all linearized transfer functions. Bottom: Rearranged block diagram with closed control loop that contains linear components only.

The transfer function of the forward path is

$$G_{OL_P_steady}(s) = G_{PI_steady}(s) \cdot G_{A_tube}(s) \cdot G_{integrator}(s) \cdot G_{slopes_FW}(s) \cdot G_{diff_FW}(s) \cdot G_{sp_T_base}(s) \cdot G_{2mDT}(s) \cdot G_{3_slope_P}(s) \cdot G_{geno_PT1}(s)$$

Equation 56

$$G_{OL_P_steady}(s) = \frac{2.02 \cdot 10^{-06} s^2 + 0.0001603s}{0.6486 s^5 + 2.063s^4 + 72.78 s^3 + 128 s^2}$$

The closed loop transfer function can be calculated with Equation 57

$$G_{CL_P_steady}(s) = \frac{G_{OL_P_steady}(s)}{1 + G_{OL_P_steady}(s)}$$

Equation 57

5.7.2 Transfer Functions in the Linearised Operating Points

As shown in the sections above, the linearization around operating points leads to different parameters that have an impact on the transfer function. There are two input variables that allow identifying operating points: Vol_fluid_tank2 and speed_gen.

Applying these two input variables allows looking up the constants from the linearisations:

- slope_R(n) – Table 5
- slope_J(n) – Table 6
- speed_gen(n) – Table 7
- speed_rot_rad(n) = speed_gen(n) · $\frac{\text{speed_base_Lss} \cdot \pi}{30}$
- slope_P(n) – Table 7

This means that all three tables are needed. However, the rows (number n) in Table 5 and Table 6 are identical (the 8th row in Table 5 can be neglected), i.e. they refer to the same Vol_fluid_tank2. Table 7 has speed_gen as input variable.

Hence, the two input variables, $speed_gen$ and Vol_fluid_tank2 , influence the parameters that are needed for defining the parameters of the linearized operating points. Therefore, the parameters of the transfer functions are matrices with the input variables $speed_gen$ and Vol_fluid_tank2 .

A program is created that contains two cascaded for loops. The inner loop runs through the different Vol_fluid_tank2 values and the outer loop runs through the different $speed_gen$ values. This way 77 transfer functions are generated and their bode plots plotted.

Figure 36 shows these bode plots of the linear control loop in Figure 35 (i.e. only the part in the middle, where no offsets are added). For deriving the bode plots in Figure 36 the controller gain is set to a constant $K_P_bypass_Psteady = -1000$.

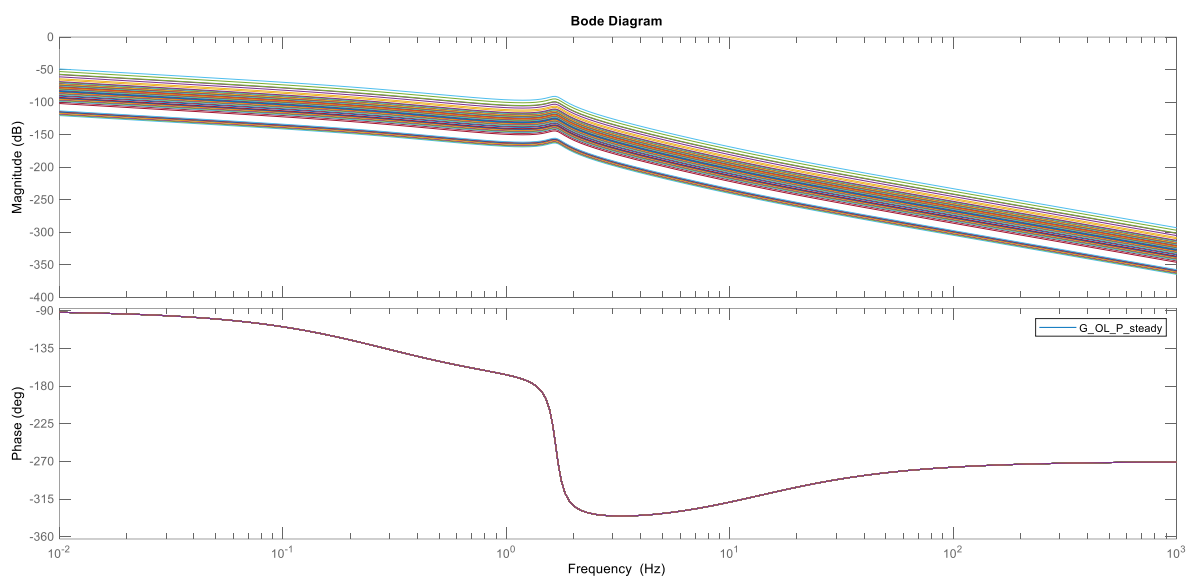


Figure 36 Bode diagrams of open P-steady control loop.

5.8 P-Steadying Controller (Proportional) Design

Due to the integral nature of the plant to be controlled (see Figure 35) the P-steadying pump bypass controller is a proportional (P) controller as shown in Figure 37. The proportional gain of this controller, $K_P_bypass_Psteady$, has to be designed such that the plant is controlled properly for any operating point. In other words, $K_P_bypass_Psteady$ has to be set such that the differences in the transfer functions of the plant (as identified in section 5.2 Transfer Functions) are compensated by the P-controller. There are different methods for finding suitable gain values conceivable. Here the step response approach is chosen.

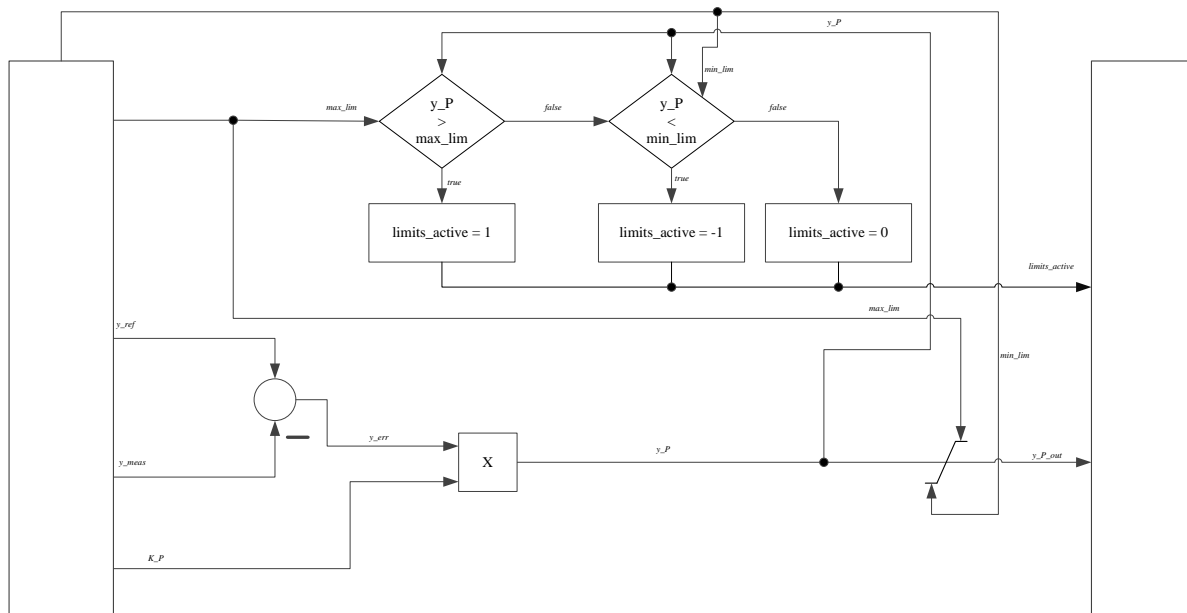


Figure 37 Block diagram of P-controller.

5.8.1 Step Response Approach

Matlab allows deriving the step response of a system, if this system is specified in terms of a linear transfer function. The step response of a system is characterised by measures like % overshoot, rise time, settling time, undershoot, peak time and others. In order to limit the criteria here only % overshoot and settling time are analysed for finding the optimal controller gains.

For stability reasons, it seems plausible to choose controller gains that limit the % overshoot to a reasonable value. If the system overshoots, it is to be expected that the controller hits its output limits, which means that the system becomes non-linear. However, linearity is the basis for this controller design, which is why the system is linearized in the different operating points (see section 5.2.2 Linearizations in the Block Diagram).

Limiting % overshoot leads to relatively small gains, which makes the system respond slowly. While slow response is good for numerical stability, it has negative effects on the energy yield of the WT. Consequently, controller gains are searched that lead to a user defined minimum % overshoot. 14 % overshoot is found to be a compromise between speed and stability. Since there are numerous gain settings that lead to at least 14 % overshoot, a second criterion is needed. For this purpose the minimum settling time is chosen.

5.8.2 Result from Proportional Controller Design

The design criteria mentioned above lead to a K_P _bypass_Psteady value for every operating point that resulted from the plant linearization (see section 5.7.2 Transfer Functions in the Linearised Operating Points). The resulting K_P _bypass_Psteady gains that are shown in Table 8.

Table 8 K_P _bypass_Psteady gains for the different operating points.

	R_var [m]						
	5.53	11.8	18.0	24.1	30.1	35.9	41.7

speed_gen [pu]	0.673	-606	-358	-258	-204	-170	-148	-138
	0.681	-1536	-910	-656	-520	-434	-376	-352
	0.715	-6978	-7340	-5300	-4198	-3508	-3036	-2844
	0.767	-8000	-5924	-4278	-3388	-2830	-2450	-2294
	0.820	-8000	-4850	-3502	-2772	-2318	-2006	-1878
	0.873	-6786	-4020	-2902	-2298	-1920	-1662	-1558
	0.926	-5688	-3370	-2432	-1926	-1610	-1394	-1304
	0.979	-4814	-2852	-2060	-1630	-1362	-1180	-1104
	1.03	-4110	-2436	-1758	-1392	-1164	-1006	-942
	1.09	-3538	-2096	-1514	-1198	-1002	-866	-812
	1.14	-3066	-1816	-1312	-1038	-868	-750	-704

The settling times and % overshoot values that lead to these controller gains are shown in Table 9 and Table 10, respectively.

Table 9 Settling times in seconds for the different operating points.

		R_var [m]						
		5.53	11.8	18.0	24.1	30.1	35.9	41.7
speed_gen [pu]	0.673	3.5571373	3.5606136	3.56287	3.5647794	3.5680672	3.5612468	3.5665711
	0.681	3.5557472	3.5558974	3.5578132	3.5567984	3.5582859	3.5571523	3.5578064
	0.715	4.0679721	3.5555735	3.5555659	3.5554439	3.5555081	3.5555972	3.5555192
	0.767	4.0360305	3.5555863	3.5554556	3.555505	3.5560358	3.5557565	3.5562159
	0.820	3.5823823	3.5555962	3.5556031	3.556257	3.5555088	3.5556641	3.5562915
	0.873	3.5555496	3.5558016	3.5560847	3.5562681	3.5565091	3.5563634	3.5554582
	0.926	3.5555676	3.5556638	3.556316	3.556392	3.5560475	3.5556147	3.55718
	0.979	3.5557415	3.5559098	3.5555326	3.5566066	3.5567449	3.5555937	3.5569653
	1.03	3.5559726	3.5556261	3.5562571	3.556527	3.5557961	3.5574863	3.5578773
	1.09	3.5557991	3.5559942	3.5555717	3.5566174	3.555626	3.5573023	3.5561242
	1.14	3.5561736	3.5566093	3.5559632	3.5571898	3.5564356	3.5584036	3.5559564

Table 10 % overshoot for the different operating points.

		R_var [m]						
		5.53	11.8	18.0	24.1	30.1	35.9	41.7
speed_gen [pu]	0.673	26.573872	26.450525	26.370231	26.302144	26.184623	26.428012	26.238143
	0.681	26.623067	26.617755	26.549924	26.585873	26.533167	26.573338	26.550166
	0.715	14.008574	26.62921	26.629478	26.633791	26.631524	26.628372	26.631131
	0.767	22.247171	26.628759	26.633379	26.631633	26.61286	26.62274	26.606489
	0.820	25.6691	26.628409	26.628165	26.605034	26.631497	26.626006	26.603813
	0.873	26.630056	26.621145	26.61113	26.60464	26.596114	26.60127	26.633289
	0.926	26.629419	26.626017	26.602946	26.600258	26.612448	26.627753	26.572358
	0.979	26.623269	26.617318	26.630656	26.592661	26.587766	26.628497	26.579964
	1.03	26.615097	26.627349	26.605031	26.595479	26.621339	26.561508	26.547653
	1.09	26.621232	26.614334	26.629275	26.59228	26.627353	26.568027	26.609733
	1.14	26.607985	26.592567	26.615428	26.572011	26.598713	26.52899	26.615669

The open loop transfer functions of the control circuit with these controller gain settings are applied to generate the bode plots shown in Figure 38.

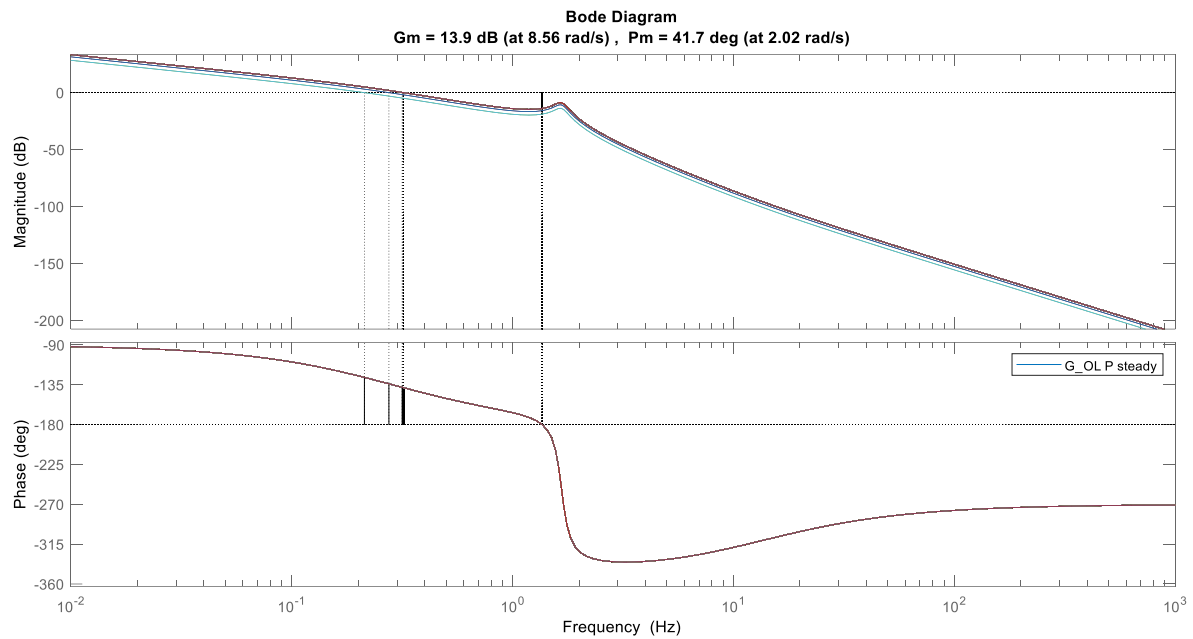


Figure 38 Bode plots for all operating points and all K_P bypass P_{steady} gains as shown in Table 8.

The bode plot in Figure 38 shows that stability is always maintained. There is sufficient gain margin and phase margin in all operating points

Figure 39 shows the pole-zero maps of the closed loop transfer functions of all 77 operating points.

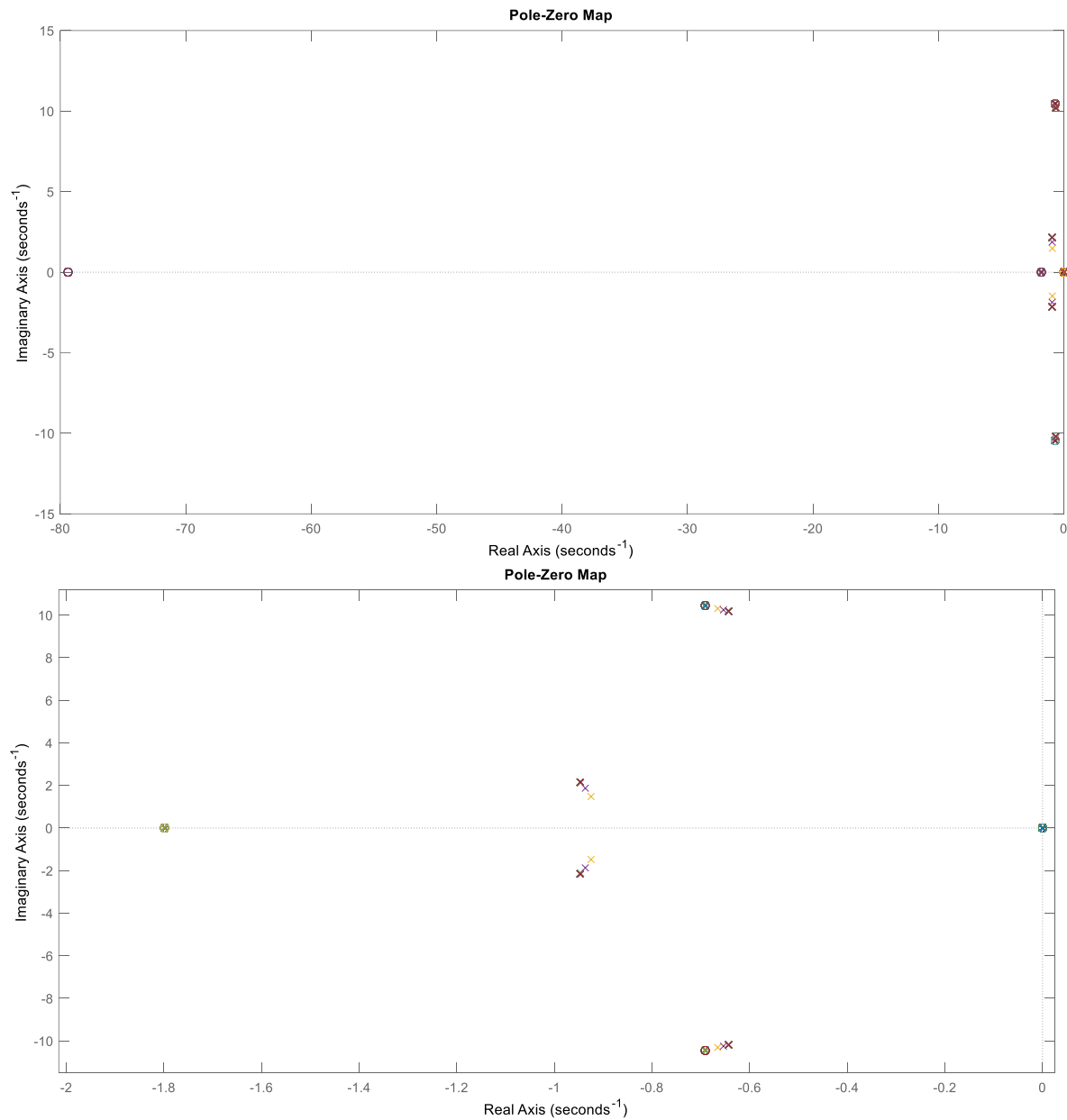


Figure 39 Pole-Zero plots of closed loop transfer functions of all operating points and all $K_{P_bypass_Psteady}$ gains as shown in Table 8. Top: full size, bottom: only fraction near imaginary axis.

Figure 39 further visualises that stability is maintained, because nothing is on the right hand side of the pole-zero map. The poles on the left hand plane reveal that the slowest decay time constant is 1.6 seconds, which is a quick enough response for the FW system.

5.9 Control Strategy for P-Steadying

The proportional controller for power steadying with the FW is embedded in a control strategy. This control strategy of P-steadying operating is shown in a simplified flow chart in Figure 40.

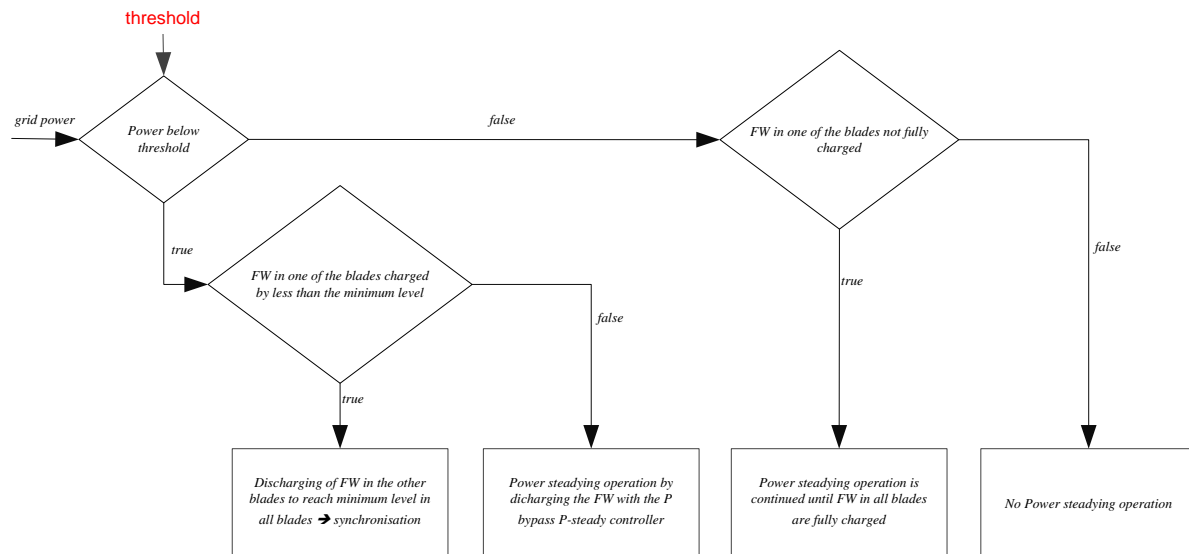


Figure 40 Simplified flow chart of power steadying control strategy.

The complete flow chart of the power steadying control strategy is shown in Figure 41.

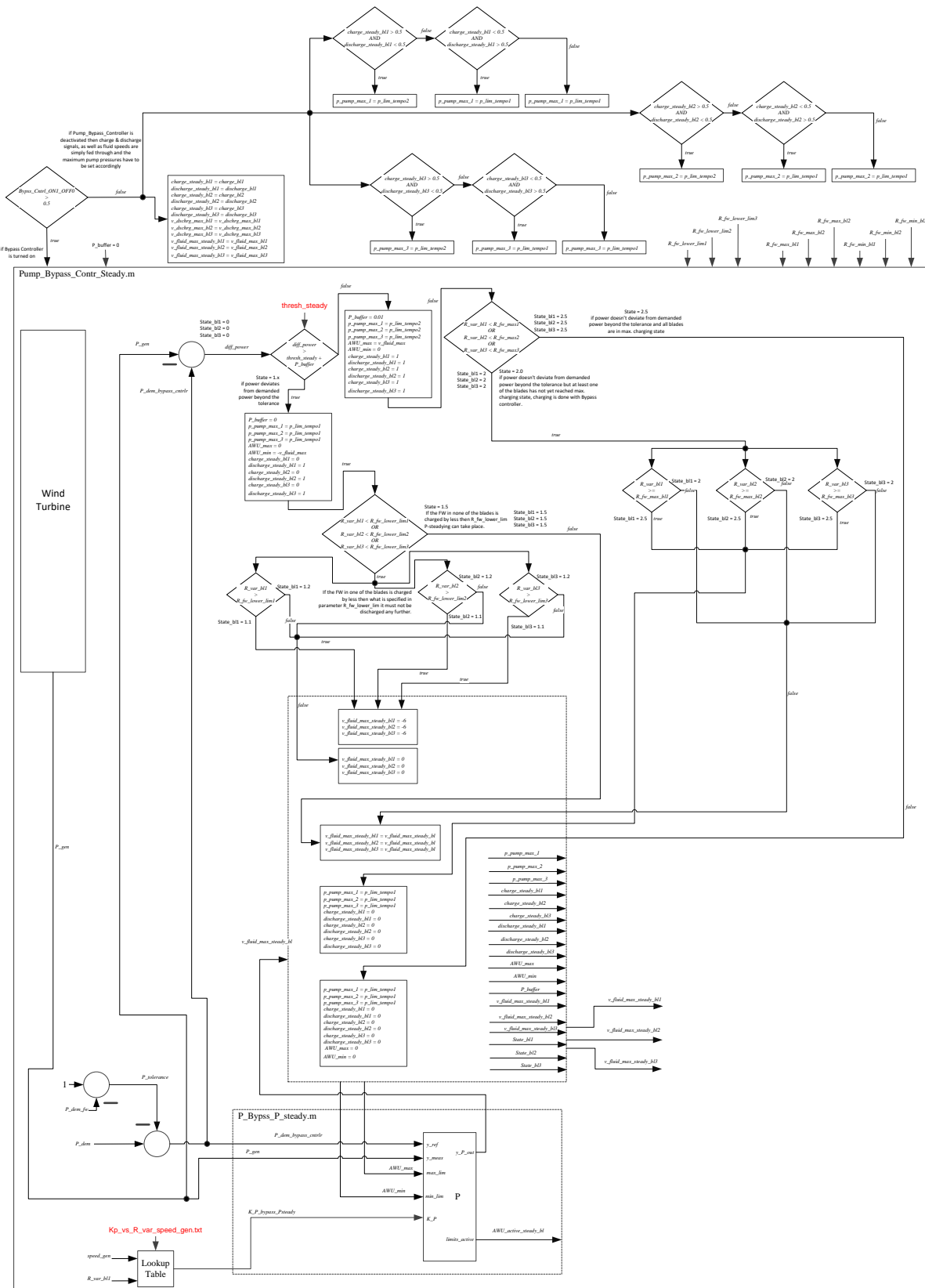


Figure 41 Flow chart of P-steadying control strategy.

5.10 Flywheel Settings for Balancing Rotor

In the control strategy shown in Figure 41 limits for the operation of the FW are introduced. I.e. the FW in a particular blade must not be charged or discharged beyond certain limits. These limits result from the fact, that there is invariably an imbalance in a WT rotor, and that a FW can be used for balancing out such an imbalance. Hence, in this section the operating limits of the FW are determined with the goal to keep the rotor of the WT balanced at all times.

5.10.1 R_var Limits

In order to keep the rotor balanced, a certain R_var ratio between the three blades needs to be maintained at all times. In order to realize this, the boundary values of R_var are determined offline.

In the 1st Eigenmodes Model of a WT an imbalance in the rotor is introduced by an additional mass in blade1: m_bladetip1 is by 100 kg larger than m_bladetip2 and m_bladetip3 [1]. To be precise, and to also cater for the fact that an imbalance could also be introduced by a variation of the blade root mass, the inertia of a whole blade is considered in the following calculation:

Inertia of blade1 with charged FW:

$$J_{\text{blade1}} = R_{\text{cntr_gravi_bladeroot}}^2 \cdot m_{\text{bladeroot}} + R_{\text{cntr_gravi_bladetip}}^2 \cdot m_{\text{bladetip1}} + R_{\text{fw_max_bl1}}^2 \cdot m_{\text{fw_fluid}} \quad \text{Equation 58}$$

The inertias of blade2 and blade3, J_blade2 and J_blade3, respectively, are derived likewise. The goal is to get equal inertias in all three blades: J_blade1 = J_blade2 = J_blade3

These equal inertias allow resolving the above equation for R_fw_max_bl1 (NB: R_fw_max_bl1 has to be smaller R_fw_max, because the blade tip mass of blade1 is larger than the blade tip masses of the other blades!):

$$R_{\text{fw_max_bl1}} = \sqrt{\frac{J_{\text{blade3}} - R_{\text{cntr_gravi_bladeroot}}^2 \cdot m_{\text{bladeroot}} - R_{\text{cntr_gravi_bladetip}}^2 \cdot m_{\text{bladetip1}}}{m_{\text{fw_fluid}}}} \quad \text{Equation 59}$$

If the FW in blade1 is charged to the limit R_fw_max_bl1, then the FW in blade2 and blade3 have to be charged to the maximum physical limit (R_fw_max [1]): R_fw_max_bl2 = R_fw_max_bl3 = R_fw_max

The same reasoning can be applied for the case when the FW is discharged. Here, however, R_fw_min_bl1 is equal to the minimum physical limit (R_fw_min [1]); while R_fw_min_bl2 and R_fw_min_bl3 will be larger than R_fw_min in order to outbalance the smaller inertias of these blades.

Inertia of blade1 with discharged FW:

$$J_{\text{blade1}} = R_{\text{cntr_gravi_bladeroot}}^2 \cdot m_{\text{bladeroot}} + R_{\text{cntr_gravi_bladetip}}^2 \cdot m_{\text{bladetip1}} + R_{\text{fw_min_bl1}}^2 \cdot m_{\text{fw_fluid}} \quad \text{Equation 60}$$

Consequently, the lower limits of the blades with the lower inertia, i.e. blade2 and blade3, can be derived with

$$R_{fw_max_bl2} = R_{fw_max_bl3} =$$

Equation 61

$$\sqrt{\frac{J_{blade1} - R_{cntr_gravi_bladeroot}^2 \cdot m_{bladeroot} - R_{cntr_gravi_bladetip}^2 \cdot m_{bladetip2}}{m_{fw_fluid}}}$$

With these limits of the FW the rotor of the WT is always balanced; in charged state of the FW as well as in discharged state of the FW.

5.10.2 R_{fw} Limits for P-Steadying Operation

For P-steadying operation also an intermediate discharge level ($R_{fw_lower_lim}$) has been defined in order to make sure that the FW only does P-steadying with a high charging level, i.e. with large effect, see also section 5.10.3 Optimal $perunit_lower_lim$ for Maximum Energy Yield.

A parameter is defined that allows the user to specify a fraction of R_{fw_max} to which the FW may be discharged in P-steadying operation: $perunit_lower_lim$

Equation 62 shows the inertia of blade1 when the FW is discharged to $perunit_lower_lim$.

$$J_{blade1} = R_{cntr_gravi_bladeroot}^2 \cdot m_{bladeroot} + R_{cntr_gravi_bladetip}^2 \cdot m_{bladetip1} + (perunit_lower_lim \cdot R_{fw_max_bl1})^2 \cdot m_{fw_fluid} \quad \text{Equation 62}$$

Hence, the lowest discharge level of the FW in blade1 is

$$R_{fw_lower_lim1} = perunit_lower_lim \cdot R_{fw_max_bl1} \quad \text{Equation 63}$$

This allows deriving the operation limits of the FW in the other two blades:

$$R_{fw_lower_lim2} = R_{fw_lower_lim3} =$$

Equation 64

$$\sqrt{\frac{J_{blade1} - R_{cntr_gravi_bladeroot}^2 \cdot m_{bladeroot} - R_{cntr_gravi_bladetip}^2 \cdot m_{bladetip2}}{m_{fw_fluid}}}$$

The computation of the operation limits $R_{fw_lower_lim2}$ and $R_{fw_lower_lim3}$ is done offline. I.e. these are parameters that are derived based on the known imbalance in the rotor. If the user specifies an inappropriate value for $perunit_lower_lim$, a while-loop runs through the equations above and increments $perunit_lower_lim$ until it has reached a value that avoids that $R_{fw_lower_lim1} < R_{fw_min_bl1}$.

5.10.3 Optimal $perunit_lower_lim$ for Maximum Energy Yield

The FW is most effective when it is almost fully charged. Figure 42 shows the performance of the FW Type VI in the rotor of the NREL 5 MW WT plotted versus the charging level, R_{var} . In Figure 42 J_{fw_bl} is the inertia of the FW in one blade, E_{kin_fw} is the kinetic energy of the whole FW (all blades) when the rotor rotates with rated speed (12.2 RPM) and P_{fw} is the power from the FW when it is discharged within 20 seconds.

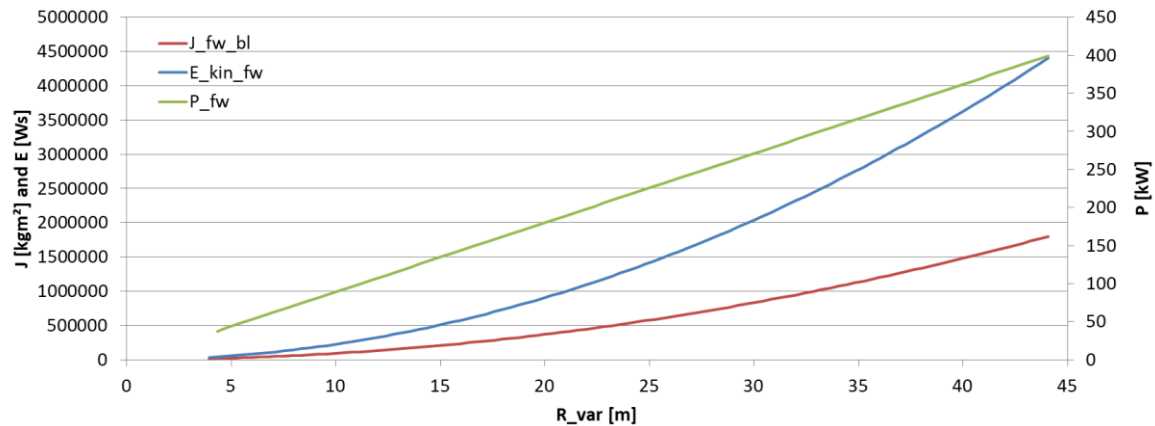


Figure 42 Inertia of FW in one blade, kinetic energy in the whole FW and power from the whole FW.

The green curve in Figure 42 shows that P_{fw} of the FW rises linearly with the state of charge. Hence, in P-steadying operation it is desirable to let the FW operate in the almost fully charged region only. However, if there is a longer dip in power, it would be advantageous to discharge the FW completely in order to get as much energy from it as possible. In other words there is tradeoff between high power and long haul.

A 250 s simulation with turbulent wind speed around rated wind speed and steps in the power setpoint is repeatedly conducted with different `perunit_lower_lim` values. Figure 43 shows the scenario for the case `perunit_lower_lim = 0.5`.

The result of all conducted simulations (`perunit_lower_lim` is incremented from 0.1 to 0.95) is shown in Figure 44.

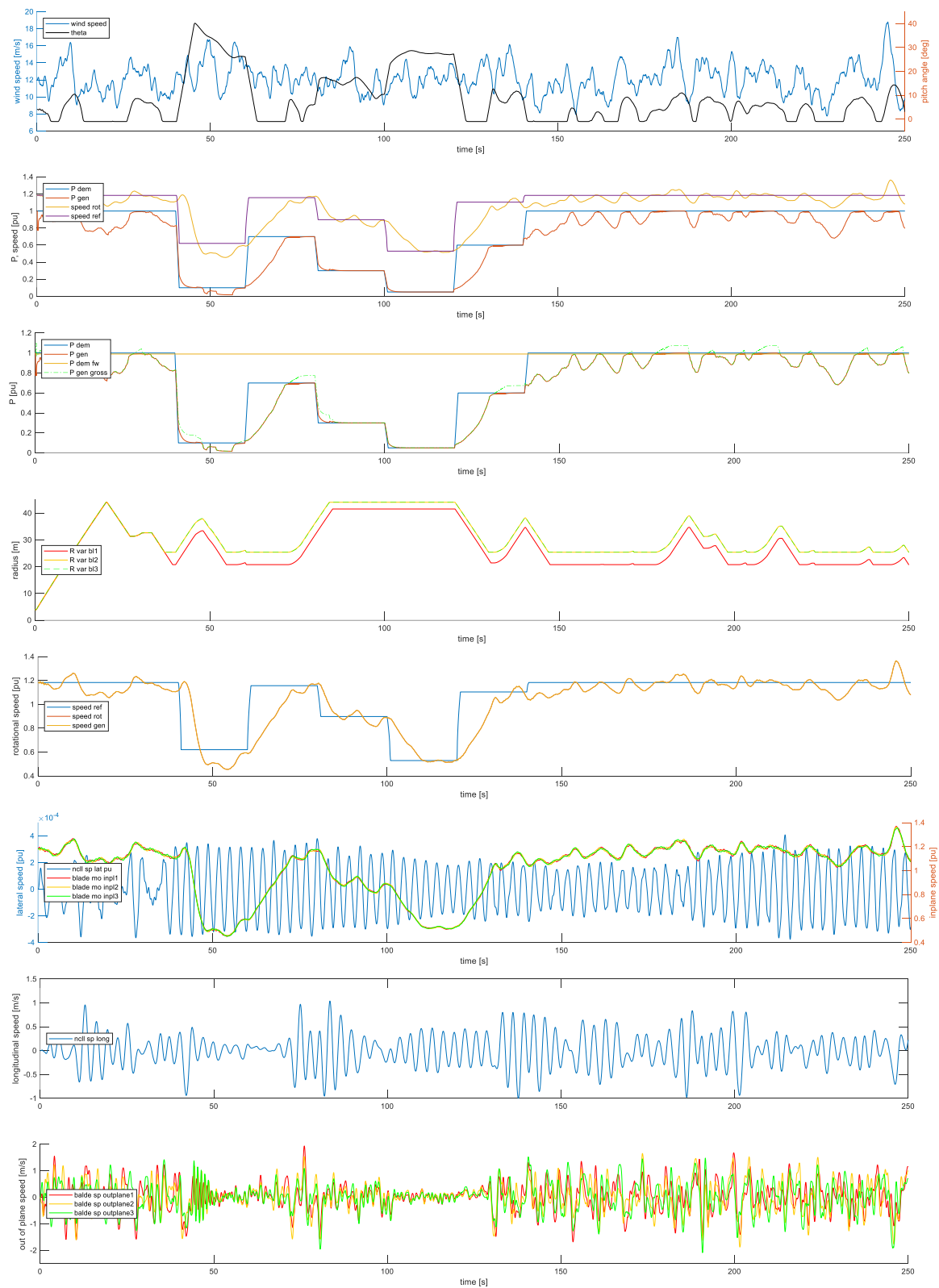


Figure 43 250s scenario for finding the optimal perunit_lower_lim value. The simulation shown here is conducted with perunit_lower_lim = 0.5.

Figure 44 reveals that $\text{perunit_lower_lim} = 0.5$ is the best tradeoff between high power and potentially long power delivery. However, it has to be kept in mind that this conclusion only applies to the scenario shown in Figure 43. A scenario with other turbulences and/or other power setpoint steps could lead to a different optimum in perunit_lower_lim .

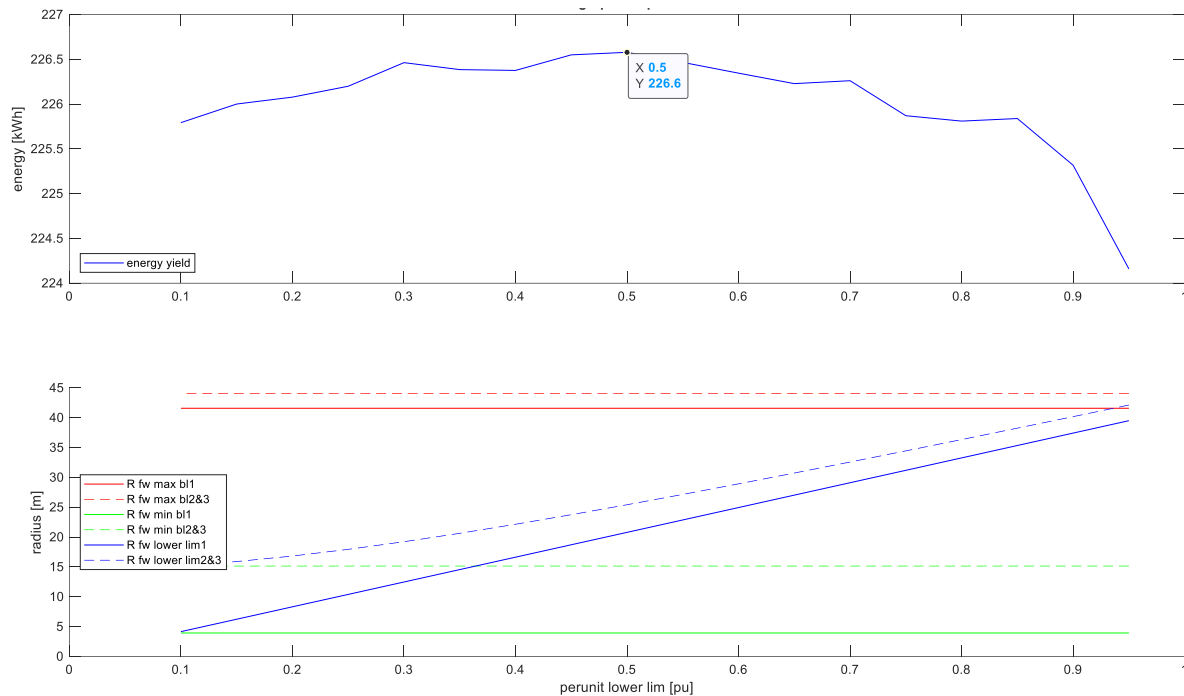


Figure 44 Energy yield versus perunit_lower_lim (top). R_{var} limits of blade 1, 2 and 3 versus perunit_lower_lim (bottom).

For further simulations shown in this report the parameter perunit_lower_lim is set to 0.5.

5.11 Adaptation of Simulation Time Step

The 1st Eigenmodes Model of a WT, in combination with the hydraulic FW and the Pump Bypass Controller runs into numerical oscillations whenever transients would require a smaller simulation time step. Therefore, a glue code is created that combines the WT model and the bypass controller model in one script based Matlab program. This program is embedded in Simulink where it is called as Interpreted MATLAB Function.

The variable limits_active in the P-controller, (see Figure 37) indicates whether or not the Pump Bypass Controller has hit its controller output limits. It is known from the flow diagram of the control strategy (Figure 41) that hitting the controller output limits means $\text{abs}(\text{AWU_active_steady_bl}) > 0$.

However, for the simulation model this is only a problem if the following conditions are given, i.e. if the Pump Bypass Controller is active:

- $\text{Bypss_Cntrl_ON1_OFF0} > 0.5$ AND
- $\text{State_bl1} > 1.2$ AND
- $\text{State_bl1} < 2.5$ AND
- $\text{State_bl2} > 1.2$ AND
- $\text{State_bl2} < 2.5$ AND

- State_b13 > 1.2 AND
- State_b13 < 2.5

If all these conditions are given, the models of the WT and of the Pump Bypass Controller are executed 10 times within one simulation time step inside the Simulink model. In order for the results to be still correct, the simulation time step that is used inside the model for the numerical integration has to be divided by 10 in this situation. The methodology is visualised in Figure 45.

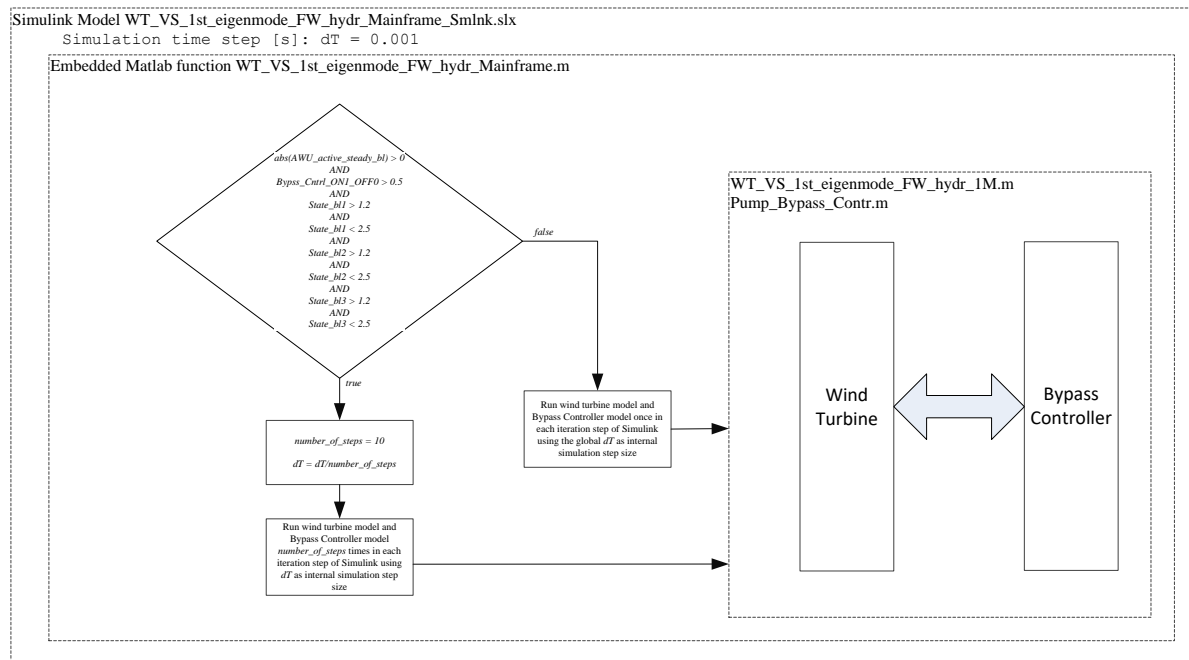


Figure 45 Adaptation of the simulation step size to avoid numerical oscillations.

Simulations show, that this solution avoids numerical oscillations and numerical instability. This solution comes at the cost of simulation time. However, automatic step size adjustment by Simulink leads to much longer simulation times.

6 Piston Accumulators Made of Composite Materials

6.1 Initial Carbon Fibre-Reinforced Plastics Design

HYDAC specified and purchased a carbon fibre-reinforced plastic (CFRP) tube from which the first prototype of a CFRP piston accumulator was built. The intention was to build a CFRP piston accumulator that does not need a metal liner. With this prototype, tests were performed at HYDAC to find out whether the material is gas-proof. Bending tests were not feasible with this prototype, as it is too rigid.

6.1.1 Specification of Initial Carbon Fibre-Reinforced Plastics Accumulator

HYDAC, in cooperation with Pronexos B.V. (pronexos.com), performed a test to specify the initial CFRP accumulator. The test was based on various criteria:

- The structural strength of the laminate is designed to withstand the working pressure of 40 bar.
- A maximum diameter increase of 0.1 mm at 40 bar working pressure.
- The laminate should rupture in longitudinal direction at burst pressure > 120 bar.
- CFRP design allowed to be maximum a factor 1.5 more expensive compared to the baseline steel design.
- Preferably, no liner should be inside the CFRP tube, in order to reduce weight and manufacturing costs.
- CFRP laminate has to be leaktight against nitrogen in case no liner is used.

The materials used for the construction of the prototype are already qualified for series manufacturing at PRONEXOS. For this test fibre volume fraction of Toho tenax STS40 E23 1600tex-Epoxy laminate~63% is used in two winding directions (hoop/helical ratio of ~ 2.15; hoop fibre wall thickness 6.3 mm – helical fibre layer thickness 2.95 mm).

This warping method, together with the used material, lead to a laminate structure of 11 layers with a total thickness of 14.64 mm.

In order to the design criteria mentioned above the prototype has the following baseline standard:

- Inner diameter of 200 mm
- Outer diameter ~ 229.5 mm
- Total tube length of 1273 mm
- Weight ~ 20kg

For the working pressure of 40 bar a load case of two global stresses can be translated as below:

$$\sigma_y = 27,32 \text{ MPa circumference}$$

$$\sigma_x = 13.66 \text{ MPa longitudinal}$$

The resulting strain is calculated using the classic laminate theory via COMPOSITOR version 4.1, as a structural computer-aided engineering tool for laminates made from fibre compound plastics.

$$\epsilon_y = 2.4487\text{E-}03 \text{ [-] circumference}$$

$$\epsilon_x = 4.5898\text{E-}04 \text{ [-] longitudinal}$$

The circumference strain leads to an inner diameter increment of 0.09 mm, which is still below the maximum increase of 0.1 mm.

6.1.2 Durability Test of the Rigid Carbon Fibre-Reinforced Plastics Accumulator

Figure 46 shows the rigid CFRP accumulator before it was tested. The purpose of this prototype test is to confirm the behaviour of CFRP as shell material when it is not protected by a metal liner on the inside.

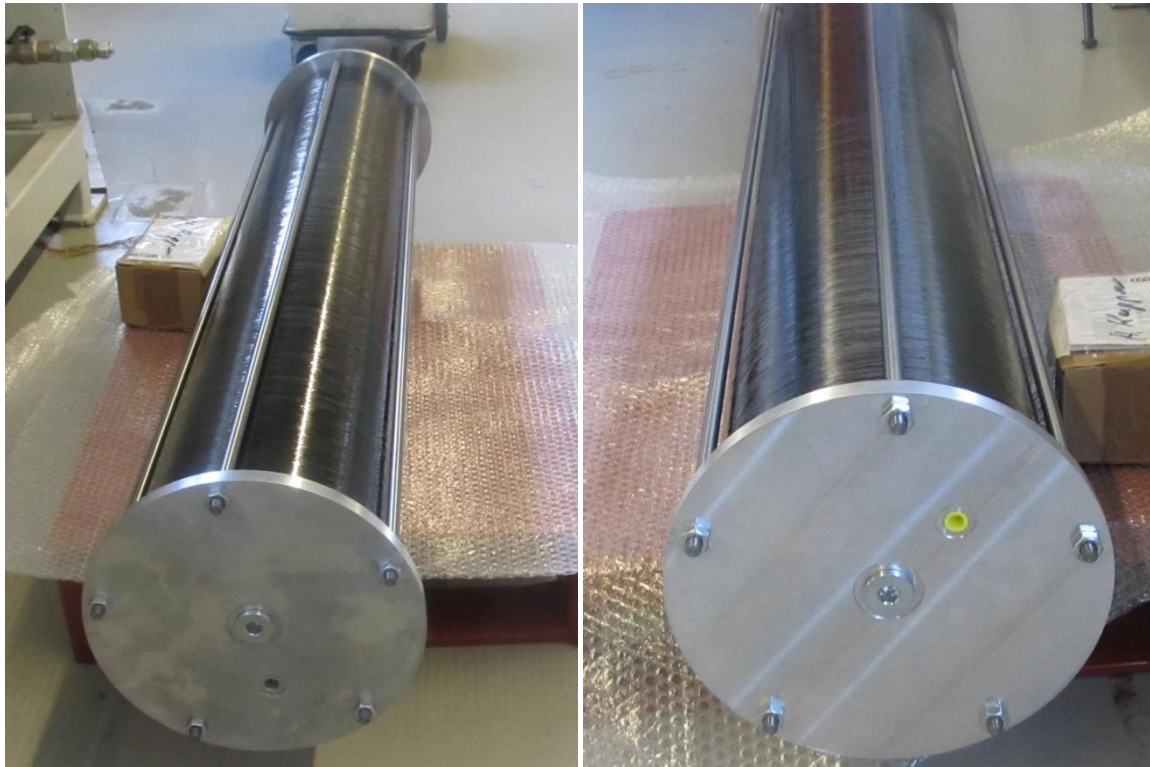


Figure 46: Prototype of rigid CFRP accumulator without liner.

This means that the piston runs directly on the CFRP surface. Also, if there are inter-fibre failures, which regularly occur from fatigue in the composite structure, the shell is bound to become leaky. Although hydraulic fluid might not leak through such small gaps, gas can leak through tiny cracks. Due to the purpose of this test the piston and the covers are not optimised for weight. Hence, they are made of aluminium, and as visible in Figure 46, the covers are kept in place by axial tie rods made of steel.

In the first durability test this piston accumulator was filled with nitrogen only. It was statically put under pressure with 40 bar, subsequently with 60 bar, for several weeks. This test was successful, as only slight pressure losses occurred at the piston seal.

In the following test the accumulator was put under pressure and the piston was cyclically moved along the length of the accumulator with pressure variations between 10 bar and 40 bar. The goal was to achieve 100,000 load changes. During this test the tie rods exhibited fatigue. Eventually the whole accumulator failed. Two damages can be observed: The tie rods broke and the laminate suffered fibre failure in peripheral direction, approximately at half the length of the accumulator, see Figure 47.

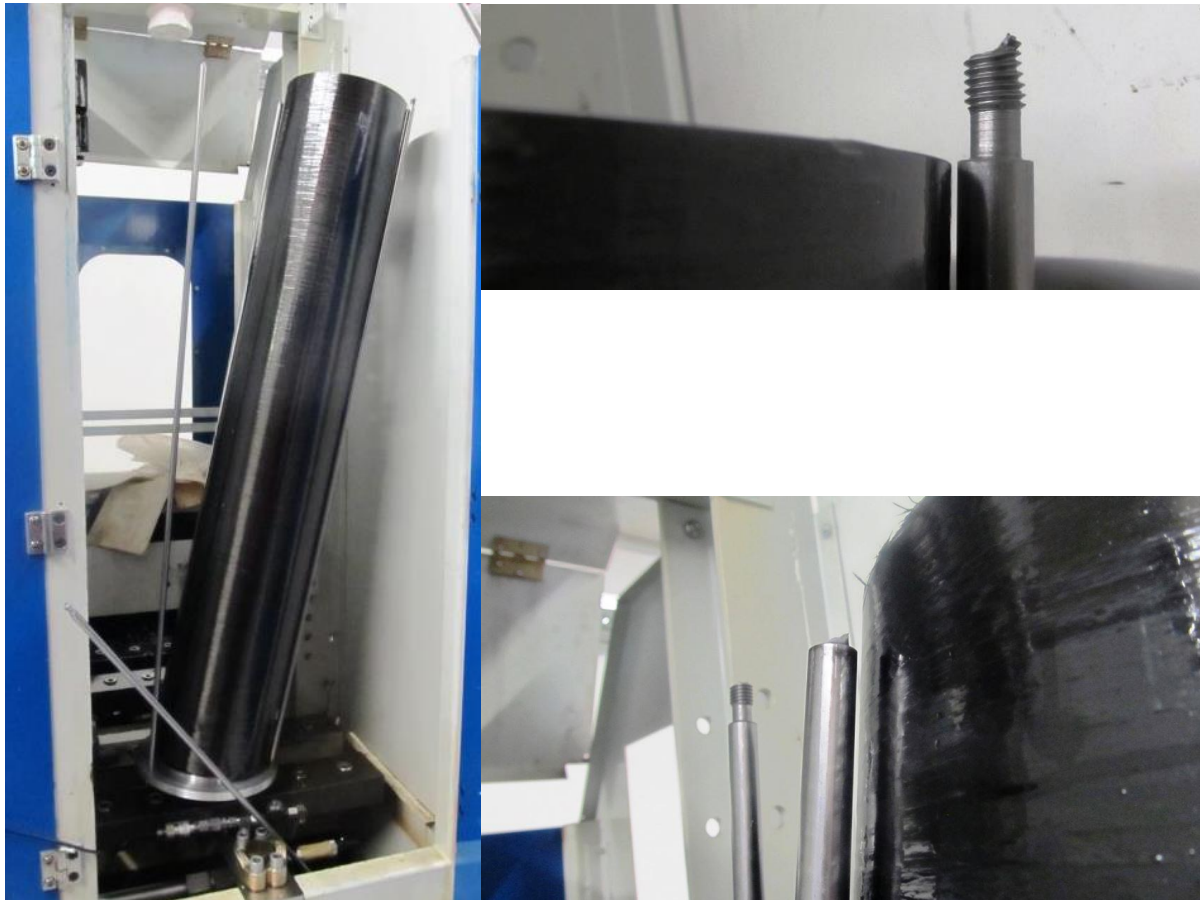


Figure 47: Prototype of rigid CFRP accumulator failed in durability test.

It is not possible to finally clarify what the cause of the failure was. The failure of the tie rods is not likely to be the initial cause. This would have led to a pressure release at the covers. It is unlikely though, that under this circumstance the laminate would not have suffered fibre failure. It is assumed that the test rig accidentally set a too high pressure, which overloaded the whole accumulator. However, this suspicion cannot be confirmed with the measurements, as pressure values were recorded with too low frequency.

6.1.3 Flywheel Configurations with Initial Carbon Fibre-Reinforced Plastics Accumulators

The specification given in section 6.1.1 is applied to all FW configurations as introduced by Hippel et al. [11].

In order to keep the maximum diameter increase by 0.1 mm for all FW types laminate analyses via COMPOSITOR are done for each FW type. I.e. the wall thickness of each CFRP tubes is adjusted as required to not exceed the maximum permissible diameter increase. The resulting masses of the piston accumulators are shown in Figure 48-Figure 52

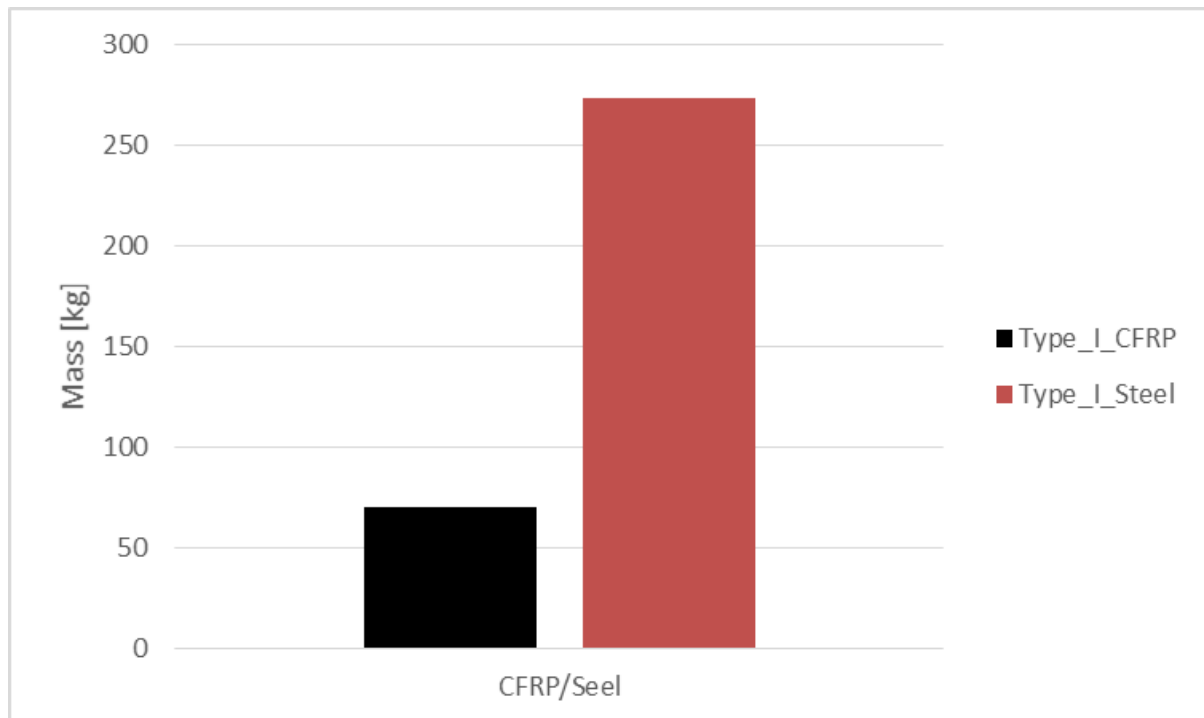


Figure 48 Masse of piston accumulator type I

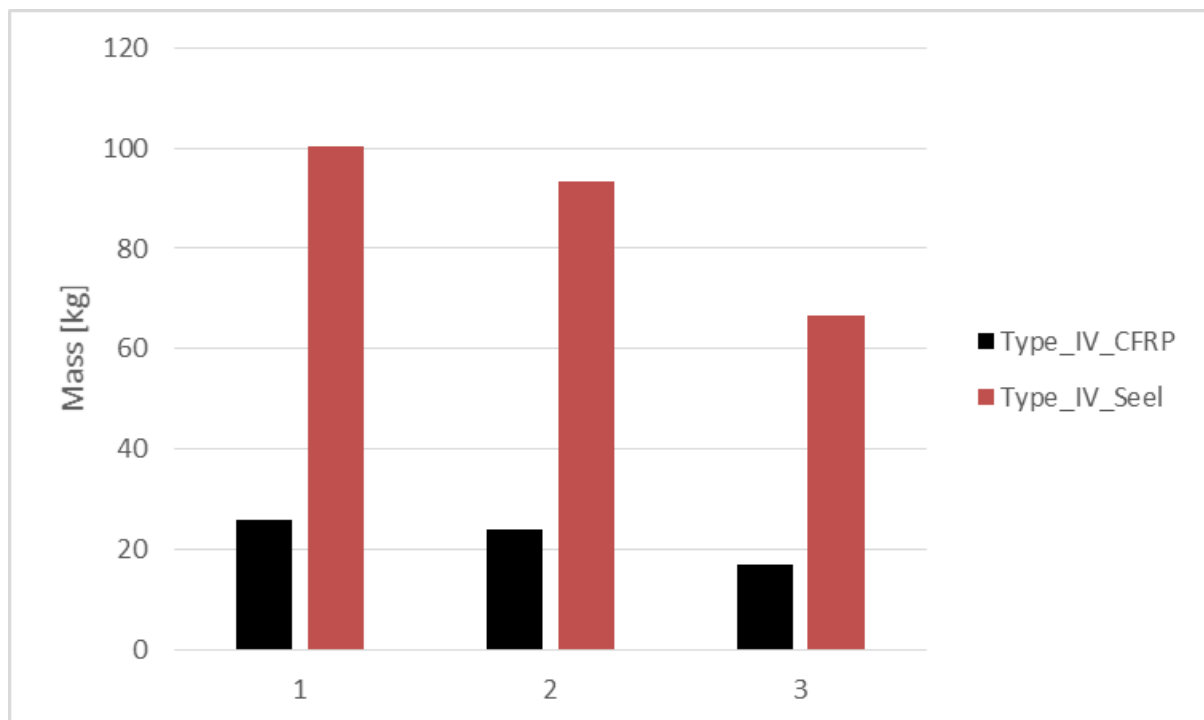


Figure 49 Masse of piston accumulator type IV

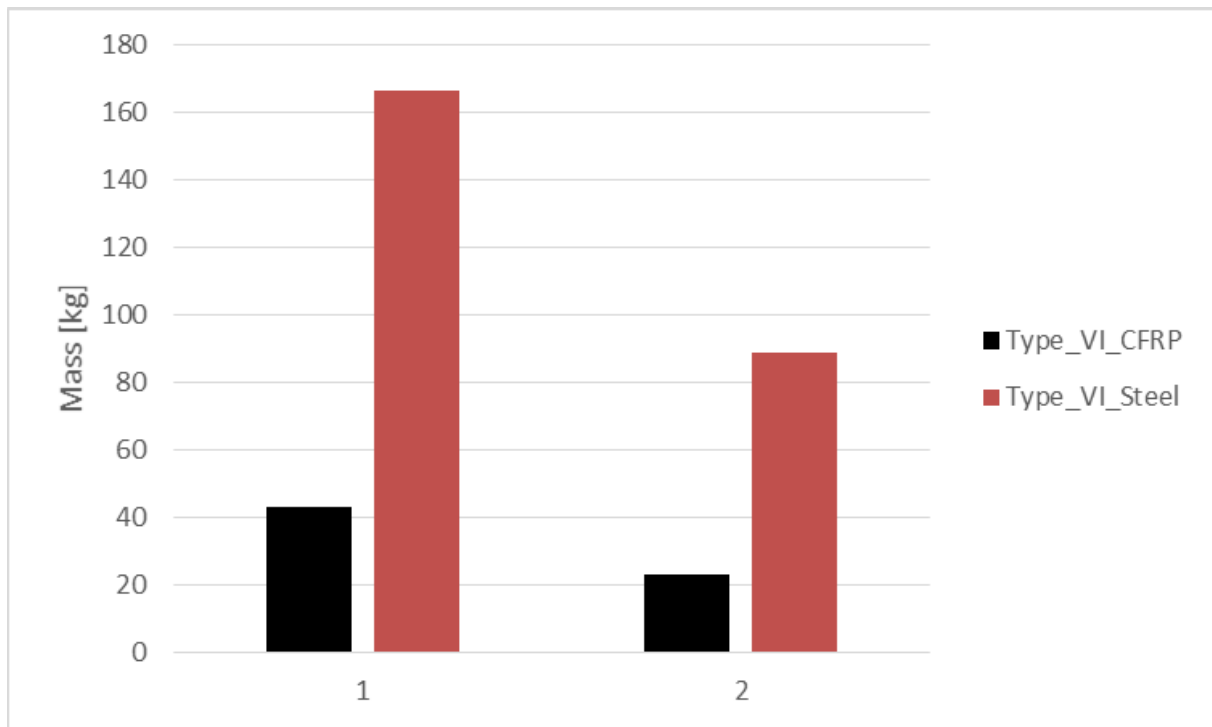


Figure 50 Masse of piston accumulator type VI

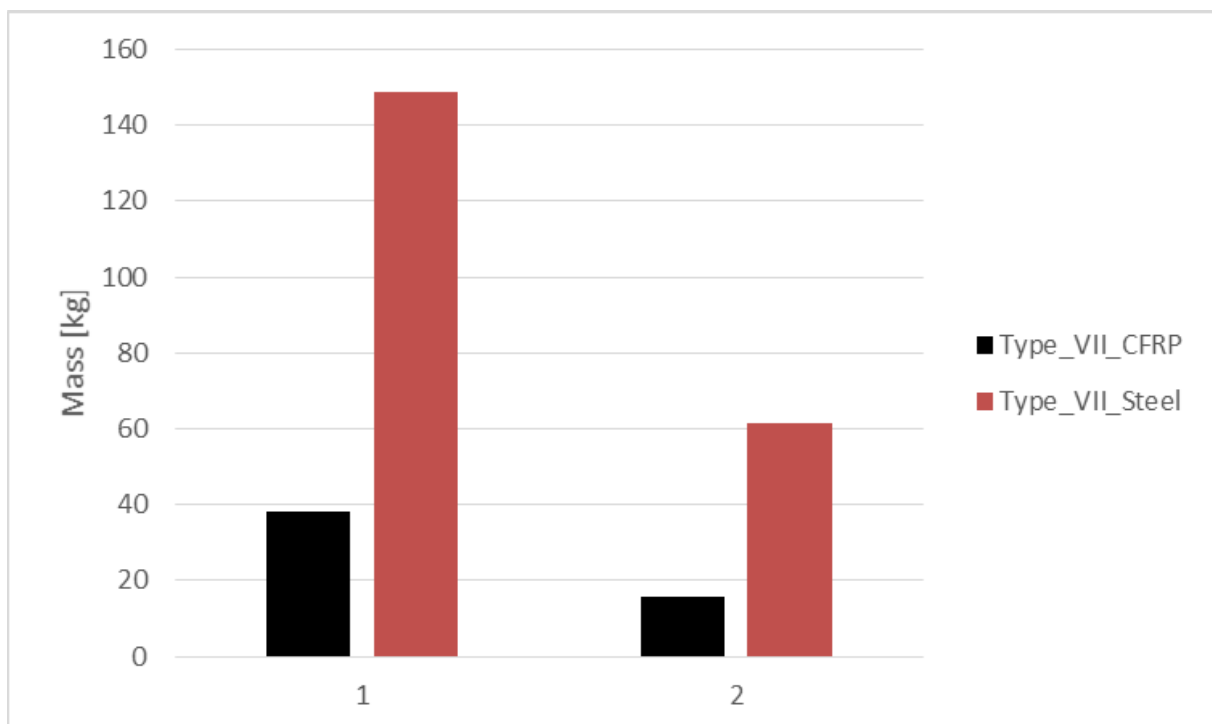


Figure 51 Masse of piston accumulator type VII

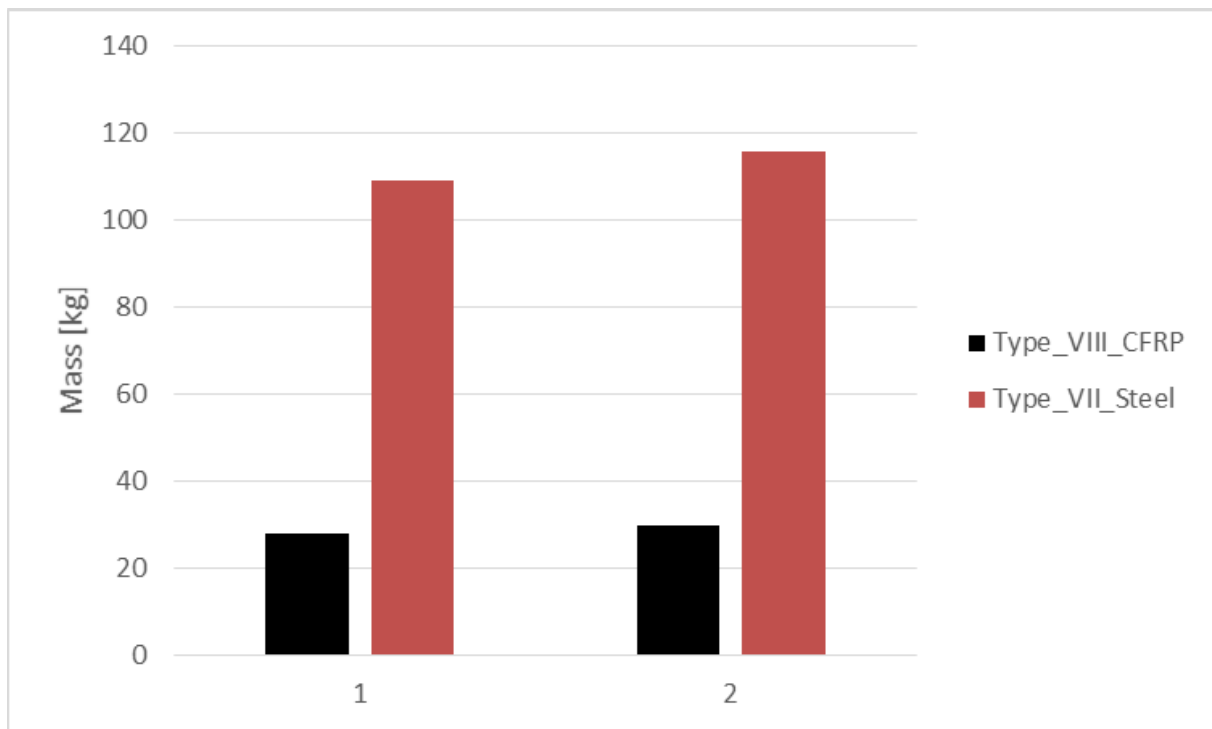


Figure 52 Masse of piston accumulator type VIII

The Figure 48-Figure 52 show a mass comparison of different types of FW tip accumulators from CFRP and steel in black and in red column diagram, respectively. Where the x axis represents the number of tip accumulators of each FW type. For details on the number of tip accumulator, see Hippel et al. 2019 [11].

Since the inner diameter of the accumulator is allowed maximally 0.1 mm to extend, a heavy-wall tube is mandatory to get such rigid CFRP accumulator and thus increase the stationary mass of the CFRP accumulator compared with the steel accumulator, as clearly to be seen in Figure 48-Figure 52.

It is obvious that such heavy CFRP component lead to larger mechanical loads in the WT. Hence, a lighter design is proposed.

By the design of lighter CFRP accumulator the wall thickness of the steel accumulator [21] is used as reference value. The structural analysis for the lighter accumulator is done here also via COMPOSITOR. However, because of time constraints the structural analysis is simplified in that fibre failure is considered only.

Figure 53-Figure 57 show in addition to mass comparison of lighter CFRP accumulator and steel accumulator, the inner diameter increase ΔD of each FW type. Since the lighter CFRP accumulator has thinner wall thickness ($t=3.85$ mm), it is obviously that such thin CFRP component has higher diameter increment ΔD compared to the steel component. However, because the light weight of the CFRP accumulator is of utmost importance for load simulation, this initial design of lighter CFRP component is used for the next load comparison.

If such CFRP FW components were used in the rotor of the NREL 5 MW reference WT, the mechanical load would vary as shown in Figure 58 and Figure 59. Here the load assessments are done as previously published by Hippel and Jauch 2019 [15].

The load simulation representing here is performed with FAST. This load simulation tool is incapable of dynamic implementation of the FW system. Hence, the load comparison was done only for two conditions, FW charged and FW discharged, in red and blue respectively (see Figure 58 and Figure 59).

Figure 58 shows a percentage comparison in bending moments at different location of the WT for a steel accumulator and CFRP accumulator. It is obvious that the use of lighter CFRP FW components leads to a noticeable reduction of bending moment overall the WT components, as a result of decrease the stationary mass of blade section properties, where previous a heavy steel FW component are used.

In relation to the ultimate loads Figure 59 represent a comparison in fatigue damage equivalent bending moment at different location of the WT for a steel accumulator (light tone) and CFRP accumulator (dark tone). Also here it is clear to see that the fatigue loads reduce significantly by using the lighter CFRP components in comparison with the steel components, due to the different of the material mass (see Figure 53-Figure 57).

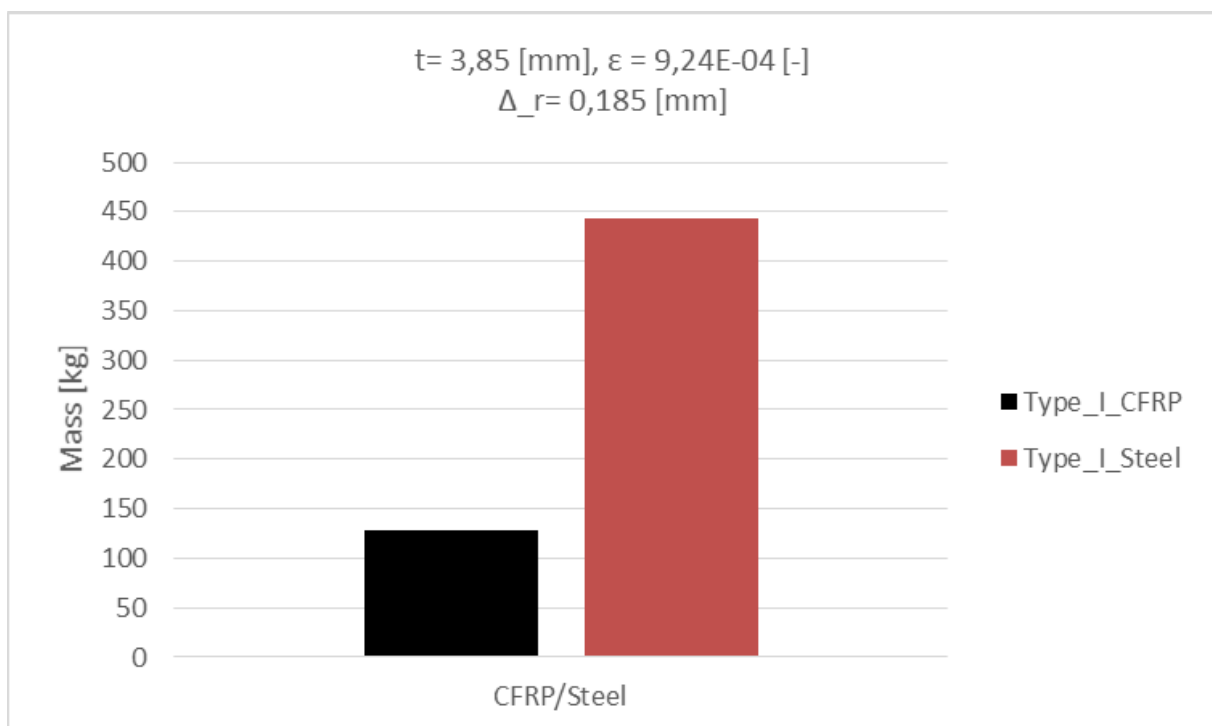


Figure 53 Masse of lighter piston accumulator type I

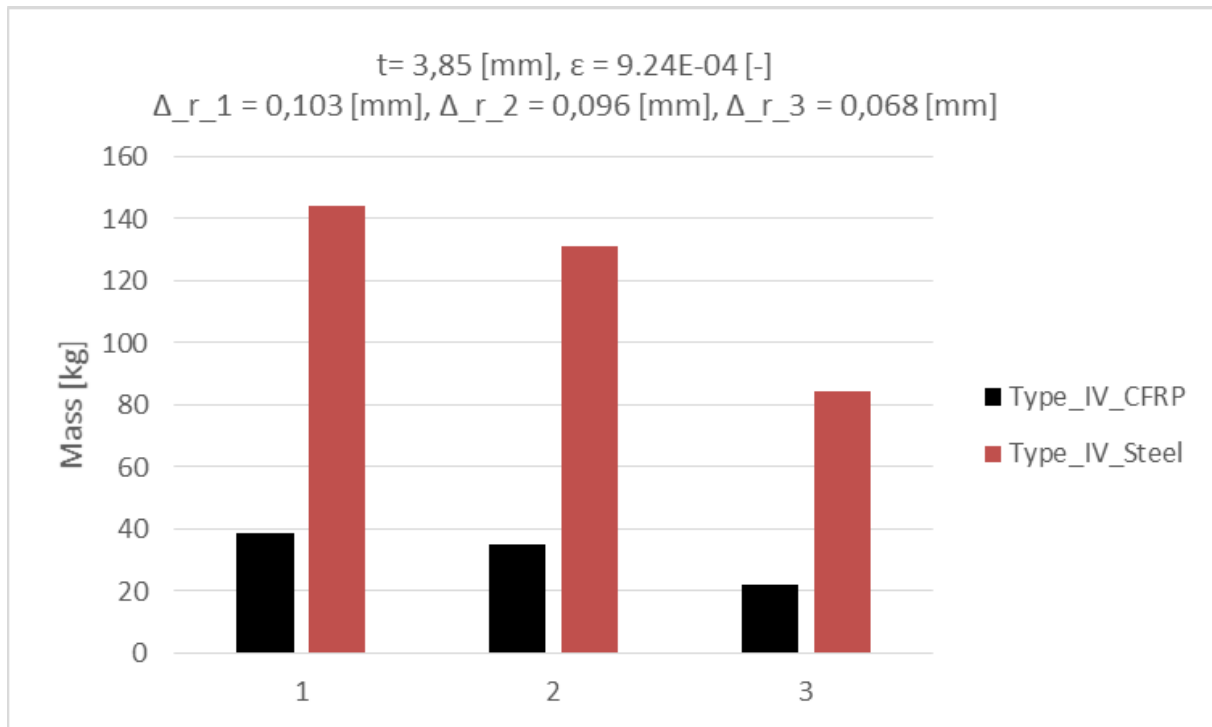


Figure 54 Masse of lighter piston accumulator type IV

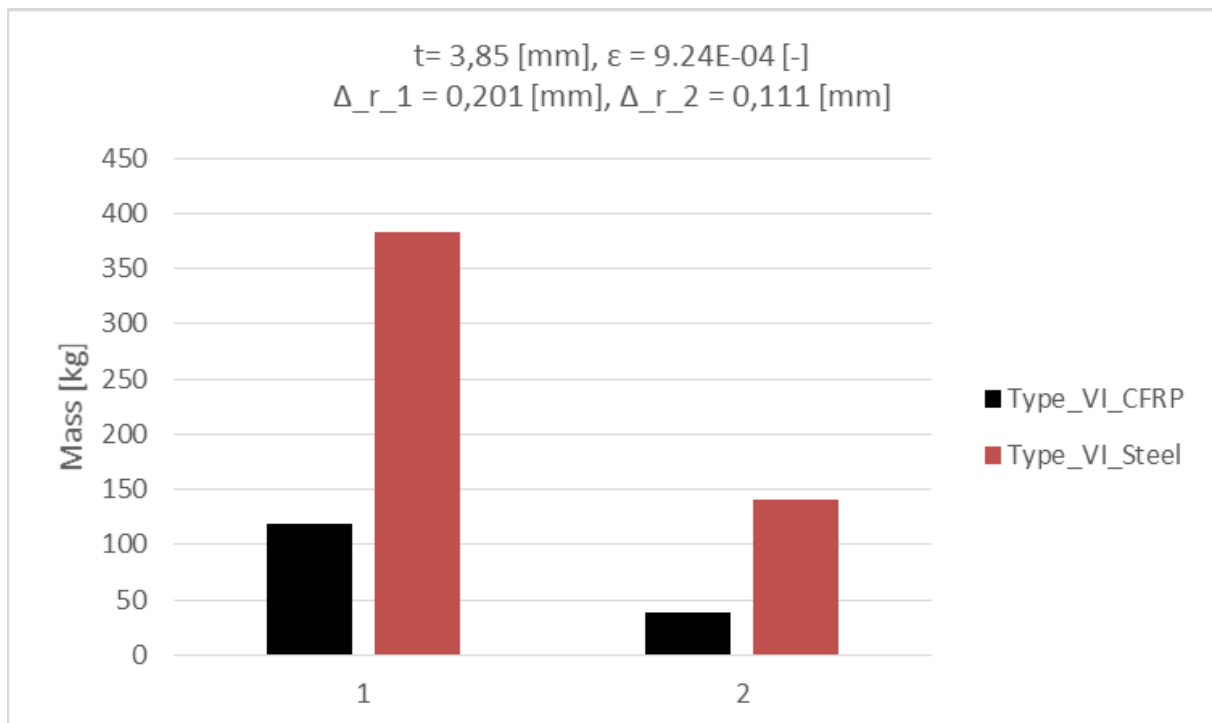


Figure 55 Masse of lighter piston accumulator type VI

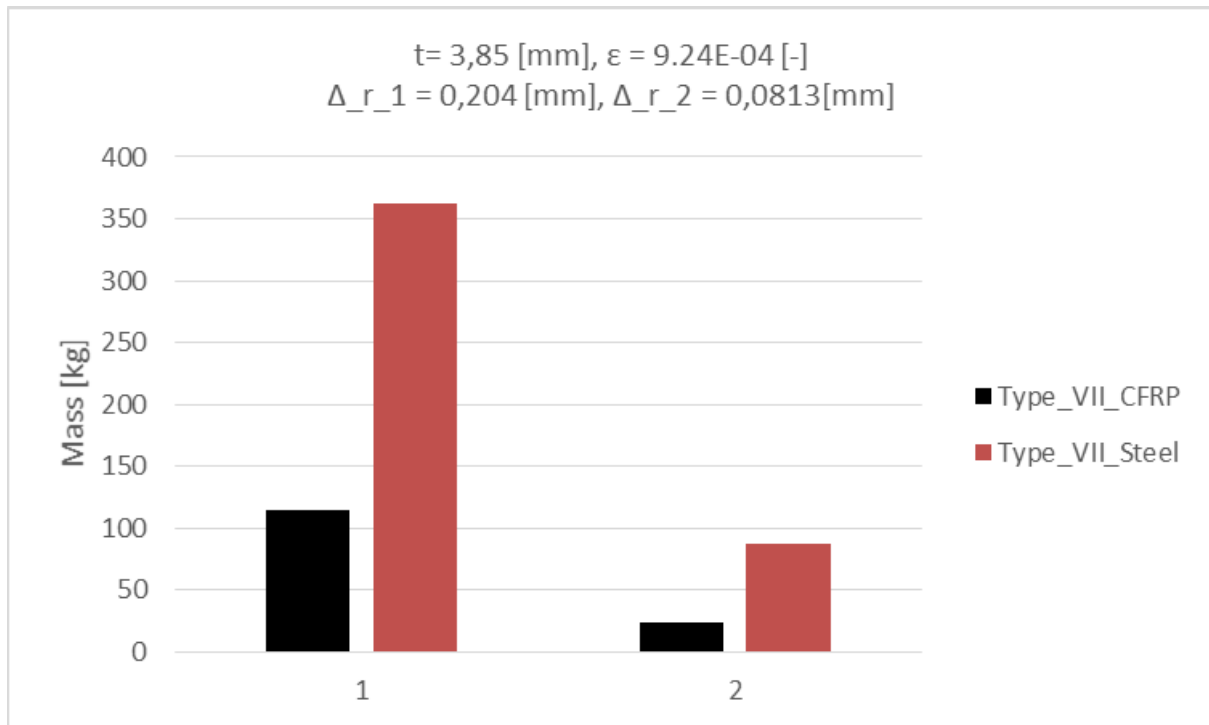


Figure 56 Masse of lighter piston accumulator type VII

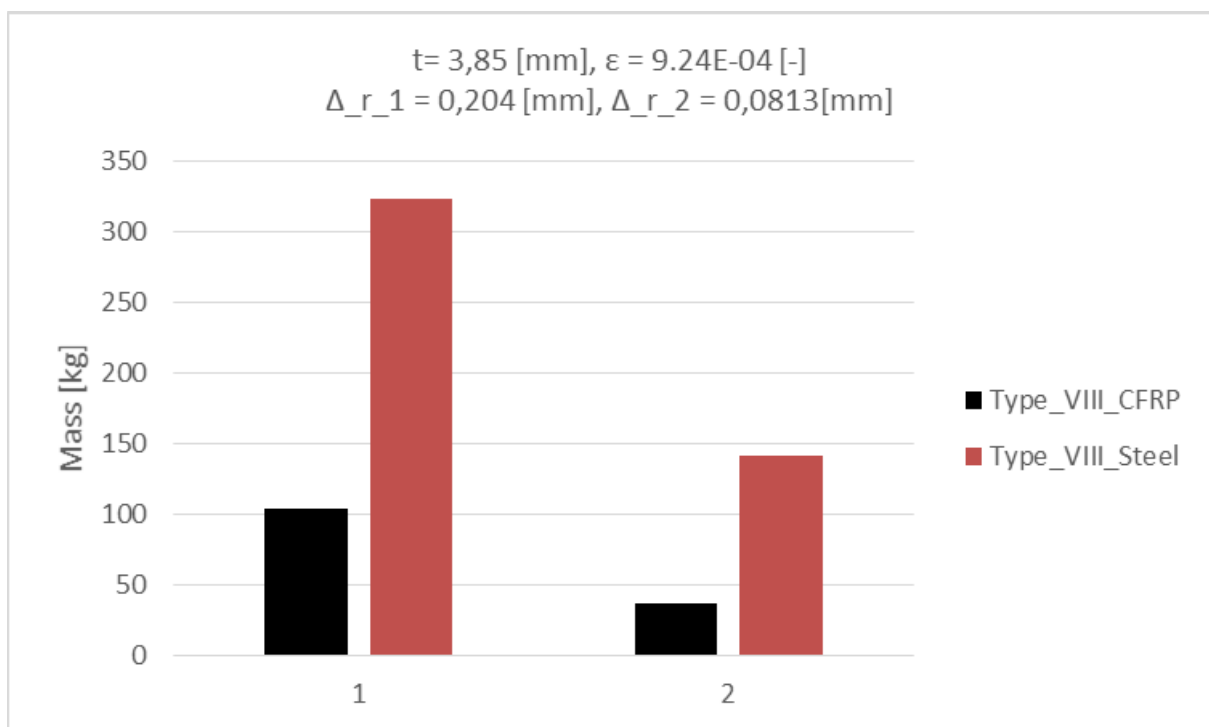


Figure 57 Masse of lighter piston accumulator type VIII

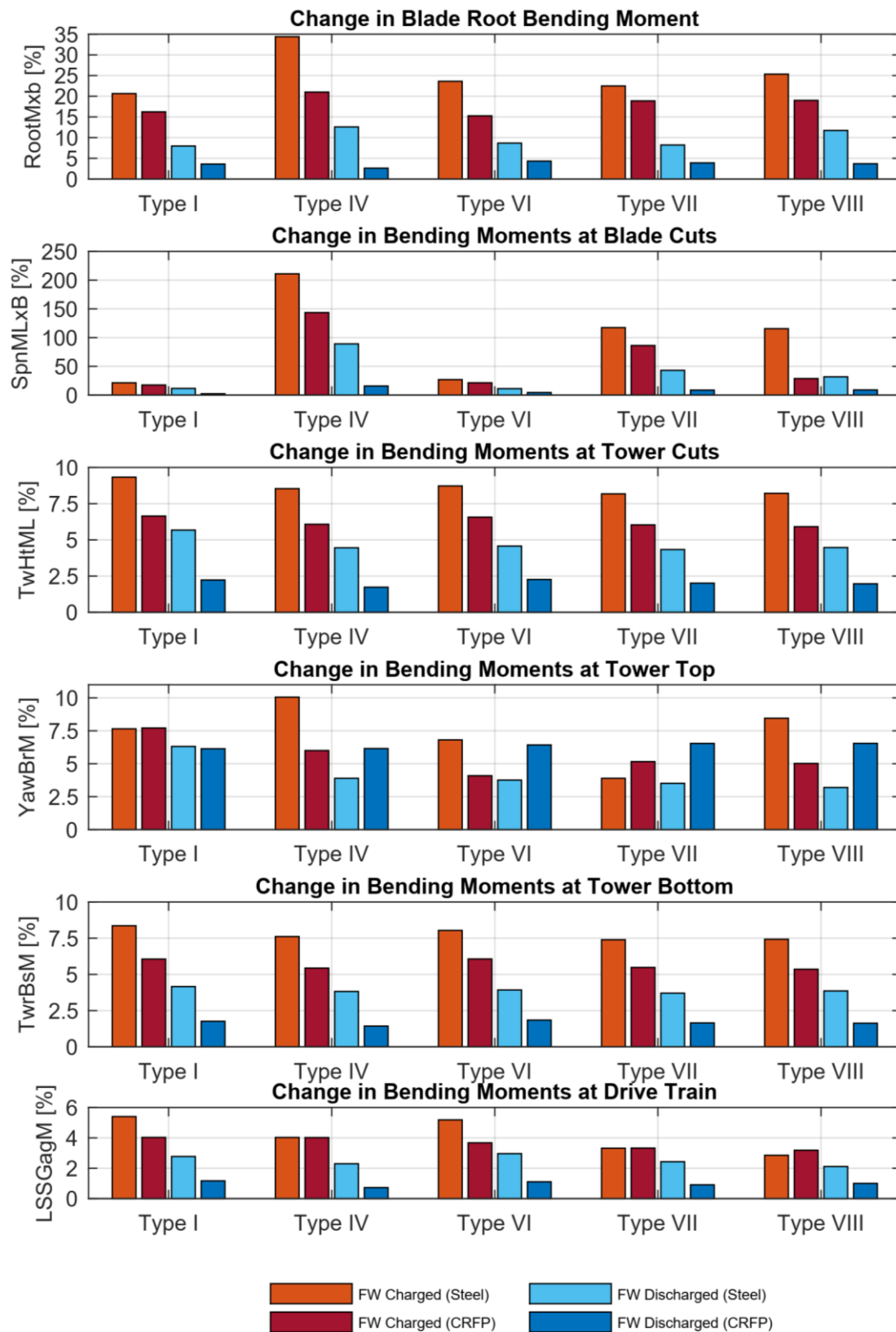


Figure 58 Comparison of changing in ultimate loads between steel accumulator and lighter CFRP accumulator

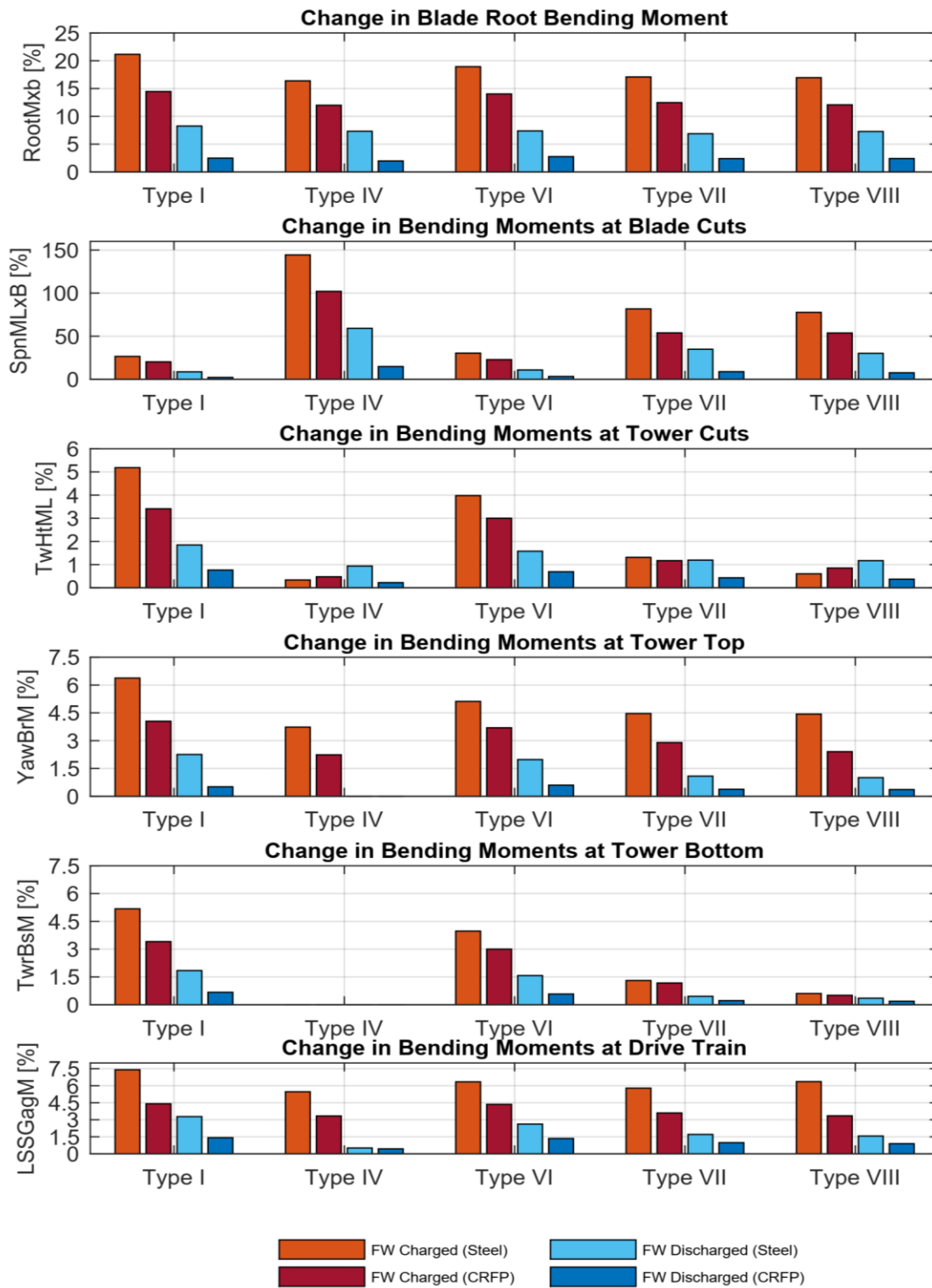


Figure 59 Comparison of changing in fatigue loads between steel accumulator and lighter CFRP accumulator

6.2 Flexible Carbon Fiber-Reinforced Plastic Designs

6.2.1 Need for Flexible Piston Accumulators

The work documented in section 6.1 leads to the conclusion that the piston accumulators should be used flexibly. They should be connected to the rotor blade along their entire length, which means that they will be bent whenever the rotor blade is bent. Figure 60 illustrates the problem by showing a section of a rotor blade that is excessively bent. Also shown in Figure 60 is a piston accumulator, which is installed between the shear webs.

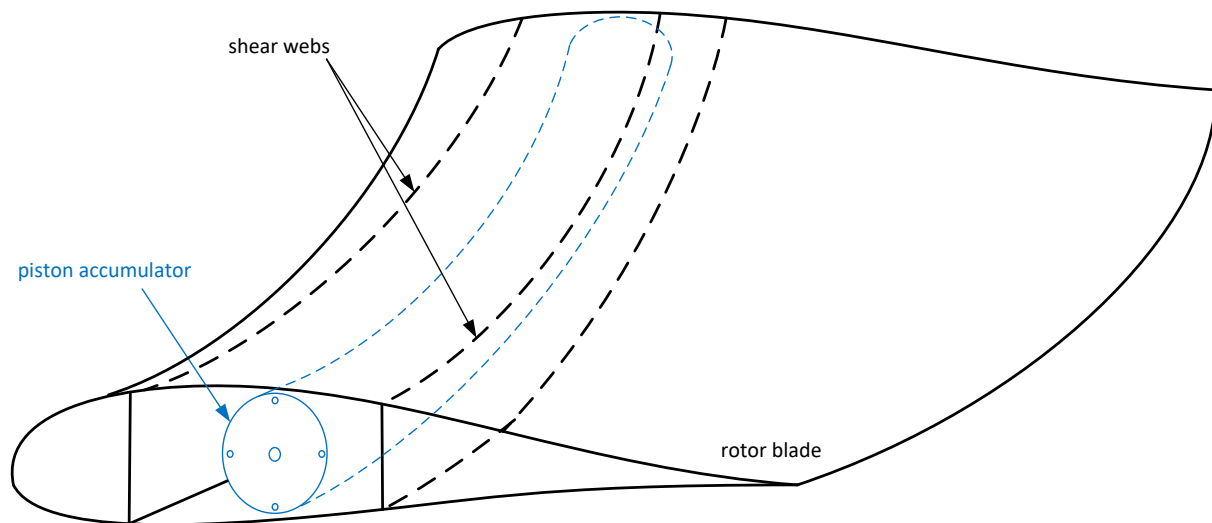


Figure 60 For illustration strongly exaggerated visualization of a bent rotor blade section.

6.2.2 Bending of Conventional Piston Accumulators

It is state of the art that hydraulic-pneumatic piston accumulators must not be bent. Otherwise, it is to be expected that the piston gets stuck and that there are gas leakages from the gas chamber into the fluid chamber or fluid leakages from the fluid chamber into the gas chamber.

Figure 61 shows a bent piston accumulator with conventional piston in side view. It can be seen that the gap between the piston and the cylinder is the only tolerance that is available for accommodating bending of the cylinder. The drawing in Figure 61 is not to scale; instead, the available gap is strongly exaggerated for illustration. Typically, the gap between piston and cylinder amounts to about 0.15 mm.

The length of a conventional piston is typically about 60 % of the diameter of the piston, as it has to be chosen such that the piston does not tilt under any circumstance. Figure 61 illustrates that the cylinder can only be bent until the gap is fully used up along the length of the piston. If the cylinder is bent further, the piston gets stuck.

Figure 61 shows that the piston ring is fully flattened on the inner radius of the bent cylinder. If the piston ring is not specifically designed for such deformation, it gets damaged. Subsequently, the piston ring would no longer be able to reliably separate gas from fluid, even if the cylinder were no longer bent.

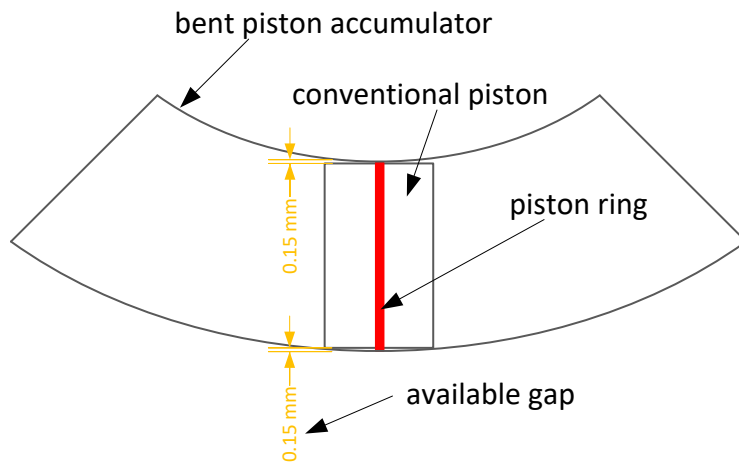


Figure 61 Illustration of a bent piston accumulator in side view (not to scale).

Another problem that leads to leakages from bending the cylinder is the cross-sectional shape of the cylinder, which has to be circular, because the cross-sectional shape of the piston is also circular. However, if a cylinder, which is made of an isotropic material, is bent in longitudinal direction, its cross-sectional shape becomes an ellipse, see Figure 62.

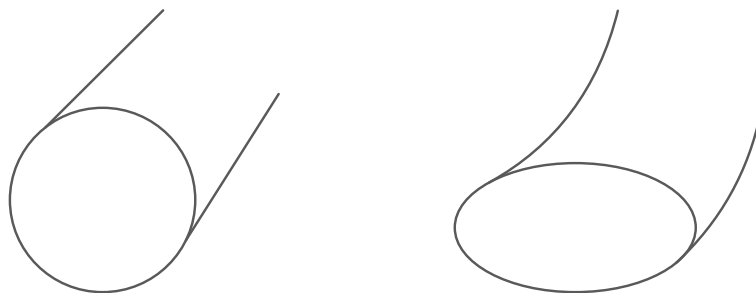


Figure 62 Cylinder made of an isotropic material. Left: in resting position with circular cross section. Right: bent in longitudinal direction, which turns the cross section into an ellipse.

In a piston accumulator, the piston is usually a lot more rigid than the cylinder. Therefore, it can neither bend, nor can it match its cross-sectional shape to the cross-sectional shape of the cylinder. Consequently, there will be leakages between the circular piston and the elliptic cylinder.

6.2.3 Preliminary Design of Flexible Piston Accumulators

The problems mentioned in section 6.2.2 are solved by HYDAC Technology GmbH (HYDAC.com), who designs flexible piston accumulators made of CFRP. This means that the piston rings have to seal the gap between the piston and the cylinder, even if the cylinder is bent. Also, the piston must be free to move under any bending. The material CFRP is advantageous because it is anisotropic, and hence, allows designing different properties in different directions. Furthermore, use of CFRP should lead to a weight reduction compared to conventional steel piston accumulators. This motivated HYDAC, in cooperation with PRONEXOS (pronexos.com), to perform a test to specify a flexible CFRP piston accumulator with a metal liner on the inside of the CFRP cylinder (see section 6.2.5). For the rotor blade, a firmly connected piston accumulator implies that the accumulator adds to the stiffness of the rotor

blade. Hence, not only the masses in the different nodes of the blades vary, also the stiffness varies, even as a function of the state of charge of the piston accumulator.

6.2.3.1 Flexible Cylinder

In a CFRP laminate carbon fibers are glued together with epoxy. By choosing the direction in which the carbon fibers are layered, the properties of the laminate in the different directions can be designed deliberately. I.e. CFRP can be built up such that it is an anisotropic material. For the problem at hand this means that the cylinder can be designed such that it has favorable properties in the different directions, as listed in the following:

- Stiffness in radial direction. I.e. the pressure on the inside of the cylinder leads to only little diameter increase, which is a premise for the piston rings to work reliably.
- Desired stiffness in longitudinal direction, to allow for a certain bending deflection from a specific external lateral force.
- For safety reasons it is advantageous that the cylinder fails in longitudinal direction when the bursting pressure is exceeded.
- When the cylinder is bent the aforementioned deformation of its cross section should be reduced to a bearable minimum. By stiffening in circumferential direction the bent cylinder behaves like an infinite number of circular rings, where each ring is slightly shifted with respect to its neighboring rings.

In the process of manufacturing the cylinder, the anisotropic properties can be achieved by winding the carbon fibres in certain directions around the cylinder. Figure 63 shows qualitatively the different winding directions.

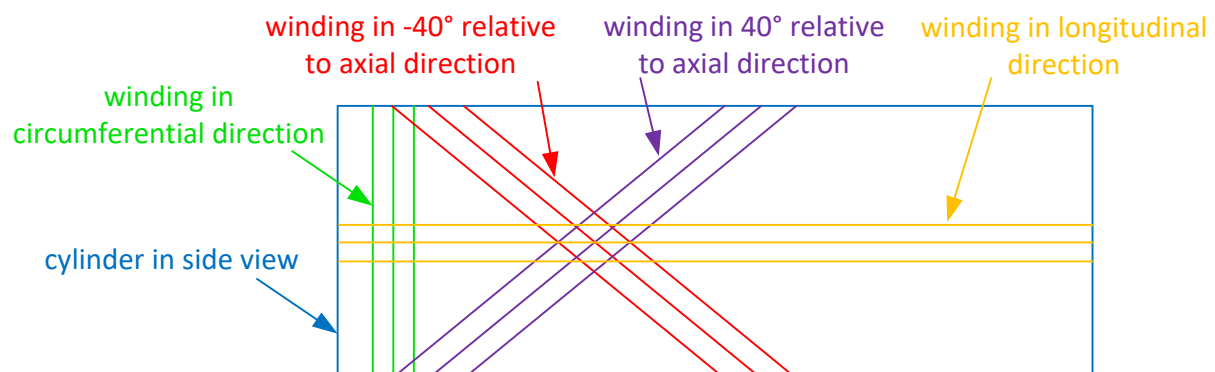


Figure 63 Qualitative illustration of the different winding directions that can be applied in the manufacturing process of a CFRP cylinder. (The angles are only examples for illustrating the concept.)

These winding directions lead to the following properties of the laminate:

- Windings in circumferential direction increase the stiffness in radial direction. The more carbon fiber layers are added in this direction, the less diameter increase the cylinder exhibits in case of internal pressure. Also, the cross-sectional shape is less prone to become an ellipse in case of longitudinal bending.
- Windings in longitudinal direction increase the stiffness in axial direction. By adding a specific number of windings in longitudinal direction, the cylinder deflects by a certain extent from a specific external force in lateral direction. The number of windings in longitudinal direction has

to be chosen such that these fibers rupture when the bursting pressure inside the cylinder is exceeded.

- Windings in a certain angle (positive and negative) with respect to the longitudinal axis, add to stiffness in radial direction and in axial direction, to an extent that depends on the angle. Most importantly, these windings add to the torsional stiffness of the cylinder. (The angles shown in Figure 63 are only arbitrary examples for illustration.)

6.2.3.2 Flexible Piston

When a piston accumulator is to be bent, the jamming of the piston, as shown in Figure 61, has to be prevented. At the same time, the piston has to reliably separate gas from fluid. I.e. the piston rings must not get damaged from bending the cylinder. These properties are achieved by making the piston from three flexibly connected discs, see Figure 64.

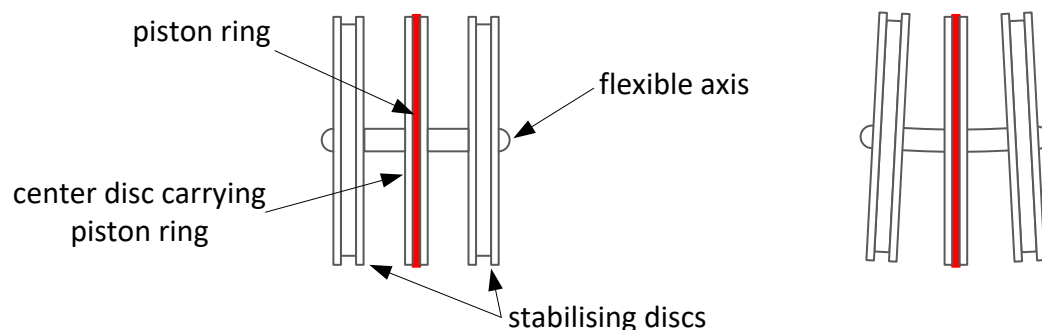


Figure 64 Flexible piston. Left: with naming of components. Right: in bent state.

The outer discs (called stabilizing discs in Figure 64) prevent the piston from tilting. The center disc carries the piston ring, and therefore, separates the gas chamber from the fluid chamber. The three discs are connected to each other via a flexible rod, which can be bent easily when the cylinder around the piston gets bent.

6.2.4 Preliminary Estimation of the Fatigue of Flexible Piston Accumulators

In order to design a composite accumulator for WTs it is important to know how the rotor blade deforms during the design loads. For this reason simulations need to be performed to illustrate the displacements between nodes, where a composite accumulator could be installed, to the desired blade and to the desired locations. Hence, load simulations should be done to illustrate the effect of such nodal displacements on the performance of the piston accumulator. Both displacement resulting from extreme loads (static loads) and from fatigue loads should be discussed.

The blade structural design presented in this report represents the Definition of a 5 MW/61.5m Wind Turbine Blade Reference Model [10]. This conception takes advantage of the extensively used 5 MW reference WT in studies by the wind energy research community as system that represents the current and future state of the art in offshore systems

6.2.4.1 Preparation of Blade Input File

In this section the preparations needed for creating a blade input file for nodal displacement calculation are briefly introduced. As mentioned above the National Renewable Energy Laboratory (NREL) 5 MW reference WT is used in this report. A blade geometry data, a composite layup concept, and layup and materials information are all available online [10].

The software used here to create the blade model is Sandia's NuMAD design tool [8] (see Figure 65) A comprehensive explanation with detailed design overview for this tool is described in NuMAD's user guide [9]. To create distributed blade properties NuMAD requires another software. PreComp [7] translates the blade input files from NuMAD into output blade section properties in tabular form, which may be readily exported to further tools in the next two sections.

Figure 66 shows the parameters that appear in the main input file, where PreComp reads this and connects with the airfoil shape and structural layup input file for each blade element.

A sample of output file of the SNL61.m blade is shown in Figure 67, where the computed section properties are output in 23 columns and 38 blade sections rows. This output file will be used later as an input file to calculate the nodal displacement of first eigenmodes.



Figure 65: Blade model as viewed in the NuMAD GUI

```
***** main input file for PreComp *****
Sample Composite Blade Section Properties

General information -----
61.5      Bl_length   : blade length (m)
38        N_sections : no of blade sections (-)
6         N_materials : no of materials listed in the materials table (material.inp)
3         Out_format  : output file   (1: general format, 2: BModes-format, 3: both)
f         TabDelim    (true: tab-delimited table; false: space-delimited table)

Blade-sections-specific data -----
Sec span   l.e.    chord   aerodynamic   af_shape   int str layup
location   position length twist      file
Span_loc   Le_loc   Chord   Tw_aero    Af_shape_file Int_str_file
(-)        (-)      (m)      (degrees)  (-)          (-)

0.0000      0.500    3.386e+000  13.31    shape_1.inp   layup_1.inp
0.0049      0.500    3.386e+000  13.31    shape_2.inp   layup_2.inp
0.0065      0.500    3.386e+000  13.31    shape_3.inp   layup_3.inp
0.0081      0.500    3.386e+000  13.31    shape_4.inp   layup_4.inp
0.0098      0.500    3.386e+000  13.31    shape_5.inp   layup_5.inp
0.0114      0.500    3.386e+000  13.31    shape_6.inp   layup_6.inp
0.0130      0.500    3.386e+000  13.31    shape_7.inp   layup_7.inp
0.0222      0.500    3.386e+000  13.31    shape_8.inp   layup_8.inp
0.0244      0.499    3.387e+000  13.31    shape_9.inp   layup_9.inp
0.0260      0.497    3.388e+000  13.31    shape_10.inp  layup_10.inp
0.0667      0.469    3.629e+000  13.31    shape_11.inp  layup_11.inp
0.0894      0.454    3.873e+000  13.31    shape_12.inp  layup_12.inp
0.1111      0.439    4.124e+000  13.31    shape_13.inp  layup_13.inp
0.1463      0.414    4.460e+000  13.31    shape_14.inp  layup_14.inp
0.1667      0.400    4.557e+000  13.31    shape_15.inp  layup_15.inp
0.1951      0.400    4.615e+000  12.53    shape_16.inp  layup_16.inp
0.2333      0.400    4.652e+000  11.48    shape_17.inp  layup_17.inp
0.2764      0.400    4.584e+000  10.68    shape_18.inp  layup_18.inp
0.3000      0.400    4.506e+000  10.16    shape_19.inp  layup_19.inp
0.3333      0.400    4.374e+000  9.63     shape_20.inp  layup_20.inp
0.3667      0.400    4.249e+000  9.01     shape_21.inp  layup_21.inp
0.4000      0.400    4.132e+000  8.40     shape_22.inp  layup_22.inp
0.4333      0.400    4.007e+000  7.79     shape_23.inp  layup_23.inp
0.5000      0.400    3.748e+000  6.54     shape_24.inp  layup_24.inp
0.5203      0.400    3.672e+000  6.18     shape_25.inp  layup_25.inp
0.5667      0.400    3.502e+000  5.36     shape_26.inp  layup_26.inp
0.6016      0.400    3.373e+000  4.75     shape_27.inp  layup_27.inp
0.6333      0.400    3.256e+000  4.19     shape_28.inp  layup_28.inp
0.6667      0.400    3.133e+000  3.66     shape_29.inp  layup_29.inp
0.6829      0.400    3.073e+000  3.40     shape_30.inp  layup_30.inp
0.7000      0.400    3.010e+000  3.13     shape_31.inp  layup_31.inp
0.7317      0.400    2.893e+000  2.74     shape_32.inp  layup_32.inp
0.7667      0.400    2.764e+000  2.32     shape_33.inp  layup_33.inp
0.8333      0.400    2.518e+000  1.53     shape_34.inp  layup_34.inp
0.8889      0.400    2.313e+000  0.86     shape_35.inp  layup_35.inp
0.9333      0.400    2.086e+000  0.37     shape_36.inp  layup_36.inp
0.9778      0.400    1.419e+000  0.11     shape_37.inp  layup_37.inp
1.0000      0.400    1.085e+000  0.00     shape_38.inp  layup_38.inp

Webs (spars) data -----
2          Nweb       : number of webs (-) ! enter 0 if the blade has no webs
8          Ib_sp_stn   : blade station number where inner-most end of webs is located (-)
37         Ob_sp_stn   : blade station number where outer-most end of webs is located (-)

Web_num    Inb_end_ch_loc  Oub_end_ch_loc (fraction of chord length)
1.0000     0.4114          0.1889
2.0000     0.5886          0.6114
```

Figure 66: PreComp main input file

Results generated by PreComp (v1.00.03, 11-Jun-2012, compiled using double precision) on 22-Oct-2018 at 15:45:20.
Sample Composite Blade Section Properties

blade length (meters) = 61.50

span_loc (-)	chord (m)	ei_flap (Nm ²)	ei_lag (Nm ²)	gj (Nm ²)	s_ft (Nm ²)	y_tc (m)	flap_iner (Kg-m)	tw_iner (deg)
0.000	3.386	0.2338E+11	0.2323E+11	0.1209E+11	0.0000E+00	0.001	0.1562E+04	15.784
0.005	3.386	0.2338E+11	0.2323E+11	0.1209E+11	0.0000E+00	0.001	0.1562E+04	15.809
0.006	3.386	0.2437E+11	0.2383E+11	0.1248E+11	0.0000E+00	0.018	0.1629E+04	14.310
0.008	3.386	0.2437E+11	0.2383E+11	0.1248E+11	0.0000E+00	0.018	0.1629E+04	14.310
0.010	3.386	0.2437E+11	0.2383E+11	0.1248E+11	0.0000E+00	0.018	0.1629E+04	14.317
0.011	3.386	0.2437E+11	0.2383E+11	0.1248E+11	0.0000E+00	0.018	0.1629E+04	14.325
0.013	3.386	0.2321E+11	0.2270E+11	0.1189E+11	0.0000E+00	0.018	0.1551E+04	14.339
0.022	3.386	0.1629E+11	0.1583E+11	0.8221E+10	0.0000E+00	0.002	0.1155E+04	13.514
0.024	3.387	0.1681E+11	0.1592E+11	0.8277E+10	0.0000E+00	0.025	0.1203E+04	13.452
0.026	3.388	0.1714E+11	0.1593E+11	0.8289E+10	0.0000E+00	0.031	0.1205E+04	13.396
0.067	3.629	0.1688E+11	0.1322E+11	0.5961E+10	0.0000E+00	0.103	0.8308E+03	18.830
0.089	3.873	0.1494E+11	0.1175E+11	0.4322E+10	0.0000E+00	0.118	0.5863E+03	16.146
0.111	4.124	0.1224E+11	0.9688E+10	0.2635E+10	0.0000E+00	0.116	0.4214E+03	16.049
0.146	4.460	0.6122E+10	0.4834E+10	0.6066E+09	0.0000E+00	0.130	0.1511E+03	16.460
0.167	4.557	0.4908E+10	0.5053E+10	0.4772E+09	0.0000E+00	0.150	0.1192E+03	16.514
0.195	4.615	0.4390E+10	0.5154E+10	0.4136E+09	0.0000E+00	0.148	0.1024E+03	15.746
0.233	4.652	0.4102E+10	0.5199E+10	0.3745E+09	0.0000E+00	0.143	0.9186E+02	14.885
0.276	4.584	0.3564E+10	0.5011E+10	0.3100E+09	0.0000E+00	0.138	0.7639E+02	14.101
0.300	4.506	0.3315E+10	0.4791E+10	0.2817E+09	0.0000E+00	0.135	0.6962E+02	13.590
0.333	4.374	0.2944E+10	0.4425E+10	0.2430E+09	0.0000E+00	0.129	0.6021E+02	12.966
0.367	4.249	0.2599E+10	0.4100E+10	0.2114E+09	0.0000E+00	0.124	0.5190E+02	12.166
0.400	4.132	0.1982E+10	0.3656E+10	0.1626E+09	0.0000E+00	0.117	0.3809E+02	10.822
0.433	4.007	0.1587E+10	0.3226E+10	0.1339E+09	0.0000E+00	0.109	0.3023E+02	9.832
0.500	3.748	0.1302E+10	0.2592E+10	0.1098E+09	0.0000E+00	0.095	0.2456E+02	8.620
0.520	3.672	0.1104E+10	0.2390E+10	0.9386E+08	0.0000E+00	0.091	0.2076E+02	7.797
0.567	3.502	0.7379E+09	0.1992E+10	0.6604E+08	0.0000E+00	0.083	0.1386E+02	6.122
0.602	3.373	0.6391E+09	0.1755E+10	0.5724E+08	0.0000E+00	0.077	0.1197E+02	5.464
0.633	3.256	0.5844E+09	0.1557E+10	0.5294E+08	0.0000E+00	0.071	0.1094E+02	4.996
0.667	3.133	0.4359E+09	0.1292E+10	0.4049E+08	0.0000E+00	0.059	0.7938E+01	3.928
0.683	3.073	0.3623E+09	0.1215E+10	0.3525E+08	0.0000E+00	0.060	0.6677E+01	3.391
0.700	3.010	0.3097E+09	0.1107E+10	0.3116E+08	0.0000E+00	0.057	0.5779E+01	2.888
0.732	2.893	0.2541E+09	0.9205E+09	0.2717E+08	0.0000E+00	0.050	0.4871E+01	2.498
0.767	2.764	0.2035E+09	0.7940E+09	0.2387E+08	0.0000E+00	0.052	0.4059E+01	2.150
0.833	2.518	0.1220E+09	0.5812E+09	0.1785E+08	0.0000E+00	0.059	0.2710E+01	1.386
0.889	2.313	0.7100E+08	0.4314E+09	0.1353E+08	0.0000E+00	0.070	0.1836E+01	0.743
0.933	2.086	0.3814E+08	0.3029E+09	0.9576E+07	0.0000E+00	0.081	0.1187E+01	0.281
0.978	1.419	0.7697E+07	0.9486E+08	0.3005E+07	0.0000E+00	0.073	0.2943E+00	0.112
1.000	1.085	0.3666E+07	0.4690E+08	0.1358E+07	0.0000E+00	0.052	0.1229E+00	-0.060

Figure 67: PreComp output file

6.2.4.2 Bending Inflicted on Piston Accumulators Due to Rotor Blade Bending

As mentioned above, piston accumulators for FW systems in WT rotor blades should be flexible. I.e. piston accumulators should be connected to the rotor blade along their entire length, which means that they will be bent whenever the rotor blade is bent. This implies for the piston accumulators that the piston rings have to seal the gap between the piston and the cylinder, even if the cylinder is bent.

Also, the piston must not clamp, i.e. it must be free to move under any realistically conceivable bending.

In order to design such a flexible piston accumulator for FW systems in rotor blades of WT's it is important to know how the considered rotor blade deforms during operation. Hence, simulations of WT operation need to be performed to illustrate the displacement between blade nodes, where a piston accumulator could be installed. Based on the information that is obtained from such simulations, a flexible piston accumulator prototype was built and tests are performed on this prototype, inter alia, to ensure gas-tightness during bending.

A rotor blade can be bent in edgewise direction and in flapwise direction. In flapwise direction it is much more flexible than in edgewise direction; hence, it can bend a lot more in flapwise direction. Since a rotor blade can be considered a beam it can vibrate with different eigenfrequencies, i.e. it has different eigenmodes. Vibration with a particular eigenfrequency leads to deformations of the blade with the respective mode shape. Due to the fact that the first and the second eigenmodes lead to the largest deflections of rotor blades, this study focusses on the first and the second eigenmodes in flapwise direction only. In order to compute the eigenmodes of a beam, like the Sandia 61.5 m rotor blade [10], a finite-element method (FEM) program is needed that provides the coupled modes of the WT blade. Such a program is also provided by NREL and is called BModes [16]. BModes applies the Euler Bernoulli beam theory combined with Hamilton's principle and is capable of computing the coupled modes of beams in general; hence, it can be used for both the blades and the tower of a WT. All the specifications that BModes needs, like rotor speed, blade geometry, and pitch control, can be derived from the specification of the NREL 5 MW WT [17]. BModes also requires structural property distributions along the rotor blade. These properties are derived from the Sandia 61.5 m rotor blade design [10]. With the aforementioned information, an input file for BModes is prepared, in order to compute mode shapes and frequencies. BModes uses FEM followed by an eigenanalysis to compute the eigenmodes [16]. As a result, BModes generate an output file, where the computed coupled mode shapes are shown as spanwise distribution of flap, edgewise, twist, and axial displacement components in a particular mode. Flap displacement is the displacement that the blade exhibits out of the rotor plane, relative to its rest position, when a pitch angle of zero degree is considered [16]. This component is used to illustrate the nodal displacement for the first and the second eigenmodes in Figure 68 and Figure 69 respectively. Based on this component, slope and curvature of modal displacement curve can be derived as follows, and shown in Figure 68 and Figure 69.

$$slope = \frac{d \text{ flap_disp}}{d \text{ blade_span}} \quad \text{Equation 65}$$

$$curvature = \frac{d^2 \text{ flap_disp}}{d \text{ blade_span}^2} \quad \text{Equation 66}$$

Where *blade_span* is the span location of a point on the blade reference axis measured with respect to blade root, *flap_disp* is the blade displacement out of the rotor plane obtained from BModes; *slope* is the first derivative of the flap displacement with respect to the *blade_span*, and *curvature* is the second derivative of the flap displacement with respect to the *blade_span*.

However, since all the FW configurations published in Hippel et al. [15] are already compared in section 6.1.3 for the conventional and for the CFRP initial design of piston accumulator, the comparison is limited in this section to three relevant FW configurations. The three selected FW configurations are those, which represent the largest, a medium and the lowest impact on the mechanical loads. In the following, the considered FW configurations are called "types" and are

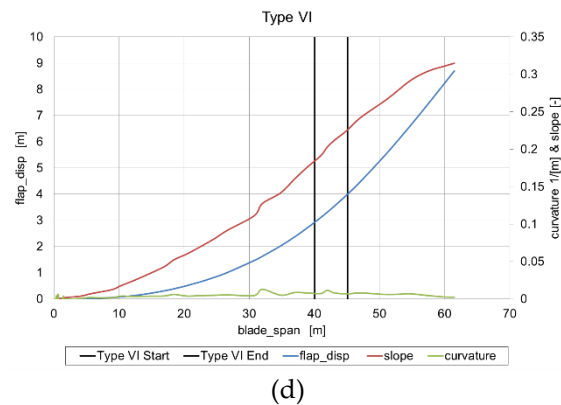
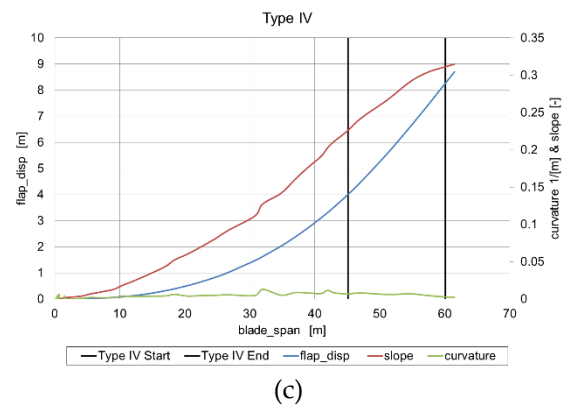
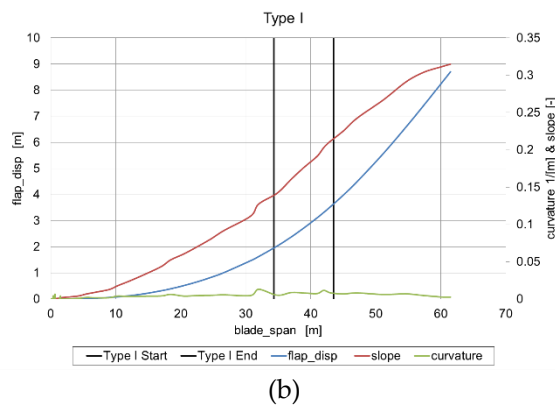
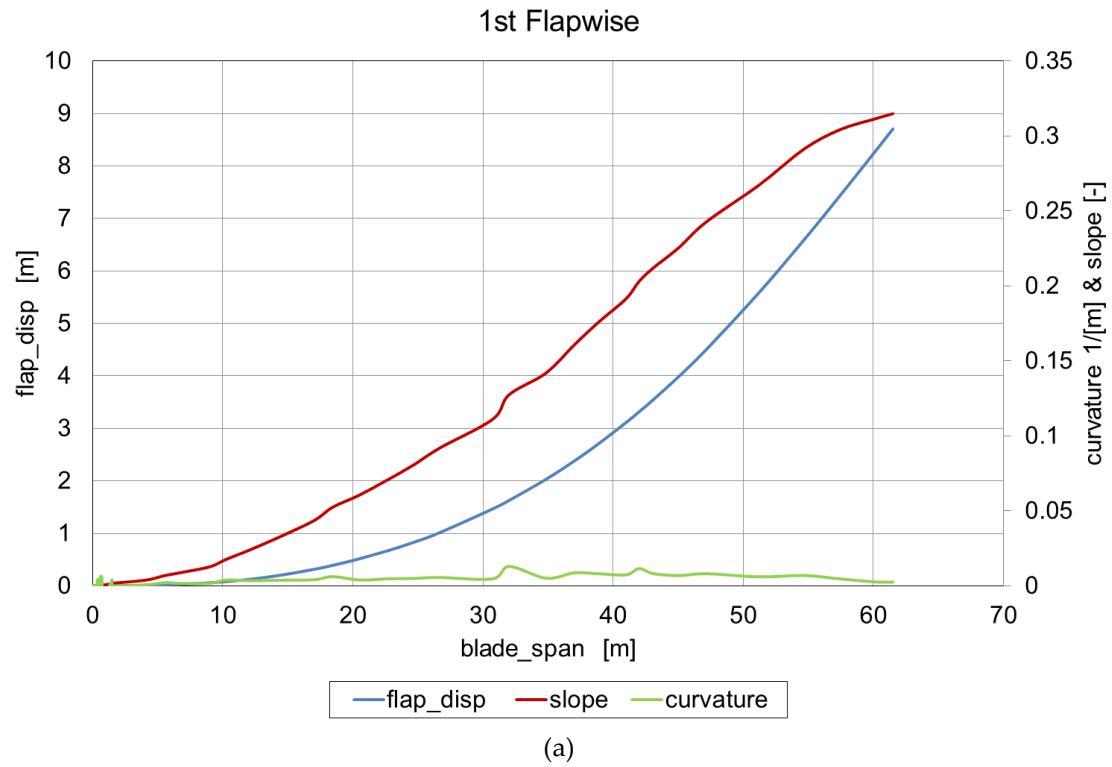


Figure 68: (a) flap deflection, slope and curvature of the first eigenmode of the considered WT blade; (b) Location of tip accumulator of type I (c) Location of tip accumulators of type IV (d) Location of tip accumulators of type VI

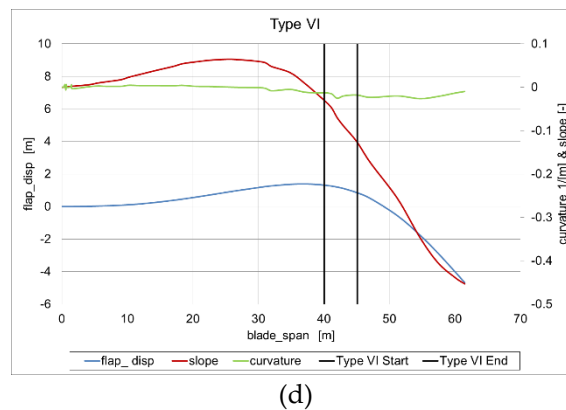
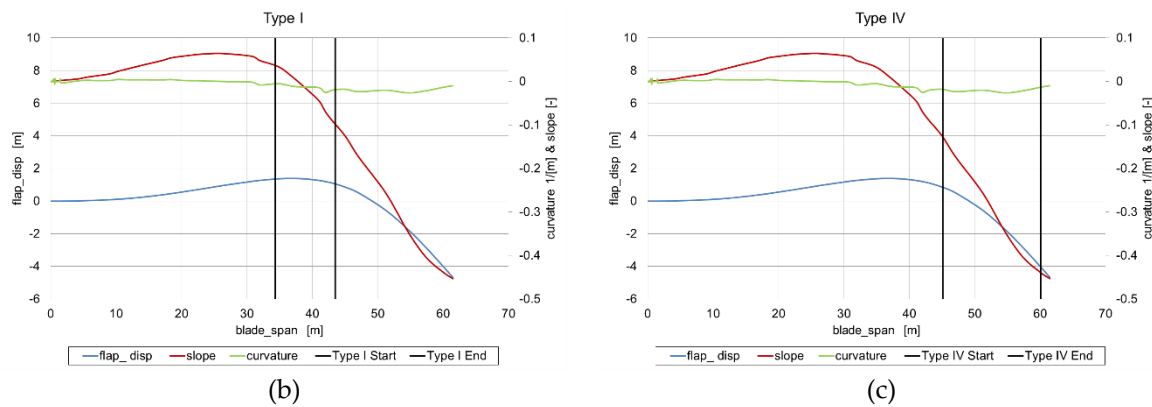
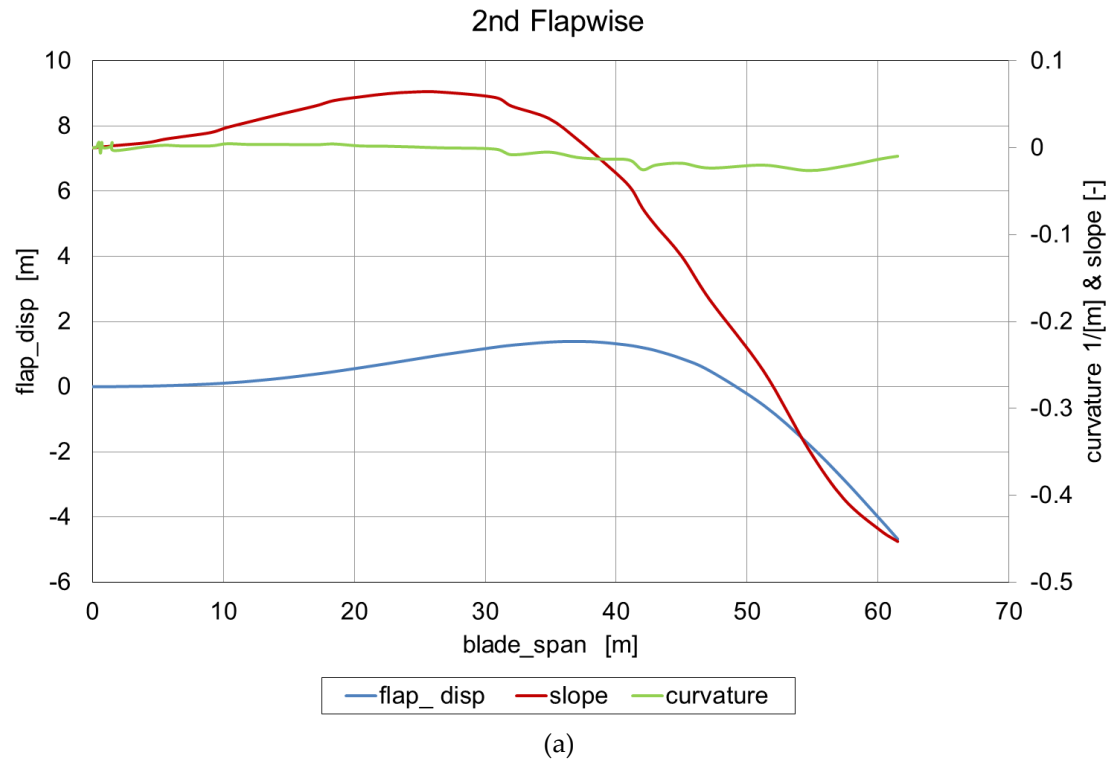


Figure 69: (a) flap deflection, slope and curvature of the second eigenmode of the considered WT blade; (b) Location of tip accumulator of type I (c) Location of tip accumulators of type IV (d) Location of tip accumulators of type VI

identified with Roman numerals as introduced in Hippel et al. [15]. FW type I causes the lowest impact on the mechanical loads of the rotor blades although this type is the heaviest, the FW type IV causes the largest impact on the mechanical loads of the rotor blades although this type is the lightest. FW type VI cause a medium impact on the mechanical loads of the rotor blade compared to the FW types I and IV. In addition type VI has an average weight between FW type I and FW type IV. Additionally, these three FW types cover the most relevant locations for installation of piston accumulators inside the rotor blades.

Regarding the three FW types mentioned above, Figure 68 and Figure 69 show the start and the end location of the tip accumulators, i.e. the tip accumulators are located between the span locations indicated by the vertical black lines in the diagrams (b), (c) and (d) of Figure 68 and Figure 69. Information about flap displacement, slope, and curvature for the installation space of tip accumulators can be derived from Figure 68 and Figure 69. This information can be used for defining the bending test for the flexible accumulator prototype. As a result, the design specifications of the prototype are applied to the FW types. In other words the design of the CFRP piston accumulators of different lengths, diameters and pressures, as needed for the three different FW types, are extrapolations of the design specifications of the prototype. This is outlined further in the next section.

6.2.5 Specification of Flexible Carbon Fibre-Reinforced Plastics Design

Based on the information about the bending behaviour of the Sandia 61.5 m rotor blade presented in section 2, HYDAC, in cooperation with PRONEXOS, built a prototype of a CFRP piston accumulator with a steel liner on the inner surface of the CFRP tube, see Figure 70. Figure 70 shows the steel liner covered with the CFRP laminate. In the background the piston can also be seen. This prototype is tested in the test area of HYDAC Technology. Further design specifications for the prototype are:

- The structural strength of the laminate with the steel liner shall withstand the working pressure of 60 bar.
- A maximum diameter increase of the accumulator tube of 0.1mm at 40 bar working pressure.
- The laminate should rupture in longitudinal direction at burst pressure (>120 bar)
- The CFRP design shall be no more than 1.5 times as expensive as a comparable steel design
- The steel liner at the inner surface shall have a wall thickness of 1 mm and its main purpose is to guarantee gas leaktightness even in case of inter-fibre cracks in the CFRP laminate.



Figure 70: A prototype of a CFRP piston accumulator with a steel liner on the inner surface of the CFRP tube.

The composite material and the flow forming steel liner used for the construction of the prototype are already qualified for series manufacturing at PRONEXOS. Table 11 illustrates the material properties and the lay-up plan of the CFRP prototype.

Table 11 Laminate lay-up and the material properties of the CFRP with steel liner prototype

Lay-up No.	Thickness mm	Direction °	Density g/cm ³	E MPa	E _⊥ MPa	G _⊥ MPa	ν _⊥ -
1	0.83	88	1.57	146324	10725	5376	0.2555
2	1.06	15	1.57	146324	10725	5376	0.2555
3	0.83	88	1.57	146324	10725	5376	0.2555
4	0.83	88	1.57	146324	10725	5376	0.2555
5	1.06	15	1.57	146324	10725	5376	0.2555
6	0.83	88	1.57	146324	10725	5376	0.2555
7	0.83	88	1.57	146324	10725	5376	0.2555
8	1.06	15	1.57	146324	10725	5376	0.2555
9	0.83	88	1.57	146324	10725	5376	0.2555
10	1	-	7.80	210000	210000	79300	0.3200
Total thickness	9.16						

Where $E_{||}$, E_{\perp} , $G_{||}$, and $\nu_{||}$ are the young's modules parallel to fibre direction, the young's modules perpendicular to fibre direction, the in-plane share modules, and the major poisson's ratio of a CFRP laminate layer, respectively.

In order to verify the validity of the prototype specification, the prototype is modelled with the design tool COMPOSITOR [41]. COMPOSITOR is a structural computer-aided engineering tool, which was developed by the Institute for Plastics Processing at RWTH Aachen University (ikv-aachen.de).

For the working pressure of 40 bar a load case of two global stresses can be translated on the basis of Barlow's formula [42]

$$\sigma_t = \frac{p \cdot d_m}{2 \cdot s} \quad \text{Equation 67}$$

$$\sigma_a = \frac{p \cdot d_m}{4 \cdot s} \quad \text{Equation 68}$$

Where σ_t and σ_a are the circumference and the longitudinal stresses, respectively. p is the internal pressure, d_m is the mean diameter and s is the wall thickness of the pressure vessel, here the tube of the piston accumulator. The material specifications and the laminate lay-up of the flexible accumulator prototype are considered in the simulation model of COMPOSITOR. As a result, two components of the strain, in circumference and longitudinal directions, are computed, based on the classical laminate theory. The resulting circumference strain can be transformed into a diameter increase, i.e. the diameter increase of the test model is about 0.08 mm at the working pressure of 40 bar, which is lower than the required maximum diameter increase of 0.1 mm.

The dimensions of the flexible piston accumulator prototype are listed in Table 12. These dimensions are limited by the dimensions of test facility at HYDAC's test area. Hence, the prototype size is obviously not comparable with the dimensions of a piston accumulator for a FW system in a multi MW WT rotor blade.

The test requirement of maximum diameter increase of 0.1 mm is so conservative that it can only be achieved by relative small piston accumulators. Applying this requirement to the FW types for a multi MW WT, leads to oversizing of the wall thickness of the piston accumulators. Therefore, the maximum diameter increase is slackened to 0.3 mm, which is a commonly used value for steel accumulators. A larger diameter increase poses a challenge for the piston rings, as they must not extrude into the gap between liner and piston. However, 0.3 mm diameter increase is a feasible value that is confirmed by piston accumulators that have been operating for a long time.

Table 12 Flexible piston accumulator prototype dimensions

Inner diameter mm	Outer diameter mm	Total length mm	Stationary weight kg
250	269.2	1995	89.78

6.2.6 Carbon fiber-reinforced plastic Flywheel Types

6.2.6.1 Geometry

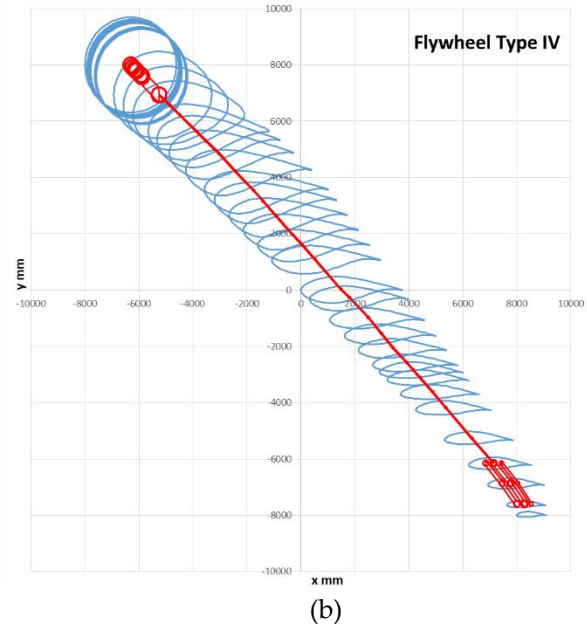
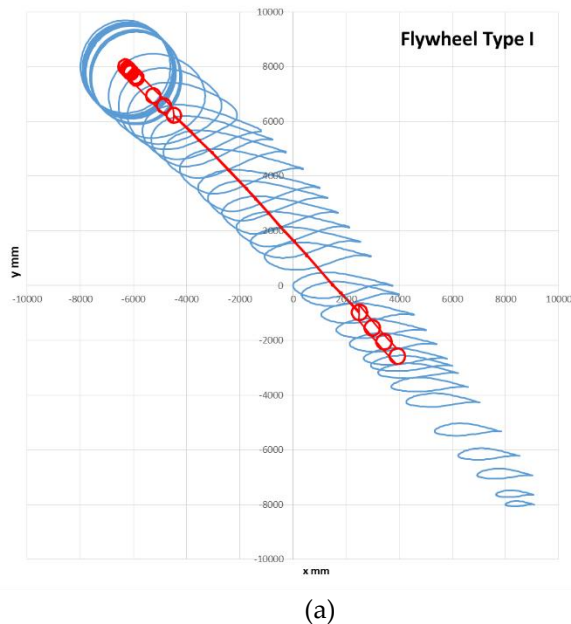
The possible installation spaces for the tip accumulators are limited by the dimensions of the airfoils of the Sandia 61.5 m blade design. In this blade, like in all state of the art rotor blades, the space inside the blade decreases towards the blade tip. As a result, a single, double, or triple tip accumulators can be installed inside the blade, in order to achieve the desired increase of the inertia of the NREL 5 MW WT.

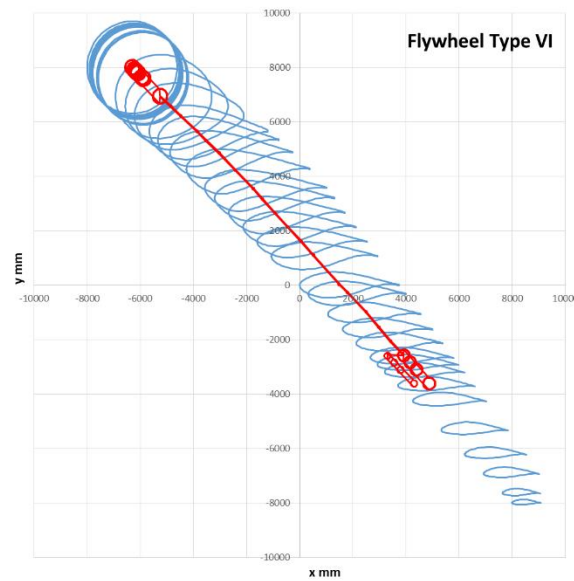
The properties of the CFRP tip accumulators of the three selected FW types are summarized in Table 13. Where rotor radius is the maximum rotor radius that can be achieved by the tip accumulators. This data is further needed in the mass and load comparison in 6.2.7 6.2.6.2 and section 6.2.7

Table 13 Properties of the CFRP piston accumulators of the three FW types

	No. of tip accumulators	Rotor radius m	Inner diameter mm	Total length mm
Type I	1	40.01	577	5477
Type IV	3	Each at 61.6	224, 209, and 149	5966, 5957, and 5920
Type VI	2	Each at 46.6	443 and 241	5047 and 4923

Based on the information about the CFRP tip accumulators properties mentioned in Table 13 the proposed installation spaces inside the Sadia 61.5 m rotor blade are illustrated in Figure 71. This figure presents the available spaces at each rotor blade section (in blue). Where Figure 71 (a) shows the root accumulator, the fluid pipe, and the tip accumulator (in red) of FW type I inside the rotor blade, Figure 71 (b) and (c) show those components for FW type IV and FW type VI, respectively.





(c)

Figure 71: Cross sections of the Sandia 61.5 m blade at the 38 blade nodes and the piston accumulators with fluid pipe of (a) FW type I; (b) FW type IV; (c) FW type VI

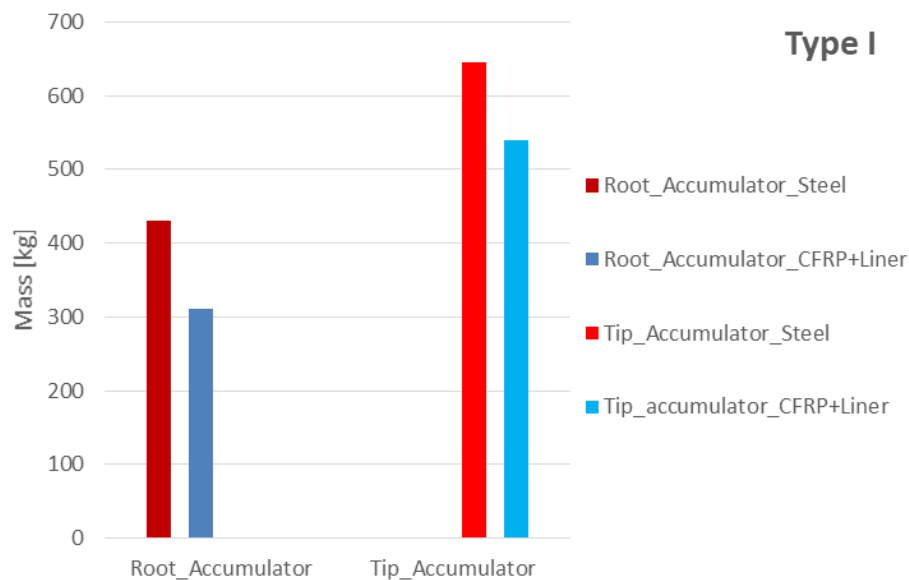
6.2.6.2 Masses Comparison

In order to design the CFRP piston accumulators for the different FW types, according to the prototype specifications (see Table 11), again COMPOSITOR is applied. For this purpose the model specifications of the prototype, as introduced in 6.2.5, are used to model the CFRP accumulator as needed for the three FW types. The three FW types that are mentioned in the Introduction are analyzed, and the wall thicknesses of the CFRP accumulators are computed according to the working pressure of each FW type and to the maximum permissible diameter increase of the steel accumulator as discussed above. As a result, simulations of the CFRP piston accumulators for the FW systems in COMPOSITOR have shown that in addition to the flexibility of the CFRP piston accumulator also the total stationary mass is decreased compared to conventional steel piston accumulators. This is due to the special technology used by winding the carbon fiber in circumferential, longitudinal, and hoop and helical (e.g. $\pm 40^\circ$ relative to axial direction) directions around the steel liner of the piston accumulator, see Figure 63. Consequently, the design of the flexible piston accumulator is noticeably lighter than the conventional steel design. Table 14 and Figure 72 compare the properties and the masses of both CFRP and conventional steel piston accumulators for the three FW types mentioned in the Introduction. In Figure 72 the CFRP accumulators and the conventional steel accumulators are represented as CFRP+Liner and as Steel in blue and red, respectively. The masses represented in Figure 72 are the total stationary masses of root and tip accumulators of each FW type, where type I has only one tip accumulator. Type IV and type VI have three and two tip accumulators, respectively. Figure 72 shows the obvious weight reduction of the total stationary masses of the root and the tip accumulators for the CFRP design compared to the conventional steel design for all represented FW types. The effect of this weight reduction on the impact of the mechanical loads of the WT is discussed in the next section.

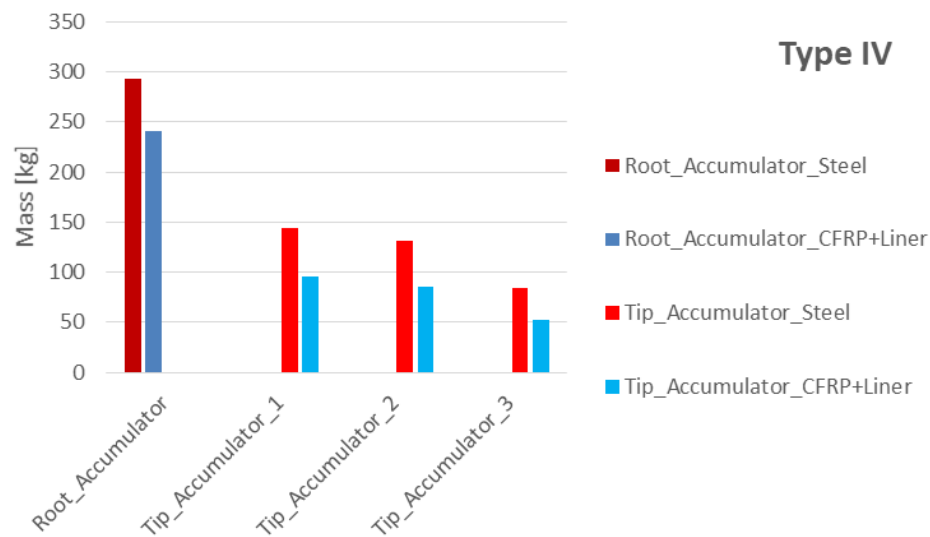
Table 14 Properties of the CFRP and the conventional piston accumulators of the three FW types

	CFRP+Liner accumulators						Steel accumulators					
	Type I	Type IV			Type VI		Type I	Type IV			Type VI	
No. of tip accumulators	1	1	2	3	1	2	1	1	2	3	1	2

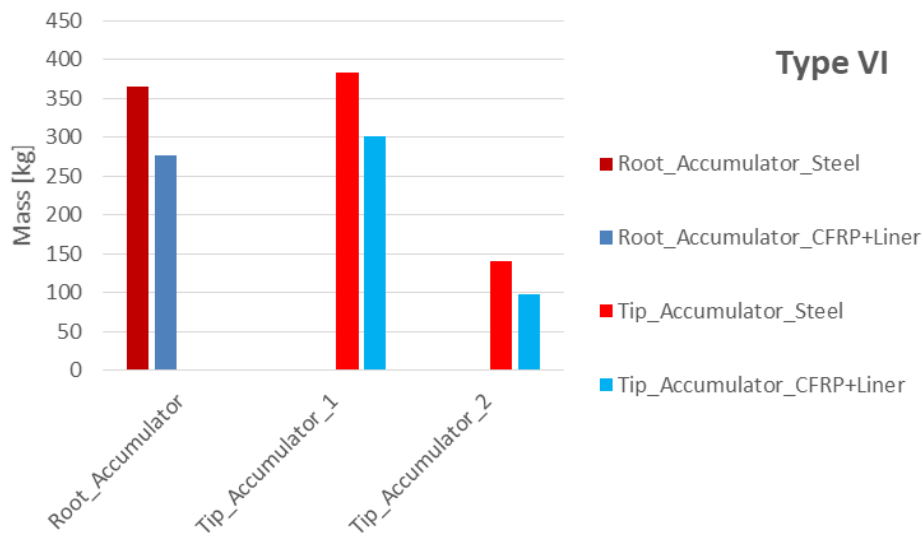
Wall thickness mm	4.24	Each 3.72	Each 3.72	3	Each 3	Each 3
Working pressure bar	13.9	Each 31.6	Each 18,7	13.9	Each 31.6	Each 18,7
Material	carbon fiber Toho tenax STS40 and S335 steel liner			34CrMo4 steel		



(a)



(b)



(c)

Figure 72 Masse comparison of blade tip and blade root accumulators from steel and from CFRP with steel liner for (a) type I; (b) type IV; (c) type VI

6.2.7 Load Analysis

The load analysis aims to quantify the effect of the weight reduction of the CFRP piston accumulators on the impact of the mechanical loads of the NREL 5 MW WT. The quantifying of loads is done firstly by computing the mechanical loads of the original WT without FW system in order to get reference load values. Afterwards, load simulations are done for the WT with a FW system comprising CFRP accumulators as well as with a FW system comprising conventional steel accumulators in the rotor blades. Eventually, the deviations of the mechanical loads from the reference values illustrate the impact of the different FW system designs on the mechanical loads of the WT.

For this analysis the program FAST is used. FAST is an aeroelastic computer-aided engineering tool developed by NREL [17], that allows computing mechanical loads in a WT.

As described in previous work of the author [15], the methodology used to implement the variable behavior of the FW system in FAST considers the FW system statically, i. e. either the system is fully charged or fully discharged. In state-of-the-art WTs, the rotor blade inertia does not vary during operation. Therefore, all common load simulation tools like Felx5 (<http://www.dtu.dk>), FAST (<https://nwtc.nrel.gov/FAST8/>), or Bladed [25] are unsuitable for simulating the dynamic operation of the FW system. This would require drastic adaptations of the source code of such load simulation tools. Future work will focus on implementing variable blade inertias in a load simulation tool to allow for the simulation of the dynamic operation of a FW system in a WT rotor.

The structural blade properties of the Sandia 61.5 m rotor blade design is described in FAST as sectional distributed masses densities and stiffnesses. Each section with its mass and stiffness is at a particular location in spanwise direction of the blade. These locations are also the locations where cross sections of the airfoil are illustrated in Figure 71. As the eigenmodes characterize the structural properties of the rotor blade, FAST requires also the mode shape coefficients of the first three eigenmodes. The impact of the FW system on the structural properties of the rotor blade is implemented in terms of increasing the mass density at those nodes of the blade, where the root and the tip accumulators are installed. Regarding the state of the charge of the FW system, the fluid mass is shifted between the tip accumulator and the root accumulator. I.e. if the FW system is charged, the complete fluid mass is added to the mass density of the nodes of the blade tip where the tip accumulator is located. If the FW system is discharged, the complete fluid mass is added to the mass density of the nodes of the

blade root where the root accumulator is located. These two scenarios are done for the three previously mentioned FW types. Additionally, the mode shape coefficients of the first three eigenmodes are computed with BMode for both states of charge, due to the change of the blade section masses. Other structural properties of the blade input data remain unchanged.

In this section load simulation results of the cases “original WT without FW system” and “WT with conventional steel accumulator FW system” are obtained from previous work of the author [15]. Hence, it is mandatory for the load simulations of the WT with a FW system comprising CFRP accumulators to take the same design load cases (DLCs) and the same wind fields. Only in this way is it possible to compare load simulation results of both FW system designs with the original WT without FW system. The selected DLCs are based on the “IEC International Standard for the Design of Wind Turbines” and they cover the most important operation modes of a WT [20]. Thus the computed ultimate and fatigue loads of the unchanged rotor blade and of the rotor blade with the conventional steel piston accumulators can be obtained from Hippel et al [15]. The results of these simulations are used as reference values. Subsequently, load simulations are performed for the WT with FW system comprising the CFRP piston accumulators. Loads are computed for the WT with the FW types I, IV, and VI in charge and discharged state. The resulting ultimate and fatigue loads are compared to the reference values. Afterwards, the changes in ultimate and fatigue loads of rotor blade, tower, and drive train are evaluated, and potentially occurring structural blade failures are discussed.

At first, the change in ultimate loads of the blades, the drive train, and the tower of the 5 MW WT due to both designs of the FW system are discussed. Figure 73 depicts the change in ultimate loads as a percent increase in bending moments. The charged and the discharged states of the FW system with CFRP accumulators are represented in Figure 73 in dark red and dark blue, whereas the charged and discharged states of the FW system with conventional steel accumulators are shown in light red and light blue, respectively. The increase in bending moments when both FW designs are in charged state are obviously greater than the bending moments when the FWs are in discharged state. The reason for this is that the fluid mass in the charged state is added to the stationary mass of the tip accumulator, where the lever arm of the gravitation force has a larger distance to the center of rotation. Also, the larger distance to the center of rotation leads to larger centrifugal forces created by the fluid mass. Due to the stationary weight reduction of the CFRP accumulator, the increase in bending moments of almost all FW types is lower for the CFRP design compared to the conventional steel design. Excepted from this is the change in bending moment at blade cuts for FW Type IV in charged state. Only in this scenario is the increase in bending moment of the CFRP design about 2% greater than the conventional steel design. The reason for this minor increase is the difference in WT operating points of both FW designs when the maximum turbulent wind speed hits the rotor blade.

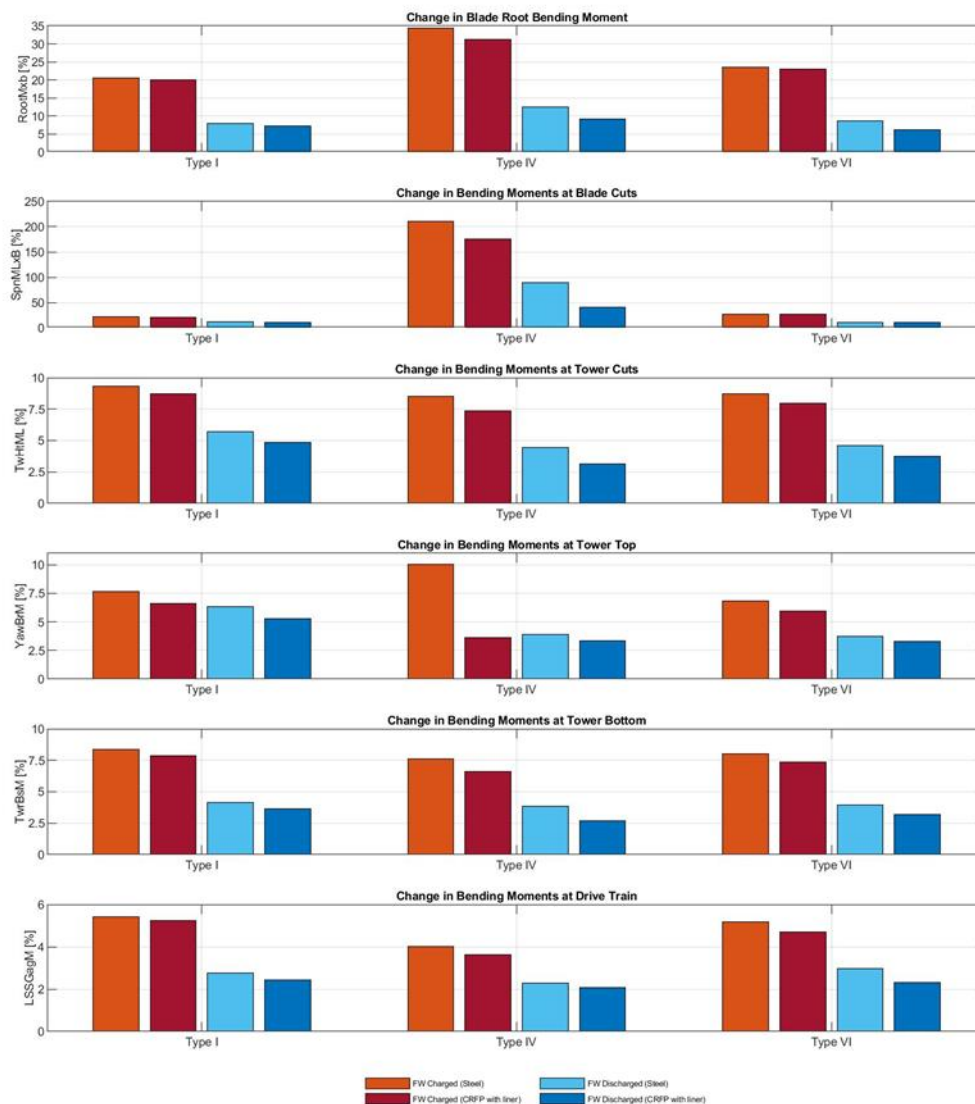


Figure 73 Comparison of changes in ultimate loads between steel accumulator and CFRP with metal liner accumulator, both with respect to the ultimate loads of the original WT without FW system

The first and the second graphs in Figure 73 show the bending moments at the blade cuts, $SpnMLxB$, and the tower cuts, $TwHtML$, where the maximum increase of these moments are indicated. The variable names are based on the conventions used in FAST [29].

Finally, the change in fatigue loads are analyzed in a similar procedure as for ultimate loads. Fatigue analysis is done twice for each FW design over the lifetime of 20 years of the WT. Once, the FW system is charged for 20 years, and once, again, the FW system is discharged for 20 years. This is, again, due to the fact that the dynamic behavior of the FW system cannot be implemented in FAST.

Figure 74 compares the change in fatigue loads for both FW designs at the rotor blade, the tower and the drive train of the 5 MW WT. The light red and the light blue bars in Figure 74 represent the charged and the discharged states of the conventional design of the FW system, respectively. The columns in dark red and in dark blue represent the charged and the discharged states of the CFRP design of the FW system, respectively.

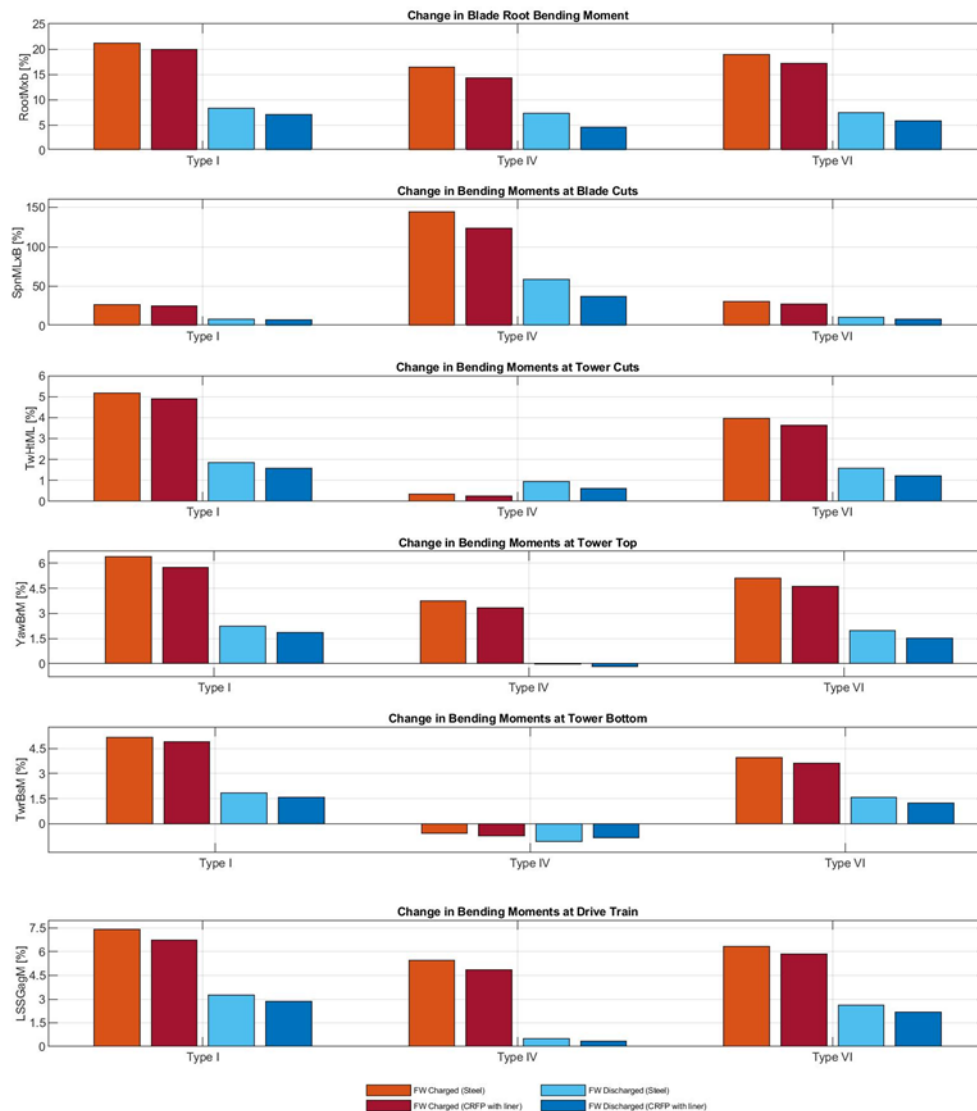


Figure 74 Comparison of changes in fatigue loads between steel accumulator and CFRP with metal liner accumulator, both with respect to the ultimate loads of the original WT without FW system.

The change in fatigue damage equivalent bending moment at the blade, the tower, and the drive train caused by the CFRP design of the FW system are obviously lower than the change in fatigue damage equivalent bending moment caused by the conventional steel design. This is due to the difference of the stationary weight between the CFRP design and the conventional steel design of the piston accumulators. For the FW type IV the fatigue equivalent bending moment at tower top in discharged state and at tower bottom in charged and discharged states are slightly decreased for both FW designs. This slight decrease of the fatigue bending moment can be traced to the low impact of Type IV on the tower top and tower bottom during the simulation time of 20 years of operation.

Consequently, ultimate and fatigue failures are evaluated to insure that there is no need for reinforcement in the original rotor blade design of the NREL 5 MW WT. The failure evaluation in this section is based on the same methodology used by Hippel et al [15], where the load simulation results were used to indicate ultimate and fatigue failures. The failure evaluation in a previous work of the

author [15] showed that neither ultimate nor fatigue failure of the rotor blade was caused by the presence of the conventional steel accumulator FW system. Figure 73 and Figure 74 show that the loads of the CFRP FW design are in general lower than those of the conventional steel FW design. This leads to the conclusion that the increase in ultimate and fatigue loads due to the installation of the CFRP FW design cause neither ultimate nor fatigue failure of the rotor blade, since the WT model and the rotor blade design are the same for both load simulations. Hence, with the flexible CFRP accumulators as designed here, and with the methodology for designing a FW system with these accumulators, a FW system can be implemented in a WT rotor. Although the previous work already indicated that a FW system could be installed in a rotor without causing failure in the blades, there was always the shortfall that the conventional steel accumulators must not be bent. Therefore, a mounting technology would have been required that attaches the accumulators the rotor blades, but that, at the same time, allows the rotor blade to bend around the accumulator without inflicting a bending moment on the accumulator. With the flexible CFRP accumulators this problem is solved. These accumulators can be laminated to the structure of the rotor blade. Hence, the accumulators bend with the rotor blade, which is no problem for these flexible CFRP accumulators.

7 Implementation of Flywheel System in OpenFAST

The general idea of the FW system is based on the variation of inertia of the rotor blades of a WT by moving a fluid mass between two accumulators in the rotor blade (see Figure 1). The physical description of such an energy storage system is introduced in previous work of the authors [22], [30].

The initial application of the FW system was developed to provide rapid controllable power to the power system [11], [23], [22]. Meanwhile the application of the FW system to control the oscillations of WT components has become one of the most important applications of that system, because of its possibilities in term of mitigating loads.

All the mechanical load simulations that have been done so far in this report or in the previous papers, considered the FW system from a static perspective, i.e. either the system fully charged or the system fully discharged. The dynamic behaviour of the FW system cannot be represented in the load simulations, without changing the source code of the load simulation tool, because state of the art simulation tools like Felx5 (<http://www.dtu.dk>), FAST (<https://nwtc.nrel.gov/FAST>), or Bladed [24] are not designed for simulating WTs with variable blade inertias.

Before discussing in detail the code adjustment to implement the dynamic behaviour of FW system it has to be decided, which load simulation tool should be selected, to perform the code adjustment.

Since OpenFAST is developed as an open-source WT simulation tool that is free, publicly available, and that is a well-documented software, this tool is used by thousands of WT designers, manufactures, consultants, certifiers, researchers, students, and educators all over the world [25]. Moreover, OpenFAST is intended to be a self-sustaining community developed software by working with OpenFAST on GitHub repository (<https://github.com/openfast/openfast>). It is the best mechanism for engaging with NREL OpenFAST team and other developers throughout the OpenFAST community. These advantages make it obvious to choose OpenFAST for implantation of the FW system. The only problem with OpenFAST is that a precompiled binaries ware was not available at the time, when the code adjustment took place. However, recompilation of the source-code should be done anyway, every time the code is adjusted. Since 13 November 2019 a precompiled binaries are available for Windows users only.

7.1 Installing and Testing of OpenFAST

There are multiple ways to obtain an OpenFAST executable. One of these ways is to build OpenFAST on Windows with Visual Studio (VS). Building OpenFAST on Windows with VS gives Windows developer a better option for developing code, compiling and debugging in a streamlined manner, due to the VS solution that OpenFAST maintains.

Guidelines for building OpenFAST from source code on Windows with VS are described online. Furthermore a complete procedure for configuration of the system and proceeding with the build process are documented in the OpenFAST documentation [26].

For building OpenFAST on Windows there are a list of prerequisites of software, of which not all are free-of-charge.

After successfully compiling OpenFAST, a regression tests and unit tests have been done for the glue code and for modules. The regression tests compare locally generated solutions to a set of baseline

solutions. The unit tests ensure that individual subroutines are functioning as intended. All test specifications are documented online (<https://openfast.readthedocs.io/en/master/source/testing/index.html>).

7.2 Architecture of OpenFAST

Understanding the architecture of OpenFAST is very important, before starting with code adjustments. Basically, the architecture of OpenFAST consists of a driver program (glue code) that couples individual modules together. The modules of OpenFAST (AeroDyn, HydroDyn, etc.) correspond to different physical domains of the coupled aero-hydro-servo-elastic solution (see Figure 75). Since the difference between the architecture of FAST v8 and OpenFAST is not so big, as well as the documentation transitioning from Fast v8 to OpenFAST is still in process, Figure 75 shows the architecture of FAST v8 only. Details on the transition from FAST v8 to OpenFAST and all organizational changes may be found in the following link (https://openfast.readthedocs.io/en/master/source/user/fast_to_openfast.html#fast-to-openfast).

7.3 Blade Structural-Dynamic Model

Users of FAST/OpenFAST have the option to choose between two blade structural-dynamic models. Whether ElastoDyn or BeamDyn is activated, this can be selected in the primary input file of FAST/OpenFAST. Figure 76 shows the interaction between ElastoDyn, BeamDyn and FAST/OpenFAST. The major difference between ElastoDyn and BeamDyn lies in the implementation of beam theory. The model underlying BeamDyn is the geometrically exact representation according to the beam theory (GEBT). This model supports full geometric nonlinearity and large deflection, with bending, torsion, shear, and extensional degree-of-freedom (DOFs); anisotropic composite material couplings (using full 6x6 mass and stiffness matrices, including bend-twist coupling); and a reference axis that permits blades that are not straight (supporting built-in curve, sweep, and sectional offsets) [26]. The model underlying ElastoDyn is the Bernoulli-Euler beam under bending, which supports beams with isotropic material, without mass or elastic offsets, without axial or torsional DOFs and without shear deformation [28].

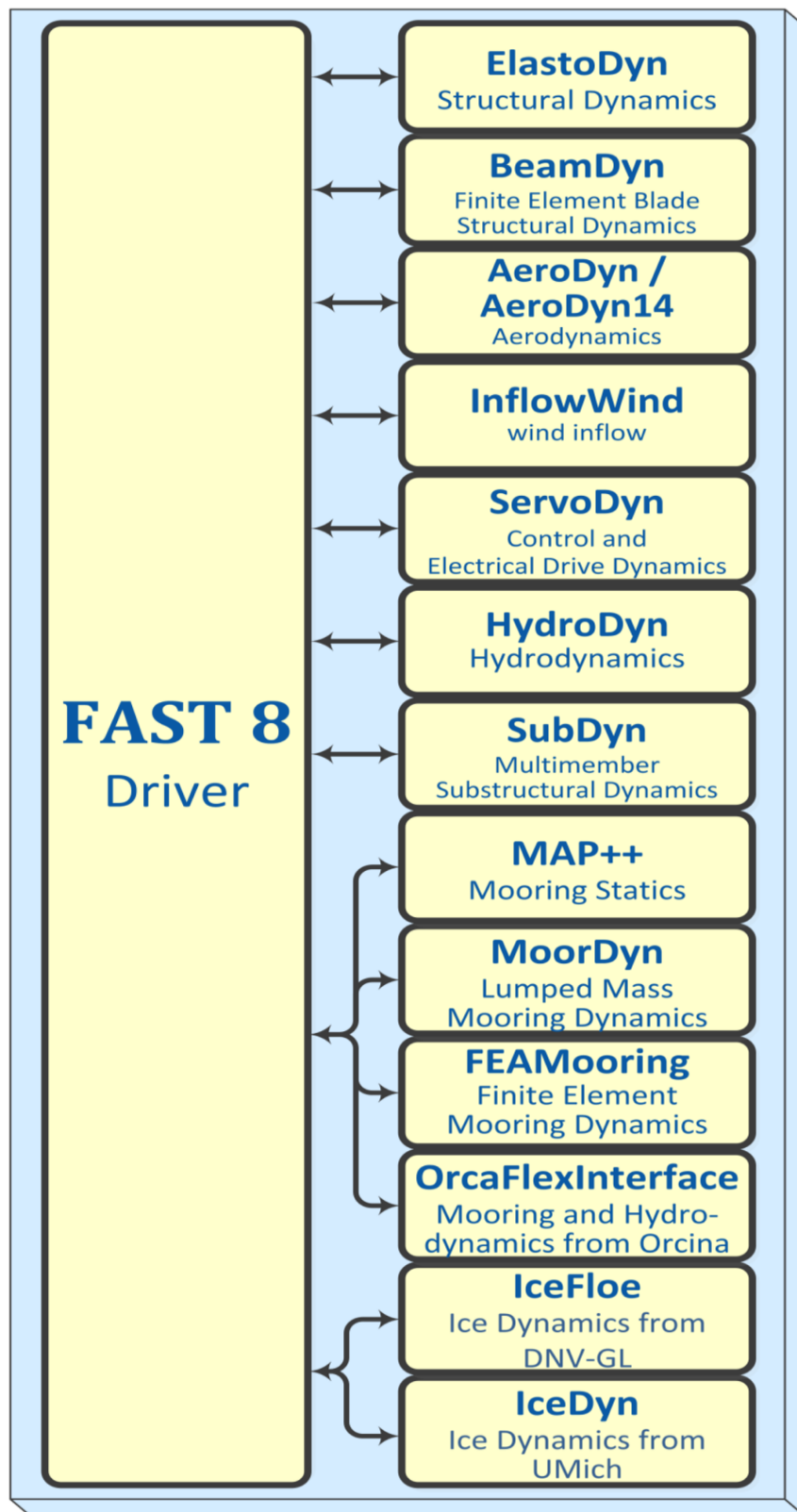


Figure 75 Architecture of FAST 8 [27]



Figure 76: Coupled interaction between BeamDyn, ElastoDyn and FAST [26]

This brief comparison (see Figure 77) helps in deciding whether the Implementation of FW system should be done in ElastoDyn or in BeamDyn. As a rule-of-thumb, code development of a software starts usually from simple to complex. Hence, it is obvious that the first code adjustment to implement the FW system will be done in ElastoDyn, because of the simplicity of this module in comparison to BeamDyn.

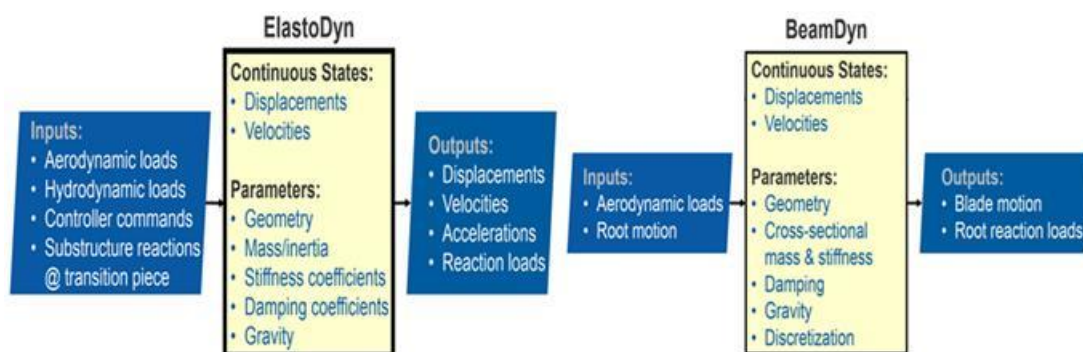


Figure 77: Inputs, Outputs, States and Parameters for ElastoDyn (left) and for BeamDyn (right) [27]

7.4 Module Structure of ElastoDyn

As ElastoDyn is a part of FAST framework, this module is formulated to fit the modules' template of FAST framework. This template standardizes the calculation procedure of the modules within the framework. Figure 78 shows the subroutines required for each operation in a sample module. By replacing the *ModName* text, for example to ED, the template will change to ElastoDyn Module. Other than replacing the *ModName*, the subroutine statements should not be modified in the template.

Template Requirements	Generated by Registry	Loose	Tight (Time Marching)	Tight (Linearization)
Initialize/End Subroutines				
• ModName_Init		✓	✓	✓
• ModName_End		✓	✓	✓
Time-Stepping Subroutines				
• ModName_UpdateStates		✓		
• ModName_CalcOutput		✓	✓	✓
• ModName_CalcContStateDeriv			✓	✓
• ModName_UpdateDiscState			✓	✓
• ModName_CalcConstrStateResidual			✓	✓
Jacobian Subroutines				
• ModName_JacobianPInput			✓	✓
• ModName_JacobianPContState				✓
• ModName_JacobianPDiscState				✓
• ModName_JacobianPConstrState			✓	✓
Input/Output Extrapolation/Interpolation Subroutines				
• ModName_Input_ExtrapInterp	✓	✓	✓	✓
• ModName_Output_ExtrapInterp	✓	✓	✓	✓
Pack/Unpack Subroutines				
• ModName_Pack	✓	✓	✓	✓
• ModName_Pack{TypeName*}	✓	✓	✓	✓
• ModName_Unpack	✓	✓	✓	✓
• ModName_Unpack{TypeName*}	✓	✓	✓	✓
Copy/Destroy Subroutines				
• ModName_Copy{TypeName*}	✓	✓	✓	✓
• ModName_Destroy{TypeName*}	✓	✓	✓	✓

Figure 78: Subroutines required for the FAST modular framework [29]

7.5 Data Types

Each of the subroutines listed in Figure 78 deals with specific data types. These data types are predefined in a separately compiled module named "*ModuleName_Types*" in order to avoid potentially circular build dependences. Figure 79 shows a list of derived data types that are operated in the subroutines in Figure 78.

Template Data Types	
Type Name	Purpose
<ul style="list-style-type: none"> • ModName_InitInputType 	Initialization input data
<ul style="list-style-type: none"> • ModName_InitOutputType 	Initialization output data
<ul style="list-style-type: none"> • ModName_InputType 	System inputs
<ul style="list-style-type: none"> • ModName_OutputType 	System outputs
<ul style="list-style-type: none"> • ModName_ParameterType 	System parameters
<ul style="list-style-type: none"> • ModName_ContinuousStateType 	Continuous states
<ul style="list-style-type: none"> • ModName_DiscreteStateType 	Discrete states
<ul style="list-style-type: none"> • ModName_ConstraintStateType 	Constraint states
<ul style="list-style-type: none"> • ModName_OtherStateType 	Other states
<ul style="list-style-type: none"> • ModName_PartialOutputPInputType 	Partial derivative of output equations with respect to inputs
<ul style="list-style-type: none"> • ModName_PartialContStatePInputType 	Partial derivative of continuous state equations with respect to inputs
<ul style="list-style-type: none"> • ModName_PartialDiscStatePInputType 	Partial derivative of discrete state equations with respect to inputs
<ul style="list-style-type: none"> • ModName_PartialConstrStatePInputType 	Partial derivative of constraint state equations with respect to inputs
<ul style="list-style-type: none"> • ModName_PartialOutputPContStateType 	Partial derivative of output equations with respect to continuous states
<ul style="list-style-type: none"> • ModName_PartialContStatePContStateType 	Partial derivative of continuous state equations with respect to continuous states
<ul style="list-style-type: none"> • ModName_PartialDiscStatePContStateType 	Partial derivative of discrete state equations with respect to continuous states
<ul style="list-style-type: none"> • ModName_PartialConstrStatePContStateType 	Partial derivative of constraint state equations with respect to continuous states
<ul style="list-style-type: none"> • ModName_PartialOutputPDiscStateType 	Partial derivative of output equations with respect to discrete state
<ul style="list-style-type: none"> • ModName_PartialContStatePDiscStateType 	Partial derivative of continuous state equations with respect to discrete states
<ul style="list-style-type: none"> • ModName_PartialDiscStatePDiscStateType 	Partial derivative of discrete state equations with respect to discrete states
<ul style="list-style-type: none"> • ModName_PartialConstrStatePDiscStateType 	Partial derivative of constraint state equations with respect to discrete states
<ul style="list-style-type: none"> • ModName_PartialOutputPConstrStateType 	Partial derivative of output equations with respect to constraint states
<ul style="list-style-type: none"> • ModName_PartialContStatePConstrStateType 	Partial derivative of continuous state equations with respect to constraint states
<ul style="list-style-type: none"> • ModName_PartialDiscStatePConstrStateType 	Partial derivative of discrete state equations with respect to constraint states
<ul style="list-style-type: none"> • ModName_PartialConstrStatePConstrStateType 	Partial derivative of constraint state equations with respect to constraint states

Figure 79: Derived data types required for the FAST modular framework [29]

The derived in *ModuleName_Types* are generated automatically using the FAST Registry module, which is a separate module written in C and supported from National Wind Technology Center (NWTC). Other than the data in *ModuleName_Types*, variables defined as local subroutines that do not retain their values between subroutine calls do not need to be stored in one of these data types. The definition and the storage of data types in the FAST framework should be well understood before starting with adding and overwriting of variable in subroutines.

7.6 ElastoDyn Source Code

Source code is much easier to understand and to adjust when it is converted into a body text. The body text includes the subroutines in the form of headlines. This transformation helps code developers to get a better overall view of the code impact, and simplified the tracing of subroutines in the whole code. Figure 80 shows ElastoDyn source code translated into body text in Word format. The subroutines are copied from the source code and pasted in the Word document as headings. Moving between subroutines can easily and quickly be done by using the key combination “Ctrl+Left click”. This procedure helps to exclude the subroutines where the code adjustment should be done.



Figure 80: Schematic body text diagram of ElastoDyn source code

7.7 Code Adjustment

Since the general idea of the FW system is based on the variation of inertia of the rotor blades during the operating cycle of WTs, the code adjustment should enable ElastoDyn/OpenFAST to change the blade properties dynamically within a given simulation. The mechanical blade properties like mass, stiffness and natural frequency are stored in the blade input file of ElastoDyn. Figure 81 shows for example the blade Input file of NRELOffshrBsline5 MW_Blade.dat, where *BMassDen*, *FlpStff*, *EdStff*, *BldFl1Sh*, *BldFl2Sh* and *BldEdgSh* are the blade mass density, blade flap stiffness, blade edge stiffness, Blade-flap-mode-1 shape coefficients, Blade-flap-mode-2 shape coefficients and Blade-edge-mode shape coefficients, respectively. The blade input file, which is represented in this study, is based on the 61.5 m blade reference model of Brian R. Resor [10]. Deriving the blade data of the 61.5 m Resor's model is already represented in a previous section (see section 6.2.4.1).

```
----- ELASTODYN V1.00.* INDIVIDUAL BLADE INPUT FILE -----
NREL 5.0 MW offshore baseline blade input properties.
----- BLADE PARAMETERS -----
      49  NBlInpSt  - Number of blade input stations (-)
0.477465 BldFlDmp(1) - Blade flap mode #1 structural damping in percent of critical (%)
0.477465 BldFlDmp(2) - Blade flap mode #2 structural damping in percent of critical (%)
0.477465 BldEdDmp(1) - Blade edge mode #1 structural damping in percent of critical (%)
----- BLADE ADJUSTMENT FACTORS -----
      1  FlStTunr(1) - Blade flapwise modal stiffness tuner, 1st mode (-)
      1  FlStTunr(2) - Blade flapwise modal stiffness tuner, 2nd mode (-)
1.04536 AdjBlMs  - Factor to adjust blade mass density (-)
      1  AdjFlSt  - Factor to adjust blade flap stiffness (-)
      1  AdjEdSt  - Factor to adjust blade edge stiffness (-)
----- DISTRIBUTED BLADE PROPERTIES -----
      BlFract      PitchAxis      StrcTwst      BMassDen      FlpStff      EdgStff
      (-)          (-)          (deg)        (kg/m)        (Nm^2)        (Nm^2)
0.0000000E+00    2.5000000E-01    1.3308000E+01    6.7893500E+02    1.8110000E+10    1.8113600E+10
3.2500000E-03    2.5000000E-01    1.3308000E+01    6.7893500E+02    1.8110000E+10    1.8113600E+10
1.9510000E-02    2.5049000E-01    1.3308000E+01    7.7336300E+02    1.9424900E+10    1.9558600E+10
3.5770000E-02    2.5490000E-01    1.3308000E+01    7.4055000E+02    1.7455900E+10    1.9497800E+10
5.2030000E-02    2.6716000E-01    1.3308000E+01    7.4004200E+02    1.5287400E+10    1.9788800E+10
6.8290000E-02    2.7941000E-01    1.3308000E+01    5.9249600E+02    1.0782400E+10    1.4858500E+10
8.4550000E-02    2.9167000E-01    1.3308000E+01    4.5027500E+02    7.2297200E+09    1.0220600E+10
.              .              .              .              .              .
.              .              .              .              .              .
.              .              .              .              .              .
.              .              .              .              .              .
9.9512000E-01    3.7500000E-01    2.3000000E-02    1.1453000E+01    2.5000000E+05    6.6100000E+06
1.0000000E+00    3.7500000E-01    0.0000000E+00    1.0319000E+01    1.7000000E+05    5.0100000E+06
----- BLADE MODE SHAPES -----
      0.0622  BldFl1Sh(2) - Flap mode 1, coeff of x^2
      1.7254  BldFl1Sh(3) - , coeff of x^3
     -3.2452  BldFl1Sh(4) - , coeff of x^4
      4.7131  BldFl1Sh(5) - , coeff of x^5
     -2.2555  BldFl1Sh(6) - , coeff of x^6
     -0.5809  BldFl2Sh(2) - Flap mode 2, coeff of x^2
      1.2067  BldFl2Sh(3) - , coeff of x^3
    -15.5349  BldFl2Sh(4) - , coeff of x^4
     29.7347  BldFl2Sh(5) - , coeff of x^5
    -13.8255  BldFl2Sh(6) - , coeff of x^6
      0.3627  BldEdgSh(2) - Edge mode 1, coeff of x^2
      2.5337  BldEdgSh(3) - , coeff of x^3
     -3.5772  BldEdgSh(4) - , coeff of x^4
      2.376   BldEdgSh(5) - , coeff of x^5
     -0.6952  BldEdgSh(6) - , coeff of x^6
```

Figure 81: An example for blade input file of NRELOffshrBsline5 MW_Blade.dat

7.7.1 Implementation of Variable Blade Element Mass

As a part of implementation of variable blade properties the code adjustment will focus in this study on changes of the blade element masses only. The implementation of variable blade element masses should help in the future to change the rest of the blade mechanical properties, i.e. blade element stiffnesses and blade natural frequencies.

The main challenge facing the implementation of variable blade element masses is that the input values of the blade input file are used to define variables, which are stored as constant (time-invariant) parameters in the source code of ElastoDyn.f90. These parameters are only called once by ElastoDyn at initialisation, and destroyed after that. Moreover, FAST/OpenFAST does not allow parameter data type (*p%*) to be changed after initialisation. These two challenges can be circumvented as follows:

_Step 1: At first, the implementation of the blade mass density *BMasssDen* specified in the ElastoDyn input file must be observed in the source code of ElastoDyn. For this purpose, a body text diagram of ElastoDyn source code can be very helpful for tracking the implementation of *BMasssDen* in the entire source code. A body text diagram of ElastoDyn is already presented in a previous section (see section 7.6). *SUBROUTINE Coeff()* in ElastoDyn.f90 is used to calculate the blade element masses *p%BEImenMass(J,K)*, where *J* and *K* are the blade nodes and the blade number, respectively. The calculation of *p%BEImenMass(J,K)* in *SUBROUTINE Coeff()* is based on the specified distributed blade mass densities in the blade input file.

_Step 2: Before making any changes to any parameter it is mandatory to check whether this parameter is used in the time-domain part of the simulation. Parameters that are used in the time-domain part of the simulation can be changed dynamically within the simulation time. Since *SUBROUTINE Coeff()* is called only once by *SUBROUTINE ED_Init()* at the initialisation of ElastoDyn, all parameters of *SUBROUTINE Coeff()* hold their value unchanged within the whole simulation, and they are not called in the time-domain part of the simulation. Hence, parameters of *SUBROUTINE Coeff()* do not have the advantageous to change dynamically within the simulation time.

_Step 3: add, remove, or change the order or the statement of any subroutine arguments in the template module is not permitted in FAST/OpenFAST [29]. Hence, it is not possible to add a time dimension to the *SUBROUTINE Coeff()* argument to enable this subroutine to be called in the time-domain calculation. Moreover, *SUBROUTINE Coeff()* depends on data stored in the ElastoDyn input file (*InputFileData%*) which are destroyed after initialisation in *SUBROUTINE ED_Ini()*. For these two reasons, the only one option left to change the blade element masses dynamically within a given simulation is to add a new independent subroutine, which allows to dynamically access those parameters that are defined as time-independent.

_Step 3: *SUBROUTINE UpdateCoeff()* is a new independent subroutine, which is added to the ElastoDyn source code. It is a very similar copy of *SUBROUTINE Coeff()* with very small differences. *SUBROUTINE UpdateCoeff()* does not use the input file data type (*InputFileData%*). The data that *SUBROUTINE UpdateCoeff()* needs from the ElastoDyn input file are overwritten in a parameter data type (*p%*) and stored in *SUBROUTINE Coeff()*. This enables *SUBROUTINE UpdateCoeff()* to be called at any simulation step.

All subroutines in `ElastoDyn.f90` are *PRIVATE* by default. In order to enable *SUBROUTINE UpdateCoeff()* to be called in the time-domain the following must be typed in the top section of `ElastoDyn.f90` before the *CONTAINS* statement:

```
PUBLIC :: UpdateCoeff()
```

_Step 4: After adding *SUBROUTINE UpdateCoeff()* to the source code of `ElastoDyn` blade element masses can be changed in the same way as for the time-depended variable. *Subroutine ED_CalcOutput()* is used to compute the output channels (motions and loads) and place them in the *WriteOutput()* array. Hence, this subroutine can be used to change the blade element mass parameter *p%BEIlnMass*. After that *SUBROUTINE UpdateCoeff()* can be called to update all parameters that related to blade element mass parameter.

_Step 5: After every source code adjustment `FAST/OpenFAST` must be compiled and tested in order to check if the changes of the source code are recognised and accepted by `FAST/OpenFAST` modules. Hence, the `ElastoDyn` input file is expanded to integrate extra input channels, in order to vary the blade element masses without changing the source code. With this procedure the source code should not be adjusted by every change of the blade element masses, and `OpenFAST` should not be compiled.

To define a new input channel in `ElastoDyn` input file two issues must be considered. The new channel must be integrated in the registry input file `ElastoDyn_Registry.txt` on the one hand, and, on the other hand, the location of the new channel in the allocate array *AllocAry* must respect the allocate sequence of `ElastoDyn` input channels in `ElastoDyn_IO.f90` file.

_Step 6: in order to plot the changes of blade element masses a new output channel is integrated in `ElastoDyn_Registry.txt` file in the same way as for the new input channel in step 5. Moreover, the new output channel should be listed with a name, a brief description of its function, convention, and unit in the `OutListParameters.xlsx` file.

While `OutListParameters.xlsx` file includes only the standard available output channels of each module in `FAST/OpenFAST`, the new output channels allow getting more information about the signals that the software developer needs (e.g. the blade element masses).

7.7.2 Criteria for Changing Blade Element Masses

Choosing the criteria for changing the blade element masses depends on the functionality of the FW system that should be applied to influence the WT operation. Since the main functionality of the FW system discussed in this report is to reduce the mechanical loads of WTs, the criteria that are chosen here should serve this purpose.

In this section two criteria for changing the blade element masses are represented. These two criteria should help latterly the developer of WTs controls to develop a control algorithm for the FW system.

_Local signal criterion: The local signal criterion uses signals that are computed within `ElastoDyn` module to control the masse addition.

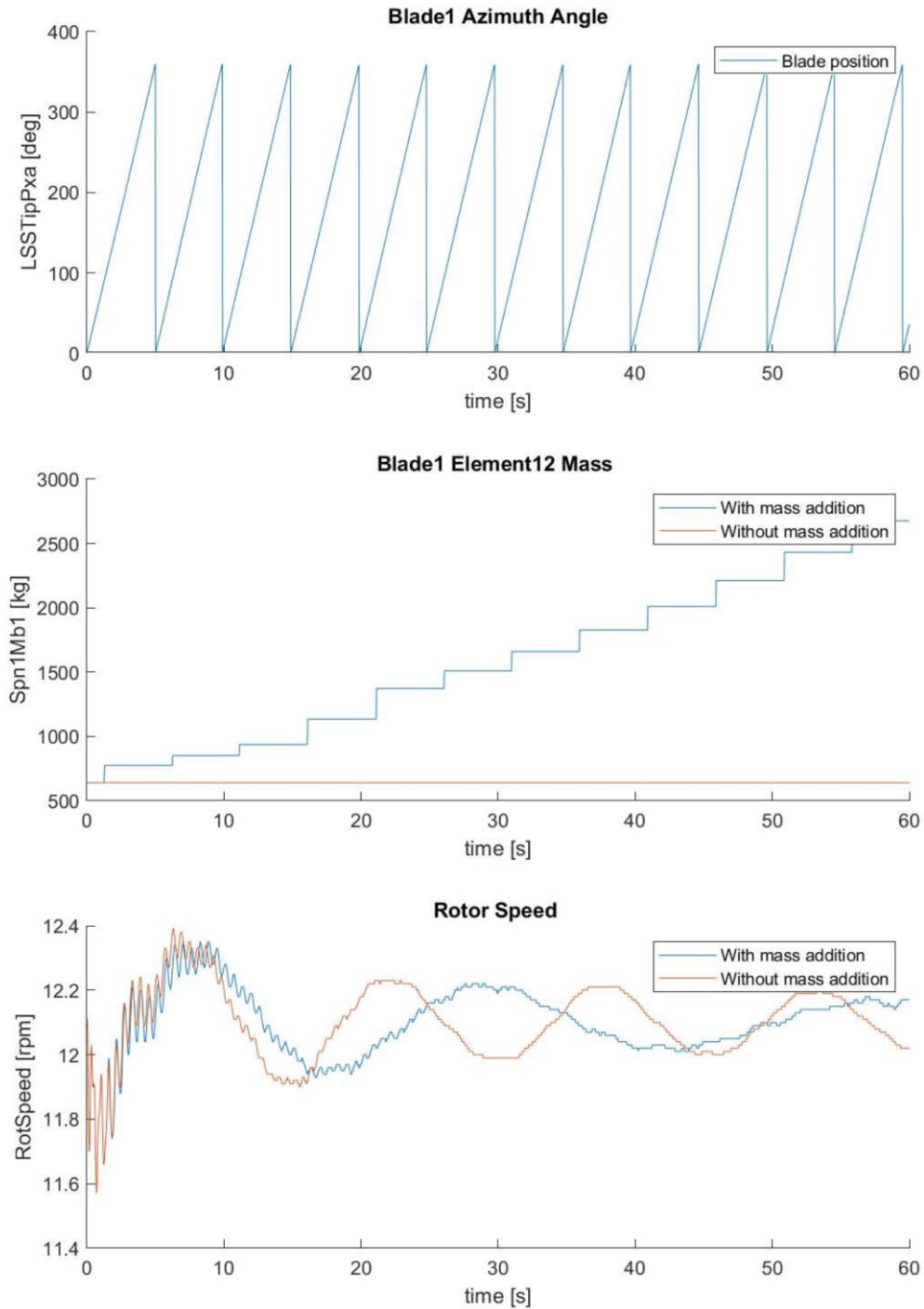


Figure 82: Blade element mass addition via the local signal criterion

Initially, the control algorithm for the FW system is based on a lot of different scenarios. Among these scenarios is the effect of the gravitational force on the charge/discharge status of the piston accumulator, which is close to the blade tip. This force is calculated depending on the blade position. Although, the blade position is a signal that is computed in AeroDyn module, the blade azimuth *BAzimuth* can be computed depending on the rotor azimuth angle (position) *LSSTipPxa* from ElastoDyn. Where the azimuth angle of blade 1 *B1Azimuth* equals the *LSSTipPxa*, the azimuth angle of blade 2 and 3 equal *LSSTipPxa* + 120 degree and *LSSTipPxa* + 240 degree, respectively.

Figure 82 shows an example for changing the blade element masses dynamically within a given simulation using the local signal criterion. In this example the mass of element 12 of blade 1 (*Spn1Mb1*) is multiplied with a factor of 1.5 when the position of blade 1 (*LSSTipPxa*) is about 90 degree. To illustrate the response of the WT on the mass addition Figure 82 shows a comparison of rotor speed (*RotSpeed*) with mass addition (in blue) and without mass addition (in red). The comparison presents that the oscillation period of rotor speed with mass addition is clearly higher than the one without mass addition, and this is due to the effect of increasing the rotor inertia.

_External signal criterion: the external signal criterion uses signals from ServoDyn Module, i.e. from outside of the ElastoDyn module to control the mass addition.

As mentioned above, in order to design a control algorithm for the FW system, control methods must be developed and linked to the FAST/OpenFAST framework. Five basic methods of control are available in FAST/OpenFAST framework: pitching the blades, controlling the generator torque, applying the high speed shaft brake, deploying the tip brakes, and yawing the nacelle. Other methods of control that are more complicated (e.g. to control the FW system) can either be written, compiled, and linked with the rest of the program. Or they can be implemented in a Simulink model via an S-Function, which can interface FAST/OpenFAST with control models that are implemented in Simulink.

For getting started with interfacing OpenFAST with these both control methods, the external signal criterion gives an overview of the interaction between ElastoDyn and ServoDyn, where ServoDyn is FAST's controls and electrical drive module. This criterion helps to understand how signals can be exported and performed between those two modules.

Signals are transferred between FAST modules via *FAST_Solver.f90*. This file is a part of the FAST driver program (glue code), which enables aero-elastic-servo interaction between FAST modules at each coupling time step. *Subroutine ED_InputSolve()* in *FAST_Solver.f90* file sets the input parameters that are required by ElastoDyn module. After the definition of the new output channel in ServoDyn and the corresponding input channel in ElastoDyn the signals can be coupled in *Subroutine ED_InputSolve()*.

The following example uses blade pitch angle *BIPitchED* from ServoDyn module to change the blade element masses in ElastoDyn model. This example illustrates the function of the external signal criterion. *y%BIPitchEd* is the new defined pitch angle output channel in ServoDyn and *u%BIPitchEd* is the corresponding pitch angle input channel in ElastoDyn. Figure 83 shows an extreme case of increasing the blade element mass when the pitch angle is between 10 and 12 degree. The purpose of such extreme scenario is to check the response of the WT in case of unrealistic increase of the blade mass. As Figure 83 shows, the computing of rotor speed breaks after circa 3 seconds when the blade element mass signal reaches a very high value.

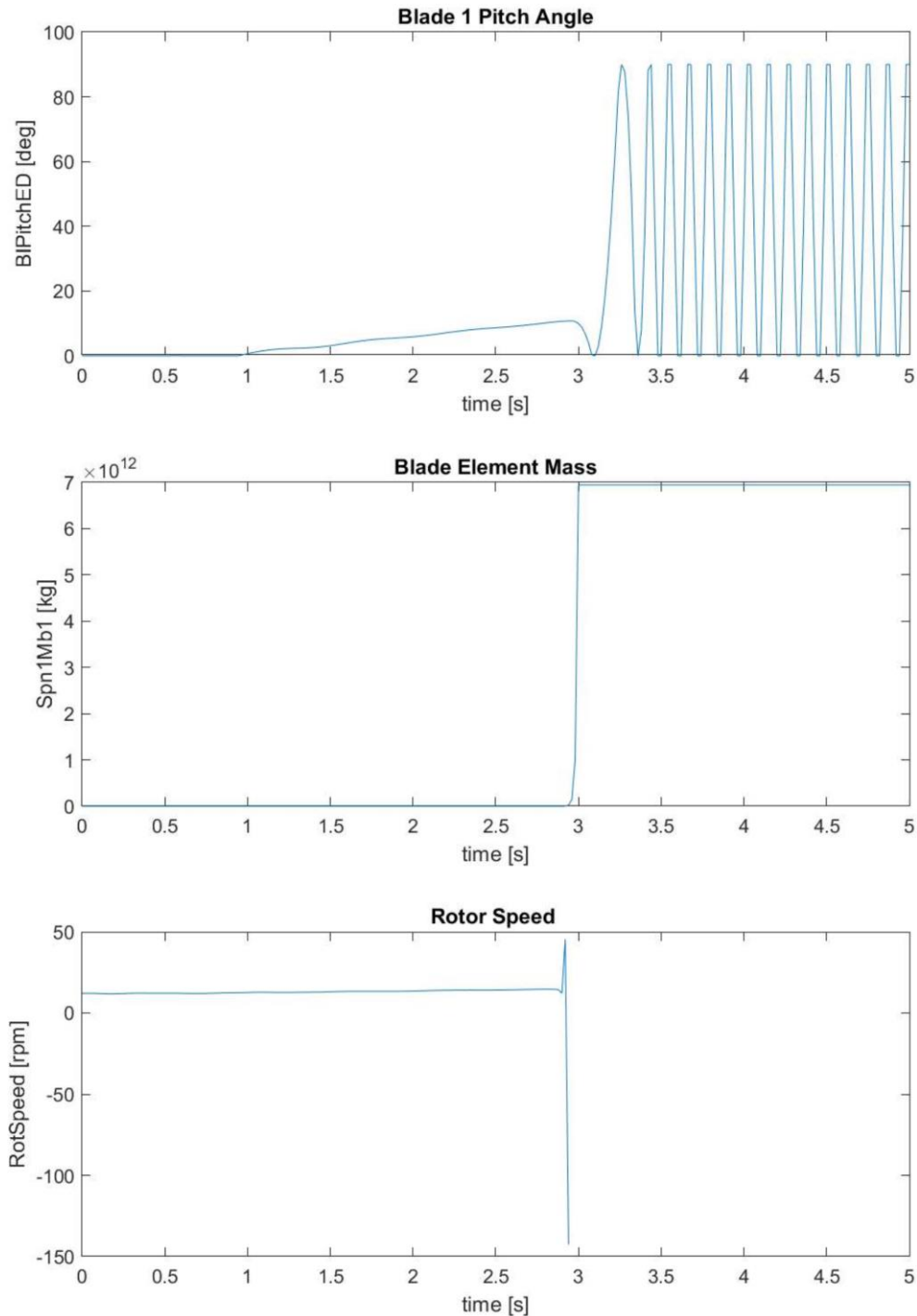


Figure 83: Extreme blade element mass addition via the external signal criterion

7.7.3 Extension of ElastoDyn Input File

In order to give the user of OpenFAST more options to change the mass addition of blade elements, the previous criteria for changing blade element masses are implemented in ElastoDyn Input file. This allows the user to choose between different options of computing the mass addition. For example with the extension of ElastoDyn the user can select the pitch and blade position ranges, the blade and the element number, and the factor with which the blade element mass is multiplied (see Figure 84). This extension helps also the code developer to save time by testing different scenarios of changing the masses, with no need to recompile the whole code.

```
----- ELASTODYN v1.03.* INPUT FILE -----
NREL 5.0 MW Baseline Wind Turbine for Use in Offshore Analysis. Properties from Dutch Offshore Wind Energy
----- SIMULATION CONTROL -----
----- MASS AND INERTIA -----
.
.
.
1  CompAddMass - Compute additional mass (switch) {0=None; 1=Blade position;
                2=Pitch angle; 3=Blade position + Pitch angle}
90  BlAziMax   - Blade position upper limet to proceed the mass addition (deg)
89  BlAziMin   - Blade position lower limet to proceed the mass addition (deg)
10  PitchMax   - Pitch angle upper limet to proceed the mass addition (deg)
11  pitchMin   - Pitch angle lower limet to proceed the mass addition (deg)
1.01 AddMassF  - Faktor to multiply by the blade element masses (-)
----- BLADE -----
17  BldNodes   - Number of blade nodes (per blade) used for analysis (-)
.
.
.
----- OUTPUT -----
.
.
.
1  BlAdM       - Number of blade that have mass addition [0 to 3] (-)
2  BldAdM      - List of blade nodes that have mass addition [1 to NumBl] (-) [unused if BlAdM=0]
1  NBlAdM      - Number of blade nodes that have mass addition [0 to 9] (-)
12  BldAdMNd   - List of blade nodes that have mass addition [1 to BldNodes] (-) [unused if NBlAdM=0]
OutList        - The next line(s) contains a list of output parameters. See OutListParameters.xlsx f
"SpnlMb1"      - Blade element mass (kg)
END of input file (the word "END" must appear in the first 3 columns of this last OutList line)
-----
```

Figure 84: Example for an extended ElastoDyn input file

8 Economical Evaluation of the Hydro Pneumatic Flywheel in a Wind Turbine Rotor for the Application of Steady Power Feed-in

8.1 Purpose of this Chapter

Since the beginning of electrification in the western world, more than hundred years ago, a centrally structured power grid with increasing coverage was built. Much development work is still aimed at ensuring a stable power grid, mainly based on large coal and nuclear power plants. In about the last decade, a new political agenda pushed the expansion of renewable energies, especially wind energy. In addition to a positive environmental assessment, the engineers also found new problems in the electricity grid. [30]

If there are differences between generation and consumption in an AC system, the grid frequency may fall to a lower level below 50 or 60 Hz. Conventional power plants usually react very slowly to these changes, so they can easily compensate it. An increasing share of wind power plants on the other hand, is causing a destabilization of the grid frequency. For this reason, WT generators are usually connected to the grid via frequency converters. The rotating masses are decoupled from the grid and the frequency does not depend on the rotating speed. Therefore, there is a demand for new state-of-the-art variable speed WTs that can replace the inertia of conventional power plants. If the frequency inverter is controlled in a reasonable way, the kinetic energy stored in the rotating drive train of the WT can support the power grid. This technique is called synthetic inertia. The synthetic inertia can keep the grid frequency at a stable level, but unfortunately it puts the WT in suboptimal operating states. These operating states cause that the WT runs uneconomically in certain situations. [30]

In the research project at hand the FW system is applied to increase the energy yield of the WT. The underlying idea is that around full load operation the power sometimes dips below rated power, while at other times there is excess power available. Hence, the FW is charged at times of excess power and it is discharged when the power in the wind dips below rated power.

8.2 Reference Wind Turbine, NREL 5-MW

A representative WT such as the reference WT NREL 5-MW is necessary to obtain a brand-independent database in order to get reliable data from the simulation of the FW storage system.

This WT replicates typical land- and sea-based multimegawatt turbines, with a rated power of 5 MW. The WT characteristics relate to the largest prototypes of its time (2009), i.e. the Multibrid M5000 and REpower 5M. Most specifications of the REpower 5M machine were used for this reference model because they are considered reliable and conventional. [17]

The U.S. Department of Energy (DOE) has published a cost study based on a rotor diameter of 128 m (compare with Figure 85). These values represents a typical 5 to 6 MW system. In addition, different organisations like Wind Partnerships for Advanced Component Technology (WindPACT), Recommendations for Design of Offshore Wind Turbines (RECOFF) and Dutch Offshore Wind Energy Converter (DOWEC) have published studies and conceptual design calculations on WT with a 5 to 6 MW rating. [17]

Rating	5 MW
Rotor Orientation, Configuration	Upwind, 3 Blades
Control	Variable Speed, Collective Pitch
Drivetrain	High Speed, Multiple-Stage Gearbox
Rotor, Hub Diameter	126 m, 3 m
Hub Height	90 m
Cut-In, Rated, Cut-Out Wind Speed	3 m/s, 11.4 m/s, 25 m/s
Cut-In, Rated Rotor Speed	6.9 rpm, 12.1 rpm
Rated Tip Speed	80 m/s
Overhang, Shaft Tilt, Precone	5 m, 5°, 2.5°
Rotor Mass	110,000 kg
Nacelle Mass	240,000 kg
Tower Mass	347,460 kg
Coordinate Location of Overall CM	(-0.2 m, 0.0 m, 64.0 m)

Figure 85: Properties NREL 5-MW [17]

8.3 Choice of Location

Choosing the right location for a WT is a key factor for profitability:

The more obstacles such as buildings or natural vegetation block the airflow, the greater the turbulence intensity (see chapter 8.9.4). In coastal areas there is a less impact on wind due to obstacles than in mountainous regions. As the turbulence intensity decreases at higher altitudes, many manufacturers of WTs developed ever higher turbines [31]. Therefore, a suitable location is the German North Sea coast.

In addition to a good location selection, a correct WT design is also very important. For this purpose, the reference WT NREL 5-MW was selected which is designed for coastal areas and offshore use. [17]

8.4 System Description

The idea of this proposed FW system is to integrate hydraulic fluid as weights inside the rotor blades of a WT. All components of the FW system are built-in in the rotor blade. It consists of a fluid tank near the blade root connected by a hydraulic tube to a piston accumulator near the blade tip. [30]

Valves, installed at the input of the accumulators, can be closed to prevent the fluid from flowing or opened to keep the system at a variable inertia. It is also possible to control the speed of flow in both directions. [30]

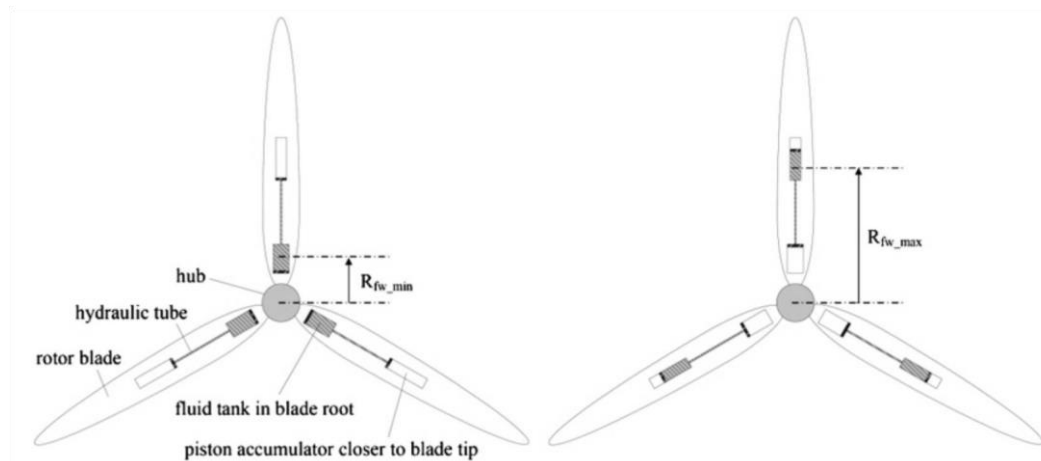


Figure 86: Hydraulic–pneumatic FW system in a WT rotor. Discharged state (left) and charged state (right) [30]

In order to obtain a simple and safe operation, it is necessary to use a hydraulic fluid with special properties:

To save volume inside the hydraulic system it is important to use a fluid with the highest possible density. Furthermore, in order to avoid pollution in case of leaks, the fluid must be environmentally friendly. A frost protection additive is very important to use the system over a wide range of temperatures. The accumulators, made of glass fiber or carbon fiber composites and a very slim design, ensure a low profile to keep the interference effect on the aerodynamic efficiency low. [30]

The purpose of this FW system is to control and regulate the kinetic energy, E_{kin} , by varying the mass moment of inertia, J , and thus the angular speed, ω is held constant. [30]

$$E_{kin} = \frac{1}{2} \cdot J \cdot \omega^2 \quad \text{Equation 69}$$

The mass inertia J depends on a mass m , which is rotating in a certain distance, r , from the centre of rotation. [30]

$$J = m \cdot r^2 \quad \text{Equation 70}$$

By controlling J of the rotor, which all rotating components in a WT depend on, it is possible to contribute to power system frequency stability. The mass m is the only variable (see Equation 70), which is able to change its location, r . [30]

8.5 Working Principle

The general working principle of a hydraulic-pneumatic FW will be described in this section:

There are two states of the FW system, discharged and charged. In the discharged state (see left Figure 86), the WT rotates with e.g. rated rotor speed, ω_{rated} , and the valves, installed at each tank, prevent the fluid from flowing towards the piston accumulator. [30]

Emptying the fluid tanks, installed at the blade roots, by centrifugal forces, gravitational forces and hydraulic pumps, the inertia increases and the system reaches the charged state. In order to push the

hydraulic fluid from the tanks to the piston accumulators, it is necessary to have excess power for driving the hydraulic pumps.

The aforementioned forces and the hydraulic pumps push the hydraulic fluid from the tanks in blade root to the piston accumulators closer to the blade tip, where nitrogen in the accumulator gets compressed. In addition, the valves must be controlled in such a way that a constant volume flow is maintained in all three blades to avoid damage caused by rotor imbalances, unless asymmetric operation is specifically desired.

The maximum of inertia and stored kinetic energy is achieved with a maximum radius R_{fw_max} . Consequently, the minimum is reached at R_{fw_min} (see Figure 86). [30]

J_{fw} , the inertia of the FW, depends on two variables: On the one hand, there is the mass of the fluid in the tanks, m_{fluid_Tank} , on the other hand the variable distance R_{var} (see section 8.8) between the centre of gravity of the weights and the centre of rotation. This inertia of a three bladed WT is described by (Equation 71). [30]

$$J_{fw} = 3 \cdot m_{fluid_Tank} \cdot R_{var}^2 \quad \text{Equation 71}$$

If the inertia of the FW increases at constant rotational speed, it causes an increasing angular momentum L [30]

$$L = J_{fw} \cdot \omega_{rot} \quad \text{Equation 72}$$

This angular momentum L results in a torque of the FW, T_{fw} [30]

$$T_{fw} = \frac{dL}{dt} = \frac{dJ_{fw}}{dt} \cdot \omega_{rot} \quad \text{Equation 73}$$

On the low-speed shaft of the turbine there is a torque, T_{lss} , caused by the torque of the FW and the rotation torque of the rotor. As a result, there is a superimposing along with the rotation torque T_{rot} . [30]

$$T_{lss} = T_{rot} + T_{fw} \quad \text{Equation 74}$$

If the grid frequency is to be kept at a constant level or a sudden increase in it is to be prevented, the electrical power output must be reduced.

This is achieved by increasing the inertia and storing kinetic energy, which slows down the rotor. [30]

Furthermore, if there is more power in the wind, this additional power can be used for charging the energy storage or it can feed into the grid. [30]

In the case of dropping grid frequency, the valves have to be opened to release the stored kinetic energy by emptying the accumulators. The inertia of the rotor is reduced by the flooding of the tanks near the rotation centre through the expanding nitrogen in the accumulators. The decreasing inertia therefore leads to an increasing torque and thus to an increase in electrical power. This additional power helps to mitigate the decline in grid frequency. [30]

8.6 Advantages and Disadvantages of the Proposed FW System

In relation to this work the biggest advantage that can be expected is that the use of the FW system generates an additional energy yield that ideally shortens the payback period of the WT.

In other previous works the advantage of mechanical load mitigation and contribution to the power system inertia was discussed. The FW system avoids operating points that affect the stability of the rotor or the drive train; on the other hand, the grid frequency can be supported [23]. To avoid these critical situations, a conventional wind plant slows down or shuts down completely which can significantly reduce the energy yield of the system.

A major disadvantage is that the FW system cannot be used in every situation. In order to gain enough kinetic energy from the wind, the wind speeds and the turbulence behaviour of the wind must be suitable (see simulation results in section 8.10).

Furthermore, the costs for a WT with installed FW system increase and there are higher maintenance costs, which, at the moment, cannot be quantified.

8.7 Model in SIMULINK

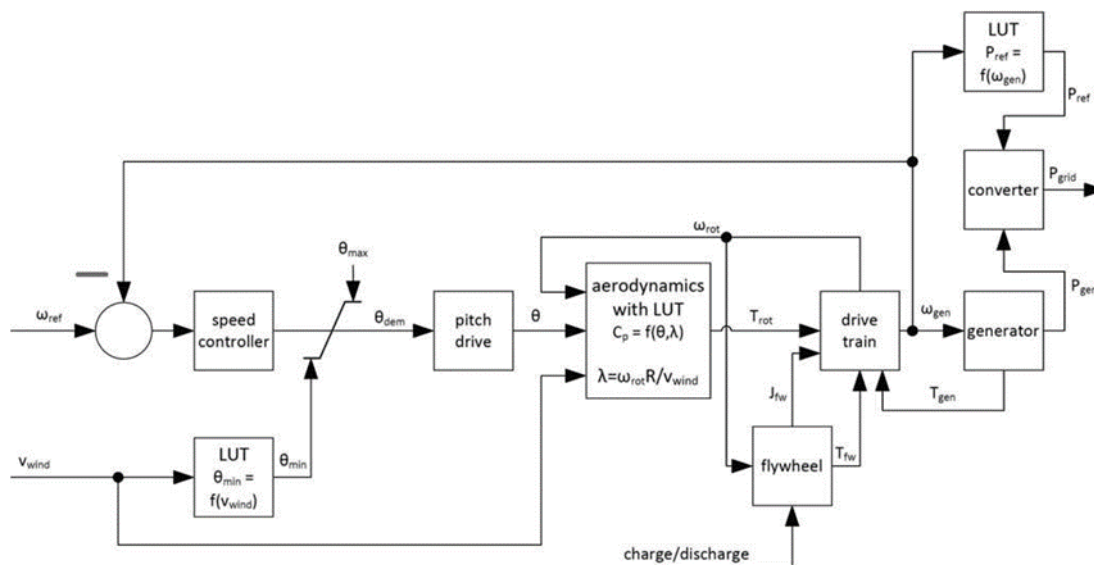


Figure 87: Block diagram of the WT model

The NREL 5-MW WT (see section 8.2) serves as the basis for the discussed model. Figure 87 shows a model implemented in MATLAB/SIMULINK. The general structure of the block diagram is conventional and resembles a standard system, but it has been extended by the block "FW". [30]

This block diagram is only intended to provide an overview, since the following chapters mainly refer to the FW system.

8.8 Simulated Variables

In order to assess the economic viability of the presented FW system, it is not enough to look only at the output power P_{gen} . The processes that run during operation are easier to explain by comparing many interdependent variables. According to this, it helps to explain possible disturbances or discontinuities.

The simulation produces a large number of variables when simulating the FW system. For simplicity, only the variables presented in this chapter will be discussed here. The following is an explanation of the scenarios to be simulated. [1]

Power output – P_{TR}

The power output P_{TR} of the transformer is the most important variable to estimate the cost-effectiveness of the FW system. Unlike P_{TR} , P_{gen} shows the currently produced power without transformer losses and time delay. [1]

Wind speed – v_{wind}

With regard to the offshore suitability of the NREL-5 MW, two average wind speeds are selected for the simulation: 10 m/s (part load operation) and 20 m/s (full load operation). These average wind speeds represent locations at the German North Sea coast. With increasing hub height, or with higher wind speeds, variations in the wind speed decrease. [31]

Speed on the low-speed shaft – $\text{speed}_{\text{rot}}$

Fluctuations in the wind, the pitch adjustment and the state of charge of the piston accumulators continuously cause changes in speed. The speed of the low-speed shaft, $\text{speed}_{\text{rot}}$, is directly related to the power P_{gen} . [30]

Pitch angle - θ

For large WT s of the multi-megawatt class an active pitch control system is used. By turning the rotor blade, the flow conditions are influenced, so that the forces acting on the rotor blade can be controlled. Above rated wind v_{rated} and below the cut-out wind $v_{\text{cut_out}}$ the power generation of the rotor can be kept constant (see Figure 88) [32].

Above $v_{\text{cut_out}}$, i.e. in a windstorm with high wind speed fluctuations, the rotor blade can be placed in vane position designated *pitch to feather* to prevent damages to the WT. [31]

Figure 88 shows that the rotor speed always maintains a constant value with increasing wind speed. A larger pitch angle therefore produces more and more drag to slow down the rotor.

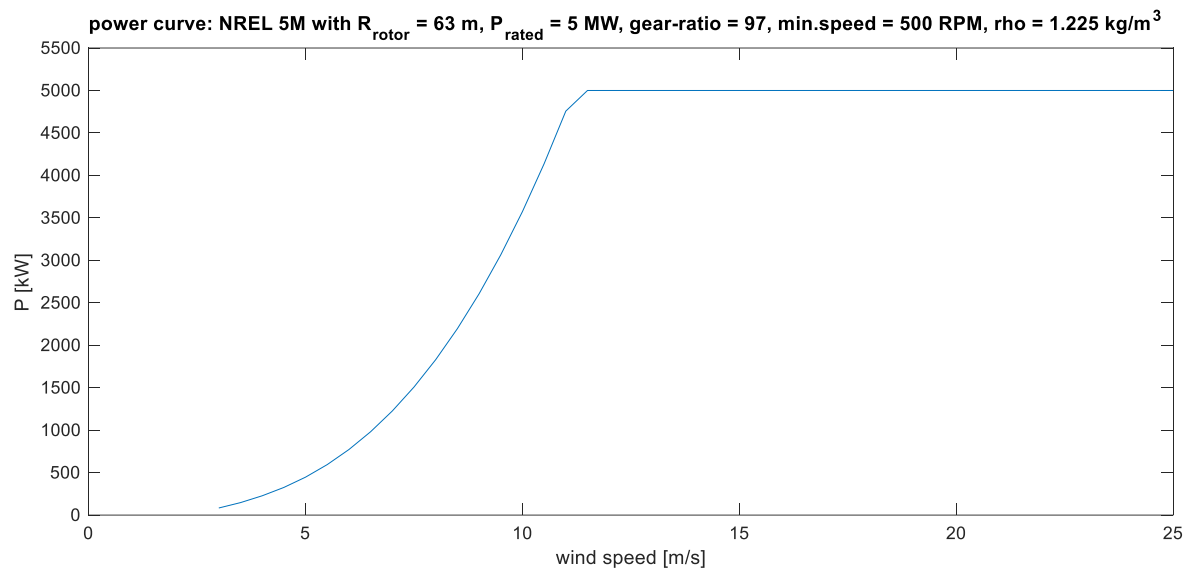


Figure 88: Power curve of NREL-5 MW

Variable distance – R_{var}

R_{var} describes the distance of the hydraulic fluid with the constant mass, $m_{\text{fluid_Tank}}$, between the centre of rotation and the blade tip (see Figure 90). The inertia, J_{fw} , changes depending on the state of charge of the piston accumulator, respectively on the distance R_{var} (see Equation 71). The total centre of gravity can be changed with the variable distance R_{var} . In addition, the changing of the inertia J_{fw} influences the resonance frequencies of the whole WT, especially of the three rotor blades and the drive train. D_{Tank} and D_{Acc} describe the inner diameter of the cylindrical tanks and piston accumulators.

Wind Speed (m/s)	Rotor Speed (rpm)	Pitch Angle (°)
11.4 - Rated	12.1	0.00
12.0	12.1	3.83
13.0	12.1	6.60
14.0	12.1	8.70
15.0	12.1	10.45
16.0	12.1	12.06
17.0	12.1	13.54
18.0	12.1	14.92
19.0	12.1	16.23
20.0	12.1	17.47
21.0	12.1	18.70
22.0	12.1	19.94
23.0	12.1	21.18
24.0	12.1	22.35
25.0	12.1	23.47

Figure 89: NREL 5-MW pitch angle control [17]

A_{Cog_Tank} and A_{Cog_Acc} are the projections of cylindrical fluid volumes in a rectangular area. The change in these areas can be explained by the length of the fluid volume, l_{fluid_Tank} and l_{fluid_Acc} . [30]. The lengths from the centre of rotation to the tanks are described by r_{Piston_Tank} and X_{Tank} . Accordingly, r_{Piston_Acc} and X_{Acc} describe these distances for the piston accumulator near the blade tip. ω_{pos} is the angular frequency and describes the speed of the rotor.

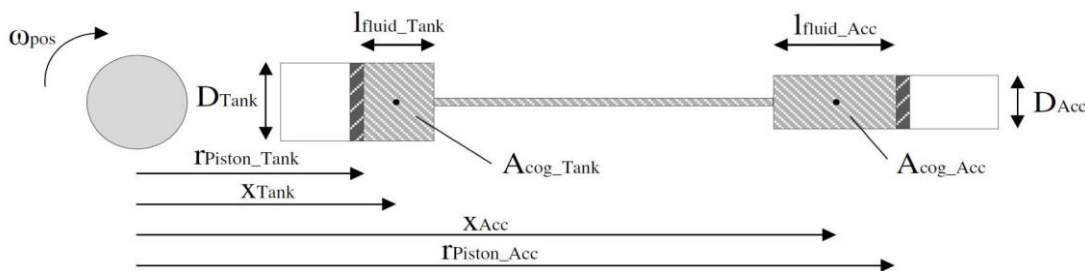


Figure 90: Hydraulic fluid system of one rotor blade [33]

8.9 Scenario Operating Points

8.9.1 Steadying and Non-Steadying Operation

In the following section 8.10, different scenarios for three specific operating modes of the FW system are simulated. There are two non-steadying operations where the FW system remains either charged or discharged.

When discharged, the system will not operate and the centre of gravity of the hydraulic fluid is at about four meters from the centre of rotation. The operating behaviour corresponds to a standard WT without the presented FW system.

When charged, the centre of gravity of the hydraulic fluid is at its maximum distance of about 45 meters from the centre of rotation. In this operation mode the inertia of the entire WT is permanently large.

In steadying operation, the distance R_{var} is automatically controlled by the bypass controller and can vary between about 4 m and 45 m, see chapter 5. During this operation, excess power is extracted from the wind and stored in the FW whenever available, and when there is a dip in the power in the wind this stored energy is released to the grid. This leads to a larger energy yield. To achieve this goal, suitable wind conditions and power setpoints must prevail. These conditions are simulated and evaluated in section 8.10.

8.9.2 Full Load Mode Average $v_{wind} = 20$ m/s and Turbulence

Analysing the behaviour of the WT in full load operation is important to see how much power the turbine can generate. The determined power in these simulations serves as an orientation to compare it with the generated power in other operating points. For the scenario at full load, a turbulent wind with a speed of 20 m/s on average is chosen. The WT outputs 100 % of its power (compare with 8.9.3) over the measured period, while the parameters for turbulent behaviour (see 8.9.4) retain the default values of the simulation preset.

8.9.3 Reduced Power Setpoint $P_{dem} < 100$ %

The grid operator in Germany requires that the grid feed-in power from renewable energies may be regulated. To avoid overloading the transmission network, the output power will be limited. This

regulatory mechanism is called "*Einspeisemanagement*". Especially in areas where the expansion of renewable energies has progressed very quickly, the necessary grid infrastructure is often missing. Nowadays, in coastal areas such as the North Sea and the Baltic Sea, this is a major problem, especially for wind energy. Wind (onshore) with 72 % and wind (offshore) with 25 % (as of 2018) of all renewable energy sources are affected by the power limitation. [34]

The network operator has the obligation to compensate for example the losses of a wind farm in case of such power curtailments. This compensation obligation is regulated in "*EEG*" §12 of the German renewable energy law. [34]

Conventional power plants, such as coal and nuclear power plants, are less affected by this power limitation. These power plants can store their fuel and, therefore, they are excluded from compensation. The grid operator has the option of controlling the affected plants to 60 %, 30% and 0 % of P_{TR} with a time interval of 15 minutes. The power control is carried out by remote control independently of the decision of the plant operator. [35]

In the following simulation with reduced power setpoints, the switching stages are chosen arbitrarily and a corresponding time interval is selected. For a better comparison, this simulation is evaluated in part load (average $v_{wind} = 10$ m/s) and in full load operation (average $v_{wind} = 20$ m/s). The turbulence behaviour parameters (see chapter 8.9.4) remain the default values of these simulations.

8.9.4 Variation of Turbulence Intensity TI

Definition of turbulence intensity: Ratio of the standard deviation of the wind speed to the mean value of the wind speed, based on time intervals of usually ten minutes. The turbulence intensity is mainly affected by obstacles in the wind, i.e. surface roughness of the terrain. Hence, it can be approximated from the roughness length of the terrain around the WT considered. [36]

$$TI = \frac{1}{\ln\left(\frac{h}{z_0}\right)} \quad \text{Equation 75}$$

Where TI [-] describes the turbulence intensity, h [m], height of the point measurement above ground and z_0 [m] the roughness length.

If the wind speed is measured for a long time period TI can also be calculated from the measured time series. In this case the following equation applies:

$$TI = \frac{STD}{v_{mean}} \quad \text{Equation 76}$$

Where STD is the standard deviation [m/s] and v_{mean} is the average wind speed [m/s] in the considered time interval. [37]

The flow state of the air is commonly defined as turbulence. It is mainly caused by surface roughness, orography in the urban area, neighbouring WTs and certain weather conditions. The turbulence intensity indicates the change of the wind speed v_{wind} in a certain time interval and decreases with increasing height or higher wind speeds (see Equation 75 and Figure 91). The knowledge of the effective turbulence of a site is of great importance for the load and stability calculation of WTs. The higher the turbulences, the more stable the mechanical structures of the WT must be. [37]

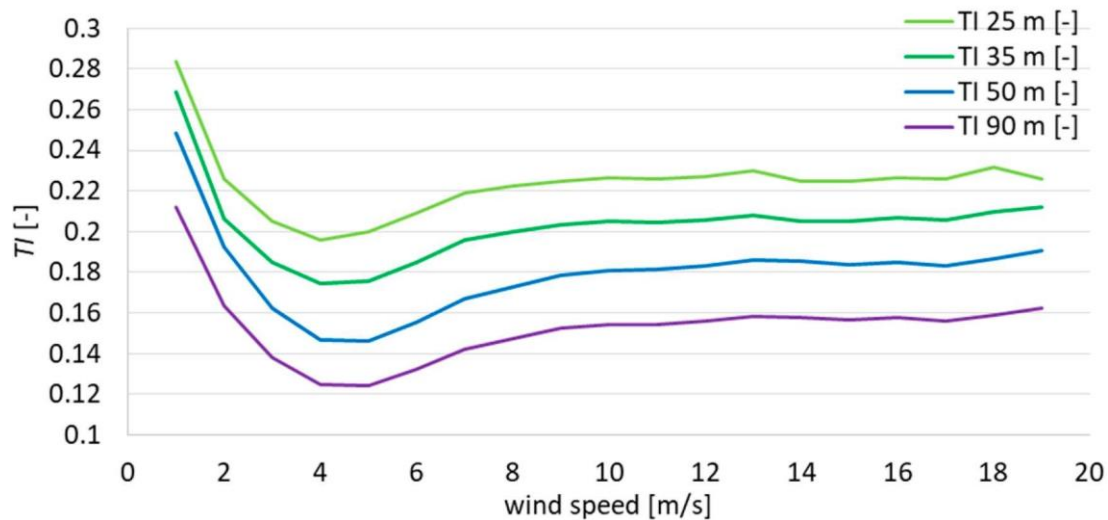


Figure 91: Turbulence intensity TI [-] versus wind speed [m/s] [38]

Figure 91 shows TI for three different heights above ground: 25 m, 35 m and 50 m. The TI for 90 m above ground is an extrapolation from the aforementioned measurements [38].

In order to evaluate the TI of a site, turbulence classes have been defined according to the IEC 61400-1 standard (edition 3). Most manufacturers set up their turbines for an effective turbulence of 6-12 % to a maximum of 20 %. [36]

Table 15: Turbulence classes

Turbulence classes	A	B	C	S
TI_{rep} (at 15m/s)	16%	14%	12%	Special class (for example offshore)

To generate different wind scenarios a wind model is implemented in SIMULINK. The block diagram of this wind model is shown in Figure 92.

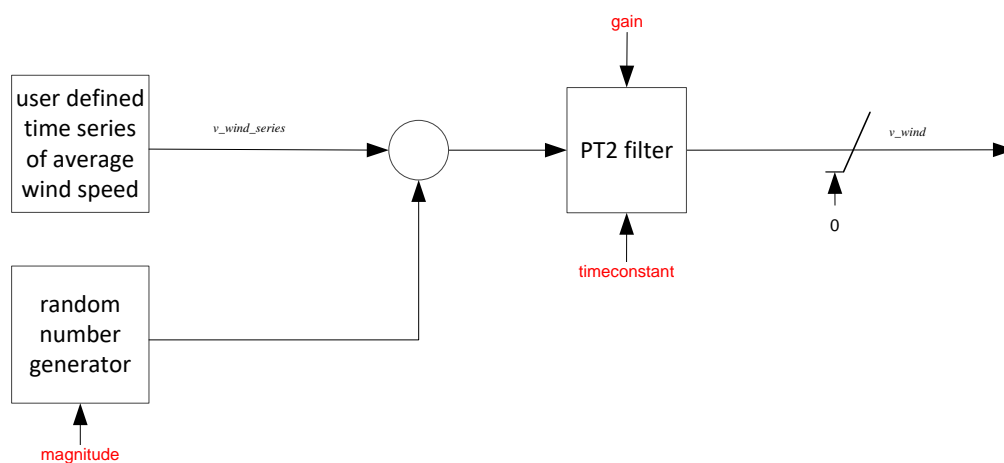


Figure 92: Block diagram of wind model [1]

The two most important parameters for variation in the wind are the timeconstant and the magnitude. The timeconstant parameter can be used to vary the frequency of the changing wind signal in a given

time period. The second parameter, magnitude, determines the maximum and minimum values of the wind in a given time period [1]. Low values are used for simulating wind in places with few obstacles in the landscape (low surface roughness) and at higher elevations [36]. Therefore, low values are applied to simulate coastal regions or offshore locations. High values correspond to places with many obstacles (high surface roughness), such as in midland.

The variation in the simulated wind speed, v_{wind} , is determined by a second order low pass filter (PT2), see Figure 92. The parameters of this filter, and their effects, are introduced in the following.

Parameter: timeconstant

The following figures show some exemplary curve shapes of the discussed parameters.

The curve shape of a turbulent wind signal depending on the parameter timeconstant is shown in Figure 93. The vibration behaviour decreases with increasing timeconstant.

If the value of timeconstant was chosen to be higher and higher, the curve shape of the wind signal would be further oriented towards the mean value of v_{wind} . This curve shape would come ever closer to the behaviour of a constant wind.

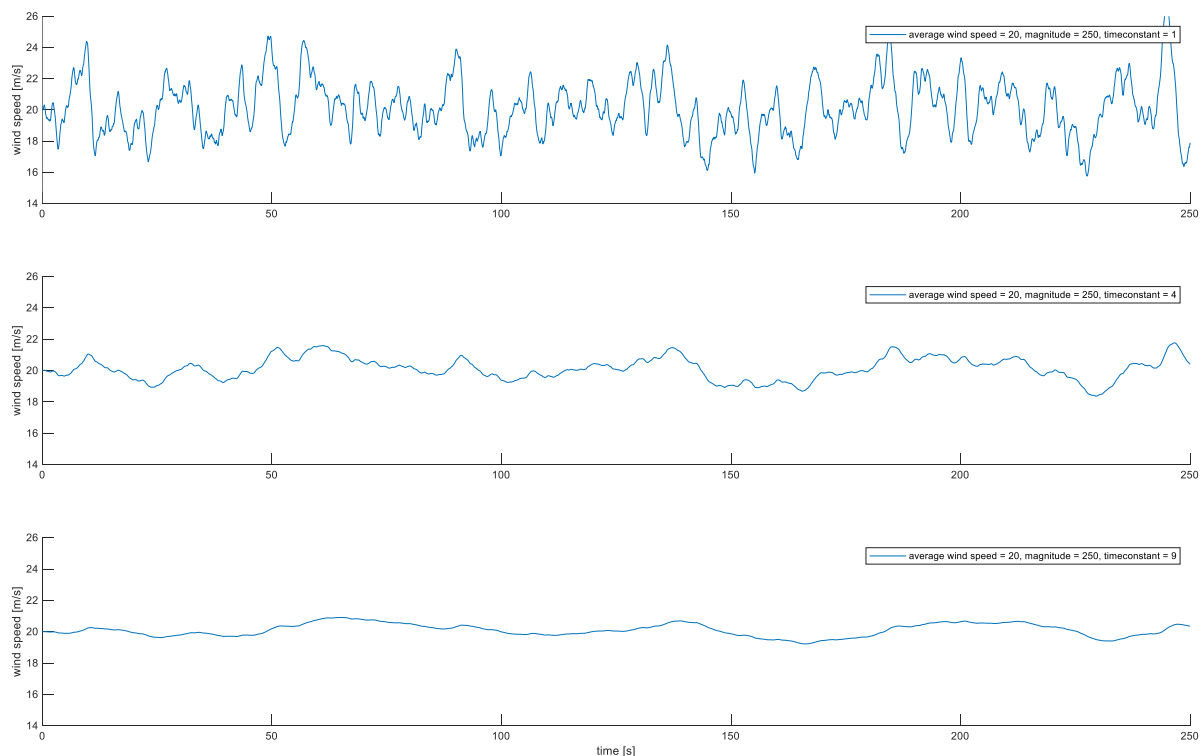


Figure 93: Comparison of different values of timeconstant (average $v_{wind} = 20$ m/s)

Parameter: magnitude

Figure 94 shows the behaviour of the parameter magnitude. As the magnitude increases, both the maximum and minimum values for the current wind speed increase.

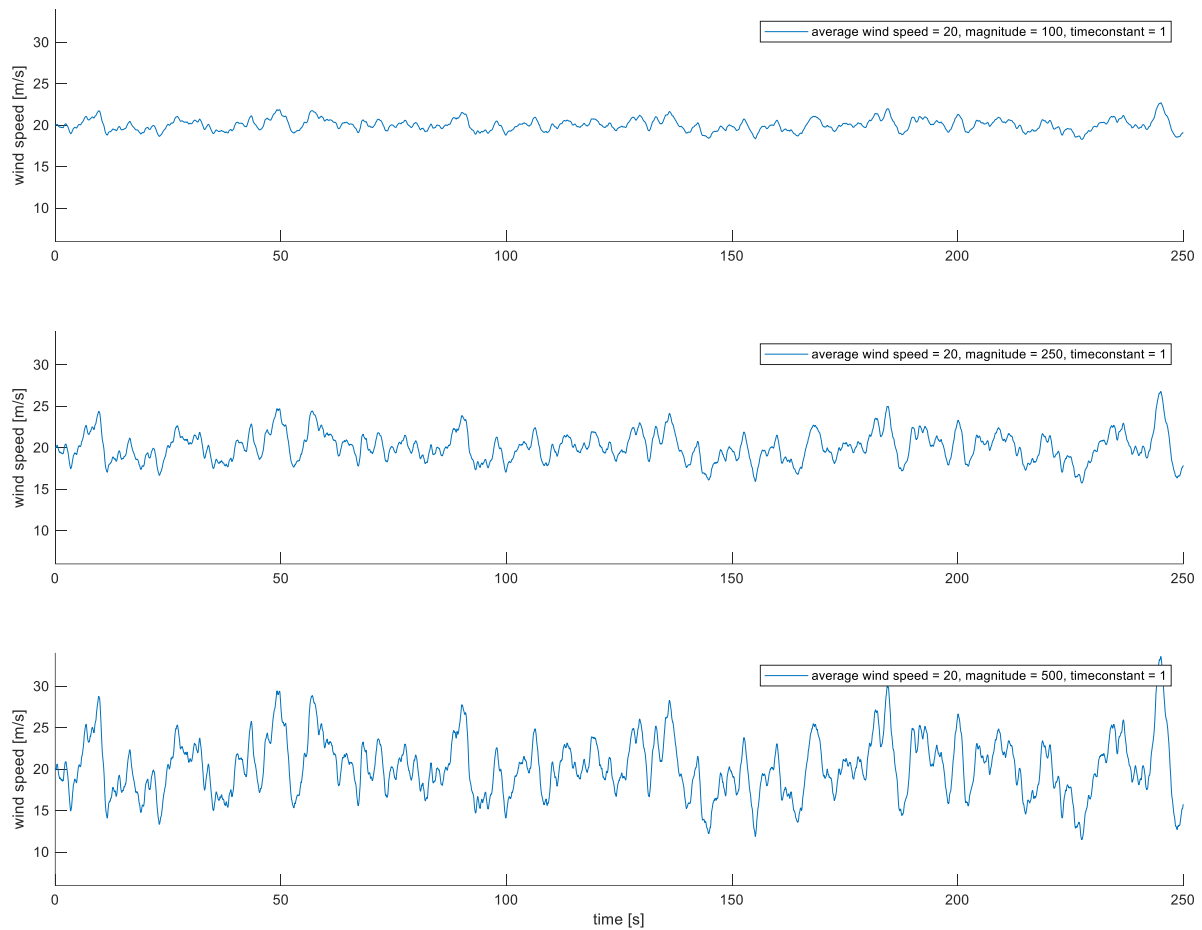


Figure 94: Comparison of different values of magnitude (average $v_{wind} = 20$ m/s)

8.10 Simulation

8.10.1 Expectations

With regard to the energy potential in the wind, low energy is expected at low wind speeds and high energy at high wind speeds. Therefore, with low energy potential, only a low chance for charging of the FW system and power steadying is expected. On the other hand, at high wind speeds, good conditions for power steadying are possible.

In full load mode with a wind speed of 20 m/s, it is expected that the power P_{TR} will be 100% at many operating points. When the wind speed v_{wind} decreases, a certain part of the power should be balanced with the FW system.

In the reduced power mode, a truncated curve shape is expected for both wind speeds of 10 m/s and 20 m/s, since the power P_{TR} is limited by the grid operator. Since more power is to be available than demanded, the WT can always deliver the required power and turbulence-induced fluctuations in P_{TR} should be mitigated by the FW at most operating points.

In turbulent wind conditions and increased values for the parameter timeconstant, a more constant wind is to be expected. Accordingly, power and speed_{rot} curve shape should be more uniform. At wind speeds of 20 m/s, the FW system should be fully charged most of the time, as it has less to compensate for due to the low wind fluctuations. The behaviour with a small value of the wind model

parameter magnitude should be comparable to that of a large timeconstant, since in this scenario also smaller wind fluctuations occur.

With a large value of magnitude strongly varying wind conditions are to be expected, which results in large changes in the power P_{TR} over the simulated period. Equivalent to this behaviour, the pitch angle and the speed of the rotor should fluctuate accordingly.

8.10.2 Simulation Results

8.10.2.1 Scenario in Full Load Operation

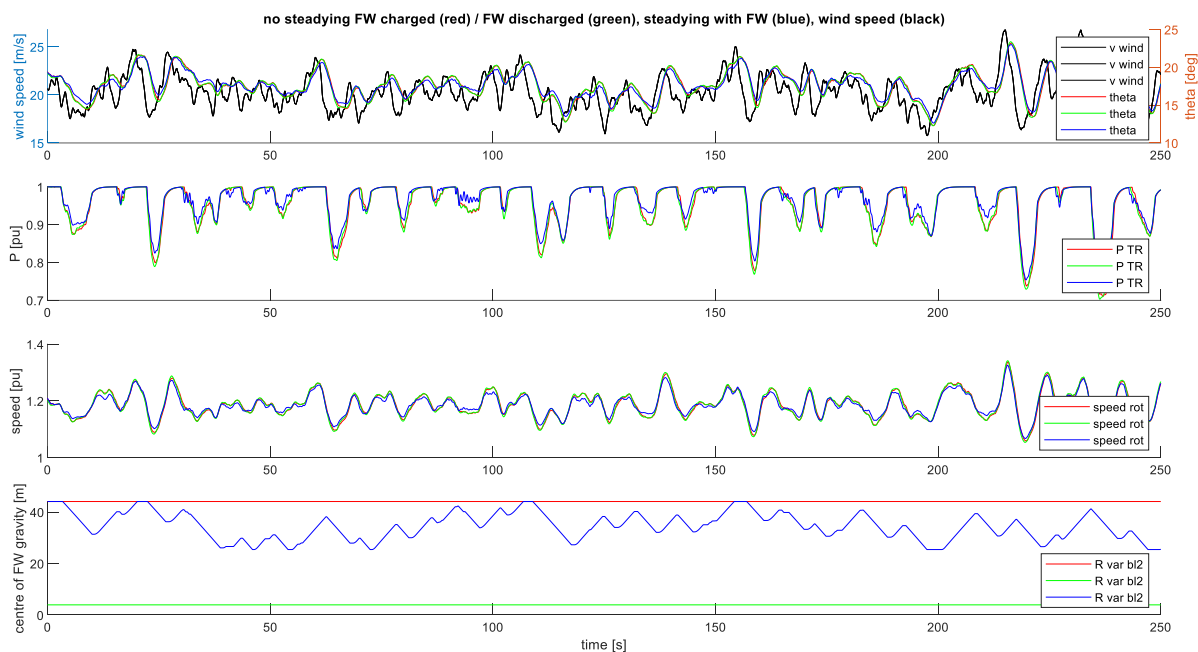


Figure 95: Full load operation ($v_{wind} = 20$ m/s): different signals

In the following evaluation, the full load behaviour of a WT with a FW system is analysed. The following parameters are used in the simulation:

An average wind speed of 20 m/s is selected, timeconstant ($= 1$) and magnitude ($= 250$) are left at standard values of the simulation preset. During the entire simulation period, the power setpoint is set to rated power ($P_{dem} = 1$).

The top figure in Figure 95 shows in a single diagram the turbulent wind signal v_{wind} and the pitch angle θ for all three operating points, discharged, charged and steadying of the FW. Differences in the operating points are negligible.

With a simulation duration of $t = 215$ seconds for example, v_{wind} reaches a very high value and ensures a high energy potential in the wind. The power on the transformer P_{TR} increases to 100 %, while the rotor blades get a very high pitch angle. Shortly after $t = 215$ seconds, the wind speed decreases very quickly and causes less energy potential in the wind. The system changes the pitch angle to stop limiting power and to get the maximum possible energy from the wind. The blade pitch setting works slowly, as the signals have to be processed via a controller and the adjustment by electric motors takes a certain time. During the entire simulation period, the signal of the pitch angle rushes behind the wind

speed v_{wind} , so that the rotor blades cannot pitch fast enough and the power P_{TR} briefly decreases by 27 %.

The next three figures show the curve shapes of P_{TR} , $speed_{rot}$ and R_{var} for the three states of steadying and non-steadying (charged, discharged) power feed-in.

In the second graph of Figure 95, in the discharged state of the FW system, the power P_{TR} assumes a very smooth value of 100 % at high wind speeds and virtually assumes the curve shape of a standard WT without a FW. The charged state for P_{TR} has almost the same curve shape as in the discharged state. At low wind speeds, however, the decreasing power is somewhat compensated by the use of the FW. The steadying operation shows that in contrast to non-steadying operation with a charged FW slightly more power (about 2 %) is compensated.

The rotor speed, $speed_{rot}$, generally has similar curve shapes for the three operating points of the FW. At points where the wind speed decreases, the speed of the rotor also decreases. These points also show that the FW system is working, because energy is fed from the FW to the generator. The curve shape in steadying operations shows in comparison to the non-steadying operations a slightly increasing value of about 1 %.

The lowest graph of Figure 95 shows the distance R_{var_bl2} for the second rotor blade. When the wind speed drops, the FW system starts to work and tries to balance:

The hydraulic system transports the fluid to the blade root, reduces the system inertia and releases kinetic energy E_{kin} . When the wind speed reaches its minimum and rises again, the system begins to transport the fluid back to the blade tip and absorbs kinetic energy. The distance R_{var_bl2} mostly changes with the maximum slew rate. Only in case of very low power differences the FW is charged or discharged slower [1]. If the FW system is in charged operation the distance R_{var_bl2} to the centre of rotation is a constant 44 m after a pumping phase of the fluid. In discharged condition, the FW system does not work and the distance R_{var_bl2} is continuously four meters to the centre. This distance cannot be further reduced (see section 8.8).

Figure 96 shows the behaviour of all three rotor blades in relation to the change in the distance R_{var} . In order to avoid an imbalance and thus damage to the WT, all 3 rotor blades act separately from each other (see section 8.5). The differences in the minimum and maximum values of R_{var} are chosen such that imbalances in the rotor are levelled out. These differences can be observed in Figure 96.

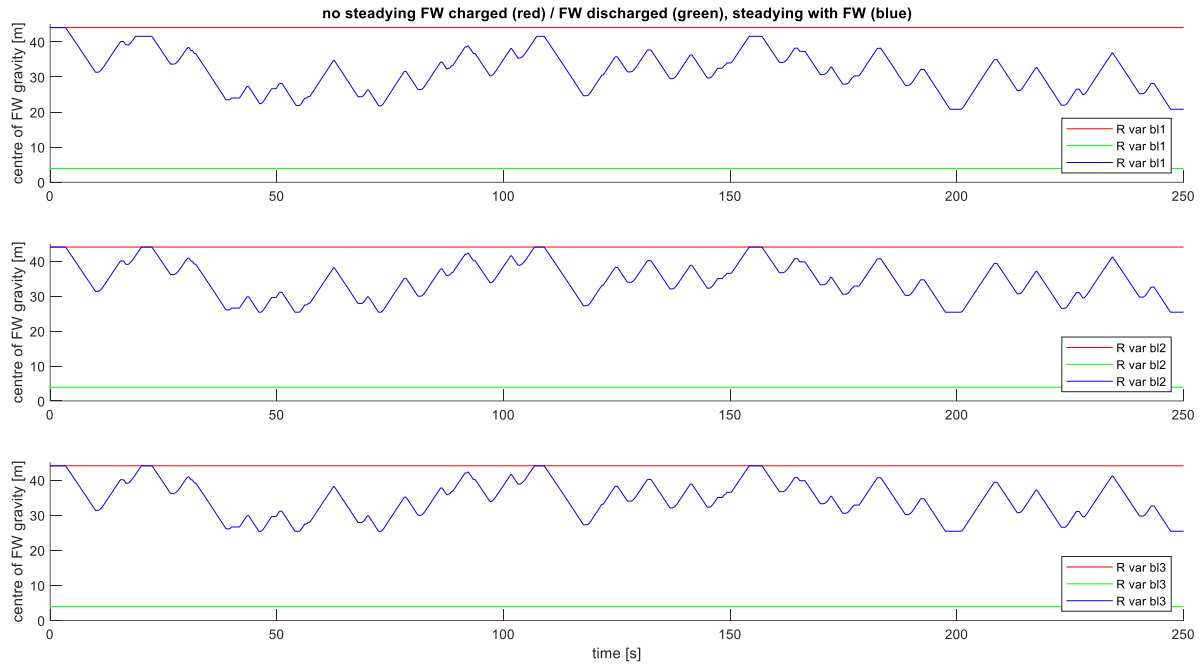


Figure 96: Full load operation ($v_{wind} = 20$ m/s): variable distance R_{var}

8.10.2.2 Scenario with Reduced Power Setpoint ($v_{wind} = 10$ m/s)

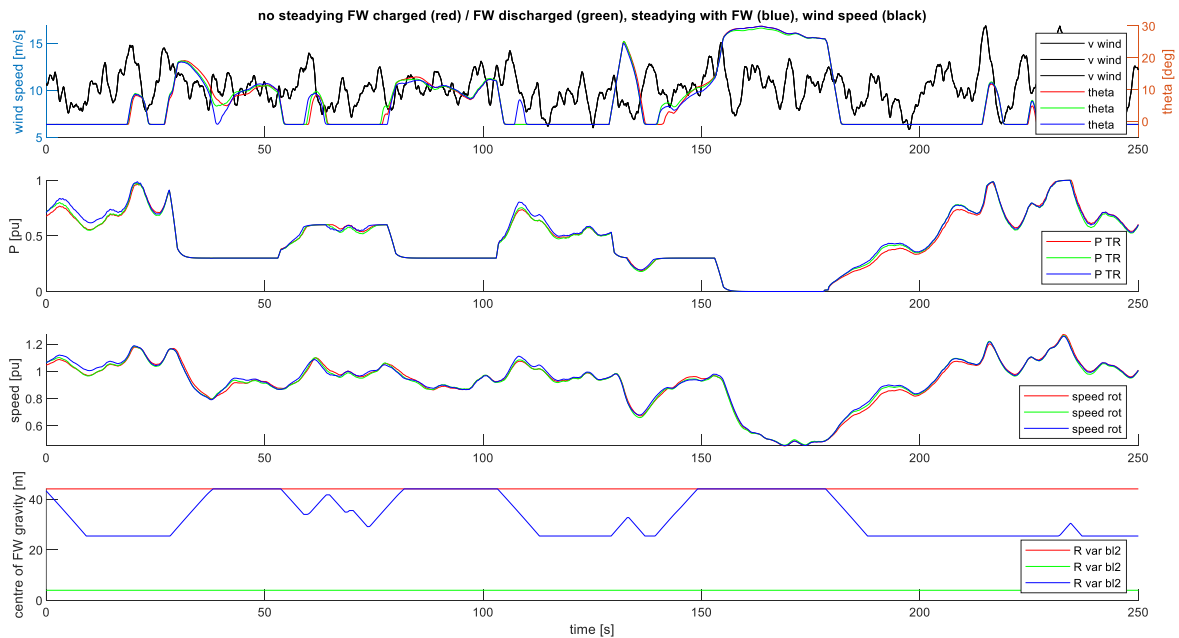


Figure 97: Reduced power setpoint ($v_{wind} = 10$ m/s): different signals

In the following scenario, the behaviour of the FW in part load operation is analysed with a wind speed of $v_{wind} = 10$ m/s. The *timeconstant* ($= 1$) and *magnitude* ($= 250$) parameters were left at the default values of the simulation preset. During the simulated period, the WT provides reduced power according to the specifications of the EEG (see section 8.9.3). The scenario is intended to show the

behaviour of the FW when using feed-in management (*Einspeisemanagement*). Modelling the specified switching times of 15 minutes, the simulation switches every 30 seconds, with a transition period of 2 seconds. Table 16 shows the switching processes P_{dem} in relation to the time t . P_{dem} represents the power demanded by the grid operator. [10]

Table 16: Switching operations of power demand P_{dem} [10]

P_{dem} [%]	100	100	30	30	60	60	30	30	100	100	30	30	0	0	60	60	100	100
t [s]	0	28	30	53	55	78	80	103	105	128	130	153	155	178	183	203	205	250

Figure 97 shows that high power demand and/or low wind speed leads to the minimum pitch angle. Only when the power in the wind exceeds the demanded power plus the power required for charging the FW (if applicable) the pitch angle reaches up to larger values.

The curve shapes of P_{TR} , $speed_{rot}$ and R_{var} are shown in the next three diagrams in Figure 97 for the three states of steadying and non-steadying power feed-in. In the second graph of Figure 97, the power P_{TR} usually runs under the control of P_{dem} over the entire simulation period. At the simulation time $t = 10$ s, it is noticeable that the FW system in steadying operation can achieve a power feed-in of about 7 % above in comparison to the other two operating states. The curve shapes from the charged and discharged state basically follow a very similar course.

By discharging the FW system, the speed $speed_{rot}$ increases for the steadying operation mode and thus the power P_{TR} . This behaviour can be recognized, e.g. when the simulation time reaches about 103 s. Starting at a simulation time of $t = 139$ s, the FW system is charging, while the rotor speed is lugging which explains the energy input to the FW.

The speed $speed_{rot}$ generally has similar curve shapes for the charged and discharged operating points of the FW.

The diagram in the bottom of Figure 97 shows the distance R_{var_bl2} for the second rotor blade. The distance R_{var_bl2} to the centre of rotation is constant 44 m after a linear pumping phase of the fluid, if the FW system is in charged unsteady operation. In discharged unsteady operation, the system does not work and the distance R_{var_bl1} is continuously four meters to the centre. Figure 98 shows the behaviour of all three rotor blades in relation to the change in the distance R_{var} .

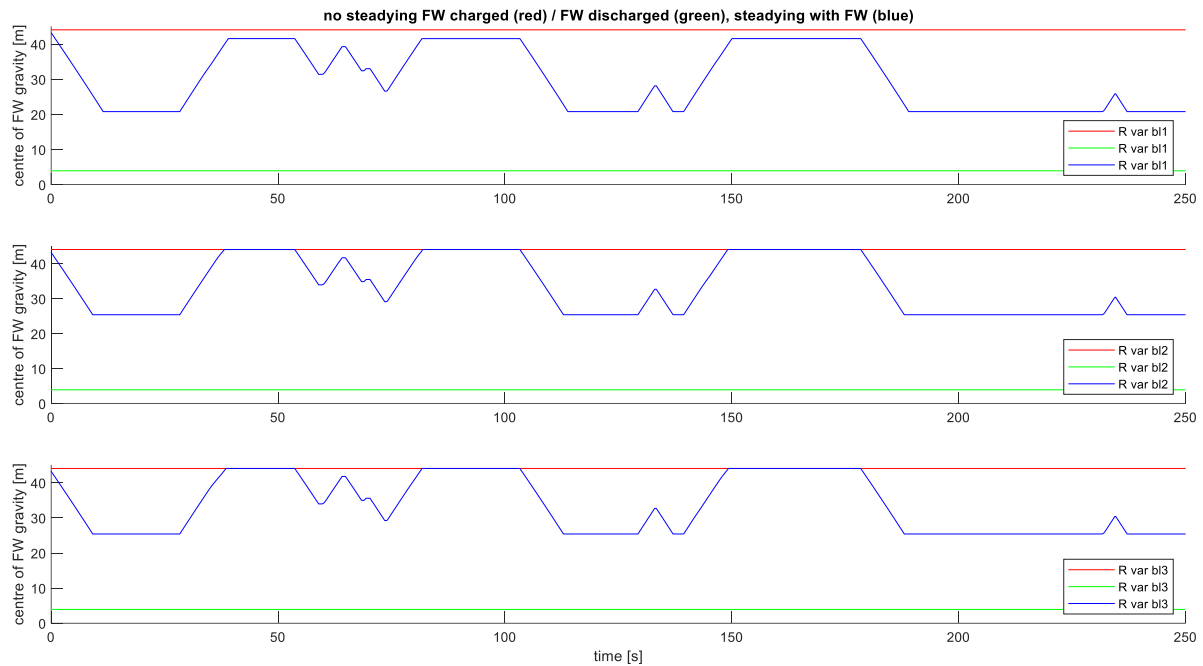


Figure 98: Reduced power setpoint ($v_{wind} = 10$ m/s): variable distance R_{var}

8.10.2.3 Scenario with Reduced Power Setpoint ($v_{wind} = 20$ m/s)

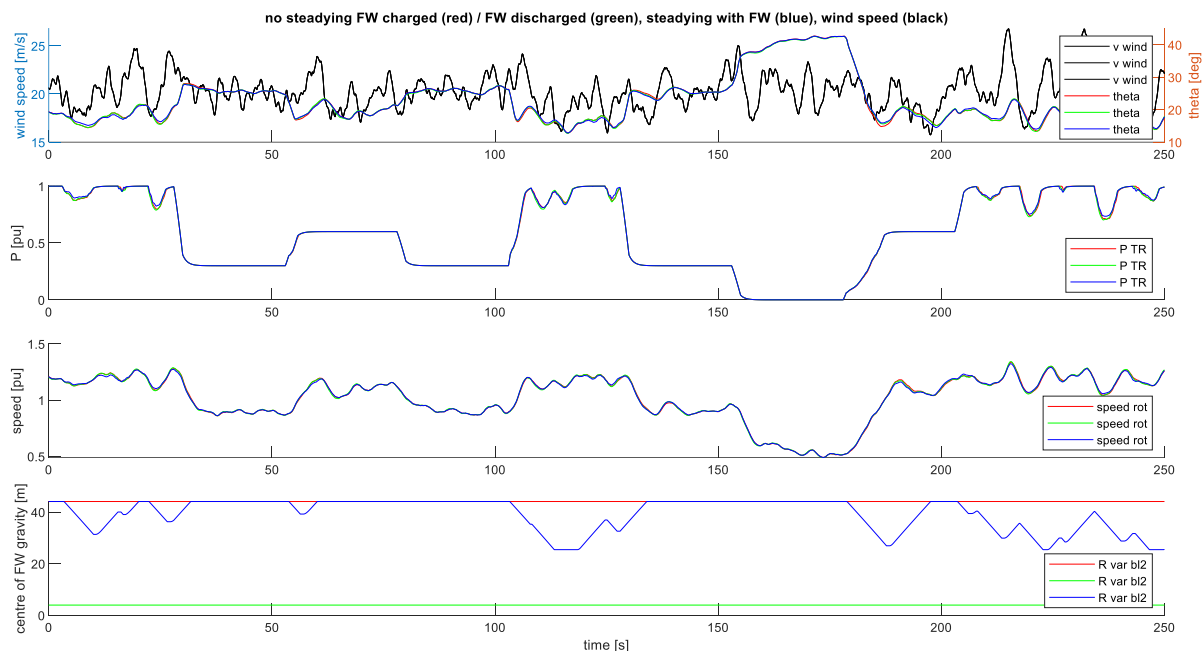


Figure 99: Reduced power setpoint ($v_{wind} = 20$ m/s): different signals

In the following evaluation, the reduced power operation of the full load behaviour of a WT with a FW system is analysed in comparison to the part load behaviour. These parameters were used in the simulation:

An average wind speed of 20 m/s was selected, *timeconstant* (= 1) and *magnitude* (= 250) were left at standard values of the simulation specification. During the simulated period, the WT provides reduced power according to the specifications of the EEG (see section 8.9.3). The simulation switches every 30 seconds, with a transition period of 2 seconds. Each switching process of P_{dem} in relation to the time, t , is shown in Table 16.

For all three operating points of the FW, the top diagram in Figure 99 shows in a single diagram the turbulent wind signal v_{wind} and the pitch angle θ . The time traces of P_{TR} , $speed_{rot}$ and R_{var} are shown in the other diagrams of Figure 99 for the three states of steadying and non-steadying power feed-in.

It can be seen that the FW only does steadying of the power infeed at large P_{dem} values. In all operating states where P_{dem} truncates the power there is no need for power steadying.

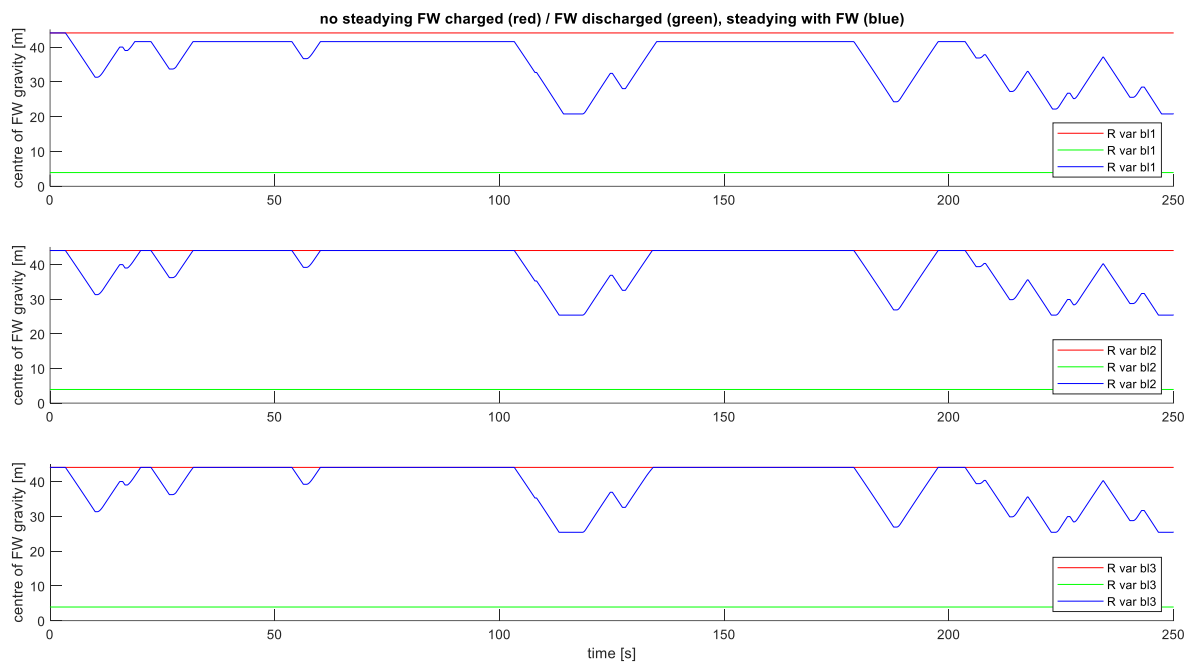


Figure 100: Reduced power setpoint ($v_{wind} = 20$ m/s): variable distance R_{var}

The Figure 100 shows the behaviour of all three rotor blades in relation to the change in the distance R_{var} . Also here the difference between blade one, in contrast to blade two and three arises from the different limit settings to balance the rotor.

8.10.2.4 Scenario with Varying Turbulence Intensities

In the previous sections the performance of the FW when steadying the power output is compared with the performance of the WT when the FW is statically charged and discharged. In the following sections, the comparison is only done between steadying with the FW and non-steadying with statically charged FW.

8.10.2.4.1 Parameter: *timeconstant*

Figure 101 shows the full load behaviour of the FW system at modified turbulence intensities. These modifications are achieved here with varying the parameter *timeconstant*. The power demand value remains unchanged at $P_{dem} = 1$. The signals shown in Figure 101 are as introduced in the previous sections.

It can be seen that at low turbulence intensity there is no need for steadying the power. In this wind condition the WT is able to level out all wind speed variations with the pitch angle, because the variations are slow enough.

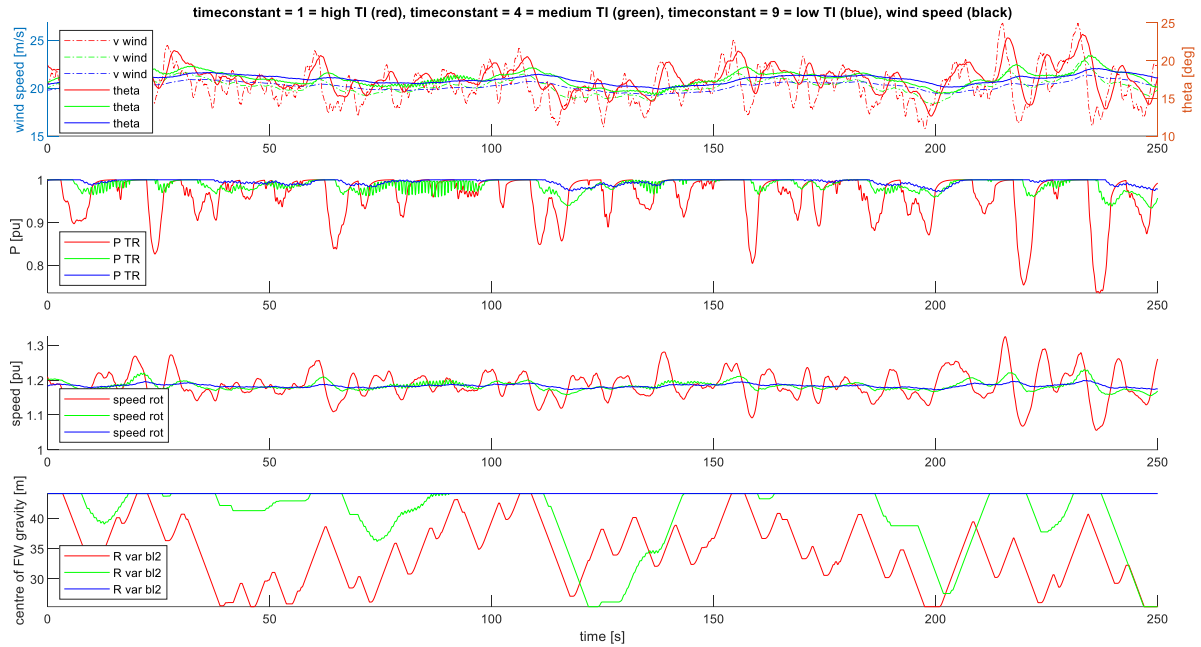


Figure 101: Varying turbulence intensities from different values of $timeconstant$ ($v_{wind} = 20$ m/s, $magnitude = 250$)

Figure 102 shows the different behaviours of R_{var} .

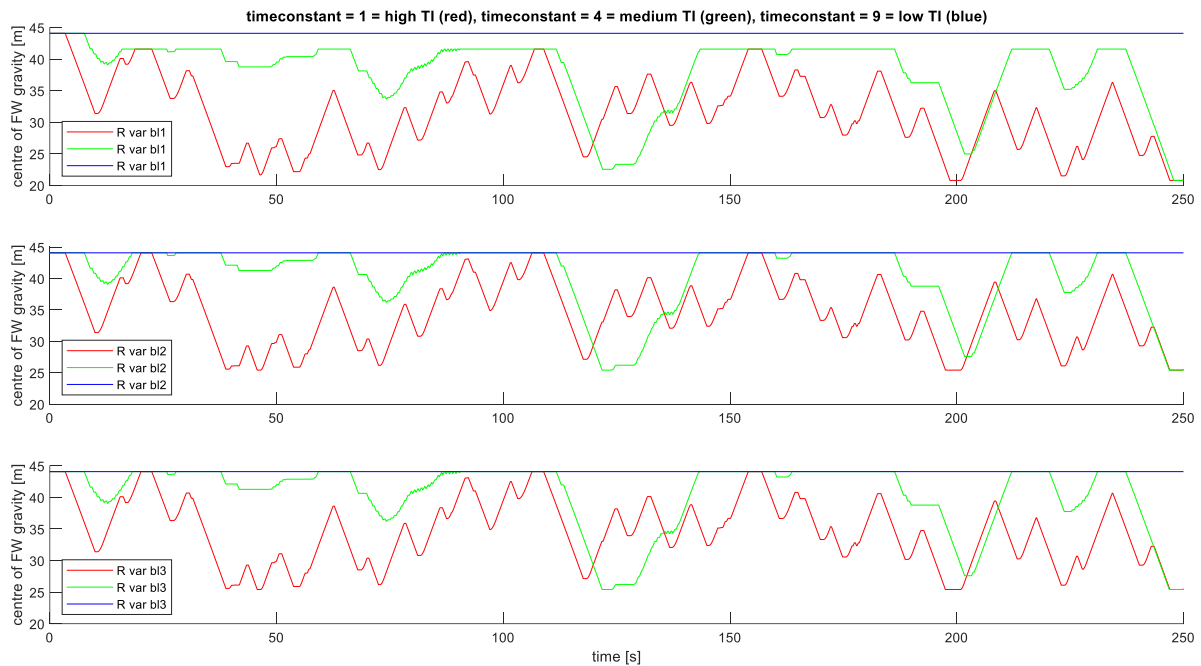


Figure 102: Varying turbulence intensities from different values of $timeconstant$ ($v_{wind} = 20$ m/s, $magnitude = 250$)

It can be seen from Figure 102 that the different limit values the FW are not applied in case of very low turbulence intensity. R_{var} of all three blades remains at about 44 meters. This is because the FW is not needed, hence, after charging the FW the Bypass Controller is not activated, which means that it does not get the chance to set the R_{var} values such that the rotor is balanced.

The differences in the performance of power steadying become most visible when comparing the power fed into the grid, see Figure 103.

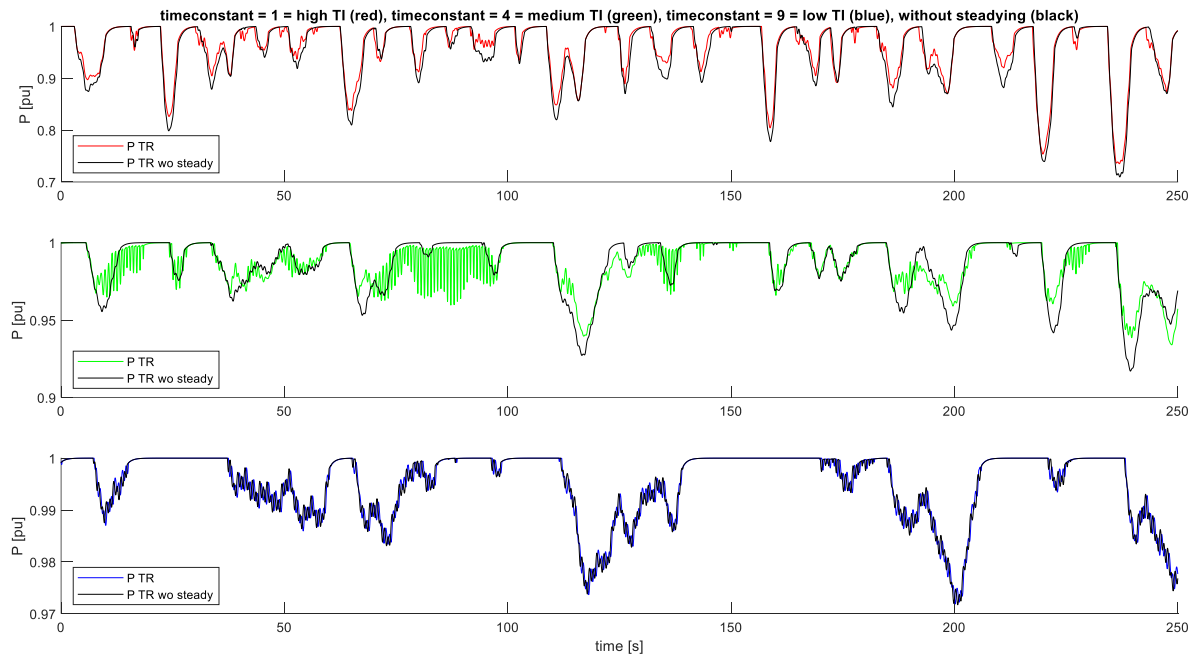


Figure 103: Varying turbulence intensities from different values of *timeconstant* ($v_{wind} = 20$ m/s, *magnitude* = 250)

8.10.2.4.2 Parameter: *magnitude*

Figure 104 shows the full load behaviour of the FW system, again, at modified turbulence intensities. In contrast to the previous section, here these modifications are achieved by varying the parameter *magnitude*. The power demand value remains unchanged at $P_{dem} = 1$. The signals shown in Figure 104 are as introduced in the previous sections.

It can be seen that also at this low turbulence intensity there is no need for steadying the power. In this wind condition, the WT is able to level out all wind speed variations with the pitch angle, because the variations are slow enough.

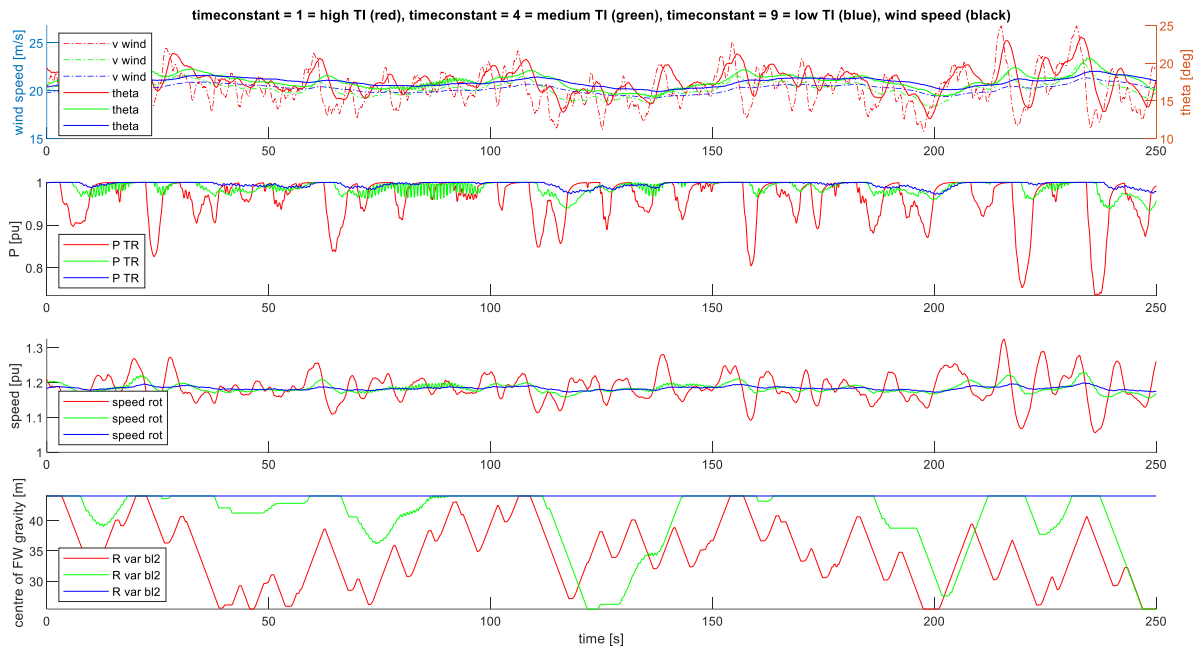


Figure 104: Varying turbulence intensities from different values of $timeconstant$ ($v_{wind} = 20$ m/s, magnitude = 250)

Figure 105 shows the different behaviours of R_{var} .

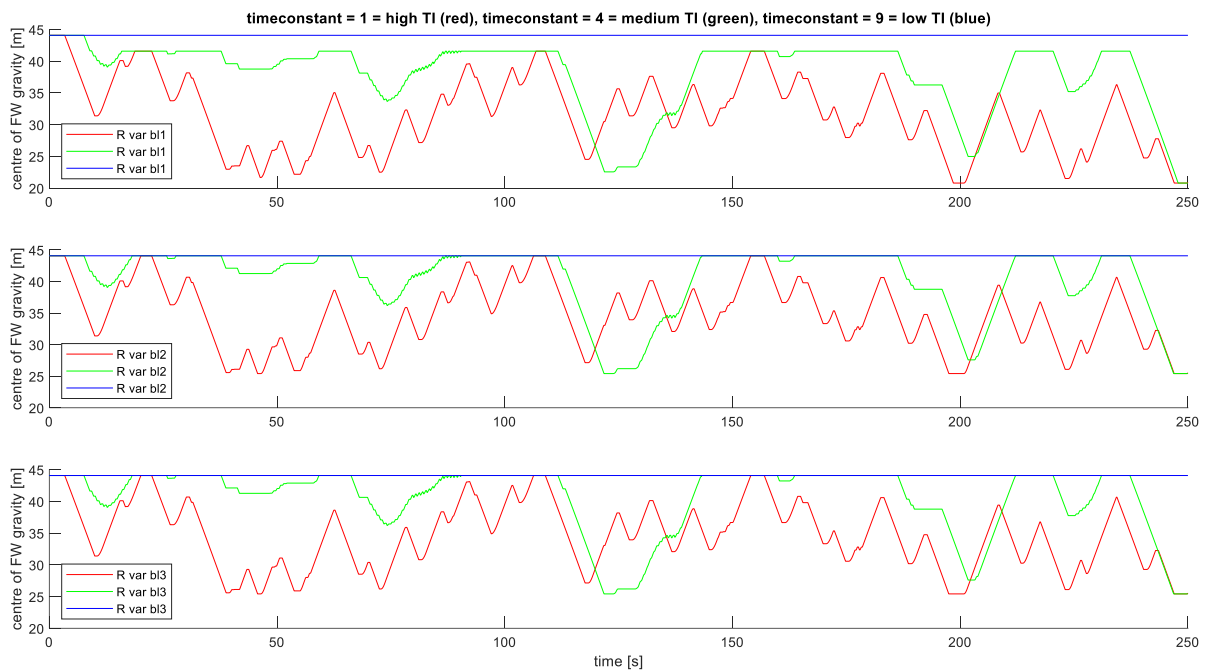


Figure 105: Varying turbulence intensities from different values of $timeconstant$ ($v_{wind} = 20$ m/s, magnitude = 250)

The differences in the performance of power steadying become most visible when comparing the power fed into the grid, see Figure 106.

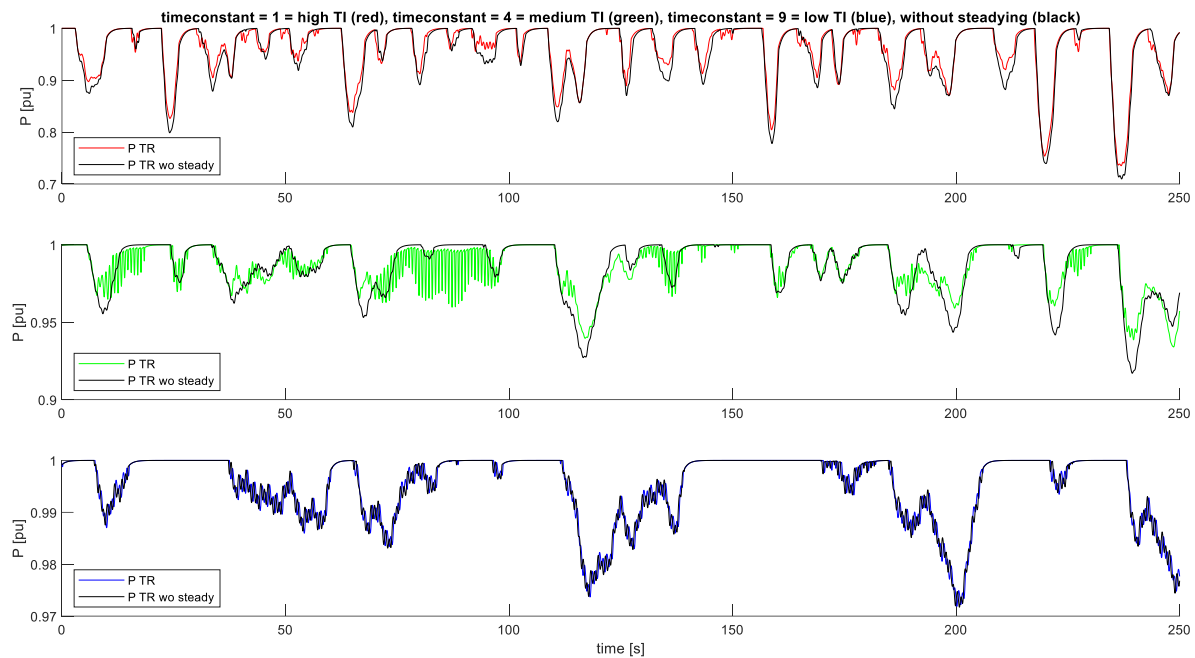


Figure 106: Varying turbulence intensities from different values of *timeconstant* ($v_{wind} = 20$ m/s, *magnitude* = 250)

8.11 Evaluation

With regard to chapter 8.10.1 and the present results of the simulation, an evaluation of the results is conducted.

The expectations in full load operation are only partially fulfilled: While high wind speeds deliver a lot of power, P_{TR} , the FW accumulator can only compensate a very small part at lower wind speeds.

In reduced power operation, steadying the power feed-in has almost never occurred. (Only when the power setpoint reached up to 100%, i.e. no limitation. Power limitation by the grid operator stores excess energy in the FW and can be used quickly when needed. Even with wind speeds of 10 m/s with potentially low energy, the FW system is fully charged all the time.

In turbulent wind conditions, the expectations are fulfilled: I.e. the FW system is not required if the wind speed varies only very slowly. If very low turbulence intensity occurs in full load wind speed, the power feed-in is virtually constant; hence, there is no need for steadying it.

8.12 Economical Evaluation

8.12.1 Energy Infeed

The following chapter examines the energy yield in the non-steadying operation modes (charged, discharged) and in the steadying operation.

Like the graphical determination of the simulation results (see chapter 8.10), the energy infeed can also be calculated after the simulations are completed (see Equation 77). In the simulation, the time is in seconds (*duration*) and the power (P_{TR}) is in per unit on the basis of the rated power of the NREL 5

MW WT (see chapter 8.2). Hence, in order to yield an energy in kWh, in Equation 77 the energy has to be multiplied by 5000 kW and divided by 3600 seconds.

$$E = P_{TR} \cdot duration \cdot \frac{5000}{3600} \quad \text{Equation 77}$$

Table 17 lists the energy yields for all three operating states of the FW and for the different load scenarios. The values given in Table 17 are the energies in kWh that result from the 250 s simulations. The simulation scenarios examined in chapter 8.10 are named in the first column of this table. In the cases where the turbulence intensity is varied, non-steadying operation is simulated only with charged FW. Therefore, in the applicable cells a “—” indicates that no energy result can be given.

Table 17: Energy infeed [kWh] of the 250 s simulations of non-steadying (charged/discharged) and steadying operation (v = average wind speed, tc = timeconstant, m = magnitude)

	Unsteading O. (FW discharged)	Unsteading O. (FW charged)	Steadying Operation
Full-load operation (v = 20m/s, tc = 1, m = 250)	331.8574	332.2316	334.2692
Reduced power setpoint (v = 10m/s, tc = 1, m = 250)	157.1880	156.7715	160.6142
Reduced power setpoint (v = 20m/s, tc = 1, m = 250)	199.4072	199.4723	200.0777
Varying turbulence intensities (v = 20m/s, tc = 1, m = 250)	—	332.2319	334.2543
Varying turbulence intensities (v = 20m/s, tc = 4, m = 250)	—	342.6217	342.6901
Varying turbulence intensities (v = 20m/s, tc = 9, m = 250)	—	345.5561	345.5606
Varying turbulence intensities (v = 20m/s, tc = 1, m = 500)	—	320.2256	334.2299
Varying turbulence intensities (v = 20 m/s, tc = 1, m = 250)	—	332.2035	334.2450
Varying turbulence intensities (v = 20 m/s, tc = 1, m = 100)	—	340.6269	342.0614

8.12.2 Outlook of Profits

In Germany, there is a law called the *Erneuerbare-Energien-Gesetz* (EEG), which regulates the use of renewable energies since 2014. In order to promote and accelerate the expansion of renewable energies, there is a feed-in tariff according to the EEG. Especially for offshore wind energy, separate tariff rates apply. The annual yields in this chapter are based on the remuneration rates that applied in 2019.

There is a base model with an initial charge of 14.9 ct/kWh for at least 12 years and an optional 18.4 ct/kWh for at least 8 years. As a rule, a plant operator plans to operate a WT with a term of 20 years. At the end of these 12 or 8 years, an extension of this increased remuneration may be granted. This is followed by a basic remuneration of 3.9 ct/kWh until the shutdown of the plant (details see in EEG, sect. 47, para.(1), cl.1).

Table 18, Table 19 and Table 20 lists the annual revenues for all three operating states for different load scenarios. The scenarios and underlying energy amounts are as listed in Table 17. The difference between Table 18, Table 19 and Table 20 is the assumed remuneration per kWh, which is the initial remuneration, the optional remuneration and the basic remuneration, respectively.

Obviously, the simulated scenarios occur at any location only for a certain fraction of the year. To be precise a certain location would have to be chosen and the duration of the applicable scenario derived from the Weibull distribution of the wind speed. Instead of doing this a constant 1000 h/a is assumed as duration for every scenario.

Table 18, Table 19 and Table 20 show in their rightmost columns the additional revenue. This is the extra revenue that results from the extra energy yield that the FW produces by steadying the power infeed.

Table 18: Annual revenue [€/a] in non-steadying (charged/discharged) and steadying operation (v = average wind speed, t_c = *timeconstant*, m = *magnitude*) for the initial remuneration of 0.149 €/kWh

	Revenue from Unsteading O. (FW discharged) [€/a]	Revenue from Unsteading O. (FW charged) [€/a]	Revenue from Steadying Operation [€/a]	Additional revenue [€/a]
Full-load operation ($v = 20\text{m/s}$, $t_c = 1$, $m = 250$)	712033.24	712836.12	717208.00	4371.87
Reduced power setpoint ($v = 10\text{m/s}$, $t_c = 1$, $m = 250$)	337262.57	336368.93	344613.83	8244.90
Reduced power setpoint ($v = 20\text{m/s}$, $t_c = 1$, $m = 250$)	427848.09	427987.77	429286.71	1298.95
Varying turbulence intensities ($v = 20\text{m/s}$, $t_c = 1$, $m = 250$)	—	712836.76	717176.03	4339.26
Varying turbulence intensities ($v = 20\text{m/s}$, $t_c = 4$, $m = 250$)	—	735129.12	735275.88	146.76
Varying turbulence intensities ($v = 20\text{m/s}$, $t_c = 9$, $m = 250$)	—	741425.17	741434.82	9.66
Varying turbulence intensities ($v = 20\text{m/s}$, $t_c = 1$, $m = 500$)	—	687076.05	717123.67	30047.63
Varying turbulence intensities ($v = 20\text{ m/s}$, $t_c = 1$, $m = 250$)	—	712775.83	717156.07	4380.24
Varying turbulence intensities ($v = 20\text{ m/s}$, $t_c = 1$, $m = 100$)	—	730849.08	733926.94	3077.86

Table 19: Annual revenue [€/a] in non-steadying (charged/discharged) and steadying operation (v = average wind speed, t_c = *timeconstant*, m = *magnitude*) for the optional remuneration of 0.184 €/kWh

	Revenue from Unsteading O. (FW discharged) [€/a]	Revenue from Unsteading O. (FW charged) [€/a]	Revenue from Steadying Operation [€/a]	Additional revenue [€/a]
--	---	--	--	--------------------------------

Full-load operation ($v = 20\text{m/s}$, $t_c = 1$, $m = 250$)	879289.37	880280.85	885679.67	5398.82
Reduced power setpoint ($v = 10\text{m/s}$, $t_c = 1$, $m = 250$)	416485.32	415381.77	425563.38	10181.62
Reduced power setpoint ($v = 20\text{m/s}$, $t_c = 1$, $m = 250$)	528349.32	528521.81	530125.87	1604.07
Varying turbulence intensities ($v = 20\text{m/s}$, $t_c = 1$, $m = 250$)	—	880281.64	885640.19	5358.55
Varying turbulence intensities ($v = 20\text{m/s}$, $t_c = 4$, $m = 250$)	—	907810.46	907991.69	181.23
Varying turbulence intensities ($v = 20\text{m/s}$, $t_c = 9$, $m = 250$)	—	915585.44	915597.37	11.92
Varying turbulence intensities ($v = 20\text{m/s}$, $t_c = 1$, $m = 500$)	—	848469.75	885575.54	37105.79
Varying turbulence intensities ($v = 20\text{ m/s}$, $t_c = 1$, $m = 250$)	—	880206.39	885615.55	5409.16
Varying turbulence intensities ($v = 20\text{ m/s}$, $t_c = 1$, $m = 100$)	—	902525.03	906325.89	3800.85

Table 20: Annual revenue [€/a] in non-steadying (charged/discharged) and steady operation (v = average wind speed, t_c = *timeconstant*, m = *magnitude*) for the basic remuneration of 0.039 €/kWh

	Revenue from Unsteady O. (FW discharged) [€/a]	Revenue from Unsteady O. (FW charged) [€/a]	Revenue from Steady Operation [€/a]	Additional revenue [€/a]
Full-load operation ($v = 20\text{m/s}$, $t_c = 1$, $m = 250$)	186371.12	186581.27	187725.58	1144.32
Reduced power setpoint ($v = 10\text{m/s}$, $t_c = 1$, $m = 250$)	88276.78	88042.87	90200.93	2158.06
Reduced power setpoint ($v = 20\text{m/s}$, $t_c = 1$, $m = 250$)	111987.08	112023.64	112363.64	339.99
Varying turbulence intensities ($v = 20\text{m/s}$, $t_c = 1$, $m = 250$)	—	186581.44	187717.21	1135.78
Varying turbulence intensities ($v = 20\text{m/s}$, $t_c = 4$, $m = 250$)	—	192416.35	192454.76	38.41
Varying turbulence intensities ($v = 20\text{m/s}$, $t_c = 9$, $m = 250$)	—	194064.31	194066.83	2.53
Varying turbulence intensities ($v = 20\text{m/s}$, $t_c = 1$, $m = 500$)	—	179838.70	187703.51	7864.81
Varying turbulence intensities ($v = 20\text{ m/s}$, $t_c = 1$, $m = 250$)	—	186565.49	187711.99	1146.51
Varying turbulence intensities ($v = 20\text{ m/s}$, $t_c = 1$, $m = 100$)	—	191296.07	192101.68	805.62

Table 18, Table 19 and Table 20 show that it makes a big difference what price per kWh is assumed. However, even in the worst case scenario (basic remuneration) the FW can generate a revenue of more

than 1100 €/a in case of medium turbulence intensity and full load wind speed. In case of higher turbulence intensity, the revenue increases substantially.

Looking at these numbers, it has to be kept in mind that the controls of the FW is kept simple by applying conventional control engineering. It is assumed that the power steadying capabilities of the FW, and with it the additional energy yield, would increase considerable if more sophisticated control mechanisms were applied.

Whether the revenues derived here are sufficient for making the FW pay off is, obviously depending on the extra costs that occur from the FW. Hence, this work is only intended to show a trend for the economic potential in some selected operating points. Therefore, these operating points presented above can be further examined in another project to determine the maximum of possible steady power feed-in.

9 Aerodynamic Investigations Aiming at Increasing Space inside the Blades

This part summarizes investigations for modified geometrical blade shapes of NREL's 5 MW reference blade with increased thicknesses close to the tip. It must be noted that changing any given thickness distribution touches the heart of the aerodynamic design of any WT blade. For example, a monotonic decreasing thickness-to-chord distribution has to be maintained. Otherwise, due to the change in circulation, blade induction would deviate from its Optimum ($a = 1/3$). A more comprehensive description of the principles of aerodynamic blade design can be found in [37]. In short, thickness defines the aerodynamic profiles which are usually chosen to have maximum lift-to-drag ratio for a given design lift-coefficient. State-of-the-art profiles of 18% relative thickness (t) – to – chord (c) – ratio (t/c) are used at most outer sections, i.e. the blade sections that are close to the blade tip. Usually, aerodynamic data (lift- and drag as function of angle-of-attack (AOA)) is used in the BEM method. In case that early flow separation leading to much less lift and much more drag, so called vortex-generators [37] are used to improve flow quality. With these, it seems to be possible to use profiles with up to 26 % relative thickness-to-chord-ratio most outwards [Marc Petsche, Bewind, formerly SENVION, priv. comm., 2020].

9.1 Aerodynamic Profiles with Increased Thickness to Cord Ratio

Details of the of NREL's 5 MW baseline blade's aerodynamic design can be found in Resor 2013 [10]. NACA 64-6-18 (The last two digits indicate relative $t/c = 0.18$) is the profile used close to the tip. Therefore, it is chosen to investigate the modified thickness to chord distributions as shown in Figure 107.

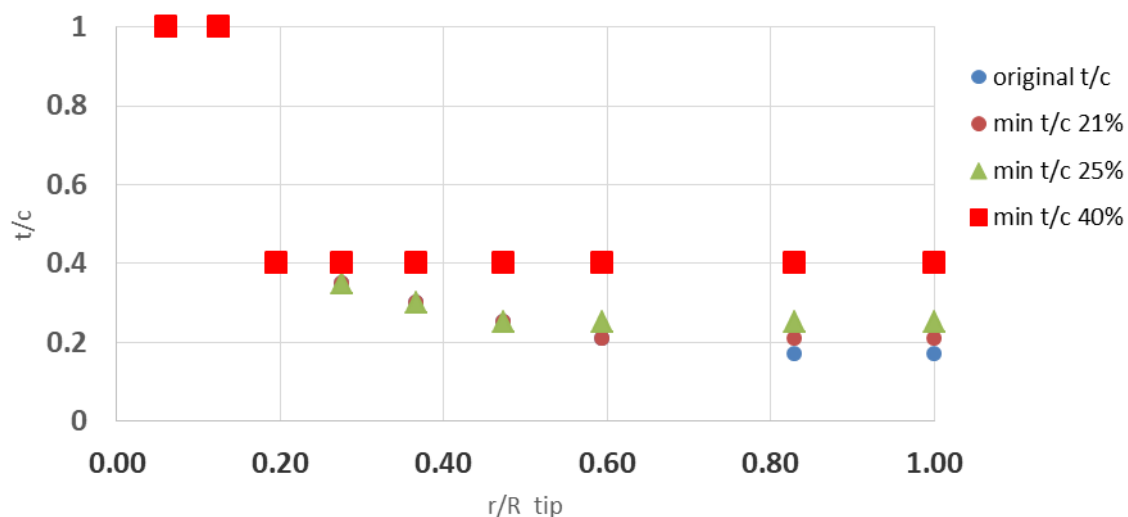


Figure 107: Relative thickness distribution (t/c) as function of relative blade-length. r is the distance from the rotational center, R_{tip} is the radius from the rotational centre to the tip.

The blades are changed by replacing the profile most outwards (lower t/c ratio) with the next inside, i.e. neighbouring profile with larger t/c ratio.

As an example, for the first modified blade (minimum thickness = 21%) there is at $r/R_{tip} > 0.6$ a new minimum thickness of $t/c = 0.21$. This corresponds to an exchange of NACA64-6-18 with DU00-W-212.

In principle, a NACA profile with increased thickness, for example NACA-42-21 could have been chosen as well, but there is no suitable aerodynamic data available.

The two other blades (with 25% and 40 % minimum thickness) are generated correspondingly.

The calculations are performed with NREL's BEM-Code *wt_perf* [39]. It uses Blade-Element-Momentum (BEM) theory in its original formulations, see [37] for the equations and how to solve them.

Power and thrust at rated wind speed (12 m/s) and rated RPM (12.1), are calculated both for the original and the modified blades, see Table 21 and Figure 108.

Table 21: Power and thrust as calculated with *wt_perf* for the original and for the modified blades

Case	Power/kW	thrust/kN	Pitch/deg
original 17%	6323	784	0
21%	6301	812	0
25%	6223	823	0
40%	5750	718	0
25%	6256	905	-2
40%	5960	818	-2

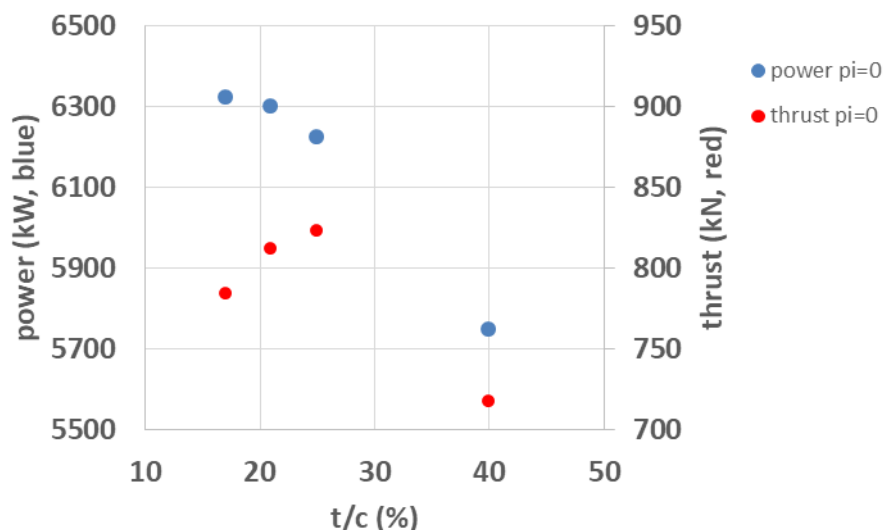


Figure 108: Power and thrust versus t/c for pitch angle of 0 deg.

Figure 108 gives an overview of the results. Power decreases smoothly with increasing thickness, whereas thrust increases. By pitching the blade by -2° (towards higher angle-of-attack) power may be increased, but on the price of even higher thrust (not shown in Figure 108).

Case 21% is investigated in more detail (see Figure 109 for the shapes).

To have a measure for the induced changes, it is decided to use power, which should not decrease by more than 1 % and thrust, as the principal load, which should not increase by more than 2 %.

For the blade with 21% thickness it is found:

Decrease of power by 1.8%,

Increase of thrust by 3.9%.

9.2 Impact on Blade Structure

As the thickness is increased a calculation of the changes in structural parameters (mass, stiffness etc.) is necessary. The well-known tool Xfoil [40] is used for computations. The geometrical definition is given as 200 points in the (x,y) plane. Chord length is normalized to one, so that the tail is at (1,0) and the nose at (0,0).

Table 22 summarises the basic geometrical parameters of the used aerodynamic profiles.

Table 22: Basic geometrical properties of used profiles.

Name	t/c	arc length (see Figure 109)	cross sectional area	camber (%)
NACA-63-6-18	0.18	2.0674	0.11242	3.9
DU00-W-212	0.21	2.0795	0.12692	1.8
DU99-W-400	0.40	2.2653	0.2417	2.1

Figure 109 illustrates the cross sectional shapes as x-y-plots of the different profiles.

Due to increasing thickness the arc lengths increase by 3.4% (DU00-W-212) and even by 9.4% (DU99-W-400). Assuming that mass change is proportional to change of arc length (as most of the added material will be close to the surface) a change in mass $\Delta m = 74 \text{ kg}$ (+0.4 %) can be estimated if a representative average mass density of $\rho = 2600 \text{ kg/m}^3$ is assumed. The reference mass of the whole original blade is 16404 kg. This small amount (+0.4 %) should be within the manufacturing tolerances.

As the model assumes that all relevant parts of the material are placed close to the surface, it can be concluded that all structural properties, like stiffness, at least should not decrease.

Comparison of basic geometrical properties

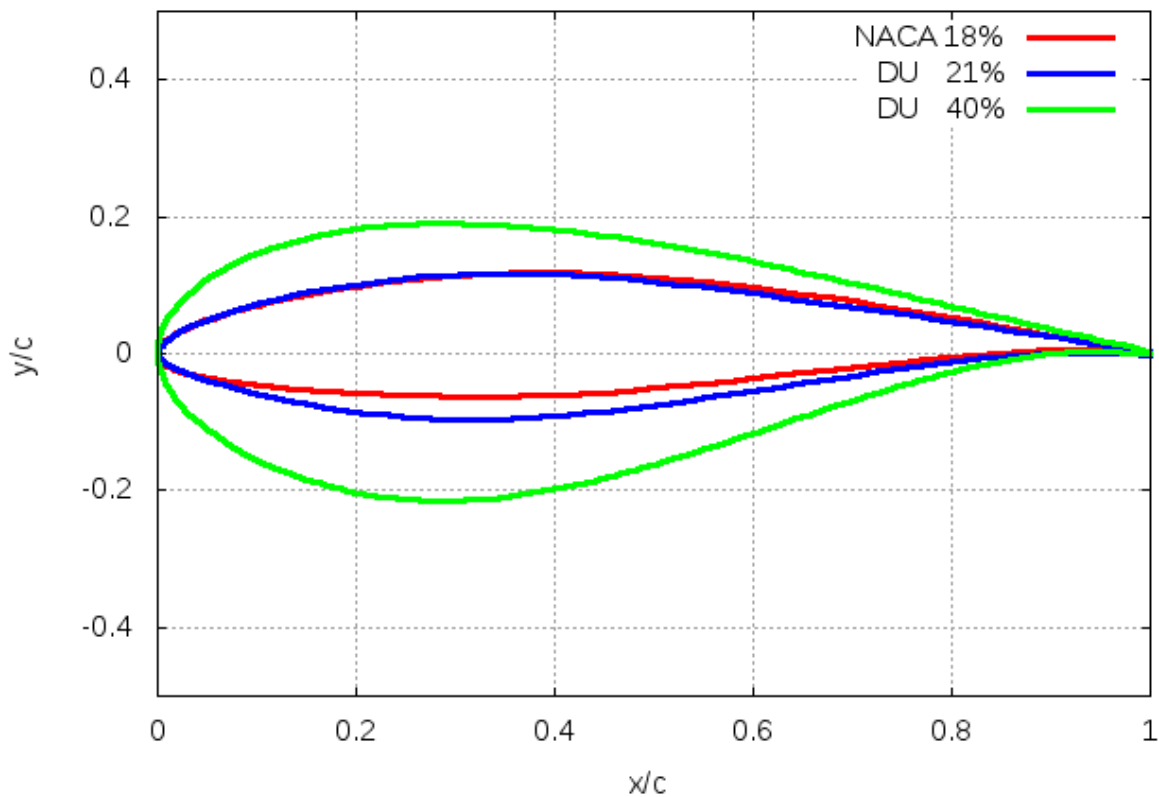


Figure 109: Geometrical shape of three most outer profiles from.

9.3 Summary and Conclusion

The NREL baseline reference blade is investigated by replacing successively the most outer profile (NACA 18%) by the next inner ones (DU 21%, DU25% and DU40%). Using a suitable BEM model, the investigation shows that the power decreases at least by 1 % and a characteristic load (thrust) increases by more than 4 %, if DU21 is used to replace NACA 18%. This trend continues if even thicker profiles (DU25, DU40) are used.

From that it may be concluded that, if a substantial change of a tried-and-tested thickness (airfoil) distribution (original NREL baseline reference blade) is demanded then an integral design approach seems to be more appropriate. All additional interior structure has to be integrated as load-carrying parts, giving rise to a much different structural design process.

References

- [1] Jauch, C., 'First Eigenmodes Simulation Model of a Wind Turbine - for Control Algorithm Design', WETI Hochschule Flensburg, 07.09.2020, DOI: 10.13140/RG.2.2.17192.19204
- [2] N. Thomsen, M. Maack, „Auslegung eines hydraulischen Pumpensystemes für hydropneumatischen Schwungradspeicher in WEA-Rotor“ Oct-2018
- [3] Xylem, „e-MP Series MPA, MPR, MPD, MPV. 155“ 2018
- [4] WEG Australia, „W22 Three Phase Electric Motor“
- [5] KÜHLSOLE GmbH, „Glykosol N Datenblatt“
[Online].<https://www.prokuehlsole.de/produkte/details/glykosol-n>, accessed 21 December 2018
- [6] KSB Aktiengesellschaft, „Auslegung von Kreiselpumpen“ (Bd. 5) (K. Aktiengesellschaft, Hrsg.) Frankfurt 2005
- [7] G. S. Bir, „User's Guide to PreComp (Pre-Processor for Computing Composites Blade Properties)“.
[Online]. <https://nwtc.nrel.gov/system/files/PreComp.pdf>, accessed 21 December 2018
- [8] J.C. Berg, and B.R. Resor, „Numerical Manufacturing And Design Tool (NuMAD v2.0) for Wind Turbine Blades: User's Guide“). [Online] <https://prod.sandia.gov/techlib-noauth/access-control.cgi/2012/127028.pdf>, accessed 21 December 2018
- [9] J. Berg, B.R. Resor, B.C. Owens, and D. Laird, „Numerical Manufacturing and Design Tool (NuMAD) for Wind Turbine Blades. (v2.0)“.
[Online].<https://energy.sandia.gov/energy/renewable-energy/wind-power/rotor-innovation/numerical-manufacturing-and-design-tool-numad/>, accessed 21 December 2018
- [10] B. Resor, „Definition of a 5MW/61.5m Wind Turbine Blade Reference Model“. April-2013 [Online]. <https://prod.sandia.gov/techlib-noauth/access-control.cgi/2013/132569.pdf>, accessed 21 December 2018
- [11] Hippel, S.; Jauch, C.; Ritschel, U., 'Hydraulic-pneumatic flywheel configurations for controlling the inertia of a wind turbine rotor', Wind Engineering, vol. 43, issue 2, pp. 114–132, DOI: 10.1177/0309524X18780386, 2019
- [12] Kundur, P.: 'Power system stability and control', McGraw-hill New York, 1994
- [13] Fischer, R.: 'Elektrische Maschinen', 10th edition, Carl Hanser, Munich, Vienne, 2000
- [14] energie.ch ag: 'Datenblatt Asynchronmaschinen', <http://www.energie.ch/datenblatt-asynchronmaschinen>, available 29 November 2018
- [15] Hippel, S.; Jauch, C., 'Load Analysis of Hydraulic-Pneumatic Flywheel Configurations Integrated in a Wind Turbine Rotor' Wind Energy, vol. 22, pp. 1190–1202, DOI: 10.1002/we.2349, 2019
- [16] G.S.Bir, „User's Guide to BModes (Software for Computing Rotating Beam Coupled Modes)“
[Online]. <https://nwtc.nrel.gov/BModes> accessed 18 February 2019
- [17] J. Jonkman, S. Butterfield, W. Musial, and G. Scott, „Definition of a 5-MW Reference Wind Turbine for Offshore System Development“
[Online]. <https://www.nrel.gov/docs/fy09osti/38060.pdf> accessed 19. February 2019
- [18] Lutz, H. and Wendt, W. „Taschenbuch Der Regelungstechnik“, Verlag Harri Deutsch, 2005, 3-8171-1749-3
- [19] Nise, N. S. "Control Systems Engineering", Third Edition, John Wiley & Sons, 2000, ISSN/ISBN: 0-471-36601-3

- [20] INTERNATIONAL STANDARD iec 61400-1, Wind turbines- Part 1: Design requirements, Third Edition, August 2005
[Online]: https://webstore.iec.ch/preview/info_iec61400-1%7Bed3.0%7Den.pdf accessed 26. February 2019
- [21] Lauer, J. 'Hydropneumatische Speicher in Rotorblättern von Windkraftanlagen' 28. February 2015
- [22] Jauch C (2014) A flywheel in a wind turbine rotor for inertia control. Wind Energy, vol. 18, pp. 16451656, DOI: 10.1002/we.1784. accessed 03. February 2020
- [23] C. Jauch, "Controls of a flywheel in a wind turbine rotor," WIND ENGINEERING, vol. 40, issue 2, pp. 173-185, DOI: 10.1177/0309524X16641577, accessed 03. February 2020
- [24] DNV GL, 'Bladed - industry standard aero-elastic wind turbine design tool',
[Online]: <https://www.dnvgl.com/services/wind-turbine-design-software-bladed-3775>, accessed 26. Jun 2019
- [25] B.J. Jonkman, J. Michalakes, J.M. Jonkman, M.L. Buhl, Jr., A. Platt, and M.A. Sprague „NWTC Programmer's Handbook: A Guide for Software Development Within the FAST Computer-Aided Engineering Tool“
[Online]:https://nwtc.nrel.gov/system/files/ProgrammingHandbook_Mod20130717.pdf accessed 04. February 2020
- [26] OpenFAST DocumentationRelease v2.1.0 National Renewable Energy Laboratory Nov 13, 2019
[Online]: <https://openfast.readthedocs.io/en/master/pdf/> accessed 05. February 2020
- [27] FAST v8.16.00a-bjj, Bonnie Jonkman and Jason Jonkman, National Renewable Energy Laboratory, July 26, 2016
[Online]: https://wind.nrel.gov/nwtc/docs/README_FAST8.pdf accessed 06. February 2020
- [28] Overview of the ElastoDyn Structural-Dynamics Module, NREL Wind Turbine Modeling Workshop November 20, 2013 EWEA Offshore Frankfurt, Germany, Jason Jonkman, Ph.D.Senior Engineer, NREL
[Online]:https://wind.nrel.gov/public/jjonkman/Presentations/WindTurbineModelingWorkshop_131120_EWEAOffshore_FrankfurtGermany/3_ElastoDyn_Jonkman.pdf accessed 11. February 2020
- [29] NWTC Programmer's Handbook: A Guide for Software Development Within the FAST Computer Aided Engineering Tool, B.J. Jonkman, J. Michalakes, J.M. Jonkman, M.L. Buhl, Jr., A. Platt, and M.A. Sprague
[Online]: https://nwtc.nrel.gov/system/files/ProgrammingHandbook_Mod20130326.pdf accessed 13. February 2020
- [30] C. Jauch and S. Hippel, "Hydraulic-pneumatic flywheel system in a wind turbine rotor for inertia control", IET Journals, May 2015, issn: 1752-1416. doi: 10.1049/iet-rpg. 2015.0223
- [31] V. Quaschnig, Regenerative Energiesysteme, 8.Auflage. Hanser Verlag München, 2013, isbn: 978-3-446-43526-1.
- [32] M. Kaltschmitt, W. Streicher, and A. Wiese, Erneuerbare Energien, 5th ed., M. Kaltschmitt, W. Streicher, and A. Wiese, Eds. Springer-Verlag Berlin Heidelberg, 2014, isbn: 9783642032486.
DOI: 10.1007/978-3-642-03249-3.

- [33] S. Hippel and C. Jauch, “Hydraulic-pneumatic energy storage in a wind turbine for enhancing the power system inertia”, Nov. 2014. doi: 10.13140/2.1.3731.6160.
- [34] N. K. GmbH. (2019). Was ist einspeisemanagement? German, [Online]. Available: <https://www.next-kraftwerke.de/wissen/einspeisemanagement>.
- [35] Bundesnetzagentur, “Leitfaden zum einspeisemanagement version 3.0”, Bundesnetzagentur für Elektrizität, Gas, Telekommunikation, Post und Eisenbahnen, Tech. Rep., Jun. 2018. [Online]. Available: www.bundesnetzagentur.de/einspeisemanagement.
- [36] D. rer. nat. Hermann van Radecke, “Wind energy basics”, Unpublished lecture notes, University of Applied Science Flensburg, 2017
- [37] A.P. Schaffarczyk, Introduction to Wind Turbine Aerodynamics, 2nd. Ed. Springer-Nature, Heidelberg, Germany (2020)
- [38] C. Jauch, A. Gloe, S. Hippel, and H. Thiesen, “Increased wind energy yield and grid utilisation with continuous feed-in management”, Energies(MDPI), Jun. 2017. DOI: 10.3390/en10070870.
- [39] M.L. Buhl, WT_Perf User’s Guide, NREL, (2004)
- [40] M. Drela, XFOIL: An Analysis and Design System for Low Reynolds Number Airfoils. In: T.J. Müller, Ed., Low Reynolds Number Aerodynamics, Springer-Verlag, June 1989, LN in Eng, No. 54
- [41] PROF. DR.-ING. DR.-ING. E.H. WALTER MICHAELI COMPOSITOR Hilfsmittel zur Analyse von Laminaten aus Faserverbundkunststoffen Bedienungsanleitung Version 4.1 03/2009 <https://www.ikv-aachen.de/>. 81.
- [42] Barlow’s Formula Available online: <https://www.amerpipe.com/reference/charts-calculators/barlows-formula/> (accessed on Aug 16, 2020).